Elucidating the Interactions between Antimicrobial Peptides and Periplasmic Osmolytes in *Escherichia coli*

Cyril Schroeder

St Edmund Hall

University of Oxford

A thesis submitted for the degree of

Doctor of Philosophy

Trinity 2025

Abstract

Elucidating the Interactions between Antimicrobial Peptides and Periplasmic Osmolytes in *Escherichia coli*

Cyril Schroeder

St Edmund Hall, University of Oxford

A thesis submitted for the degree of Doctor of Philosophy

Trinity 2025

Antimicrobial resistance poses a major threat to global health, and Gram-negative bacteria remain particularly difficult to combat due to their complex cell envelopes. Antimicrobial peptides (AMPs) are promising therapeutic candidates, but their precise mechanisms of action remain debated, and only a few have been successfully translated into effective drugs. A critical but underexplored factor is how interactions with the crowded, chemically heterogeneous periplasm influence AMP behaviour during their envelope translocation. In particular, the role of periplasmic osmolytes in modulating peptide aggregation, membrane interactions, and pore formation has received little attention.

This thesis investigates how osmolytes affect AMP behaviour in both solution and membrane environments. Three representative α-helical amphipathic cationic peptides were selected to capture differences in charge density. Atomistic molecular dynamics simulations were used to investigate peptide aggregation in crowded solutions representing the *E. coli* periplasm. Complementary coarse-grained simulations of magainin 2 with realistic *E. coli* inner membranes under an induced transmembrane potential were performed to study peptide-mediated pore formation.

Both membrane protein-independent and -dependent translocation mechanisms were observed.

In solution, all AMPs aggregated into micelle-like structures, with sequence, initial conformation, and solute phase composition strongly influencing aggregation. Osmolytes stabilised aggregates through residue-specific electrostatic shielding of repulsive same-charge interactions and through more promiscuous polar interactions, providing the first mechanistic insight into how periplasmic solutes shape AMP organisation before membrane encounter.

In membranes, four pore-formation pathways were identified, with two predominating: single-peptide “snorkelling” along membrane proteins and AMP aggregate-induced bulk membrane rupture. Osmolytes did not alter the overall pore formation frequency but shifted the mechanism distributions, favouring aggregate-driven rupture over snorkelling, by promoting larger aggregates.Overall, this work demonstrates that realistic periplasmic environments fundamentally shape AMP behaviour in ways not captured by simplified models, offering mechanistic insights to guide the rational design of AMPs that retain their activity within the complex cell envelope of Gram-negative bacteria.

Acknowledgments

Firstly, I would like to thank Professor Syma Khalid for her patient guidance throughout this academic journey and for teaching me how to think from the ground up. Without her time and support, I would not have reached this point.

I owe immense gratitude to my family for their unwavering support and encouragement, without whom I would not be where I am today: my parents, Anne and Marc, and my brother, Louis.

To my wonderful partner, Luisa, thank you for always being by my side and for bringing light and warmth into my life.

I would also like to thank all members of the Khalid Lab, past and present, for making the lab such a supportive and inspiring environment. I am especially grateful to Nikolai Juraschko and Zephyr Ford for sticking together since the beginning.

To the members of SBCB past and present, including but not limited to Dheeraj Prakaash, Mingyu Qin, Robert Clark, Iain Smith, Jonathan Colburn, Nitishwer Anand, David Seiferth, Eden Gage, and Ziwei Pang: Thank you for the fun lunches and countless laughs.

To my Teddy friends, I hope we will always continue to look out for each other. Thank you to Momo Komatsu and Edward Taylor, Rebekka Geremew, Oleksii Malyshev, Matthew Filipovich, Sarah Savić Kallesøe, and Marek Grzesiuk for making college feel like home.

Thank you to Thibault Jouen-Tachoire for all the fun and stylish self-care outings.

To my old friends from home, Maximilian Hartung and Lex Scholtes, thank you for keeping up our near-weekly calls over the years and for walking through life together. I am also grateful to the G-Unit, Adrian Woenckhaus-Alvarez, Patrick Finkelstein, and Tom Schatteburg, as well as to Marc Siggel and Markus Fischer for staying in touch since we were academic neophytes, and to Konstantin Zouboulis for looking out for me in Oxford since before we arrived.

To my newest friends, Kieran Didi and Jérôme Zürcher, thank you for your kindness and for being there when it truly mattered.

In writing these acknowledgements, I am reminded of how many people have shaped this journey for the better. We are, after all, the sum of the people around us, and I have been incredibly fortunate to have met so many wonderful ones during my time down here.

Per aspera ad astra

Contents

List of figures

List of tables

List of acronyms and abbreviations

Å	Ångström
AA	All-atom
AMP	Antimicrobial peptide
ANOVA	Analysis of variance
ATP	Adenosine triphosphate
C1	Cupiennin-1a
Ca, CA	Calcium
CD	Circular dichroism
CG	Coarse-grained
Cl, CL	Chloride
CompEL	Computational Electrophysiology
DMPC	1,2-Dimyristoyl-*sn*-glycero-3-phosphocholine
DMPG	1,2-Dimyristoyl-*sn*-glycero-3-phospho-(1′-*rac*-glycerol)
DNA	Deoxyribonucleic acid
DOPC	1,2-Dioleoyl-*sn*-glycero-3-phosphocholine
DOPE	1,2-Dioleoyl-*sn*-glycero-3-phosphoethanolamine
DOPG	1,2-Dioleoyl-*sn*-glycero-3-phospho-(1′-*rac*-glycerol)
DPC	Dodecylphosphocholine
DPPC	1,2-Dipalmitoyl-*sn*-glycero-3-phosphocholine
DPPE	1,2-Dipalmitoyl-*sn*-glycero-3-phosphoethanolamine
DPPG	1,2-Dipalmitoyl-*sn*-glycero-3-phospho-(1′-*rac*-glycerol)
E. coli	*Escherichia coli*
FFT	Fast Fourier Transform

HPC	High-Performance Computing
KDE	Kernel density estimate
L1	Latarcin 1
LacY	Lactose permease
LINCS	Linear Constraint Solver
LPS	Lipopolysaccharides
M2	Magainin 2
MD	Molecular dynamics
MLP	Machine-learned potential
MM	Molecular mechanics
Na, NA	Sodium
nm	Nanometre
NMR	Nuclear Magnetic Resonance
NPT	Isothermal-isobaric ensemble
NT	N-terminus
NVE	Microcanonical ensemble
NVT	Canonical ensemble
O	Order
OPG	Osmoregulated periplasmic glucan
p	p-value
PBC	Periodic Boundary Conditions
PDB	Protein Data Bank
PE	Phosphatidylethanolamine
PG	Phosphatidylglycerol
PHE	Phenylalanine

PHOS	Hydrogen phosphate anion (HPO_4^{2-})
PME	Particle Mesh Ewald
PMF	Proton motive force
POPE	1-Palmitoyl-2-oleoyl-*sn*-glycero-3-phosphoethanolamine
POPG	1-Palmitoyl-2-oleoyl-*sn*-glycero-3-phospho-(1′-*rac*-glycerol)
PUT	Putrescine
PW	Polarisable water
QM	Quantum mechanics
RDF	Radial distribution function
SDS	Sodium dodecyl sulphate
SPER	Spermidine
TREH	Trehalose
V-rescale	Velocity-rescale thermostat
VAP	Ventilator-associated pneumonia
ε_r	Relative dielectric constant
μs	Microseconds
τ	Thermostat coupling constant

Chapter 1

Introduction

Antimicrobial resistance (AMR) occurs when microorganisms undergo evolutionary changes and become insensitive to previously effective antimicrobial treatments.[1] A study led by the Oxford Global Burden of Disease Group highlighted that AMR is a critical global health crisis, directly causing an estimated 1.27 million deaths and associated with nearly 5 million deaths in 2019, surpassing fatalities from HIV/AIDS and malaria combined.[1] Of the six leading pathogens associated with AMR-related mortality in 2019, four were Gram-negative bacteria, with *Escherichia coli* being the most lethal among them.[1] These excess deaths would be compounded by severe economic repercussions, with projections that unchecked AMR could reduce the global GDP by up to 3.8% and cost the world economy $1.7 trillion annually by 2050.[2,3]

To address this crisis, expert bodies have recommended that 6-15 new antibiotics should be discovered per decade to replace old therapies and ensure multiple treatment options are available for priority pathogens.[3–5] Despite the growing public health threat, large pharmaceutical companies have increasingly withdrawn from antibiotic development due to poor economic returns on investment.[6] As a result, the responsibility for early-stage antibiotic research and development has shifted mainly to academic groups, smaller biotech firms, and non-profit organisations.[6] This fragmented and stagnant innovation landscape, combined with rising rates of antimicrobial resistance, underscores the urgent need for a renewed focus on fundamental research. Enhancing our understanding of antimicrobial modes of action and bacterial resistance mechanisms is thus essential to guide the

development of effective new therapeutics and to meaningfully address the AMR crisis.

1.1 The cell

Building on Robert Hooke's initial discovery of cells in 1665, the cell theory was first formally established by Theodor Schwann and Matthias Jakob Schleiden in 1839.[7–10] This theory states that all known life forms on Earth are composed of cells, the fundamental structural and functional units of life.[10]

Based on differences in cellular structure and genetics, Carl Richard Woese and colleagues developed a taxonomic system classifying life into three domains: Eukarya, Archaea, and Bacteria.[11] The distinction between eukaryotes (the former domain) and prokaryotes (the latter two domains) lies in their internal complexity, as schematically represented in **Figure 1.1**.[11] Eukaryotic cells are characterised by the presence of a membrane-bound nucleus and other compartmentalised organelles that perform specialised functions, such as mitochondria or the endoplasmic reticulum.[12] In contrast, prokaryotic cells are defined by their lack of both these features, with their genetic material freely located in the cytoplasm, and carry out cellular functions within an undivided cytoplasmic compartment.[12] Furthermore, while eukaryotic organisms can be either unicellular or multicellular, prokaryotes are strictly unicellular and generally substantially smaller, usually ranging in size from 1 to 10 μm, compared to the larger eukaryotes, which range from 10 to 100 μm.[13]

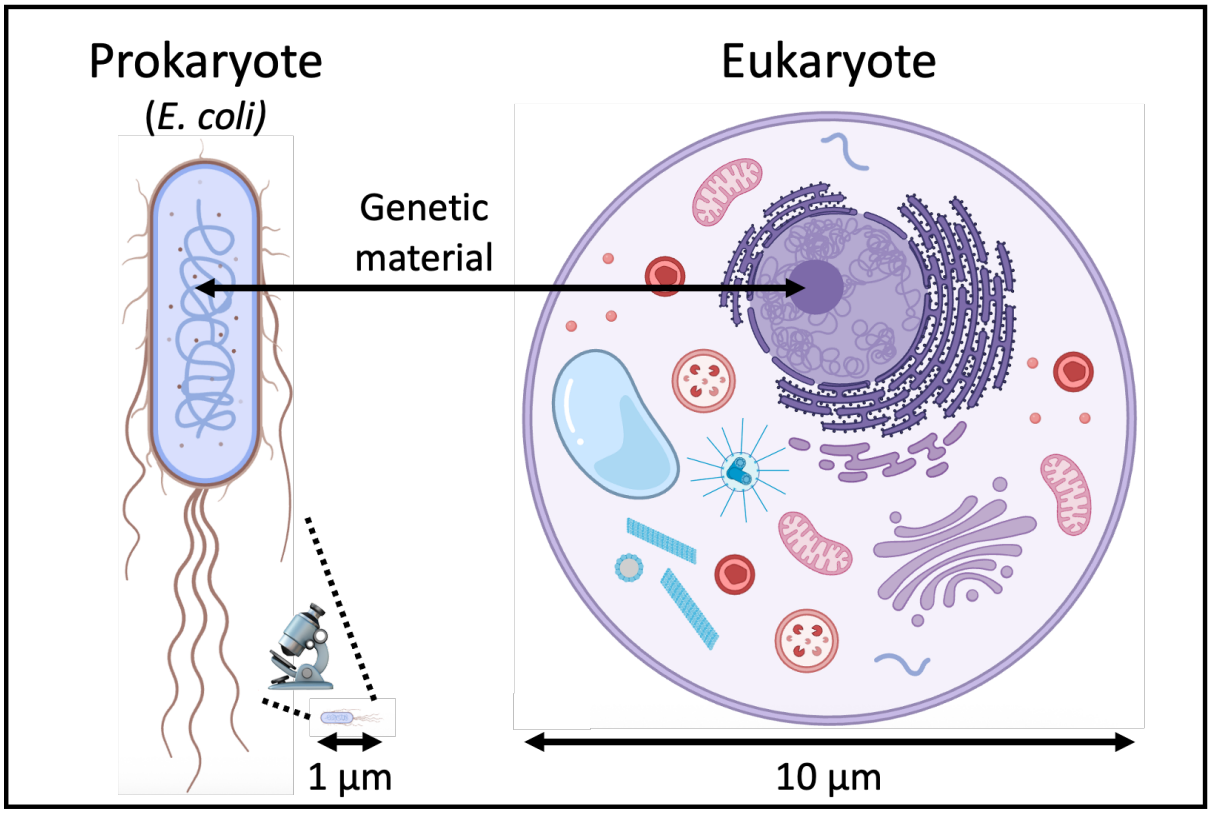

Figure 1.1. *Schematic representation contrasting a typical prokaryotic cell (left) and a eukaryotic cell (right), with relative size shown to scale and a zoomed-in view of the smaller prokaryotic cell. The genetic material of the prokaryote is represented by the unbounded purple coil, while the nucleus (purple circle) holds the genetic material of the eukaryote. Image generated using BioRender.com.*

Despite their relative simplicity compared to eukaryotes, prokaryotic cells are nonetheless complex structures and are organised into two primary regions: the cytoplasm and the cell envelope.[11] The cytoplasm is a crowded and viscous matrix containing the cellular genetic material and metabolic machinery.[11] Surrounding this is the cell envelope, a vital and multi-layered structure that protects the cell and mediates interactions with its environment.[14] Given its dual importance as the primary target and critical barrier for many antimicrobials, the distinct molecular architecture of the bacterial cell envelope requires a detailed structural

characterisation to inform our understanding of the mechanisms of action of bactericidal therapeutics.[15]

1.2. The bacterial cell envelope

In bacteria, the cell envelope encompasses all structures surrounding the cytoplasm, forming the outermost boundary of the cell. It plays a central role in maintaining cellular shape and rigidity, while also acting as a selective permeability barrier that regulates the transport of nutrients, waste, and signalling molecules.[14] Furthermore, bacterial cell envelopes consistently present a net negative surface charge, a key feature that differentiates them from the typically zwitterionic membranes of normal mammalian cells.[16]

Beyond this shared trait, the cell envelope structure varies between Gram-positive and Gram-negative bacteria, resulting in differences in permeability and ability to resist external stressors such as antibiotics or antimicrobial peptides.[14,16,17] Gram-positive bacteria, also referred to as monoderms, possess a comparatively simpler envelope, defined by a thick layer of peptidoglycan surrounding a single cytoplasmic membrane.[12] In contrast, Gram-negative bacteria have a more complex diderm structure, with both a protective outer membrane (OM) and an inner membrane (IM) surrounding the cytoplasm.[12] Sandwiched between these membranes is the periplasm, a compartment that contains the cell wall, a thin layer of peptidoglycan (PG).[12] These contrasting cell envelope structures are detailed in the following sections and are schematically represented in **Figure 1.2**.

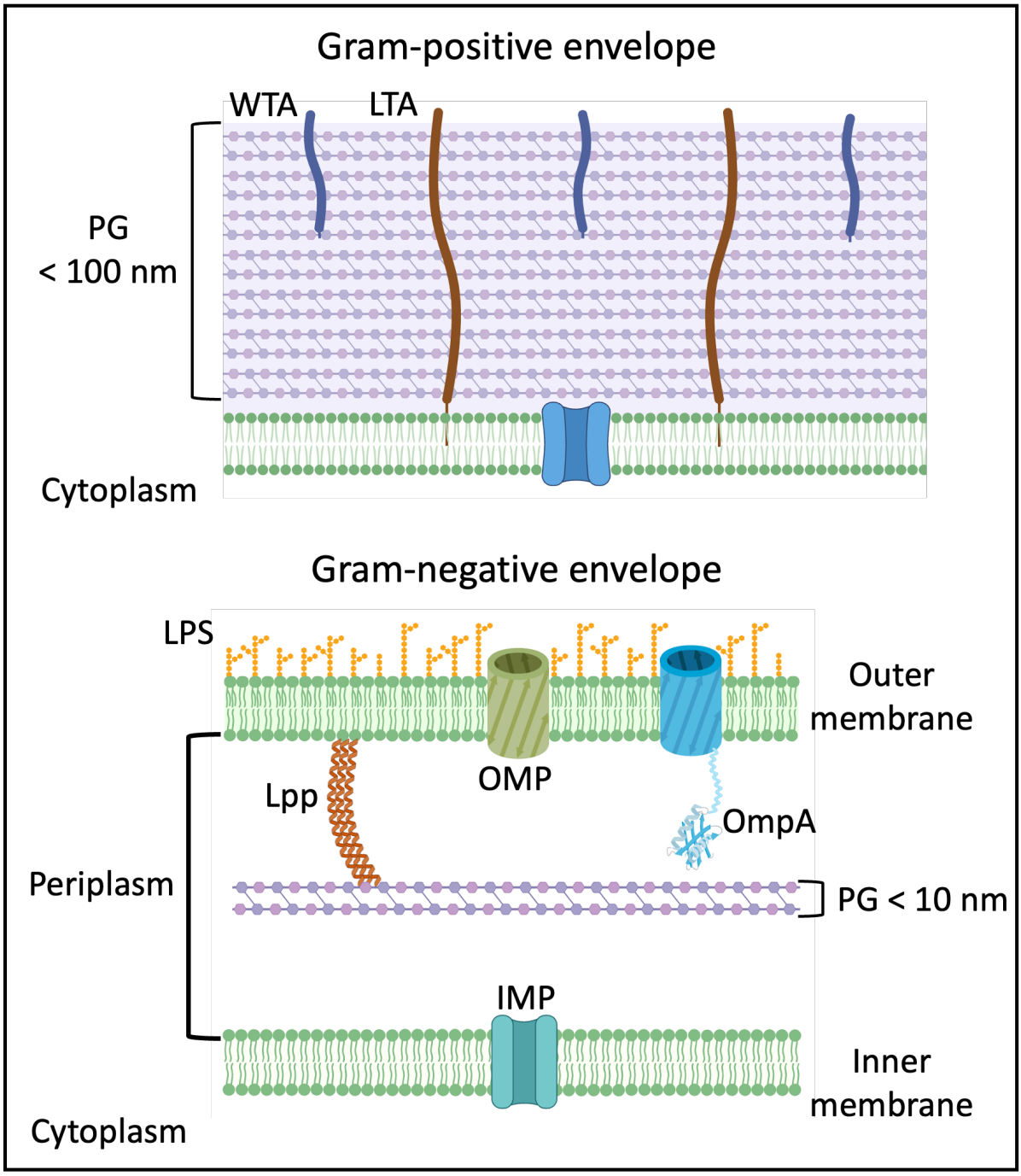

Figure 1.2. *Schematic comparison of the Gram-positive and Gram-negative cell envelope, highlighting the different envelope structures and peptidoglycan cell wall thicknesses. Membranes are shown in green, and peptidoglycan is shown as pink cross-linked hexagons. In Gram-positive bacteria (top), a thick multilayered peptidoglycan matrix contains wall teichoic acids (WTA, blue) and is anchored to the cytoplasmic membrane via lipoteichoic acids (LTA, brown). Legend for the Gram-*

negative bacteria (bottom): lipopolysaccharide (orange, above OM), Braun's lipoprotein (Lpp, orange tri-coiled structure), outer membrane proteins (OMP, green and blue β-barrels), and inner membrane protein (IMP, teal). Image generated using BioRender.com.

1.2.1 Gram-positive and Gram-negative bacteria

The fundamental classification of bacteria into Gram-positive and Gram-negative groups originates from a differential staining technique developed by Hans Christian Gram in 1884 while investigating bacteria in lung tissue sections from patients who had died of pneumonia.[18–20]

The procedure begins by staining all bacteria purple with crystal violet, followed by the addition of iodine, which forms dye-iodine complexes. The differential step is the alcohol wash: in Gram-positive bacteria, the alcohol dehydrates their thick, exposed peptidoglycan wall, trapping the purple dye complex. In contrast, the alcohol disrupts the outer membrane of Gram-negative bacteria, which their Gram-positive counterparts lack, and their thin peptidoglycan layer cannot retain the complex. Finally, a safranin counterstain is applied, which colours the now-colourless Gram-negative cells pink but leaves the purple Gram-positive cells unaffected.

This classification is not merely descriptive but reflects an essential ultrastructural difference with direct medical relevance: Gram-positive bacteria, such as *Staphylococcus aureus* and *Bacillus subtilis*, are generally more susceptible to antibiotics and antimicrobial peptides than Gram-negative bacteria like *Escherichia coli* and *Pseudomonas aeruginosa*.[14,21] This difference in antibiotic susceptibility is primarily due to the protective outer membrane of the latter category, as detailed below.[14]

1.2.2 Cell wall

The bacterial cell wall is an essential bacterial structure that provides mechanical strength and maintains cell shape under turgor pressure.[14,22] It is primarily composed of peptidoglycan (PG), a rigid, mesh-like polymer previously referred to as murein.[14,22] The basic PG structure is conserved across bacterial species and consists of linear glycan strands composed of alternating *N*-acetylglucosamine (NAG) and *N*-acetylmuramic acid (NAM) residues.[14,22] Each NAM unit is linked to a short peptide stem, which cross-links neighbouring glycan strands and forms a continuous three-dimensional structure referred to as the sacculus.[14,22] The chemical structure of this cross-link is shown in **Figure 1.3**.

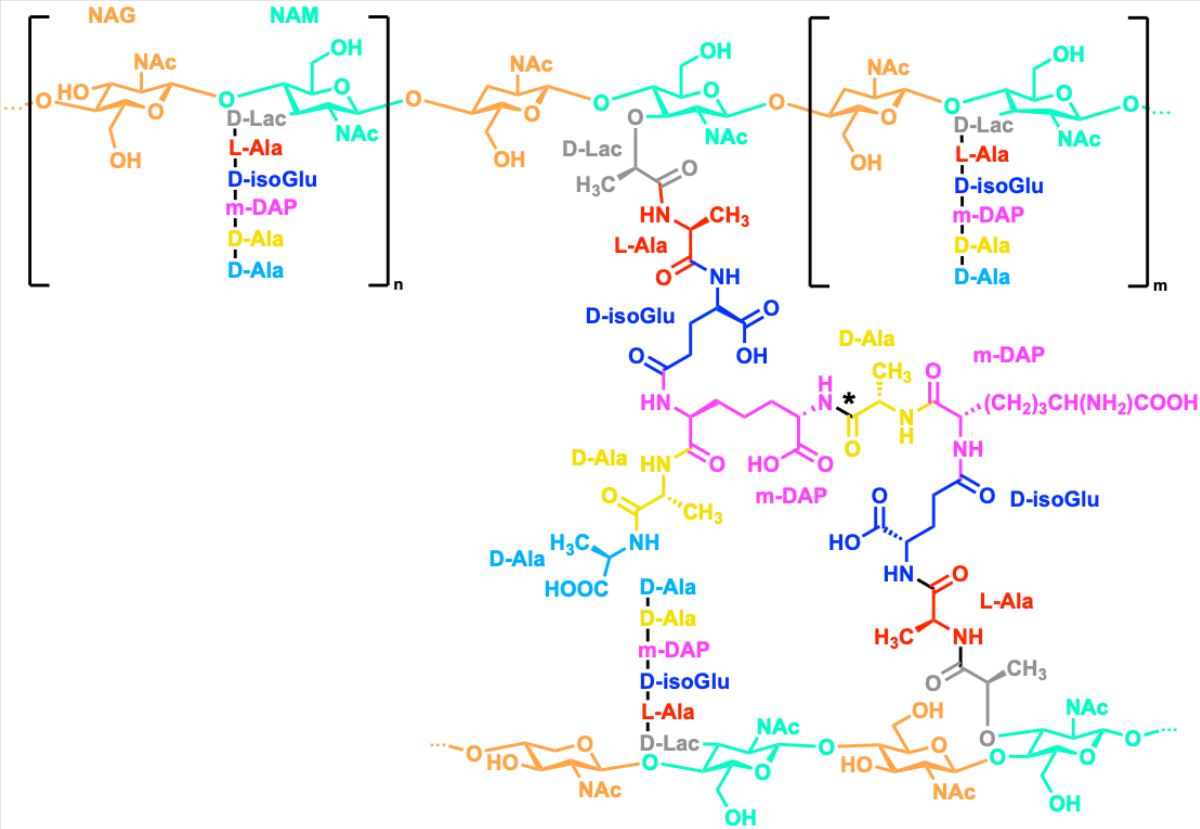

Figure 1.3. *Chemical structure of the E.coli peptidoglycan cell wall coloured by residue. The peptide cross-linking bond between neighbouring glycan strands in the*

centre is highlighted by an asterisk (, bond in black).*[23] *Abbreviations: NAG: N-acetylglucosamine,*
NAM: N-acetylmuramic acid, D-Lac: D-lactic acid, L-Ala: L-alanine, D-isoGlu: D-isoglutamic acid, m-DAP: meso-diaminopimelic acid, D-Ala: D-alanine.

Despite this shared biochemical foundation, the architecture of the PG layer differs markedly between Gram-positive and Gram-negative bacteria, as previously shown in **Figure 1.2**. In Gram-positive species, the cell wall is an exterior-facing structure that is 30-100 nm thick, heavily cross-linked and interwoven with anionic polymers such as teichoic acids, being either wall teichoic acids (WTA), which are covalently attached to the peptidoglycan, or lipoteichoic acids (LTA), which are anchored in the cytoplasmic membrane. These polymers contribute to cation homeostasis and resistance to antimicrobial compounds.[14]

In contrast, Gram-negative bacteria possess a much thinner cell wall, typically only a few nm thick, located within the periplasmic space between the inner and outer membranes. This cell wall consists of only 1-3 PG layers, which are less densely cross-linked than those of Gram-positive species and lack teichoic acids.[14,24,25] Instead, it is anchored to the outer membrane by the lipoprotein called Braun's lipoprotein (Lpp), which forms covalent attachments to the PG, and the β-barrel protein OmpA, which attaches to the cell wall through non-covalent interactions, as schematically represented in **Figure 1.2**.[26,27] The PG layer is not static but is continuously remodelled during growth and division through the coordinated activity of biosynthetic and hydrolytic enzymes.[28] As a key structural component of the envelope, the cell wall is also a primary target of antibiotics such as β-lactams and

vancomycin, which inhibit transpeptidase activity and block glycopeptide cross-linking.[29,30]

1.2.3 Outer membrane

The outer membrane (OM) of Gram-negative bacteria is a unique, asymmetric lipid bilayer essential for their survival.[14,25] The outer leaflet, which faces the external environment, is almost exclusively composed of the glycolipid lipopolysaccharide (LPS), while the inner leaflet consists of a mixture of phospholipids.[14,25] This mixture primarily contains phosphatidylethanolamine (PE), phosphatidylglycerol (PG), and cardiolipin (CDL) headgroups, with acyl tails of variable saturation and length (usually 12-18 carbons).[31–33]

LPS molecules consist of linked three domains: a hydrophobic lipid A anchor embedded in the membrane, a highly variable O-antigen that forms an outward-facing polysaccharide shield, and a core oligosaccharide bridge between them, as schematically illustrated in **Figure 1.4**.[34,35] This O-antigenic structural diversity directly contributes to antigenic variation, facilitating bacterial evasion of the host immune system.[34,35] Strains possessing a complete O-antigen are termed “smooth” and are generally more virulent, as they are well-protected from the host immune response.[36,37] “Rough” strains lack the full O-antigen, leaving them more exposed to immune defences and certain antibiotics.[36,37]

The LPS layer on the bacterial surface carries a strong negative charge due to the numerous phosphate groups in the lipid A and core oligosaccharide domains.[34] To counteract the resulting electrostatic repulsion, divalent cations (mainly Mg^{2+} and Ca^{2+}) stabilise the membrane by forming ionic cross-bridges between adjacent LPS molecules.[21,38,39] These strong interactions substantially slow down the lateral

diffusion of LPS, resulting in a tightly packed outer leaflet with low fluidity that functions as a potent permeability barrier.[21,38] This barrier is a key factor in the innate resistance of Gram-negative bacteria to many antibiotics when compared to their Gram-positive counterparts, with the sugar moieties allowing Gram-negative bacteria to evade the host immune system.[17,34,37]

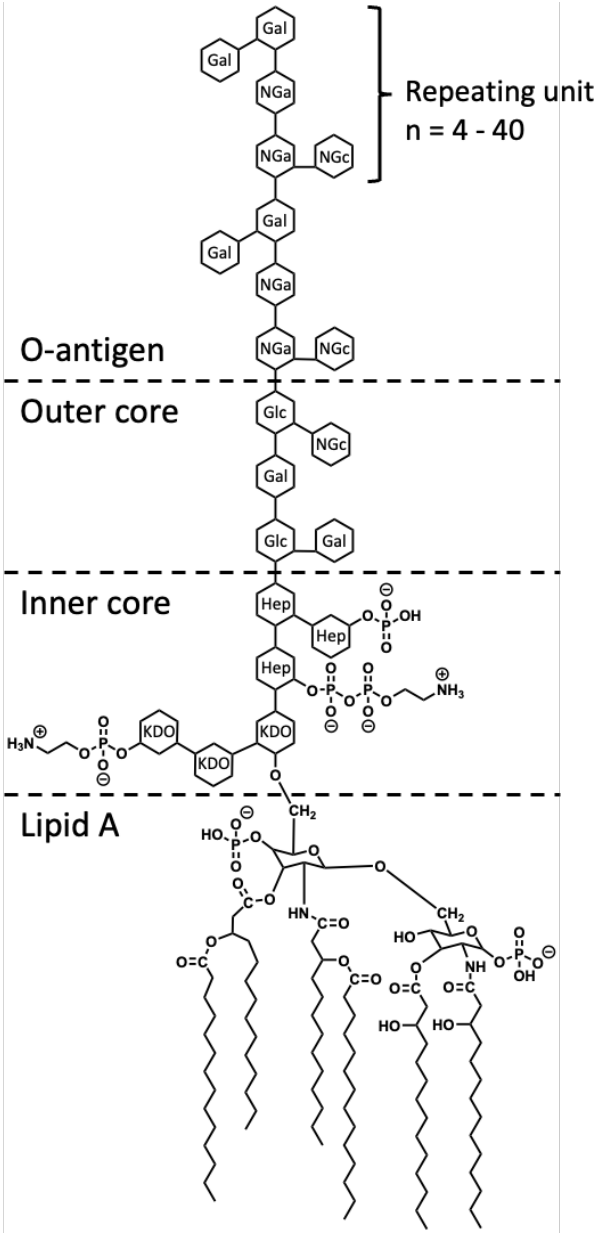

Figure 1.4. *Chemical structure of E. coli LPS with an R3 core.[40] Saccharide abbreviations: Gal: galactose; Glc: glucose; Hep: L-glycero-D-manno-heptose; KDO:*

3-deoxy-D-manno-oct-2-ulosonic acid; Nga: N-acetylgalactosamine; NGc: N-acetylglucosamine.

Embedded in this matrix are numerous outer membrane proteins (OMPs), constituting up to 50% of the total OM mass.[14] OMPs typically form membrane-spanning β-barrel structures that perform various transport functions: porins, such as OmpF, form channels for passive diffusion of small hydrophilic molecules;[21] active transporters, like the TonB system, facilitate nutrient uptake;[41] and efflux pumps, such as AcrAB-TolC, expel antibiotics.[42] In contrast to these, the most abundant OMP is the structural protein Lpp described previously, which covalently attaches the outer membrane to the cell wall, regulating the distance between them and providing mechanical stability.[14,26]

1.2.4 Periplasm

The periplasm is the crowded, aqueous compartment located between the inner and outer membranes of Gram-negative bacteria.[12,14] While cryo-electron microscopy data of *E. coli* shows a periplasmic space of approximately 11 nm, it can expand substantially upon osmotic shock, with its volume ranging from 13% to over 40% of the total cell volume depending on the osmolarity of the growth medium.[43,44] Contained within this space is the thin, mesh-like peptidoglycan wall along with high concentrations of proteins, ions, and osmolytes.[14,45] While older models described the periplasm as a rigid gel, “fluorescence recovery after photobleaching” experiments have revealed it to be a viscous compartment with a fluidity comparable to that of the cytoplasm instead.[46]

A key feature of the periplasm is that it is maintained in approximate osmotic equilibrium with the cytoplasm.[47,48] This osmotic pressure balance is achieved, among others, through large, anionic polymers called osmoregulated periplasmic glucans (OPGs).[47,49] In *E. coli*, osmoregulated periplasmic glucans (OPGs) are branched glucose polymers with β-1,2 main-chain and β-1,6 branch-point linkages.[47,49–51] OPGs are heterogeneous in size, typically ranging from 5 to 12 glucose residues (~800–1920 Da), with species containing 8 to 9 units being the most abundant.[49] As OPGs are too large to pass through the outer membrane, they remain trapped in the periplasm where, along with their neutralising cations, they maintain an osmolality that matches that of the cytoplasm.[47,48] Crucially, this isoosmotic state distributes the turgor pressure evenly across the entire cell envelope, thereby protecting the flexible inner membrane, which cannot sustain a large pressure gradient on its own.[47]

Complementing these large anionic glucans, the periplasm also accumulates a diverse array of low-molecular-weight organic compounds, with all of these species collectively referred to as osmolytes or compatible solutes.[52] In *E. coli*, these include sugars like trehalose, polyols like glycerol, and polyamines.[53,54] These osmolytes alter the physicochemical properties of biological fluids, such as viscosity and diffusion rates, and protect cells from environmental stress, such as osmotic shock or extreme temperatures, by helping osmoregulation and stabilising proteins and other macromolecules against denaturation.[52,55] Throughout this thesis, the term “osmolyte” refers specifically to these organic stress-response molecules (e.g., urea, glycerol, putrescine, spermidine, trehalose, OPG), whereas “solute” will be used as a broader category encompassing all species dissolved in the solvent phase, including inorganic ions (e.g. Na^+, Cl^-, Ca^{2+}).

Beyond its structural and osmotic functions, the periplasm is a distinct biochemical compartment that is devoid of ATP, as the inner membrane blocks ATP generated in the cytoplasm from crossing into the periplasmic space.[14] This resulting energetic constraint thus dictates that essential processes, such as protein folding and transport, are carried out by ATP-independent chaperones like SurA and Skp.[14,56]

The unique environment of the periplasm furthermore serves as a defensive layer against antimicrobials. It contains enzymes that can degrade antibiotics, such as β-lactamases, and employs dedicated binding proteins like YdeI in *E. coli* to capture and sequester incoming antimicrobial peptides (AMPs).[57–59]

The complexity of this crowded environment, which is schematically represented in **Figure 1.5**, can also lead to unexpected molecular behaviours. For instance, recent atomistic molecular dynamics (MD) simulations featuring a realistic periplasmic model have shown that the antimicrobial peptide polymyxin B could traverse this space by "hitching a ride" on the lipoprotein transporter LolA.[60] This surprising transport mechanism, which co-opts a system evolved for an entirely different purpose, highlights the importance of accurately representing the diverse molecular species of the periplasm to capture its full functional complexity.
Furthermore, other atomistic MD simulations have shown that, in the absence of competing periplasmic components, cationic polymyxin AMPs would bind irreversibly to the anionic PG cell wall.[54] This immobilisation was mitigated in a more complete periplasmic environment, where small cations, polyamines, and macromolecules competed for the same negative binding sites, allowing the AMPs to be released and diffuse towards their ultimate target, the inner membrane.[54]

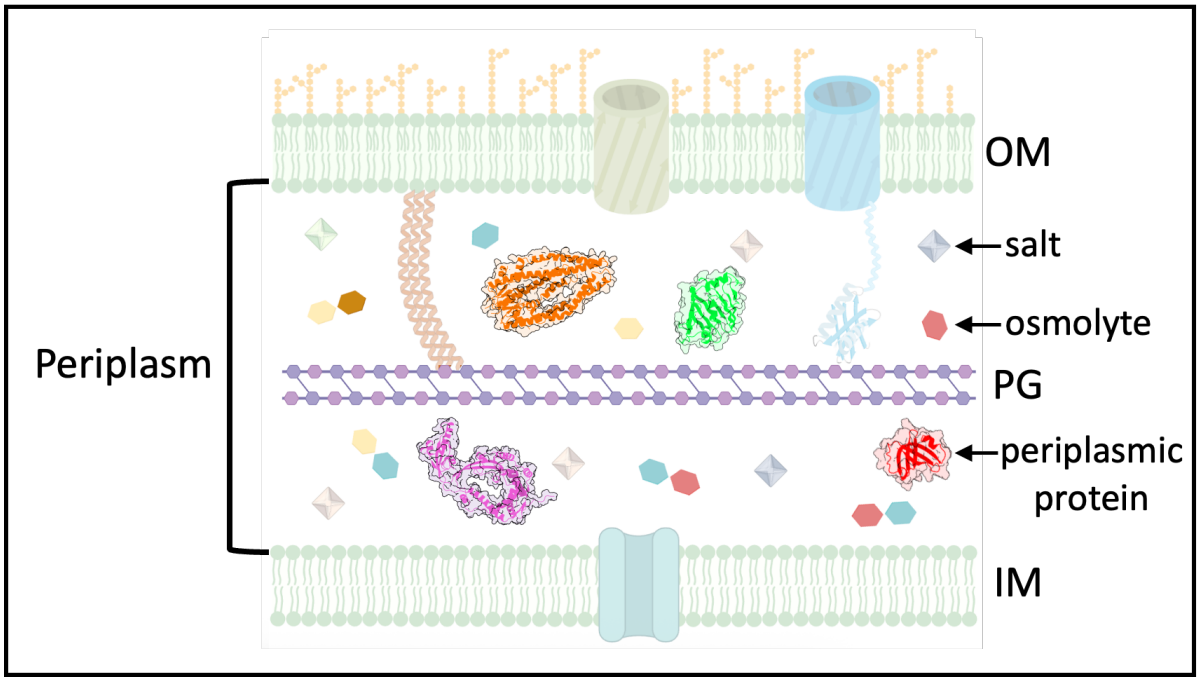

Figure 1.5. *Schematic representation of the E. coli periplasm, showing the molecular crowding and chemical complexity that antimicrobial peptides may encounter. The periplasmic space contains various small molecules, such as salts (cubes) and osmolytes (hexagons), as well as soluble proteins, which are illustrated with overlaid surface representations: LolA (green), Skp (orange), SurA (purple), and YdeI (red).*

1.2.5 Inner membrane

The inner membrane is the essential boundary that surrounds the bacterial cytoplasm.[20] Because bacteria lack organelles, the IM must be highly multifunctional and handle processes that are compartmentalised in eukaryotic organelles. These functions include energy production *via* the electron transport chain and F_0F_1-ATP synthase (analogous to mitochondria), as well as lipid synthesis by membrane-bound enzymes such as PlsB and PlsC and protein secretion through channels like the SecYEG translocon (analogous to the endoplasmic reticulum).[14] The IM also acts as a selective permeability barrier, controlling the passage of molecules through

diverse transmembrane proteins, including ATP-powered ABC transporters, the Sec and Tat protein secretion systems, and various permeases and channels such as the sugar-proton symporter LacY and aquaporins like AqpZ.[61]

In 1972, Seymour Jonathan Singer and Garth L. Nicolson proposed their “fluid mosaic” model to describe the structure of plasma membranes, replacing the prevailing “sandwich” theory which depicted them as static lipid bilayers coated on both sides by sheets of protein.[62] Their new model instead described such membranes as a two-dimensional liquid in which individual proteins are embedded within a lipid bilayer and are free to diffuse laterally.[62]

However, this “fluid mosaic" model is now understood to be an oversimplification which failed to capture the heterogeneous and dynamic nature of real biological membranes.[63] These limitations are particularly relevant for the bacterial IM, a protein-dense environment where, in model organisms like *E. coli*, proteins constitute up to 75% of the membrane mass and their encoding genes represent 20-30% of the total genome.[64,65] The original concept furthermore ignored the asymmetry in lipid composition between the inner and outer leaflets, and failed to account for the complex spatial organisation of proteins into functional assemblies or the formation of distinct lipid domains.[66]

The IM is primarily composed of the same phospholipids found in the inner leaflet of the outer membrane: the zwitterionic phosphatidylethanolamine, and the anionic lipids phosphatidylglycerol and cardiolipin.[67] The zwitterionic PE has been reported to be enriched in the inner (cytoplasmic) leaflet (a distribution of ~75% inner vs. 25% outer leaflet) in rod-shaped *E. coli*, with the opposite enrichment occurring in its filamentous form.[68] This asymmetric composition is actively maintained in an

asymmetric arrangement by lipid transporters, such as the ABC transporter MsbA, which acts as a “floppase” for various phospholipids. These biological subtleties are, however, still often simplified in contemporary computational simulation studies.

The proton-motive force (PMF), generated by the electron transport chain through the oxidation of metabolic donors such as NADH, is central to the IM role in energy production. The PMF consists of two components: a chemical proton gradient (ΔpH) and an electric potential (Δψ). Both components are established as respiratory chain complexes that actively pump protons out of the cytoplasm, maintaining a charge separation and concentration difference across the inner membrane.[69–71] Because the cytoplasmic pH is efficiently buffered, this electric potential arising from charge separation becomes the principal contributor to the PMF.[69–71] In *E. coli* at neutral pH, Δψ is the dominant component and creates an “inside-negative” potential of -140 to -220 mV during the exponential growth phase.[71–73]

The combination of an anionic outer leaflet surface and this negative potential makes the IM a primary target for cationic antimicrobial peptides.[74] Following an initial electrostatic attraction to the negatively charged surface, the electric potential Δψ drives their electrophoretic insertion into the bilayer. Many AMPs work by causing membrane permeabilisation, leading to the collapse of the PMF.[75] This PMF disruption then halts all dependent processes, such as ATP synthesis, and results in rapid cell death.[75] Notably, the electric potential Δψ across the IM is almost entirely neglected in contemporary simulation studies, with a few exceptions.[76]

1.3 Antimicrobial peptides

Antimicrobial peptides (AMPs) are small, naturally occurring peptides found across all domains of life. AMPs are an integral part of the innate immune system and exhibit potent activity against a broad spectrum of pathogens, including Gram-negative and Gram-positive bacteria, fungi, and viruses.[77] Ranging from 10 to 50 amino acids in length, AMPs are typically amphipathic and cationic, carrying a net charge between +2 *e* and +9 *e*.[77] AMPs adopt diverse structural motifs as shown in **Figure 1.6**, with α-helices being the most common, followed by β-sheets often stabilised by disulfide bonds, as well as linear extended/disordered structures or cyclic configurations.[77]

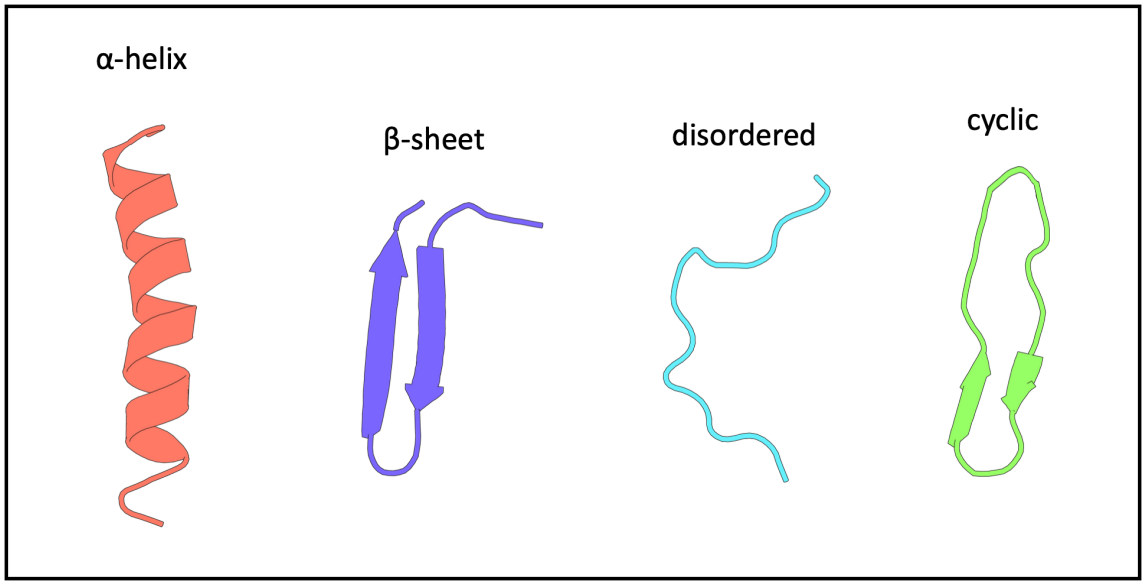

Figure 1.6. *Cartoon representations of common AMP structural classes. From left to right: exemplary α-helical (e.g. magainin 2, PDB: 2MAG), β-sheet (e.g. protegrin-1, PDB: 1PG1), extended/disordered (e.g. indolicidin, PDB: 1G89), and cyclic (e.g. retrocyclin 2, PDB: 2LZI) structures.*

AMPs frequently act by permeabilising microbial membranes through a variety of mechanisms, including both transient and stable pore formation such as the barrel-stave and toroidal pore models (ordered or disordered), as well as detergent-like micellisation, also referred to as "carpet mechanism".[77] These classical, membrane-disrupting modes are summarised in **Figure 1.7**. Beyond membrane disruption, an increasing number of AMPs have been shown to target intracellular components such as DNA, RNA, or proteins, either following membrane permeabilisation or *via* direct translocation across intact membranes.[77]

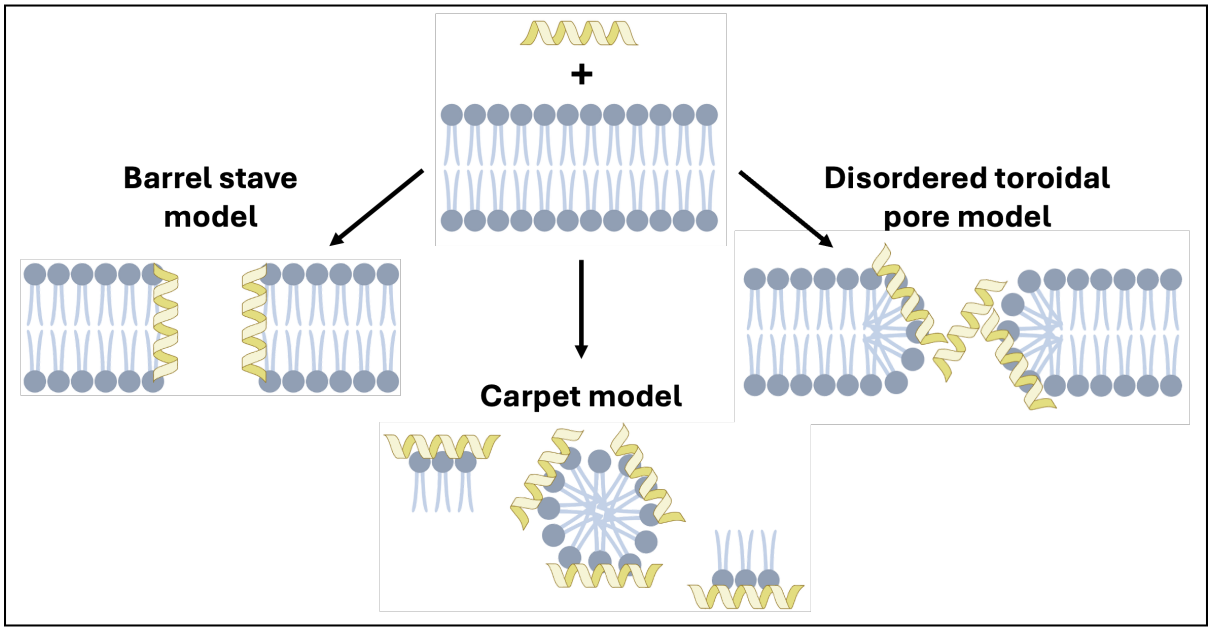

Figure 1.7. *Schematic overview of classical AMP-induced membrane disruption mechanisms.[77] Following initial electrostatic attraction to the membrane surface, AMPs insert into the lipid bilayer and compromise membrane integrity via several distinct modes: left, the barrel-stave model, in which peptides insert perpendicularly and form transmembrane pores; bottom, the toroidal pore model, where both peptides and lipid headgroups line the pore interior; right, the carpet model, in which surface-bound peptides destabilise the membrane in a detergent-like manner.*

The history of AMPs now spans nearly a century: In 1928, Alexander Fleming made the landmark discovery of the antibiotic dipeptide penicillin from mould, marking the start of the antibiotic era.[78] That same year, Lore Alford Rogers and Earle Whittier identified nisin, the first true antimicrobial peptide, which was later commercialised in 1957 as a food preservative.[79–81] In 1939, gramicidins A, B, and C, linear channel-forming peptides produced by soil bacteria, became the first commercially manufactured and clinically used AMPs.[82]

Since these early discoveries, over 3000 AMPs have been reported across a wide range of organisms, including bacteria, plants, insects, fish, and humans.[83,84] However, their clinical translation remains limited: to date, only seven AMPs have received FDA approval, with most restricted to topical or intravenous use in the treatment of severe infections, largely due to issues such as poor stability, cytotoxicity, and unfavourable pharmacokinetics.[85,86] Furthermore, while AMPs exhibit potent antimicrobial activity *in vitro*, their efficacy often diminishes under physiological conditions, with factors such as physiological ionic strength, proteolytic degradation, and sequestration by serum proteins impairing their ability to act on microbial targets *in vivo*.[77] This discrepancy highlights the need to study AMPs in biologically relevant settings to bridge the gap between their potent *in vitro* activity and their successful application as therapeutics.

1.3.1 Magainin 2

Magainin 2 (Mag2) is one of the most extensively studied antimicrobial peptides and was discovered by Michael Alan Zasloff in 1987 as part of a family of AMPs secreted by the skin of the African clawed frog, *Xenopus laevis*.[16,87,88] At the time, *Xenopus* was a key model organism for RNA expression studies, which required the surgical removal of its ovaries for oocyte retrieval.[89–91] Zasloff described it as "medically remarkable" that these incisions rarely became infected despite the non-sterile surgical and husbandry conditions.[87] This observation led Zasloff to investigate the underlying cause and identify the magainin family as the AMPs responsible for the innate *Xenopus* immune defence.[87] Magainins have since been shown to possess activity against a broad spectrum of targets, including Gram-positive and Gram-negative bacteria, fungi, protozoan parasites, and various tumour cell lines, such as ovarian or bone marrow cancer, while exhibiting low haemotoxicity and cytotoxicity.[87,92,93]

The wild-type form of Mag2 is 23 amino acids long and has the sequence H-GIGKFLHSAKKFGKAFVGEIMNS-OH, giving the amphipathic AMP a net cationic charge of +4 *e* at physiological pH.[87] While predominantly unstructured in aqueous solution, Mag2 folds into its distinct α-helical conformation upon binding anionic phospholipid membranes, which is represented in **Figure 1.8**.[94]

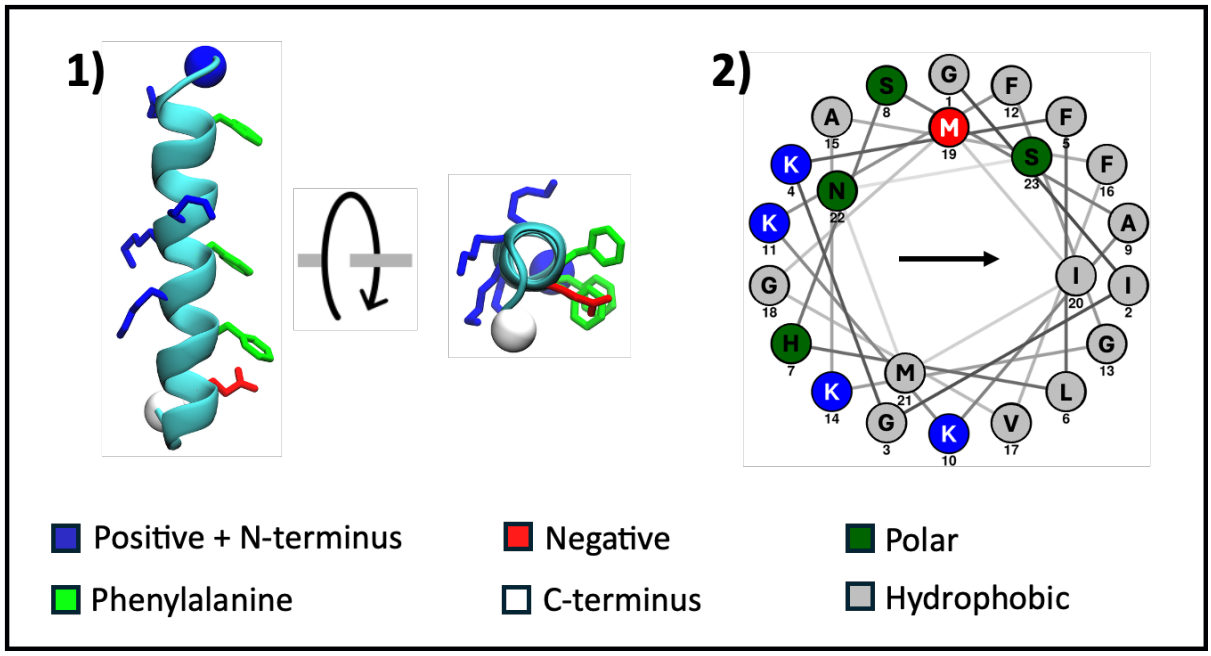

Figure 1.8. *Structural representations of the antimicrobial peptide magainin 2 in its alpha-helical conformation (PDB: 2MAG, NMR). Individual residues are colour-coded by their chemical properties. 1) left: side view of M2, right: top view of Mag2. 2) Helical wheel projection of Mag2, showing the distribution and orientation of amino acid residues in two separate faces: a positively charged face on the left and a mostly apolar face on the right.*[95] *The arrow indicates the hydrophobic moment of the peptide.*[96]

Once bound to the membranes, Mag2 exerts its bactericidal effect primarily through membrane permeabilisation.[97] The prevailing literature mechanism of action involves the formation of toroidal pores, a process that is both concentration-dependent and governed by electrostatics. The affinity for this initial membrane binding step has been shown to depend on both the net positive charge on the AMP and the negative surface charge of the membrane by coarse-grained (CG) MD simulations using the Martini 2 and Martini 3 force fields.[98,99] This electrostatic attraction has been shown to be complemented by a biophysical preference of Mag2 for partitioning into the

more fluid, liquid-disordered domains that are characteristic of bacterial membranes.[100]

Following this initial association, the peptide adsorbs onto the bilayer in a surface-aligned S-state, interacting with lipid headgroups and causing local membrane thinning.[99] Once a critical local peptide-to-lipid ratio is reached, the AMP undergo an orientation transition, moving from the S-state to adopt a tilted transmembrane orientation, referred to as the T-state, and can further insert into a fully transmembrane I-state.[101] These configurations are schematically represented in

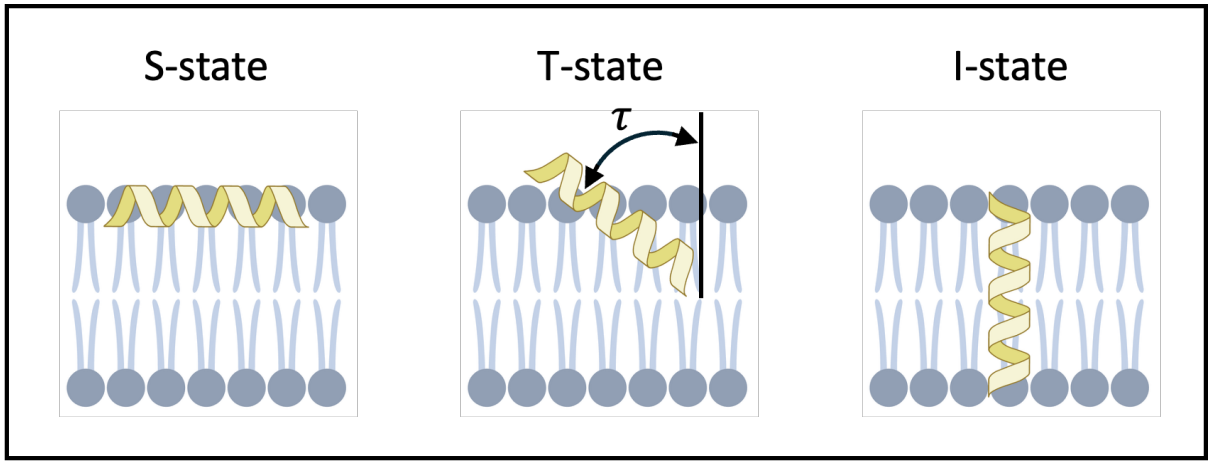

Figure 1.9. This Mag2 insertion is thought to result in pore formation as the assembled AMP helices associate with lipid headgroups, inducing high local membrane curvature and forming the water-filled channels, lined by both peptides and lipids, that are characteristic of the toroidal pore model.[102–104] These transient and heterogeneous pores compromise membrane integrity, leading to membrane depolarisation and the leakage of cellular contents, causing cell death.[75,105] This multi-stage mechanism is supported by evidence from oriented circular dichroism, solid-state NMR, and neutron and X-ray scattering, as well as increased lipid flip-flop rates in the presence of Mag2.[103,106,107]

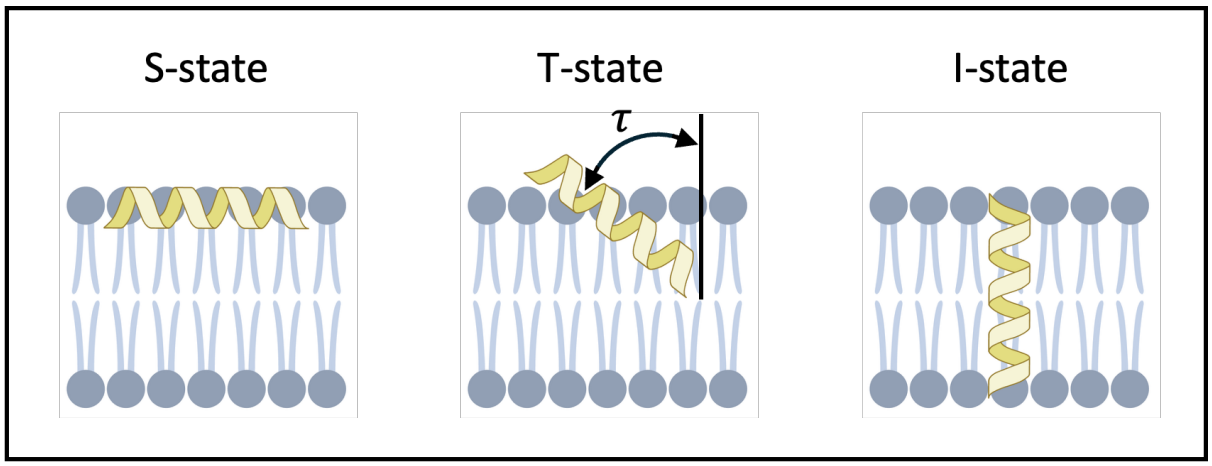

Figure 1.9. *Schematic representation of the different modes of AMP-membrane association in the context of the angle τ between the AMP and the membrane normal, with the AMP shown as a yellow helix and phospholipid bilayer in grey. These states are defined by the AMP orientation relative to the membrane normal: the S-state is orthogonal, the I-state is parallel, and the T-state covers all intermediate angles.*

While these experimental findings provide strong evidence for the toroidal pore model, they give a static or ensemble-averaged view of intrinsically dynamic processes. In addition, the toroidal pore mechanism model has thus been investigated, corroborated, and expanded upon by computational studies. All-atom (AA) multimicrosecond simulations, performed on pre-formed Mag2 tetramers embedded in a lipid bilayer, have provided direct visual confirmation of the toroidal pore model, showing lipid headgroups being pulled into the membrane core to line the water-filled channel alongside the peptides.[101] These simulations revealed that magainin-induced pores constitute a dynamic environment where peptides can move and switch between different conformational states.[101] These included a transmembrane T-state and a more deeply inserted I-state.[101] These dynamic AMP configurations were sensitive to the initial arrangement of the peptides: the more

stable antiparallel configuration of Mag2 dimers led to a more ordered pore whose structure closely resembled those determined by experimental NMR and crystallography.[101,108,109] A notable discrepancy remained, as simulated pores, typically with a radius of around 10 Å, were smaller than those suggested by experimental techniques like neutron scattering and cryo-electron microscopy, reporting radii up to 40 Å.[101,103,110] This suggests that current computational models may only capture "nascent" or intermediate pore states, leaving the full assembly process of larger pores as a key challenge for future research.[101]

To study the spontaneous formation of pores while avoiding the use of artificially pre-inserted peptides, further computational studies have employed coarse-grained (CG) molecular dynamics simulations. For example, a study using the Martini 2 force field to simulate multiple Mag2 copies interacting with a simple DPPC membrane revealed that the resulting toroidal pores are not the highly ordered, symmetrical structures of classical models, but are more accurately described as disordered assemblies.[111] Furthermore, a different study using the Martini 2 force fields showed that Mag2 not only prefers localising in the liquid-disordered membrane phase, but also prefers forming toroidal pores in it compared to the liquid-ordered phase.[100]

To conclude, due to its well-characterised structure and mode of action, as well as its representation of the most common class of AMPs (α-helical), Mag2 serves as a widely accepted model system and motivated our decision to focus primarily on this AMP in this work.[75]

1.3.2 Artificial Intelligence and AMP research

To provide an outlook on where parts of the AMP field are heading, it is worth introducing the Artificial Intelligence (AI) methods that have been introduced in AMP research over the last two decades.[112–114] These computational approaches have evolved substantially, mirroring the advancements in the broader field of AI, and have progressed from simple predictive models to more sophisticated generative systems capable of *de novo* AMP design.[112–114]

Early approaches relied on classical machine learning models, such as Support Vector Machines and Random Forests, to mine existing sequences and predict the properties of potential AMP candidates.[112,114] These methods were defined by their dependence on "feature engineering", requiring researchers to use their domain expertise to manually select physicochemical AMP properties as model inputs. For example, the AntiBP2 server served as a sequence classifier, predicting whether peptides had antimicrobial properties based on their amino acid composition.[115] The CAMP platform emerged in parallel, serving as both a prediction tool and a centralised AMP database for researchers. However, these initial approaches were inherently limited by pre-existing knowledge and human bias, with the potential to overlook novel features.[116]

The subsequent introduction of deep learning in AMP research marked a paradigm shift, with neural networks automatically learning complex features directly from raw peptide sequence data.[112] This approach reduced the dependency on manual feature engineering, minimising human bias and leading to more powerful predictions. An early and prominent success of this approach was the repurposing of halicin, a structurally novel antibiotic identified by a deep neural network, which was

found to exert its broad-spectrum bactericidal activity by disrupting the proton motive force across the bacterial membrane.[117]

The next evolution in the field involved advancing from predicting the properties of existing AMP sequences to the *de novo* design of novel peptides using generative models.[112] These models learn the underlying statistical distributions of peptide composition, such as amino acid frequencies and recurring sequence motifs, and the sequence-activity relationships from known antimicrobial peptides to generate novel sequences.[112] Among the generative architectures, the Variational Autoencoder (VAE) framework has proven particularly effective, consisting of an encoder that maps input peptides to a continuous, lower-dimensional latent space, and a decoder that samples from this space to reconstruct or generate new peptide sequences.[118–120] For example, the HydrAMP framework used a conditional VAE to design novel AMP sequences, generating 15 new AMPs with validated activity against multidrug-resistant pathogens. Bridging the gap between AI generation and wet-lab validation, atomistic molecular dynamics simulations were used as a final *in silico* filter to rank novel peptides based on their predicted physical ability to embed into a model bacterial membrane before their synthesis and laboratory testing.[121]

Representing the current state-of-the-art, Large Language Models (LLMs) are pre-trained on massive databases of protein sequences to learn the fundamental "grammar" of protein biology.[122] The BroadAMP-GPT framework illustrates this approach through a multi-stage pipeline where the authors first developed and trained their own custom Generative Pre-Training Transformer (GPT) model on known AMPs to generate a library of novel candidate sequences.[123] They then used the pretrained ProtBERT model to encode these candidates for a subsequent

filtering step *via* a deep neural net, leading to the discovery of two lead candidates with potent activity.[122,123] In a post-hoc analysis, the proposed membrane-targeting mechanisms of these final candidates were then explored using atomistic MD simulations, which suggested distinct binding modes with a simple lipid bilayer.[123]

However, a key limitation of many advanced AI models is their “black box” nature, as they can in some cases identify promising candidates without clarifying the specific interactions that drive their activity. This is where traditional, physics-based methods such as MD simulations remain essential, providing the level of detail needed to understand how novel AMPs interact with pathogens. This mechanistic understanding is crucial for guiding rational AMP development. Accelerating the development of safer, more effective antimicrobial peptides will therefore depend on creating a feedback loop that uses the mechanistic details of biophysical simulations to guide the predictive power of AI.

1.4 Importance of using biologically relevant systems

Many AMP studies still rely on oversimplified models of the Gram-negative cell envelope, overlooking factors such as membrane proteins, periplasmic crowding, or the transmembrane potential across the inner membrane. This approach effectively assumes that AMPs interact with bare lipid bilayers in simple solute environments. However, this simplified view is now being challenged, as a growing body of research acknowledges that these physiological features do shape AMP behaviour on its journey across the bacterial cell envelope.[54,60,76]

This historical neglect of biological complexity is not only a hypothetical concern but likely underlies the discrepancy between AMP activity in laboratory settings and their actual usefulness as therapeutics.[124] Indeed, this translational chasm is exemplified by the high-profile, late-stage clinical failures of candidates such as Pexiganan, Murepavadin, and Iseganan, all of which were selected for potent activity in reductionist assays but were ultimately derailed by the complex physiological realities in patients.

Pexiganan, a synthetic analogue of magainin 2, showed excellent *in vitro* activity against clinical isolates from diabetic foot ulcers.[125] Despite this, its large-scale Phase III clinical trials failed to demonstrate a statistically significant advantage over a placebo cream when added to standard wound care. Furthermore, the treatment arm was associated with a higher incidence of serious adverse events in patients, notably osteomyelitis and cellulitis.[126]

Murepavadin is an AMP that specifically targets the LptD protein, which is critical for LPS transport in *P. aeruginosa*, and showed strong potency against multidrug-resistant strains in preclinical studies.[127,128] It was investigated for treating hospital-acquired pneumonia, but its Phase III trials were terminated prematurely. A safety review identified that the murepavadin arm had an unexpectedly high rate of acute kidney injury, occurring in 56% of patients, a severe side effect not predicted by earlier models.[129,130]

Iseganan, an analogue of protegrin-1, was investigated for preventing ventilator-associated pneumonia (VAP) and oral mucositis due to its broad-spectrum activity against bacteria and a favourable early safety profile, with both of its Phase III trials however ultimately failing. The VAP trial was halted for futility, showing no significant

reduction in pneumonia rates and a concerning trend towards higher mortality in the Iseganan group.[131] For oral mucositis, the failure was attributed to the inability of the peptide to penetrate the dense pseudomembrane covering the ulcers, preventing access to the underlying microbes.[132]

Taken together, these cases illustrate a fundamental problem in AMP development: the consistent failure to translate promising candidates into clinical therapeutics due to traditional models overlooking crucial factors such as realistic physiological barriers. Recognising this critical shortcoming, this work aims to help bridge this gap by investigating how the complex environment of the *E. coli* cell envelope, in particular interactions with the periplasmic solute phase and the energised inner membrane, governs AMP activity.

References

1. Murray, C. J. L. *et al.* Global burden of bacterial antimicrobial resistance in 2019: a systematic analysis. *The Lancet* **399**, 629–655 (2022).

2. McDonnell, A. *et al.* Forecasting the Fallout from AMR: Economic Impacts of Antimicrobial Resistance in Humans. https://www.cgdev.org/publication/forecasting-fallout-amr-economic-impacts-antimicrobial-resistance-humans (2024).

3. *Ambitious USG Advanced Commitment for Subscription-Based Purchasing of Novel Antimicrobials and Its Expected Return on Investment*. (Center for Global Development, 2022).

4. Boucher, H. W. *et al.* 10 × ’20 Progress—Development of New Drugs Active Against Gram-Negative Bacilli: An Update From the Infectious Diseases Society of America. *Clin. Infect. Dis.* **56**, 1685–1694 (2013).

5. O’Neill, J. Tackling drug-resistant infections globally: final report and recommendations. 84 pp. (2016).

6. Plackett, B. Why big pharma has abandoned antibiotics. *Nature* **586**, S50–S52 (2020).

7. Hooke, R. *Micrographia: Or Some Physiological Descriptions of Minute Bodies Made by Magnifying Glasses, with Observations and Inquiries Thereupon*. (Courier Corporation, 2003).

8. Schleiden, M. J. Arch Anat Physiol. *Wiss Med* **13**, 137–176 (1838).

9. Schwann, T. *Mikroskopische Untersuchungen Über Die Uebereinstimmung in Der Struktur Und Dem Wachsthum Der Thiere Und Pflanzen: Mit 4 Kupfertafeln*. (Reimer, 1839).

10. Mazzarello, P. A unifying concept: the history of cell theory. *Nat. Cell Biol.* **1**, E13–E15 (1999).

11. Woese, C. R. & Fox, G. E. Phylogenetic structure of the prokaryotic domain: the primary kingdoms. *Proc. Natl. Acad. Sci.* **74**, 5088–5090 (1977).

12. Alberts, B. *et al. Molecular Biology of the Cell: Seventh International Student Edition with Registration Card*. (WW Norton & Company, 2022).

13. Schulz, H. N. & Jørgensen, B. B. Big bacteria. *Annu. Rev. Microbiol.* **55**, 105–137 (2001).

14. Silhavy, T. J., Kahne, D. & Walker, S. The bacterial cell envelope. *Cold Spring Harb. Perspect. Biol.* **2**, a000414 (2010).

15. Brown, E. D. & Wright, G. D. Antibacterial drug discovery in the resistance era. *Nature* **529**, 336–343 (2016).

16. Yeaman, M. R. & Yount, N. Y. Mechanisms of Antimicrobial Peptide Action and Resistance. *Pharmacol. Rev.* **55**, 27–55 (2003).

17. Delcour, A. H. Outer membrane permeability and antibiotic resistance. *Biochim. Biophys. Acta BBA-Proteins Proteomics* **1794**, 808–816 (2009).

18. Gram, C. Ueber die isolirte Farbung der Schizomyceten in Schnitt-und Trockenpraparaten. *Fortschritte Med.* **2**, 185–189 (1884).

19. Beveridge, T. J. Use of the Gram stain in microbiology. *Biotech. Histochem.* **76**, 111–118 (2001).

20. Madigan, M. T., Martinko, J. M. & Parker, J. *Brock Biology of Microorganisms*. vol. 11 (Prentice hall Upper Saddle River, NJ, 1997).

21. Nikaido, H. Molecular basis of bacterial outer membrane permeability revisited. *Microbiol. Mol. Biol. Rev.* **67**, 593–656 (2003).

22. Vollmer, W., Blanot, D. & De Pedro, M. A. Peptidoglycan structure and architecture. *FEMS Microbiol. Rev.* **32**, 149–167 (2008).

23. Vaiwala, R., Sharma, P., Puranik, M. & Ayappa, K. G. Developing a Coarse-Grained Model for Bacterial Cell Walls: Evaluating Mechanical Properties and Free Energy Barriers. *J. Chem. Theory Comput.* **16**, 5369–5384 (2020).

24. Yao X., Jericho M., Pink D., & Beveridge T. Thickness and Elasticity of Gram-Negative Murein Sacculi Measured by Atomic Force Microscopy. *J. Bacteriol.* **181**, 6865–6875 (1999).

25. Nikaido, H. *Outer Membrane, Gram-Negative Bacteria. Encyclopedia of Microbiology*. (Academic Press, Cambridge Mass. USA, 2009).

26. Braun, V. & Rehn, K. Chemical Characterization, Spatial Distribution and Function of a Lipoprotein (Murein-Lipoprotein) of the E. coli Cell Wall. *Eur. J. Biochem.* **10**, 426–438 (1969).

27. De Mot, R. & Vanderleyden, J. The C-terminal sequence conservation between OmpA-related outer membrane proteins and MotB suggests a common function

in both Gram-positive and Gram-negative bacteria, possibly in the interaction of these domains with peptidoglycan. *Mol. Microbiol.* **12**, 333–334 (1994).

28. Typas, A., Banzhaf, M., Gross, C. A. & Vollmer, W. From the regulation of peptidoglycan synthesis to bacterial growth and morphology. *Nat. Rev. Microbiol.* **10**, 123–136 (2012).

29. Reynolds, P. E. Structure, biochemistry and mechanism of action of glycopeptide antibiotics. *Eur J Clin Microbiol Infect Dis* **8**, (1989).

30. Kohanski, M. A., Dwyer, D. J. & Collins, J. J. How antibiotics kill bacteria: from targets to networks. *Nat. Rev. Microbiol.* **8**, 423–435 (2010).

31. Zhang, Y.-M. & Rock, C. O. Membrane lipid homeostasis in bacteria. *Nat. Rev. Microbiol.* **6**, 222–233 (2008).

32. Ernst, R., Ejsing, C. S. & Antonny, B. Homeoviscous adaptation and the regulation of membrane lipids. *J. Mol. Biol.* **428**, 4776–4791 (2016).

33. Rilfors, L. & Lindblom, G. Regulation of lipid composition in biological membranes—biophysical studies of lipids and lipid synthesizing enzymes. *Colloids Surf. B Biointerfaces* **26**, 112–124 (2002).

34. Raetz, C. R. & Whitfield, C. Lipopolysaccharide endotoxins. *Annu. Rev. Biochem.* **71**, 635–700 (2002).

35. Whitfield, C. & Trent, M. S. Biosynthesis and export of bacterial lipopolysaccharides. *Annu. Rev. Biochem.* **83**, 99–128 (2014).

36. Maldonado, R. F., Sá-Correia, I. & Valvano, M. A. Lipopolysaccharide modification in Gram-negative bacteria during chronic infection. *FEMS Microbiol. Rev.* **40**, 480–493 (2016).

37. Alexander, C. & Rietschel, E. T. Invited review: Bacterial lipopolysaccharides and innate immunity. *J. Endotoxin Res.* **7**, 167–202 (2001).

38. Snyder, S., Kim, D. & McIntosh, T. J. Lipopolysaccharide Bilayer Structure: Effect of Chemotype, Core Mutations, Divalent Cations, and Temperature. *Biochemistry* **38**, 10758–10767 (1999).

39. Jeworrek, C. *et al.* Effects of Specific versus Nonspecific Ionic Interactions on the Structure and Lateral Organization of Lipopolysaccharides. *Biophys. J.* **100**, 2169–2177 (2011).

40. Rietschel, E. T. *et al.* Bacterial endotoxin: molecular relationships of structure to activity and function. *FASEB J.* **8**, 217–225 (1994).

41. Postle, K. & Kadner, R. J. Touch and go: tying TonB to transport. *Mol. Microbiol.* **49**, 869–882 (2003).

42. Li, X.-Z., Plésiat, P. & Nikaido, H. The challenge of efflux-mediated antibiotic resistance in Gram-negative bacteria. *Clin. Microbiol. Rev.* **28**, 337–418 (2015).

43. Matias, V. R. F., Al-Amoudi, A., Dubochet, J. & Beveridge, T. J. Cryo-transmission electron microscopy of frozen-hydrated sections of gram-negative bacteria. *J Bacteriol* **185**, 6112–6118 (2003).

44. Stock, J. B., Rauch, B. & Roseman, S. Periplasmic space in Salmonella typhimurium and Escherichia coli. *J. Biol. Chem.* **252**, 7850–7861 (1977).

45. Neu, H. C. & Heppel, L. A. The release of enzymes from Escherichia coli by osmotic shock and during the formation of spheroplasts. *J. Biol. Chem.* **240**, 3685–3692 (1965).

46. Mullineaux, C. W., Nenninger, A., Ray, N. & Robinson, C. Diffusion of Green Fluorescent Protein in Three Cell Environments in Escherichia Coli. *J. Bacteriol.* **188**, 3442–3448 (2006).

47. Bohin, J.-P. Osmoregulated periplasmic glucans in Proteobacteria. *FEMS Microbiol. Lett.* **186**, 11–19 (2000).

48. Scott Cayley, D., Guttman, H. J. & Thomas Record, M., Jr. Biophysical Characterization of Changes in Amounts and Activity of Escherichia coli Cell and Compartment Water and Turgor Pressure in Response to Osmotic Stress. *Biophys. J.* **78**, 1748–1764 (2000).

49. Kennedy, E. P. Osmotic regulation and the biosynthesis of membrane-derived oligosaccharides in Escherichia coli. *Proc. Natl. Acad. Sci.* **79**, 1092–1095 (1982).

50. Bontemps-Gallo, S. & Lacroix, J.-M. New insights into the biological role of the osmoregulated periplasmic glucans in pathogenic and symbiotic bacteria. *Environ. Microbiol. Rep.* **7**, 690–697 (2015).

51. Bontemps-Gallo, S., Bohin, J.-P. & Lacroix, J.-M. Osmoregulated periplasmic glucans. *EcoSal Plus* **7**, 10.1128/ecosalplus. ESP-0001–2017 (2017).

52. Yancey, P. H. Organic osmolytes as compatible, metabolic and counteracting cytoprotectants in high osmolarity and other stresses. *J. Exp. Biol.* **208**, 2819–2830 (2005).

53. Pedebos, C., Smith, I. P. S., Boags, A. & Khalid, S. The hitchhiker's guide to the periplasm: Unexpected molecular interactions of polymyxin B1 in E. coli. *Structure* **29**, 444-456.e2 (2021).

54. Smith, I. P., Pedebos, C. & Khalid, S. Molecular crowding alters the interactions of polymyxin lipopeptides within the periplasm of E. coli: insights from molecular dynamics. *J. Phys. Chem. B* **128**, 2717–2733 (2024).

55. Vanaporn, M. & Titball, R. W. Trehalose and bacterial virulence. *Virulence* **11**, 1192–1202 (2020).

56. Sklar, J. G., Wu, T., Kahne, D. & Silhavy, T. J. Defining the roles of the periplasmic chaperones SurA, Skp, and DegP in Escherichia coli. *Genes Dev.* **21**, 2473–2484 (2007).

57. Drawz, S. M. & Bonomo, R. A. Three decades of β-lactamase inhibitors. *Clin. Microbiol. Rev.* **23**, 160–201 (2010).

58. Bush, K. & Bradford, P. A. β-Lactams and β-lactamase inhibitors: an overview. *Cold Spring Harb. Perspect. Med.* **6**, a025247 (2016).

59. Pilonieta, M. C., Erickson, K. D., Ernst, R. K. & Detweiler, C. S. A protein important for antimicrobial peptide resistance, YdeI/OmdA, is in the periplasm and interacts with OmpD/NmpC. *J. Bacteriol.* **191**, 7243–7252 (2009).

60. Pedebos, C., Smith, I. P. S., Boags, A. & Khalid, S. The hitchhiker's guide to the periplasm: Unexpected molecular interactions of polymyxin B1 in E. coli. *Struct. Lond. Engl. 1993* **29**, 444-456.e2 (2021).

61. Paulsen, I. T., Sliwinski, M. K. & Saier, M. H. Microbial genome analyses: global comparisons of transport capabilities based on phylogenies, bioenergetics and substrate specificities11Edited by G. Von Heijne. *J. Mol. Biol.* **277**, 573–592 (1998).

62. Singer, S. J. & Nicolson, G. L. The Fluid Mosaic Model of the Structure of Cell Membranes. *Science* **175**, 720–731 (1972).

63. Kusumi, A., Ike, H., Nakada, C., Murase, K. & Fujiwara, T. Single-molecule tracking of membrane molecules: plasma membrane compartmentalization and dynamic assembly of raft-philic signaling molecules. *Spacial Organ. Immune Cell Signal.* **17**, 3–21 (2005).

64. Raetz, C. R. & Dowhan, W. Biosynthesis and function of phospholipids in Escherichia coli. *J. Biol. Chem.* **265**, 1235–1238 (1990).

65. Daley, D. O. *et al.* Global Topology Analysis of the Escherichia coli Inner Membrane Proteome. *Science* **308**, 1321–1323 (2005).

66. Tachi, T., Epand, R. F., Epand, R. M. & Matsuzaki, K. Position-Dependent Hydrophobicity of the Antimicrobial Magainin Peptide Affects the Mode of Peptide−Lipid Interactions and Selective Toxicity. *Biochemistry* **41**, 10723–10731 (2002).

67. Dowhan, W. Understanding phospholipid function: Why are there so many lipids? *J. Biol. Chem.* **292**, 10755–10766 (2017).

68. Bogdanov, M. *et al.* Phospholipid distribution in the cytoplasmic membrane of Gram-negative bacteria is highly asymmetric, dynamic, and cell shape-dependent. *Sci. Adv.* **6**, eaaz6333 (2020).

69. Booth, I. R. Regulation of cytoplasmic pH in bacteria. *Microbiol. Rev.* **49**, 359–378 (1985).

70. Zilberstein, D., Agmon, V., Schuldiner, S. & Padan, E. Escherichia coli intracellular pH, membrane potential, and cell growth. *J. Bacteriol.* **158**, 246–252 (1984).

71. Kashket E R. Effects of aerobiosis and nitrogen source on the proton motive force in growing Escherichia coli and Klebsiella pneumoniae cells. *J. Bacteriol.* **146**, 377–384 (1981).

72. Felle, H., Porter, J. S., Slayman, C. L. & Kaback, H. R. Quantitative measurements of membrane potential in Escherichia coli. *Biochemistry* **19**, 3585–3590 (1980).

73. Terradot, G., Krasnopeeva, E., Swain, P. S. & Pilizota, T. Escherichia coli Maintains pH via the Membrane Potential. *PRX Life* **2**, 043015 (2024).

74. Hancock, R. E. W. & Sahl, H.-G. Antimicrobial and host-defense peptides as new anti-infective therapeutic strategies. *Nat. Biotechnol.* **24**, 1551–1557 (2006).

75. Brogden, K. A. Antimicrobial peptides: pore formers or metabolic inhibitors in bacteria? *Nat. Rev. Microbiol.* **3**, 238–250 (2005).

76. Weerakoon, D., Marzinek, J. K., Pedebos, C., Bond, P. J. & Khalid, S. Polymyxin B1 in the Escherichia coli inner membrane: A complex story of protein and lipopolysaccharide-mediated insertion. *J. Biol. Chem.* **300**, 107754 (2024).

77. Oliveira Júnior, N. G., Souza, C. M., Buccini, D. F., Cardoso, M. H. & Franco, O. L. Antimicrobial peptides: structure, functions and translational applications. *Nat. Rev. Microbiol.* 1–14 (2025) doi:10.1038/s41579-025-01200-y.

78. Fleming, A. On the Antibacterial Action of Cultures of a Penicillium, with Special Reference to their Use in the Isolation of B. influenzæ. *Br. J. Exp. Pathol.* **10**, 226–236 (1929).

79. Rogers, L. A. THE INHIBITING EFFECT OF STREPTOCOCCUS LACTIS ON LACTOBACILLUS BULGARICUS. *J. Bacteriol.* **16**, 321–325 (1928).

80. Mattick, A. T. R., Hirsch, A. & Berridge, N. J. FURTHER OBSERVATIONS ON AN INHIBITORY SUBSTANCE (NISIN) FROM LACTIC STREPTOCOCCI. *The Lancet* **250**, 5–8 (1947).

81. Delves-Broughton, J., Blackburn, P., Evans, R. J. & Hugenholtz, J. Applications of the bacteriocin, nisin. *Antonie Van Leeuwenhoek* **69**, 193–202 (1996).

82. Dubos, R. J. STUDIES ON A BACTERICIDAL AGENT EXTRACTED FROM A SOIL BACILLUS. *J. Exp. Med.* **70**, 1–10 (1939).

83. Wang, G., Li, X. & Wang, Z. APD3: the antimicrobial peptide database as a tool for research and education. *Nucleic Acids Res.* **44**, D1087–D1093 (2016).

84. Pirtskhalava, M. *et al.* DBAASP v3: database of antimicrobial/cytotoxic activity and structure of peptides as a resource for development of new therapeutics. *Nucleic Acids Res.* **49**, D288–D297 (2021).

85. Chen, C. H. & Lu, T. K. Development and Challenges of Antimicrobial Peptides for Therapeutic Applications. *Antibiot. Basel Switz.* **9**, 24 (2020).

86. Asif, F., Zaman, S. U., Arnab, Md. K. H., Hasan, M. & Islam, Md. M. Antimicrobial peptides as therapeutics: Confronting delivery challenges to optimize efficacy. *The Microbe* **2**, 100051 (2024).

87. Zasloff, M. Magainins, a class of antimicrobial peptides from Xenopus skin: isolation, characterization of two active forms, and partial cDNA sequence of a precursor. *Proc. Natl. Acad. Sci. U. S. A.* **84**, 5449–5453 (1987).

88. Zasloff, M. Antimicrobial peptides of multicellular organisms. *Nature* **415**, 389–395 (2002).

89. Zasloff, M., Rosenberg, M. & Santos, T. Impaired nuclear transport of a human variant tRNAiMet. *Nature* **300**, 81–84 (1982).

90. Tobian, J. A., Drinkard, L. & Zasloff, M. tRNA nuclear transport: Defining the critical regions of human tRNAimet by point mutagenesis. *Cell* **43**, 415–422 (1985).

91. Castaño, J. G., Ornberg, R., Koster, J. G., Tobian, J. A. & Zasloff, M. Eukaryotic pre-tRNA 5′ processing nuclease: Copurification with a complex cylindrical particle. *Cell* **46**, 377–387 (1986).

92. Baker, M. A., Maloy, W. L., Zasloff, M. & Jacob, L. S. Anticancer Efficacy of Magainin2 and Analogue Peptides. *Cancer Res.* **53**, 3052–3057 (1993).

93. Gaspar, D., Veiga, A. S. & Castanho, M. A. R. B. From antimicrobial to anticancer peptides. A review. *Front. Microbiol.* **4**, (2013).

94. Matsuzaki, K. *et al.* Magainin 1-induced leakage of entrapped calcein out of negatively-charged lipid vesicles. *Biochim. Biophys. Acta BBA - Biomembr.* **981**, 130–134 (1989).

95. Galaxy Community. The Galaxy platform for accessible, reproducible and collaborative biomedical analyses: 2022 update. *Nucleic Acids Res.* **50**, W345–W351 (2022).

96. Gautier, R., Douguet, D., Antonny, B. & Drin, G. HELIQUEST: a web server to screen sequences with specific alpha-helical properties. *Bioinforma. Oxf. Engl.* **24**, 2101–2102 (2008).

97. Matsuzaki, K., Sugishita, K., Harada, M., Fujii, N. & Miyajima, K. Interactions of an antimicrobial peptide, magainin 2, with outer and inner membranes of Gram-negative bacteria. *Biochim. Biophys. Acta BBA - Biomembr.* **1327**, 119–130 (1997).

98. Montero Vega, S., Booth, V. & Rowley, C. N. Interaction between Antimicrobial Peptide Magainin 2 and Nonlipid Components in the Bacterial Outer Envelope. *J. Phys. Chem. B* **126**, 5473–5480 (2022).

99. Simcock, P. W. *et al.* Membrane Binding of Antimicrobial Peptides Is Modulated by Lipid Charge Modification. *J. Chem. Theory Comput.* **17**, 1218–1228 (2021).

100. Su, J., Marrink, S. J. & Melo, M. N. Localization preference of antimicrobial peptides on liquid-disordered membrane domains. *Front. Cell Dev. Biol.* **8**, 350 (2020).

101. Pino-Angeles, A., Leveritt, J. M. & Lazaridis, T. Pore Structure and Synergy in Antimicrobial Peptides of the Magainin Family. *PLoS Comput. Biol.* **12**, e1004570 (2016).

102. Matsuzaki, K. Why and how are peptide–lipid interactions utilized for self-defense? Magainins and tachyplesins as archetypes. *Biochim. Biophys. Acta BBA - Biomembr.* **1462**, 1–10 (1999).

103. Ludtke, S. J. *et al.* Membrane pores induced by magainin. *Biochemistry* **35**, 13723–13728 (1996).

104. Ludtke, S. J., He, K., Wu, Y. & Huang, H. W. Cooperative membrane insertion of magainin correlated with its cytolytic activity. *Biochim. Biophys. Acta BBA-Biomembr.* **1190**, 181–184 (1994).

105. Wimley, W. C. Describing the Mechanism of Antimicrobial Peptide Action with the Interfacial Activity Model. *ACS Chem. Biol.* **5**, 905–917 (2010).

106. Matsuzaki, K., Murase, O., Fujii, N. & Miyajima, K. An Antimicrobial Peptide, Magainin 2, Induced Rapid Flip-Flop of Phospholipids Coupled with Pore Formation and Peptide Translocation. *Biochemistry* **35**, 11361–11368 (1996).

107. Bechinger, B., Zasloff, M. & Opella, S. J. Structure and interactions of magainin antibiotic peptides in lipid bilayers: a solid-state nuclear magnetic resonance investigation. *Biophys. J.* **62**, 12–14 (1992).

108. Wakamatsu, K., Takeda, A., Tachi, T. & Matsuzaki, K. Dimer structure of magainin 2 bound to phospholipid vesicles. *Biopolymers* **64**, 314–327 (2002).

109. Hayouka, Z. *et al.* Evidence for phenylalanine zipper-mediated dimerization in the X-ray crystal structure of a magainin 2 analogue. *J. Am. Chem. Soc.* **135**, 15738–15741 (2013).

110. Han, M., Mei, Y., Khant, H. & Ludtke, S. J. Characterization of antibiotic peptide pores using cryo-EM and comparison to neutron scattering. *Biophys. J.* **97**, 164–172 (2009).

111. Santo, K. P. & Berkowitz, M. L. Difference between magainin-2 and melittin assemblies in phosphatidylcholine bilayers: results from coarse-grained simulations. *J. Phys. Chem. B* **116**, 3021–3030 (2012).

112. Wan, F., Wong, F., Collins, J. J. & de la Fuente-Nunez, C. Machine learning for antimicrobial peptide identification and design. *Nat. Rev. Bioeng.* **2**, 392–407 (2024).

113. Szymczak, P. *et al.* AI-Driven Antimicrobial Peptide Discovery: Mining and Generation. *Acc. Chem. Res.* **58**, 1831–1846 (2025).

114. Aronica, P. G. A. *et al.* Computational Methods and Tools in Antimicrobial Peptide Research. *J. Chem. Inf. Model.* **61**, 3172–3196 (2021).

115. Lata, S., Mishra, N. K. & Raghava, G. P. AntiBP2: improved version of antibacterial peptide prediction. *BMC Bioinformatics* **11**, S19 (2010).

116. Thomas, S., Karnik, S., Barai, R. S., Jayaraman, V. K. & Idicula-Thomas, S. CAMP: a useful resource for research on antimicrobial peptides. *Nucleic Acids Res.* **38**, D774–D780 (2010).

117. Stokes, J. M. *et al.* A Deep Learning Approach to Antibiotic Discovery. *Cell* **180**, 688-702.e13 (2020).

118. Renaud, S. & A. Mansbach, R. Latent spaces for antimicrobial peptide design. *Digit. Discov.* **2**, 441–458 (2023).

119. Zhao, W., Hou, K., Shen, Y. & Hu, X. A conditional denoising VAE-based framework for antimicrobial peptides generation with preserving desirable properties. *Bioinformatics* **41**, btaf069 (2025).

120. Dean, S. N., Alvarez, J. A. E., Zabetakis, D., Walper, S. A. & Malanoski, A. P. PepVAE: Variational Autoencoder Framework for Antimicrobial Peptide Generation and Activity Prediction. *Front. Microbiol.* **12**, (2021).

121. Szymczak, P. *et al.* Discovering highly potent antimicrobial peptides with deep generative model HydrAMP. *Nat. Commun.* **14**, 1453 (2023).

122. Elnaggar, A. *et al.* ProtTrans: Toward Understanding the Language of Life Through Self-Supervised Learning. *IEEE Trans. Pattern Anal. Mach. Intell.* **44**, 7112–7127 (2022).

123. Li, Y. *et al.* BroadAMP-GPT: AI-Driven generation of broad-spectrum antimicrobial peptides for combating multidrug-resistant ESKAPE pathogens. *Gut Microbes* **17**, 2523811 (2025).

124. Mahlapuu, M., Håkansson, J., Ringstad, L. & Björn, C. Antimicrobial Peptides: An Emerging Category of Therapeutic Agents. *Front. Cell. Infect. Microbiol.* **Volume 6-2016**, (2016).

125. Ge, Y. *et al.* In vitro antibacterial properties of pexiganan, an analog of magainin. *Antimicrob. Agents Chemother.* **43**, 782–788 (1999).

126. Dipexium Pharmaceuticals, Inc. *A Randomized, Double-Blind, Multicenter, Superiority, Placebo-Controlled Phase 3 Study of Pexiganan Cream 0.8% Applied Twice Daily for 14 Days in the Treatment of Adults With Mild Infections of Diabetic Foot Ulcers*. https://clinicaltrials.gov/study/NCT01594762 (2017).

127. Srinivas, N. *et al.* Peptidomimetic antibiotics target outer-membrane biogenesis in Pseudomonas aeruginosa. *Science* **327**, 1010–1013 (2010).

128. Sader, H. S., Dale, G. E., Rhomberg, P. R. & Flamm, R. K. Antimicrobial activity of murepavadin tested against clinical isolates of Pseudomonas aeruginosa from the United States, Europe, and China. *Antimicrob. Agents Chemother.* **62**, 10.1128/aac. 00311-18 (2018).

129. Polyphor Ltd. *A Multicenter, Open-Label, Randomized, Active-Controlled, Parallel Group, Pivotal Study to Investigate the Efficacy, Safety and Tolerability, and Pharmacokinetics of Murepavadin Combined With One Anti-Pseudomonal Antibiotic Versus Two Anti-Pseudomonal Antibiotics in Adult Subjects With Ventilator-Associated Bacterial Pneumonia Suspected or Confirmed to Be Due to Pseudomonas Aeruginosa*. https://clinicaltrials.gov/study/NCT03409679 (2019).

130. Polyphor Ltd. *A Multicenter, Open Label, Sponsor Blinded, Randomized, Active Controlled, Parallel Group, Pivotal Study to Evaluate the Efficacy, Safety, and Tolerability of Murepavadin Given With Ertapenem Versus an Anti-Pseudomonal-β-Lactam-Based Antibiotic in Adult Subjects With Nosocomial Pneumonia Suspected or Confirmed to Be Due to Pseudomonas Aeruginosa*. https://clinicaltrials.gov/study/NCT03582007 (2019).

131. Kollef, M. *et al.* A randomized double-blind trial of iseganan in prevention of ventilator-associated pneumonia. *Am. J. Respir. Crit. Care Med.* **173**, 91–97 (2006).

132. Trotti, A. *et al.* A multinational, randomized phase iii trial of iseganan hcl oral solution for reducing the severity of oral mucositis in patients receiving radiotherapy for head-and-neck malignancy. *Int. J. Radiat. Oncol.* **58**, 674–681 (2004).

Chapter 2

Methods

2.1 Principles of molecular simulations

While experimental methods such as X-ray crystallography or cryogenic electron microscopy provide high-resolution structural data, they often lack dynamic information. Computational modelling methods allow us to bridge this gap, revealing the time-dependent behaviour of molecules at atomistic resolution.[1,2] While quantum mechanics (QM) methods offer a first-principles description of molecular systems, their high computational costs limit their application to small systems and short timescales, making them impractical for studying the dynamics of complex biological systems.[3]

To study large biological systems such as proteins or membranes over relevant timescales, more computationally tractable approaches are needed, such as the molecular mechanics (MM) framework.[4] MM is based on the Born-Oppenheimer approximation and thus treats atoms as classical particles whose interactions are described by a potential energy function known as a force field, which will be described in more detail in subsequent sections.[3] Force fields are semi-empirical models parametrised using a combination of QM calculations, for example to determine atomic partial charges, and experimental data, such as spectroscopic data for vibrational frequencies and thermodynamic data such as partition coefficients.[3]

2.2 Molecular dynamics

Molecular dynamics (MD) is a computational simulation technique used to simulate the time-dependent behaviour of atomic and molecular systems.[3] MD simulations generate a so-called trajectory, a series of molecular configurations (“frames”) recorded over time at defined intervals, by numerically solving Newton's classical equations of motion for a given N-body system where neighbouring particles influence each other. These equations form a set of high-dimensional, coupled differential equations that govern the time evolution of molecular systems. The forces that govern particle movements are derived from the aforementioned force field, the components of which are detailed in subsequent sections.

Molecular dynamics was first formally conceptualised in 1959, with Berni Alder and Thomas Wainwright studying the phase transitions of simple hard-sphere systems interacting *via* elastic collisions.[5] The method was subsequently expanded by Aneesur Rahman in 1964 with the first simulation using a Lennard-Jones potential for liquid argon, paving the way for simulations of liquid water by himself and Frank Stillinger in 1974.[6,7] The first application to a biological macromolecule followed in 1977 with a picosecond (ps) simulation of the bovine pancreatic trypsin inhibitor in vacuum by Andrew McCammon, Bruce Gelin, and Martin Karplus.[8] At the time of writing this thesis, MD enables simulations of millions of atoms on the microsecond timescale, providing dynamic insights into biological systems.[9]

2.2.1 Newtonian mechanics

MD simulations describe the evolution in time of a system by solving the classical equations of motion for every particle.[4,10] The fundamental principle is Newton's

second law of motion, which relates the force $\boldsymbol{F}_i$ acting on a particle i to its mass m_i and acceleration $\boldsymbol{a}_i$ as follows:

$$\boldsymbol{F}_i = m_i \boldsymbol{a}_i \tag{2.1}$$

Acceleration is the first derivative of velocity v with respect to time t, and can also be expressed as the second derivative of position r with respect to time.

$$\boldsymbol{a}_i = \frac{d\boldsymbol{v}_i}{dt} = \frac{d^2\boldsymbol{r}_i}{dt^2} \tag{2.2}$$

Combining these principles yields the equation of motion for each particle in the system. To generate a trajectory, one must therefore be able to calculate the force $\boldsymbol{F}_i$ acting on each particle at a specific moment. In MD, these forces are derived from the potential energy function U of the system, defined by the equations and associated parameters that constitute the force field. The force on a given particle i is the negative gradient of this potential energy:

$$\boldsymbol{F}_i = -\boldsymbol{\nabla}_i U \tag{2.3}$$

where $\boldsymbol{\nabla}_i$ is the gradient operator taken with respect to the coordinates of particle i.

2.3 Force fields

In all-atom (AA) force fields, every atom is explicitly represented as an individual particle, including hydrogens. In this work, the CHARMM36m all-atom force field was used.[11] While these atomistic models provide high resolution, their computational expense limits the size and timescales of the systems that can be simulated.

To address the fundamental trade-off between model accuracy and computational cost, methods such as coarse-graining (CG) have become essential. In CG models,

groups of atoms are simplified into multi-atom "beads", quantitatively reducing computational complexity. This results in a smoother energy landscape and allows for the use of larger integration timesteps than in atomistic simulations due to the removal of the fastest atomic motions.[4] Taken together, these factors lead to a substantial computational speed-up and enable simulations to reach longer timescales at the cost of reduced resolution.[12]

The work in this thesis used the coarse-grained Martini 2.2P force field.[13] This model is generally based on a "four-to-one" mapping, where four heavy atoms are represented as a single "bead". In Martini, protein secondary structures are typically preserved using a so-called elastic network, which applies distance restraints between backbone beads.[14] The standard Martini 2 water model represents four real water molecules as a single non-polar, neutral bead. This simplification introduces challenges for correctly modelling electrostatics, since charges in Martini are concentrated at bead centres rather than distributed over multiple atoms.[15] Combined with the non-polar water model, this can result in insufficient dielectric screening and artefacts such as exaggerated ion pairing.[15,16] To mitigate this, the polarisable water model was developed in Martini 2.2P.[16] In this variant, the original neutral bead representing four water molecules is extended by attaching two oppositely charged dummy particles, generating an explicit dipole that provides a more realistic description of dielectric screening and ion solvation.[16]
While Martini 3, the most recent version of this force field family, introduced improvements such as different bead sizes and additional bead types for enhanced chemical transferability, it also presents specific limitations that prevented its use in this work.[17] One notable issue is the excessive polarity of the protein backbone beads, which can cause peptides to remain artificially solvated and prevent their

expected insertion into membranes, an artefactual behaviour documented in the literature and confirmed in discussions with Prof Marrink.[18] Furthermore, Martini 3 currently lacks a polarisable water model, a feature that we deemed essential for correctly capturing polarisation effects in the electrophysiology simulations in this thesis.

The two molecular abstraction levels mentioned above are represented schematically in **Figure 2.1** below.

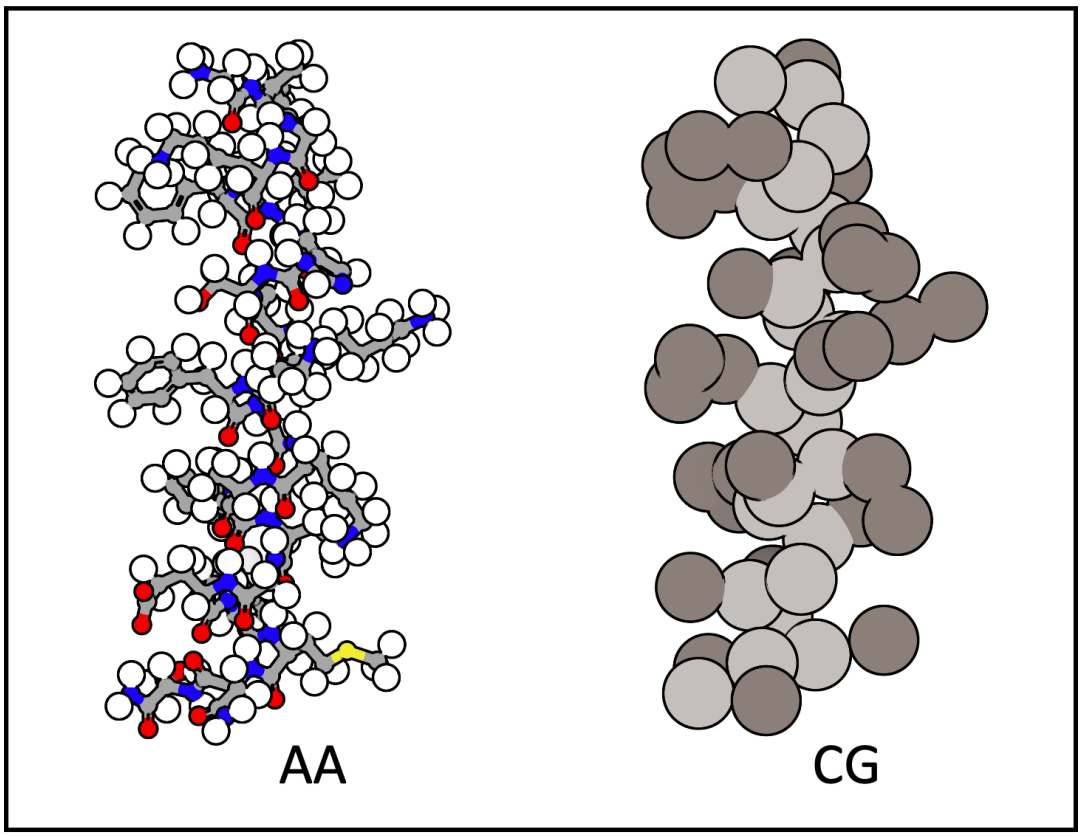

Figure 2.1. *Schematic representations of the antimicrobial peptide magainin 2 (PDB: 2MAG) as all-atom (AA) and coarse-grained force field (CG) model. Legend: AA: white: hydrogen, grey: carbon, blue: nitrogen, red: oxygen, yellow: sulfur atoms; CG: light grey: backbone beads, dark grey: side chain beads.*

More recently, machine-learned potentials (MLPs) have emerged, which are trained on data from quantum mechanical calculations and offer accuracy comparable to the underlying first-principles method at a reduced computational cost.[19–21]

These algorithmic advancements and the increased availability of High-Performance Computing (HPC) clusters enable the modelling of increasingly complex and larger-scale biological systems, such as the crowded bacterial cell envelope and entire viral capsids, all while being fundamentally governed by the accuracy of the underlying models and the parameters of the force fields used.

2.3.1 Force field components

The equations and associated parameters that define the potential energy function constitute the force field. The total potential energy U_{total} is typically expressed as the sum of the terms for bonded interactions U_{bonded} and those for non-bonded interactions $U_{non-bonded}$.[4,10]

$$U_{total} = U_{bonded} + U_{non-bonded} \tag{2.4}$$

The bonded terms describe intramolecular forces that maintain the covalent structure of molecules, while the non-bonded terms describe intermolecular and long-range intramolecular forces:

$$U_{bonded} = \sum U_{bond} + \sum U_{angle} + \sum U_{dihedral} + \sum U_{improper} \tag{2.5}$$

$$U_{non-bonded} = \sum U_{van\ der\ Waals} + \sum U_{Coulombic} \tag{2.6}$$

The functional forms of these terms are detailed in subsequent sections.

2.3.1.1 Bonded interactions

The bonded terms of the force field are intramolecular potentials that define the covalent geometry of a molecule and are applied to a defined list of connected atoms. These terms are typically described by four types of 2-, 3-, and 4-body interactions: bond stretching (2-body), angle bending (3-body), dihedral torsions (4-body), and improper dihedrals (4-body).

2.3.1.1.1 Bond stretching

The bond stretching potential U_{bond} describes the energy associated with the vibration of a covalent bond between two atoms i and j around its equilibrium length r_0. This interaction is commonly modelled as a harmonic potential, treating covalent bonds as undamped springs.

$$U_{bond}(r) = \frac{1}{2} k_{ij}^{r} \left(r_{ij} - r_0\right)^2 \tag{2.7}$$

Here, k_{ij}^{r} is the force constant that defines the bond stiffness and r_{ij} is the distance between the two atoms, as represented schematically in **Figure 2.2**.

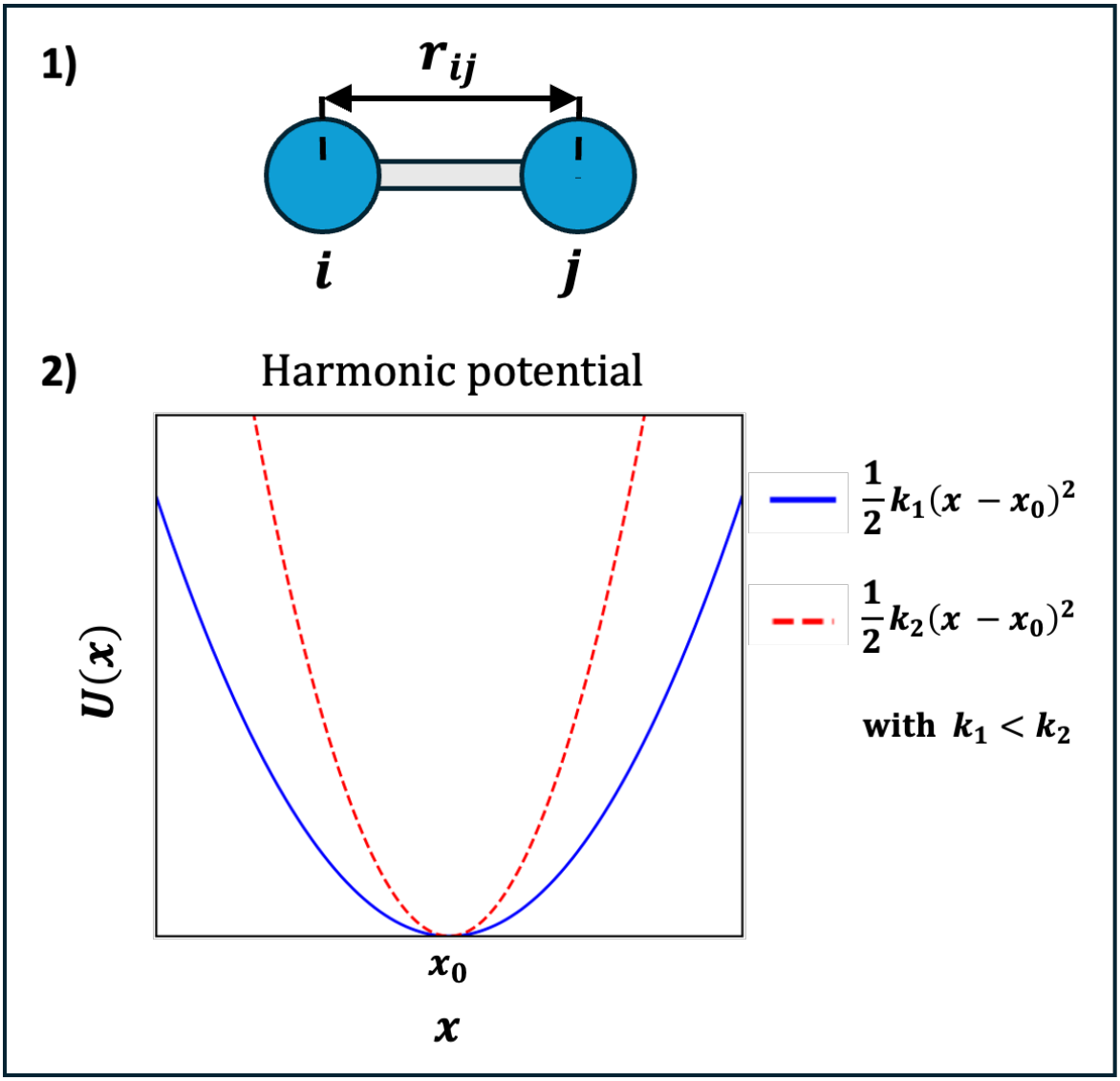

Figure 2.2. *Schematic representations of the quantities related to the bond stretching potential and other potentials modelled as harmonic potentials. 1) Schematic of two atoms i and j (blue spheres) which are linked by a bond (grey connector) at a distance r_{ij}. 2) Harmonic potential energy $U(x)$ as a function of the deviation x from the equilibrium coordinate x_0, shown for two different force constants.*

2.3.1.1.2 Angle bending

The angle bending potential U_{angle} accounts for the energy required to deform the

angle θ_{ijk} formed by three bonded atoms i, j, and k away from its equilibrium value θ_0, as represented schematically in **Figure 2.3.** Similarly to the bond stretching potential, this interaction is typically represented by a harmonic potential.

$$U_{angle}(\theta) = \frac{1}{2} k_{ijk}^{\theta} \left(\theta_{ijk} - \theta_0\right)^2 \tag{2.8}$$

Here, k_{ijk}^{θ} is the force constant of the angle deviation.

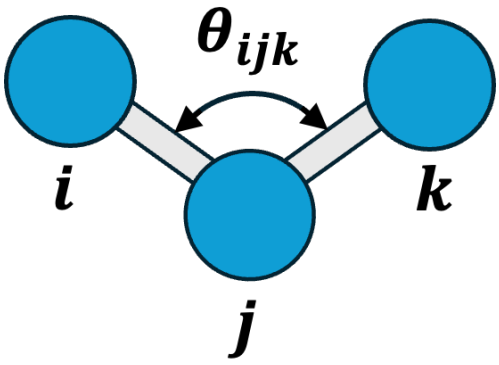

Figure 2.3. *Schematic representation of the quantities related to the angle bending potential. Atoms i, j, and k (blue spheres) are linked by bonds (grey connectors), with the central atom j defining the vertex of the bond angle θ_{ijk}.*

The CHARMM force field family includes an additional correction term to this potential, known as the Urey-Bradley potential.[11,22] This term applies a harmonic restraint not on the angle itself, but on the distance r_{ik} between the two outer atoms i and k of the triplet, aiming to improve the description of vibrational frequencies, particularly for bending modes. The functional form of the Urey-Bradley potential is:

$$U_{Urey-Bradley}(r) = \frac{1}{2} k_{ik}^{UB} \left(r_{ik} - r_{0,ik}\right)^2 \tag{2.9}$$

Where k_{ik}^{UB} is the corresponding force constant and $r_{0,ik}$ is the equilibrium distance between atoms i and k.

2.3.1.1.3 Dihedral torsion

The dihedral torsion term $U_{dihedral}$ models the energy associated with the rotation around the central bond of four contiguously bonded atoms i, j, k, and l, as represented schematically in **Figure 2.4.** This potential describes the energy levels corresponding to different rotamers. The dihedral potential is represented by a periodic function, typically a cosine, to account for the energetic barriers and multiple minima that occur during bond rotation.

$$U_{dihedral}(\phi) = k_{ijkl}^{\phi}\left[1 + \cos(n\phi_{ijkl} - \delta)\right] \tag{2.9}$$

Here, k_{ijkl}^{ϕ} is the force constant, ϕ_{ijkl} is the current dihedral angle, n is the periodicity which defines the number of minima in a 360° rotation, and δ is the phase shift angle.

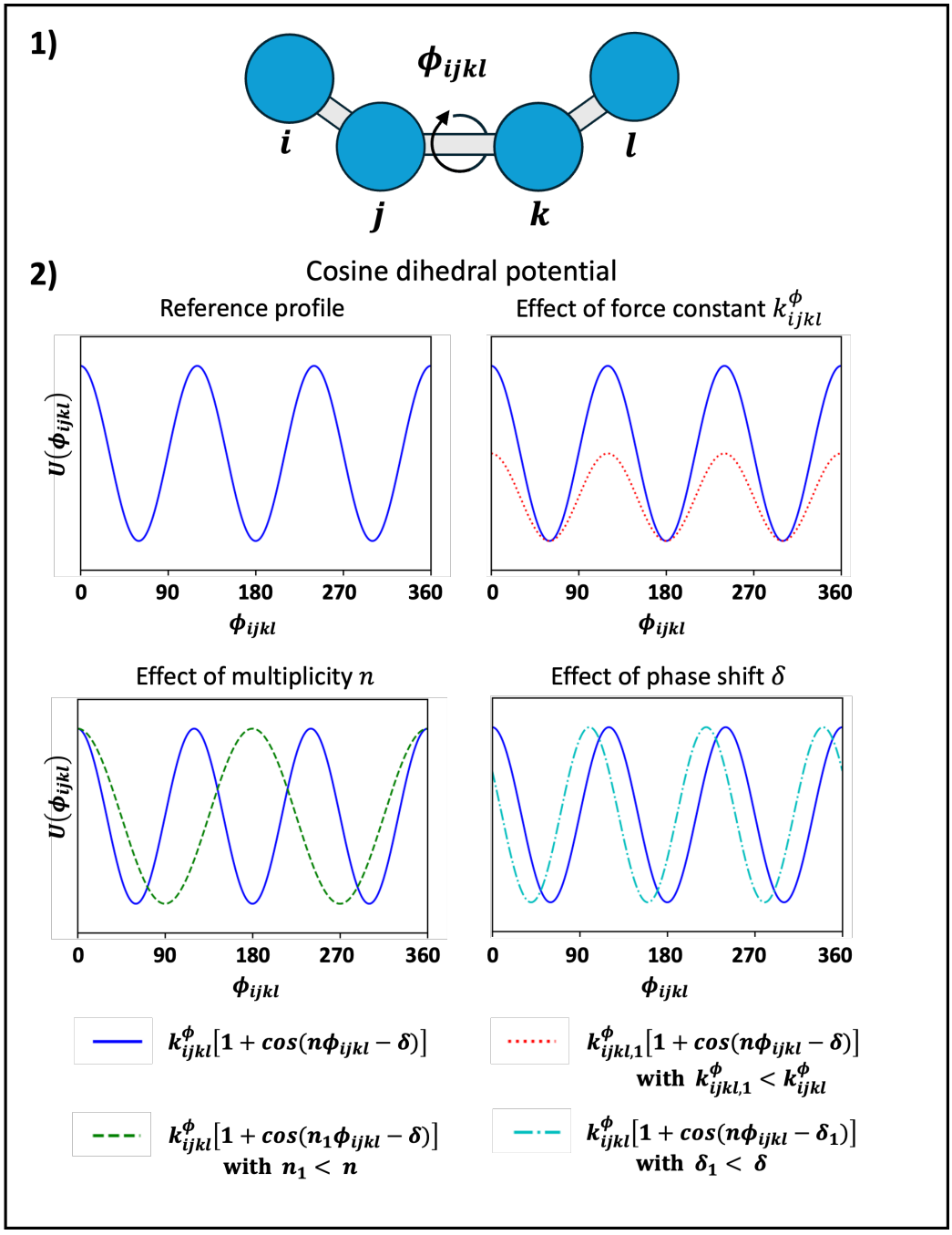

Figure 2.4. *Schematic representation of the quantities related to the dihedral torsion potential. 1) Atoms i, j, k, and l (blue spheres) are linked by bonds (grey connectors), with the central bond between j and k defining the axis of rotation for the dihedral angle ϕ_{ijkl}. 2) Cosine dihedral potential energy $U(\phi)$ as a function of the dihedral angle ϕ_{ijkl}, with the effects of varying the force constant, multiplicity, and phase shift illustrated.*

2.3.1.1.4 Improper dihedrals

An improper dihedral angle ω_{ijkl} is defined by four atoms i, j, k, and l, and represents the angle between the plane containing atoms i, j, and k and the plane containing atoms j, k, and l, as represented schematically in **Figure 2.5**. This term acts as a restraint potential to maintain a specific local geometry, such as the planarity of aromatic rings or the chirality of stereocenters. The corresponding potential $U_{improper}$ is typically represented by a harmonic potential:

$$U_{improper}(\omega) = \frac{1}{2} k_{ijkl}^{\omega} \left(\omega_{ijkl} - \omega_0\right)^2 \tag{2.10}$$

Here, k_{ijkl}^{ω} is the force constant that determines the stiffness of the restraint and ω_0 is the equilibrium value of the improper dihedral angle ω_{ijkl}.

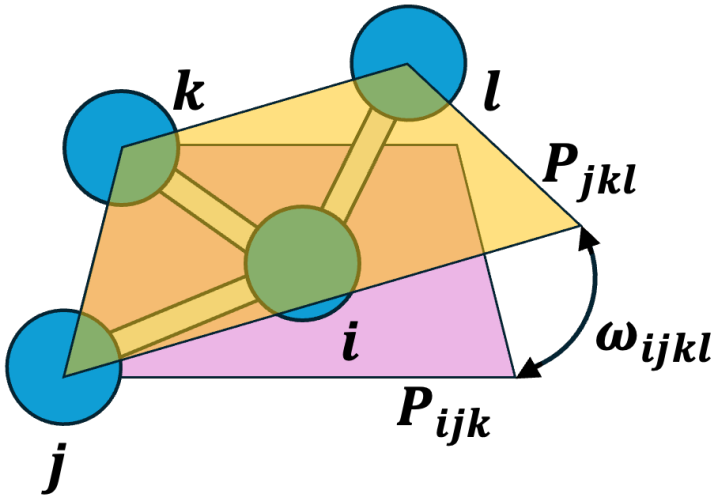

Figure 2.5. *Schematic representation of the quantities related to the improper dihedral torsion potential. Atoms i, j, k, and l (blue spheres) are linked by bonds (grey connectors) via the central atom i. This central atom i and its bonded neighbours define two intersecting planes P_{ijk} (pink) and P_{jkl} (yellow), with the improper dihedral angle ω_{ijkl} representing the angle between these planes.*

2.3.1.2 Non-bonded interactions

Non-bonded interactions describe the forces between atoms that are not directly linked by covalent bonds. These include forces between atoms in different molecules (intermolecular) as well as between atoms in the same molecule that are separated by more than three covalent bonds (long-range intramolecular). They are primarily described by two types of potentials: van der Waals and Coulombic interactions.

2.3.1.2.1 Van der Waals interactions

Van der Waals interactions are short-range forces that account for both the repulsion and attraction between non-bonded atoms.[23] The repulsive component arises at very short distances due to the Pauli exclusion principle (postulated in 1925 by Wolfgang Pauli), which forbids electrons with the same spin from occupying the same quantum state.[24] As atoms approach one another closely, their outer electron orbitals begin to overlap, resulting in said repulsive force.[23]

The attractive component arises from transient fluctuations in the electron density of atoms or molecules, and is known as the London dispersion force (postulated in 1930 by Fritz London).[25] These spontaneous fluctuations create a temporary, instantaneous dipole, which in turn induces a complementary dipole in neighbouring atoms. The transient alignment of these induced dipoles results in a weak, net attractive force.[23]

In most classical force fields, van der Waals interaction between atoms i and j is approximated by the Lennard-Jones potential.[26]

$$U_{Lennard-Jones} = 4\varepsilon_{ij}\left[\left(\frac{\sigma_{ij}}{r_{ij}}\right)^{12} - \left(\frac{\sigma_{ij}}{r_{ij}}\right)^{6}\right] \tag{2.11}$$

Here, r_{ij} is the distance between the two interacting atoms i and j, ε_{ij} represents the depth of the potential well and defines the strength of the interaction, and σ_{ij} is the distance at which the potential energy is zero. The Lennard-Jones potential is schematically represented in **Figure 2.6**.

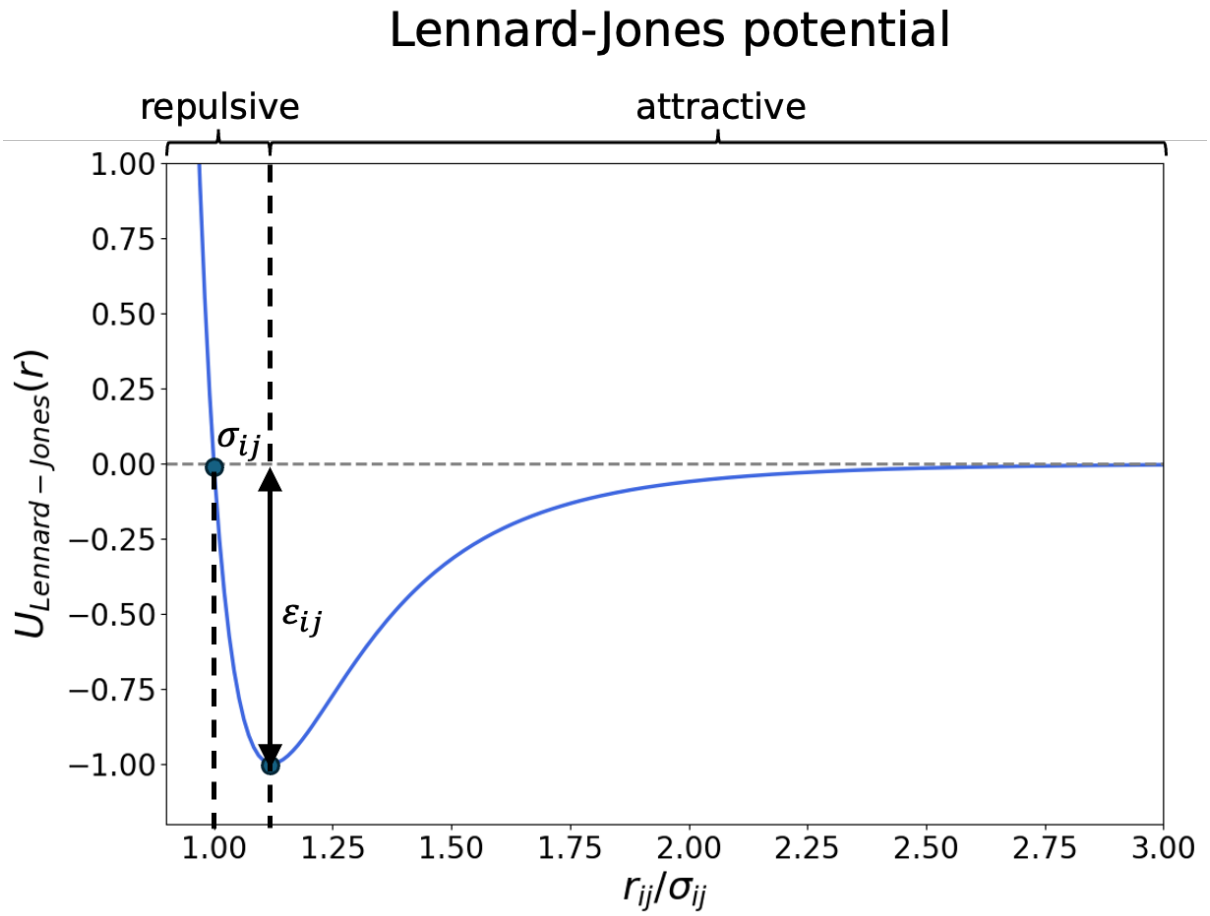

Figure 2.6. *Plot showing Lennard-Jones potential $U_{Lennard-Jones}$ as a function of the normalised distance (σ_{ij}/r_{ij}) between two particles i and j, with the attractive and repulsive interaction regions. The plot shows the key parameters of the potential: σ_{ij}, the particle separation at which the potential energy is zero, and the depth of the potential well ε_{ij}, which represents the maximum energy of attraction.*

The r^{-12} term models the strong short-range repulsion, while the term proportional to r^{-6} models the weaker long-range attraction. While the r^{-6} term has some theoretical grounding in quantum perturbation theory and reflects dispersion interactions between fluctuating dipoles, both it and the purely empirical r^{-12} repulsion term are chosen for their good balance of accuracy and computational efficiency rather than strict physical derivation.

2.3.1.2.2 Coulombic interactions

Coulombic, or electrostatic interactions describe the forces between atoms i and j which carry electric charges q_i and q_j at rest. This type of interaction is modelled using the Coulomb potential, which is derived from Coulomb's Law (formulated in 1785 by Charles-Augustin de Coulomb).[27]

$$U_{Coulomb} = \sum_{i<j} \frac{q_i q_j}{4\pi\varepsilon_0 r_{ij}} \tag{2.12}$$

Here, ε_0 is the permittivity of free space and r_{ij} is the distance between atoms i and j.

The long-range nature of electrostatic forces means that direct pairwise computation scales quadratically with the number of particles N ($O(N^2)$), making it computationally prohibitive to evaluate for larger systems.[28] To manage this cost, simulations typically employ a cut-off scheme, in which electrostatic interactions are explicitly computed for particles closer than the designed cut-off distance value and beyond which they are truncated.[28] This simple truncation method is, however, known to introduce artefacts, as it violates the conservation of energy and

momentum, which becomes particularly severe in systems simulated with periodic boundary conditions.[28]

For this reason, modern force fields instead use methods to approximate the long-range electrostatic contributions, with the most common method being the Particle Mesh Ewald (PME) algorithm.[28] The PME method splits the electrostatic potential into a short-range component, computed explicitly for atom pairs within a cut-off distance, and a long-range component, which is evaluated in reciprocal space for the entire system using Fast Fourier Transforms (FFT). This decomposition of the electrostatic potential reduces the computational scaling to the order of $O(N \log N)$ and enables accurate and efficient long-range electrostatics treatment in larger simulations.

2.4 Integration of the equations of motion

With the forces acting on each particle and thus their instantaneous acceleration determined from the force field potential energy function *via* **Equations 2.1** and **2.3**, a numerical integrator must then be used to solve Newton's equations of motion to calculate how the system should evolve over a specified time step, as analytical solutions are intractable for many-body systems. This new system configuration results in a new potential energy and consequently in a new set of forces acting on each particle. The continuous alternation between calculating these forces and updating the particle positions is what propagates the system through time and generates the desired trajectory.

One of the most widely used numerical algorithms for integrating the equations of motion of a particle is the leapfrog algorithm.[10] This method can be derived by

approximating the continuous derivatives from **Equation 2.2** with a central difference approximation over a discrete time step Δt.

First, to update the velocity, the derivative $\boldsymbol{a} = \frac{d\boldsymbol{v}}{dt}$ at time t is approximated by the change in velocity centred around that point in time:

$$\boldsymbol{a}(t) \approx \frac{\boldsymbol{v}\left(t + \frac{\Delta t}{2}\right) - \boldsymbol{v}\left(t - \frac{\Delta t}{2}\right)}{\Delta t} \tag{2.13}$$

Rearranging this expression gives the velocity update rule, which calculates the velocity $\boldsymbol{v}$ at the next half-step $t + \frac{\Delta t}{2}$ based on the previous half-step $t - \frac{\Delta t}{2}$:

$$\boldsymbol{v}\left(t + \frac{\Delta t}{2}\right) = \boldsymbol{v}\left(t - \frac{\Delta t}{2}\right) + \boldsymbol{a}(t)\Delta t \tag{2.14}$$

To then update the position $\boldsymbol{r}$, the derivative $\boldsymbol{v} = \frac{d\boldsymbol{r}}{dt}$ is approximated at the half-step $t + \frac{\Delta t}{2}$:

$$\boldsymbol{v}\left(t + \frac{\Delta t}{2}\right) \approx \frac{\boldsymbol{r}(t + \Delta t) - \boldsymbol{r}(t)}{\Delta t} \tag{2.15}$$

Rearranging this expression then yields the position update rule, which uses the newly calculated velocity $\boldsymbol{v}$ at time $t + \frac{\Delta t}{2}$ to find the position $\boldsymbol{r}$ at the following whole time step $t + \Delta t$:

$$\boldsymbol{r}(t + \Delta t) = \boldsymbol{v}\left(t + \frac{\Delta t}{2}\right)\Delta t + \boldsymbol{r}(t) \tag{2.16}$$

Once the new position $\boldsymbol{r}(t + \Delta t)$ has been calculated, the integration cycle repeats: the new positions are used to determine the new forces $\boldsymbol{F}(t + \Delta t)$ from the potential energy function U. This yields the new acceleration $\boldsymbol{a}(t + \Delta t)$, which is then used to

calculate the velocity at the next half-step $\boldsymbol{v}\left(\frac{3\Delta t}{2}\right)$, and so on.

As the name of the leap-frog integrator suggests, the velocities and positions “leap-frog” over each other, as they are never known for the same time step.

2.5 Bond constraints and the integration timestep

To maximise computational efficiency and sample the longest possible timescale, it is desirable to use the largest possible integration timestep Δt. However, the timestep must be substantially smaller than the period of the fastest motion in the system to maintain numerical stability and prevent simulations from “blowing up”. In atomistic simulations, this fastest motion is typically the ~10 fs vibration of bonds involving hydrogen atoms. While the Nyquist-Shannon sampling theorem sets a theoretical limit of two samples per period to avoid aliasing artefacts, the integration algorithms used in MD are much stricter because they assume forces are nearly constant over Δt.[29–31] To ensure this assumption holds for such rapid oscillations and that the rapidly changing forces are accurately resolved, a timestep of ~1 fs (roughly one-tenth of the vibrational period) is required.[31]

To overcome this limitation, constraint algorithms are employed to replace these fast, high-frequency vibrations with rigid mathematical constraints. These bonds are then no longer treated as fast-vibrating "springs" but as "rods" of fixed, unchangeable lengths. To enforce this rigidity, a correction is applied after each unconstrained integration step. Two common algorithms for this are SHAKE and LINCS.[32,33]

The SHAKE algorithm is an iterative procedure that adjusts particle positions to satisfy the distance constraints.[32] It solves the constrained equations of motion by introducing Lagrange multipliers, which represent the constraint forces required to

maintain the fixed bond lengths. The algorithm repeatedly cycles through all constraints, correcting the positions until they converge within a specified tolerance.

The LINCS (Linear Constraint Solver) algorithm is a non-iterative approach that is generally faster and more stable than SHAKE for large molecules.[33] Instead of iterating, LINCS projects the new, unconstrained bond vectors onto the directions of the previous bonds and then applies a correction based on a matrix inversion to reset all bond lengths simultaneously.[33] By eliminating the fastest vibrational motions from the system, these constraints allow for the use of a larger integration timestep (typically 2 fs), markedly increasing the computational efficiency of the simulations.

2.6 Periodic Boundary Conditions

MD simulations are performed within a finite system, usually within a box. The finite size of any simulation box introduces edge effects, as particles near box boundaries would interact with a vacuum unless specific measures are taken.[10] The most common approach to address this limitation is to use Periodic Boundary Conditions (PBCs): by surrounding the central simulation box, also called “unit cell”, with infinitely many identical copies of itself in all directions, the periodic images effectively imitate an infinite system.[10] Under this scheme, when a particle exits one face of the box, its periodic image simultaneously re-enters through the opposite face, ensuring the number of particles in the unit cell remains constant and that particles at the edge of the simulation box encounter a bulk environment rather than a vacuum. This is schematically represented in **Figure 2.7**.

In practice, the equations of motion are solved only for the particles within the central unit cell, and interactions are then computed based on the minimum image convention. This principle ensures that each particle interacts only with the singular

closest image of other particles in the system. To prevent a particle from interacting with its own image, resulting in simulation artefacts, the box dimensions must be at least twice the cut-off radius used for non-bonded interactions described above. By eliminating edge effects, PBCs allow a small, computationally tractable system to reproduce the macroscopic properties of bulk matter accurately, such as a bulk solvent or an infinite membrane patch for example.[10]

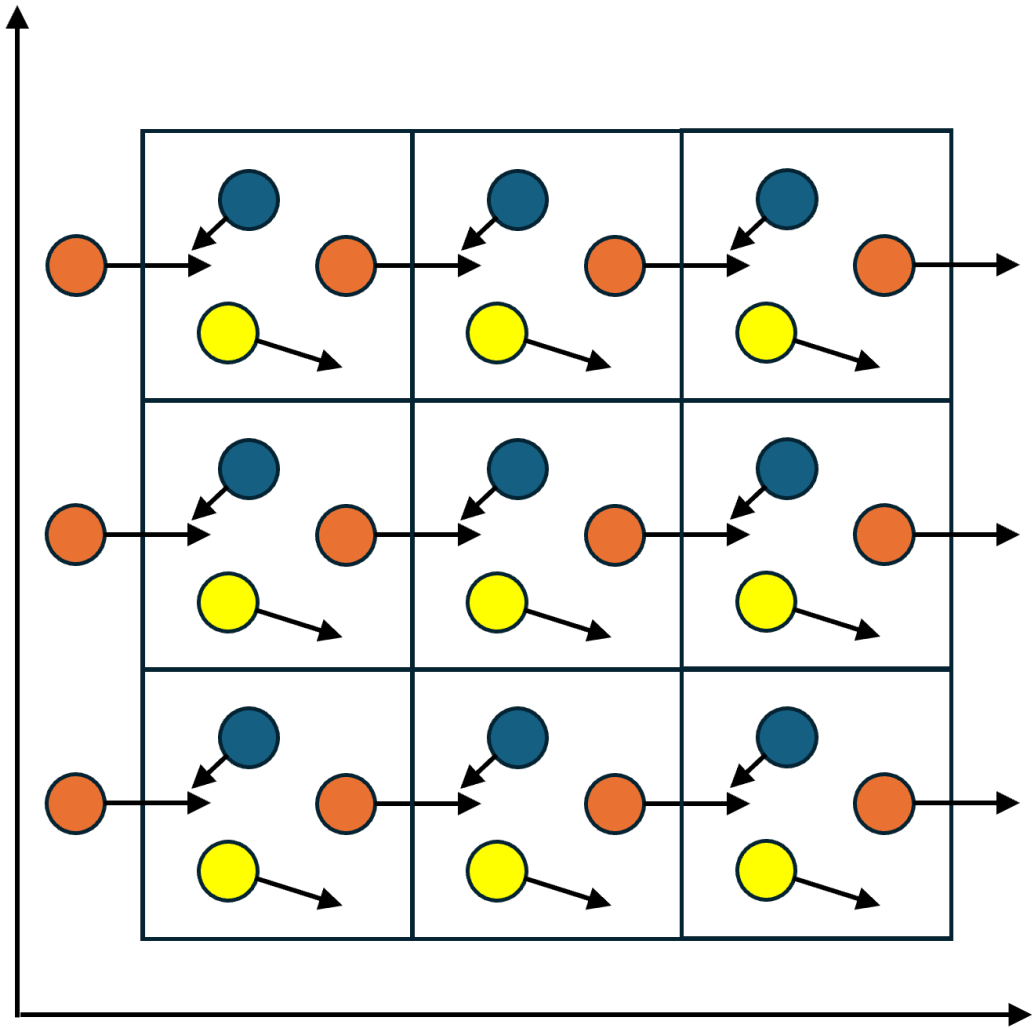

Figure 2.7. *Schematic representation of a simulation box replicated in two dimensions via PBCs to mimic an infinite system. Identically coloured particles correspond to the same particle appearing in adjacent periodic images. The grid*

outlines the repeating simulation box boundaries, and arrows indicate particle trajectories across them.

2.7 Thermodynamic ensembles

Having previously introduced periodic boundary conditions to mimic the properties of bulk systems, I now turn to statistical mechanics to provide the theoretical connection between microscopic MD simulations and macroscopic observables such as temperature and pressure. This link enables us to replicate correct thermodynamic conditions in simulations through ensembles and to compare observables with experimental values.

For a classical system composed of N particles, the phase space $\boldsymbol{\Gamma}$ represents the set of all possible particle positions and momenta, with each particle contributing three spatial coordinates $\boldsymbol{r_i}$ and three momentum coordinates $\boldsymbol{p_i}$:

$$\boldsymbol{\Gamma} = (\boldsymbol{r_i}, \dots, \boldsymbol{r_N}; \boldsymbol{p_i}, \dots, \boldsymbol{p_N}) \tag{2.17}$$

with $\boldsymbol{r_i} = (x_i, y_i, z_i)$ and $\boldsymbol{p_i} = (p_{xi}, p_{yi}, p_{zi})$.

A microstate corresponds to a specific point in this phase space, and fully characterises the system configuration, *i.e.* all particle positions and momenta. For brevity, a microstate is also commonly denoted as Γ.

In contrast, a macrostate is defined by bulk properties such as the particle number N, system volume V, temperature T, pressure P, or energy E; these macroscopic quantities correspond to thermodynamic observables, with many microstates being consistent with the same macrostate. This averaging is formalised through the concept of an ensemble, a probability distribution over all microstates consistent with a given macrostate.

For a property of interest A, represented at the microscopic level as a function $A(\Gamma)$ of the microstate Γ, the corresponding macroscopic observable is obtained as an ensemble average:

$$\langle A \rangle = \int A(\Gamma)\, \mathrm{P}(\Gamma)\, d\Gamma \tag{2.18}$$

where $\langle A \rangle$ is the macroscopic value of property A, $\mathrm{P}(\Gamma)$ is the probability density of microstate Γ, and $d\Gamma$ is the differential volume element in phase space. For example, if $A(\Gamma)$ represents the combined microscopic kinetic energies of all particles in a given microstate, $\langle A \rangle$ corresponds to the thermodynamic temperature of the system.

While **Equation 2.18** defines a microscopic observable as an average over all possible microstates, evaluating this exactly would require integrating over a virtually infinite number of configurations. This could be achieved in principle by running an infinitely long simulation. For ergodic systems, such a trajectory would sample microstates according to their statistical weights, so time averages are equal to ensemble averages:

$$\langle A \rangle = \lim_{t \to \infty} \frac{1}{t} \int_0^t A\big(\Gamma(t')\big)\, dt' \tag{2.19}$$

where $\Gamma(t')$ represents the microstate Γ at time t'. In contrast, non-ergodic systems may remain trapped in subregions of phase space, for example when separated by high energy barriers, requiring enhanced sampling methods to achieve correct ensemble averages.

In practice, the number and duration of simulations that can be performed are necessarily finite, producing a finite set of sampled configurations at regular

intervals. The system property is thus approximated by the time average over the observation window:

$$A \approx \langle A \rangle_{time} = \frac{1}{N_{obs}} \sum_{\tau=1}^{N_{obs}} A(\Gamma(\tau)) \tag{2.20}$$

where N_{obs} is the number of sampled configurations, τ is the frame index, and $A(\Gamma(\tau))$ is the value of property A in the τ-th microstate.

The precise form of the probability distribution $\mathrm{P}(\Gamma)$ introduced in **Equation 2.18** depends on which macroscopic thermodynamic variables are held constant and which are free to fluctuate for a given system. Which quantities fluctuate, such as energy, pressure, or volume, depends on the type of exchange permitted with the system surroundings, and this in turn determines the statistical weight assigned to each microstate.

Different sets of fixed variables correspond to the standard thermodynamic ensembles: the microcanonical ensemble (NVE), the canonical (or isochoric) ensemble (NVT), or the isothermal-isobaric ensemble (NPT), where the quantities mentioned in parentheses are constrained for each. In MD simulations, the NVT and NPT ensembles are typically employed because they reproduce realistic experimental conditions with fixed temperature and/or pressure, and their control is described in the following subchapter.

2.8 Controlling system temperature and pressure

For MD simulations to be biologically relevant, they must be performed under controlled thermodynamic conditions, such as regulated temperature and pressure, that reflect a realistic physiological state. This is achieved by coupling the system to conceptual "baths" *via* algorithms known as thermostats and barostats. These mathematical constructs serve as theoretical reservoirs of heat or pressure, allowing the system to exchange energy or work to mimic a macroscopic environment at a defined temperature or pressure.

2.8.1 Thermostats

Thermostats regulate the system temperature by adjusting particle velocities to maintain the desired average kinetic energy, allowing for simulations in the canonical (NVT) ensemble, where the number of particles N, volume V, and temperature T are kept constant.

The Berendsen thermostat is a "weak-coupling" algorithm that corrects deviations from the reference temperature T_0 by ensuring they decay exponentially.[34] The rate of temperature T change is given by:

$$\frac{dT(t)}{dt} = \frac{T_0 - T(t)}{\tau_T} \tag{2.21}$$

Here, τ_T is the time constant that determines the strength of the coupling to the heat bath. While this thermostat is very effective for bringing a system to the target temperature during equilibration, its deterministic relaxation of temperature deviations acts as a damper that suppresses the natural kinetic energy fluctuations required for a correct canonical ensemble.

The Velocity-rescale (V-rescale) thermostat is an extension of the Berendsen method that corrects its primary deficiency.[35] It includes an additional stochastic term that ensures the system generates the correct kinetic energy distribution, with the change in kinetic energy K being modified according to:

$$dK = \left(\frac{K_0 - K}{\tau_T}\right) dt + 2\sqrt{\frac{KK_0}{N_f}}\frac{dW}{\sqrt{\tau_T}} \tag{2.22}$$

Here, K_0 is the target kinetic energy of the system, N_f is the number of degrees of freedom of the atoms that are controlled by the thermostat, and dW represents a Wiener process, the mathematical description of a random walk, which introduces stochastic noise and counteracts the temperature damping. By ensuring the correct temperature fluctuations around the target value, the V-rescale thermostat generates a true canonical ensemble, making it a robust choice for production simulations.

2.8.2 Barostats

Barostats regulate the pressure of a system by adjusting the volume of the simulation box, which can be done isotropically or anisotropically. This enables simulations to be performed in the isothermal-isobaric (NPT) ensemble, where the number of particles N, pressure P, and temperature T are kept constant.

The Berendsen barostat operates analogously to the Berendsen thermostat and uses a weak-coupling scheme to relax the pressure $\boldsymbol{P}$ of a system towards the reference value $\boldsymbol{P_0}$[34]:

$$\frac{d\boldsymbol{P}(t)}{dt} = \frac{\boldsymbol{P_0} - \boldsymbol{P}(t)}{\tau_p} \tag{2.23}$$

This pressure correction is achieved by scaling the simulation box vectors and the particle coordinates at regular intervals, with the time constant τ_p determining the strength of the coupling. Like its thermostat counterpart, the Berendsen barostat is effective for equilibration, but it does not generate a correct NPT ensemble and should thus not be used for production simulations.

The Parrinello-Rahman barostat is a more rigorous extended-ensemble method where the box vectors are treated as dynamic variables that fluctuate according to their own equations of motion.[36] This allows the simulation box to change both its size and shape in response to the internal pressure of the system. The matrix equation of motion for the matrix of box vectors $\boldsymbol{b}$ is:

$$\frac{d^2\boldsymbol{b}}{dt^2} = V\boldsymbol{W}^{-1}(\boldsymbol{b}')^{-1}(\boldsymbol{P} - \boldsymbol{P}_0) \tag{2.24}$$

Here, V is the box volume, $\boldsymbol{W}$ is a matrix that determines the strength of the coupling of the system to the barostat and is proportional to the isothermal compressibility parameter, and $\boldsymbol{P}$ and $\boldsymbol{P}_0$ are the current and reference pressure tensors respectively. By allowing the box to fluctuate naturally, this algorithm correctly generates the NPT ensemble and is the standard approach for production NPT simulations.

2.9 System preparation and equilibration

With the theoretical and algorithmic foundations of MD simulations established, the next stage involves the practical preparation of the system of interest for a production run, generating the desired molecular trajectory for analysis.[31,37] The initial coordinates for proteins are typically obtained from experimental repositories

such as the Protein Data Bank (PDB), or increasingly from predictive methods such as AlphaFold.[38,39]

These initial structures are first processed by adding missing atoms and determining appropriate residue protonation states. Builder tools like CHARMM-GUI or custom scripts can then be used to assemble the complete system.[40] The resulting structure however often contains artefacts from the building process, such as unfavourable steric clashes or strained geometries. Therefore, an initial energy minimisation step is required to relax these energetically unfavourable interactions and produce a stable, low-energy state before proceeding to system equilibration.

2.9.1 Energy Minimisation

Energy minimisation is a process that adjusts the atomic coordinates of the initial structure to find a nearby local minimum on the potential energy surface with the goal of relaxing energetically unfavourable interactions. This is a static procedure without a time coordinate, and for the initial relaxation of systems that are far from equilibrium, the steepest descent algorithm is commonly used due to its robustness.[37] This algorithm is an iterative method that moves the atoms "downhill" on the potential energy surface, *i.e.* in the direction of the steepest gradient, which is parallel to the force $\boldsymbol{F}$ acting on each atom. At each step, the atomic positions $\boldsymbol{r}$ are updated according to:

$$\boldsymbol{r}_{n+1} = \boldsymbol{r}_n + \frac{\boldsymbol{F}_n}{\max(|\boldsymbol{F}_n|)} h_n \tag{2.25}$$

Here, n is the iteration number, $\boldsymbol{r}_n$ and $\boldsymbol{r}_{n+1}$ are the atomic positions before and after the step n, $\boldsymbol{F}_n$ is the force on an individual atom at step n, and h_n is the maximum step size. The $\max(|\boldsymbol{F}_n|)$ term is the magnitude of the largest force component on

any atom in the entire system and normalises the step size. This ensures the atom with the largest force moves by h_n, while all other atoms move a proportionally smaller distance, leading to a more controlled minimisation. The new configuration is only accepted if it results in a lower total potential energy. This process is repeated until a stopping criterion is met, such as when the maximum force on any atom falls below a specified tolerance or a certain number of steps have been performed. While the steepest descent algorithm is very efficient when a system is far from an energy minimum, it converges slowly as it approaches minima compared to more sophisticated methods such as the Conjugate Gradient algorithm.[41]

2.9.2 System equilibration

Following energy minimisation, the system is in a stable, low-energy state but lacks kinetic energy and is not yet at the target temperature or pressure of the desired physiological environment. The purpose of equilibration is to gently bring the system to these conditions, allowing the solvent and other mobile components to relax around the solute. It is at this stage that the time dimension and particle velocities are introduced, and the first trajectories are generated.

A staged equilibration protocol, popularised by CHARMM-GUI and now widely adopted, including in this thesis, proceeds in two phases, as described below.[40] Positional restraints are typically applied to the biomolecules of interest during this protocol to prevent them from deforming, while the surrounding environment settles into an equilibrium state. The strength of these restraints is often reduced to zero in a stepwise manner during equilibration.[40]

In the above-mentioned protocol, the first phase is performed in the canonical (NVT) ensemble, where the system is heated to the target temperature while maintaining a fixed volume, allowing the solvent to redistribute around the restrained solute without perturbing the system density. During this stage, a thermostat is applied while the box volume is held fixed. This allows the initially ordered or randomly placed solvent molecules to rearrange themselves into a thermally stable configuration around the fixed protein, while the system temperature is being monitored for drifting behaviour.[42]

The system is then switched to the isothermal-isobaric (NPT) ensemble, as it best reflects experimental conditions of constant temperature and pressure. Equilibration is assessed *via* the system density, along with other quantities where relevant.[42] Position restraints on the molecules of interest are typically maintained but may be gradually weakened over several NPT stages, allowing them to relax in the now-equilibrated solvent environment. Once these conditions are satisfied, the system is ready for production simulations in the NPT ensemble.

2.10 Computational Electrophysiology

The Computational Electrophysiology (CompEL) method was developed to enable molecular dynamics simulations under realistic transmembrane potentials by maintaining a constant charge imbalance across membranes.[43,44] In practice, CompEL is implemented using systems composed of two membrane bilayers that separate two aqueous compartments, as illustrated in **Figure 2.8**.[43] Membrane pore proteins connect adjacent compartments, allowing ion and water exchange between them. A defined charge imbalance ΔQ is maintained by periodically replacing ions that have crossed compartments with water molecules from the side the ions

originated from. This exchange sustains a constant electric field across the membranes and maintains ionic homeostasis, with the resulting transmembrane potential ΔV related to the charge imbalance and the bilayer capacitance C:

$$\Delta V = \frac{\Delta Q}{C} \tag{2.26}$$

where C is typically on the order of 1 $\mu\mathrm{F/cm^2}$.[43,45]

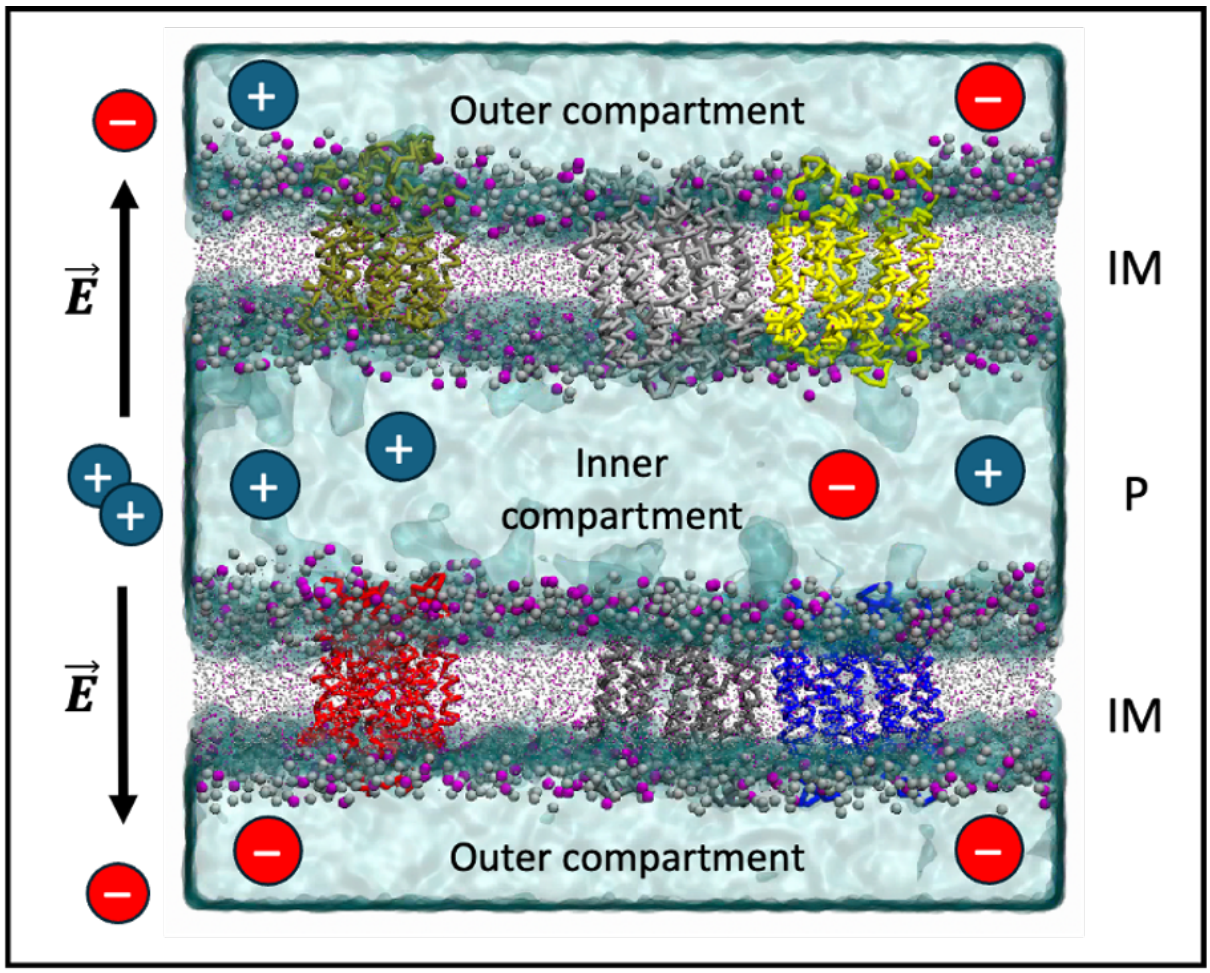

Figure 2.8. *Schematic representation of a double bilayer system used in this and subsequent chapters to induce an electric membrane potential using the Computational Electrophysiology (CompEL) protocol, representing the inner membrane (IM) and periplasm (P). Lipid headgroups are shown as grey*

(phosphatidylethanolamine, PE) and purple (phosphatidylglycerol, PG) beads, and tails as point representations. Aqueous compartments are shown as a transparent cyan surface. Membrane pore protein backbones are shown as stick representations.

This method has been instrumental in studying the mechanisms of ion channel conductance and selectivity, as well as for investigating electroporation phenomena.[43,44,46] More recently, it has also been applied to investigate the membrane-penetrating behaviour of polymyxin AMPs in Gram-negative bacterial inner membranes.[47] In particular, simulations using CompEL have revealed that polymyxin B1 can translocate through electroporation-induced pores at protein-phospholipid interfaces, suggesting that AMPs may be capable of exploiting local membrane defects such as membrane proteins to cross the inner membrane. In this thesis, CompEL was thus used to mimic the inside-negative potential of the *E. coli* inner membrane and investigate the mechanisms by which AMPs interact with and cross this bilayer.

Crucially, the standard CompEL swap-exchange algorithm is not designed to accommodate the swapping of larger species, such as osmolytes or antimicrobial peptides, which leads to system instability. Consequently, the translocation of these species through a membrane pore is irreversible and permanently alters the charge difference between compartments, rendering simulations with different periplasmic compositions non-comparable once membrane permeabilisation occurs. Therefore, all quantitative analyses in this work were truncated at the visually determined onset of pore formation.

2.11 Methods of analysis

Analyses used built-in GROMACS tools and in-house Python 3 scripts using the MDAnalysis, NumPy, pandas, Matplotlib, SciPy, NetworkX, and lifelines libraries.[48–57] The CG2AT tool was used for backmapping CG simulations to atomistic resolution.[58] Visualisation was performed using VMD and ChimeraX.[59,60]

2.11.1 Contact analysis

Contacts between molecules of interest were determined at the residue level using the FastNS neighbour search algorithm with cell lists, as implemented in MDAnalysis.[51] For each trajectory, relevant atom groups were defined. For each frame, unique contacts were counted whenever any atoms from two different molecules were within 4.5 Å in atomistic simulations and 6.0 Å in coarse-grained simulations. The resulting contact data were used to quantify AMP-AMP interactions and aggregation, AMP-solute associations, and AMP interactions with membranes and membrane proteins.

2.11.2 Interaction lifetimes

Interaction lifetimes between molecule pairs were calculated at the molecular or residue level from the contact data described above. For each simulation and interactant pair, contiguous frames where a contact was present were identified and converted into lifetimes. Right-censored events, where a contact persisted until the end of a trajectory, were included. Lifetimes were aggregated across conditions and analysed with the Kaplan-Meier estimator to generate survival probability curves using the lifelines library:

$$S(t) = \prod_{i:t_i \leq t} \left(1 - \frac{d_i}{n_i}\right) \tag{2.27}$$

where $S(t)$ is the estimated probability that an interaction survives beyond time t, t_i marks a time point at which a contact-breaking event occurred, d_i is the number of contact-breaking events at t_i, and n_i is the number of ongoing interactions (the population "at risk") just before t_i.[57]

2.11.3 Lipid flip-flop analysis

Lipid flip-flops were identified using the MDAnalysis LeafletFinder algorithm.[50] Leaflet assignments were determined at the start and at regular intervals throughout each trajectory for all bilayers present. For each lipid, changes in leaflet assignment over time were counted as a flip-flop event.

2.11.4 Membrane thickness analysis

Membrane thickness was computed from the positions of phosphate headgroups in each lipid bilayer, with leaflets assigned using the MDA LeafletFinder algorithm.[50] For each leaflet, a smooth two-dimensional surface was fitted to the phosphate positions using radial basis function interpolation with a thin plate spline function, as implemented in the SciPy Python package.[55] Local bilayer thickness was defined as the vertical distance between the upper and lower interpolated surfaces.

Local membrane thickness profiles were similarly computed in the vicinity of membrane proteins, only considering proteins distant at least 15 Å from other neighbouring membrane proteins. A polar sampling grid centred on the protein centre-of-mass was used to record the membrane thickness as a function of distance and angle relative to the protein.

References

1. Hollingsworth, S. A. & Dror, R. O. Molecular dynamics simulation for all. *Neuron* **99**, 1129–1143 (2018).

2. Khalid, S., Schroeder, C., Bond, P. J. & Duncan, A. L. What have molecular simulations contributed to understanding of Gram-negative bacterial cell envelopes? *Microbiology* **168**, 001165 (2022).

3. Leach, A. R. *Molecular Modelling: Principles and Applications*. (Prentice Hall, 2001).

4. Frenkel, D. & Smit, B. *Understanding Molecular Simulation: From Algorithms to Applications*. (Elsevier, 2023).

5. Alder, B. J. & Wainwright, T. E. Studies in molecular dynamics. I. General method. *J. Chem. Phys.* **31**, 459–466 (1959).

6. Rahman, A. Correlations in the motion of atoms in liquid argon. *Phys. Rev.* **136**, A405 (1964).

7. Stillinger, F. H. & Rahman, A. Improved simulation of liquid water by molecular dynamics. *J. Chem. Phys.* **60**, 1545–1557 (1974).

8. McCammon, J. A., Gelin, B. R. & Karplus, M. Dynamics of folded proteins. *nature* **267**, 585–590 (1977).

9. Oostenbrink, C., Villa, A., Mark, A. E. & Van Gunsteren, W. F. A biomolecular force field based on the free enthalpy of hydration and solvation: the GROMOS

force-field parameter sets 53A5 and 53A6. *J. Comput. Chem.* **25**, 1656–1676 (2004).

10. Allen, M. P. & Tildesley, D. J. *Computer Simulation of Liquids*. (Oxford university press, 2017).

11. Huang, J. *et al.* CHARMM36m: an improved force field for folded and intrinsically disordered proteins. *Nat. Methods* **14**, 71–73 (2017).

12. Dror, R. O., Dirks, R. M., Grossman, J. P., Xu, H. & Shaw, D. E. Biomolecular Simulation: A Computational Microscope for Molecular Biology. *Annu. Rev. Biophys.* **41**, 429–452 (2012).

13. Marrink, S. J., Risselada, H. J., Yefimov, S., Tieleman, D. P. & De Vries, A. H. The MARTINI force field: coarse grained model for biomolecular simulations. *J. Phys. Chem. B* **111**, 7812–7824 (2007).

14. Monticelli, L. *et al.* The MARTINI coarse-grained force field: extension to proteins. *J. Chem. Theory Comput.* **4**, 819–834 (2008).

15. De Jong, D. H. *et al.* Improved parameters for the martini coarse-grained protein force field. *J. Chem. Theory Comput.* **9**, 687–697 (2013).

16. Yesylevskyy, S. O., Schäfer, L. V., Sengupta, D. & Marrink, S. J. Polarizable water model for the coarse-grained MARTINI force field. *PLoS Comput. Biol.* **6**, e1000810 (2010).

17. Souza, P. C. T. *et al.* Martini 3: a general purpose force field for coarse-grained molecular dynamics. *Nat. Methods* **18**, 382–388 (2021).

18. Spinti, J. K., Neiva Nunes, F. & Melo, M. N. Room for improvement in the initial martini 3 parameterization of peptide interactions. *Chem. Phys. Lett.* **819**, 140436 (2023).

19. Behler, J. Perspective: Machine learning potentials for atomistic simulations. *J. Chem. Phys.* **145**, (2016).

20. Behler, J. Four generations of high-dimensional neural network potentials. *Chem. Rev.* **121**, 10037–10072 (2021).

21. Unke, O. T. *et al.* Machine learning force fields. *Chem. Rev.* **121**, 10142–10186 (2021).

22. MacKerell, A. D. Jr. *et al.* All-Atom Empirical Potential for Molecular Modeling and Dynamics Studies of Proteins. *J. Phys. Chem. B* **102**, 3586–3616 (1998).

23. Atkins, P. W., Paula, J. D. & Keeler, J. *Atkins' Physical Chemistry*. (Oxford University Press, 2023).

24. Pauli, W. Über den Zusammenhang des Abschlusses der Elektronengruppen im Atom mit der Komplexstruktur der Spektren. *Z. Für Phys.* **31**, 765–783 (1925).

25. London, F. Zur Theorie und Systematik der Molekularkräfte. *Z. Für Phys.* **63**, 245–279 (1930).

26. Jones, J. E. & Chapman, S. On the determination of molecular fields. —II. From the equation of state of a gas. *Proc. R. Soc. Lond. Ser. Contain. Pap. Math. Phys. Character* **106**, 463–477 (1997).

27. Coulomb, C. A. (Charles A. *et al. Mémoires sur l'électricité et la magnétisme*. (Paris : Chez Bachelier, libraire ..., 1789).

28. Darden, T., York, D. & Pedersen, L. Particle mesh Ewald: An N·log(N) method for Ewald sums in large systems. *J. Chem. Phys.* **98**, 10089–10092 (1993).

29. Nyquist, H. Certain Topics in Telegraph Transmission Theory. *Trans. Am. Inst. Electr. Eng.* **47**, 617–644 (1928).

30. Shannon, C. E. Communication in the Presence of Noise. *Proc. IRE* **37**, 10–21 (1949).

31. Leach, A. R. *Molecular Modelling: Principles and Applications*. (Pearson Education, 2001).

32. Ryckaert, J.-P., Ciccotti, G. & Berendsen, H. J. C. Numerical integration of the cartesian equations of motion of a system with constraints: molecular dynamics of *n*-alkanes. *J. Comput. Phys.* **23**, 327–341 (1977).

33. Hess, B., Bekker, H., Berendsen, H. J. C. & Fraaije, J. G. E. M. LINCS: A linear constraint solver for molecular simulations. *J. Comput. Chem.* **18**, 1463–1472 (1997).

34. Berendsen, H. J. C., Postma, J. P. M., van Gunsteren, W. F., DiNola, A. & Haak, J. R. Molecular dynamics with coupling to an external bath. *J. Chem. Phys.* **81**, 3684–3690 (1984).

35. Bussi, G., Donadio, D. & Parrinello, M. Canonical sampling through velocity rescaling. *J. Chem. Phys.* **126**, 014101 (2007).

36. Parrinello, M. & Rahman, A. Polymorphic transitions in single crystals: A new molecular dynamics method. *J. Appl. Phys.* **52**, 7182–7190 (1981).

37. Van Der Spoel, D. *et al.* GROMACS: Fast, flexible, and free. *J. Comput. Chem.* **26**, 1701–1718 (2005).

38. Berman, H., Henrick, K. & Nakamura, H. Announcing the worldwide Protein Data Bank. *Nat. Struct. Mol. Biol.* **10**, 980–980 (2003).

39. Jumper, J. *et al.* Highly accurate protein structure prediction with AlphaFold. *Nature* **596**, 583–589 (2021).

40. Jo, S., Kim, T., Iyer, V. G. & Im, W. CHARMM-GUI: A web-based graphical user interface for CHARMM. *J. Comput. Chem.* **29**, 1859–1865 (2008).

41. Standards, U. S. N. B. of. *Journal of Research of the National Bureau of Standards*. (The Bureau, 1952).

42. Abraham, M. *et al.* GROMACS 2025.3 Manual. https://zenodo.org/records/16992569 (2025).

43. Kutzner, C., Grubmüller, H., de Groot, B. L. & Zachariae, U. Computational Electrophysiology: The Molecular Dynamics of Ion Channel Permeation and Selectivity in Atomistic Detail. *Biophys. J.* **101**, 809–817 (2011).

44. Kutzner, C. *et al.* Insights into the function of ion channels by computational electrophysiology simulations. *Biochim. Biophys. Acta BBA - Biomembr.* **1858**, 1741–1752 (2016).

45. Delemotte, L., Dehez, F., Treptow, W. & Tarek, M. Modeling Membranes under a Transmembrane Potential. *J. Phys. Chem. B* **112**, 5547–5550 (2008).

46. Piggot, T. J., Holdbrook, D. A. & Khalid, S. Electroporation of the E. coli and S. aureus membranes: molecular dynamics simulations of complex bacterial membranes. *J. Phys. Chem. B* **115**, 13381–13388 (2011).

47. Weerakoon, D., Marzinek, J. K., Pedebos, C., Bond, P. J. & Khalid, S. Polymyxin B1 in the *Escherichia coli* inner membrane: A complex story of protein and lipopolysaccharide-mediated insertion. *J. Biol. Chem.* **300**, 107754 (2024).

48. Van Rossum, G. & Drake, F. L. *Python 3 Reference Manual*. (CreateSpace, Scotts Valley, CA, 2009).

49. Abraham, M. J. *et al.* GROMACS: High performance molecular simulations through multi-level parallelism from laptops to supercomputers. *SoftwareX* **1–2**, 19–25 (2015).

50. Michaud-Agrawal, N., Denning, E. J., Woolf, T. B. & Beckstein, O. MDAnalysis: a toolkit for the analysis of molecular dynamics simulations. *J. Comput. Chem.* **32**, 2319–2327 (2011).

51. Gowers, R. J. *et al.* MDAnalysis: A Python Package for the Rapid Analysis of Molecular Dynamics Simulations. *Proc. 15th Python Sci. Conf.* 98–105 (2016) doi:10.25080/Majora-629e541a-00e.

52. Harris, C. R. *et al.* Array programming with NumPy. *Nature* **585**, 357–362 (2020).

53. McKinney, W. Data Structures for Statistical Computing in Python. *Proc. 9th Python Sci. Conf.* 56–61 (2010) doi:10.25080/Majora-92bf1922-00a.

54. Hunter, J. D. Matplotlib: A 2D graphics environment. *Comput. Sci. Eng.* **9**, 90–95 (2007).

55. Virtanen, P. *et al.* SciPy 1.0: fundamental algorithms for scientific computing in Python. *Nat. Methods* **17**, 261–272 (2020).

56. Hagberg, A., Swart, P. J. & Schult, D. A. Exploring network structure, dynamics, and function using NetworkX. https://www.osti.gov/biblio/960616 (2008).

57. Davidson-Pilon, C. lifelines: survival analysis in Python. *J. Open Source Softw.* **4**, 1317 (2019).

58. Vickery, O. N. & Stansfeld, P. J. CG2AT2: an Enhanced Fragment-Based Approach for Serial Multi-scale Molecular Dynamics Simulations. *J. Chem. Theory Comput.* **17**, 6472–6482 (2021).

59. Humphrey, W., Dalke, A. & Schulten, K. VMD: Visual molecular dynamics. *J. Mol. Graph.* **14**, 33–38 (1996).

60. Goddard, T. D. *et al.* UCSF ChimeraX: Meeting modern challenges in visualization and analysis. *Protein Sci. Publ. Protein Soc.* **27**, 14–25 (2018).

Chapter 3

Effects of periplasmic osmolytes on antimicrobial peptides interactions in solution

3.1 Introduction

Antimicrobial peptides (AMPs) that act on the inner membrane or intracellular targets of Gram-negative bacteria must first traverse their outer membrane and then the periplasm.[1] The periplasm is a crowded and viscous compartment between the outer and inner membranes that contains the peptidoglycan cell wall, numerous periplasmic proteins, and a complex mixture of small ions, metabolites, and osmolytes.[2–4] Experimental information on the concentrations of the latter non-protein species in *E. coli* is sparse, as such quantifications in this compartment are technically challenging, and most reported values are indirect estimates rather than direct measurements.[4,5] Following the precedent of recent computational studies, I model periplasmic crowding with literature-derived estimates, treating them as representative osmolytes rather than exact compositions and concentrations.[3,4]

Reported non-protein periplasmic species include glycerol, urea, putrescine, spermidine, trehalose, and osmoregulated periplasmic glucans (OPGs), which have different biological functions and together contribute to the crowdedness of the periplasm.[3,4] These species are all polar in nature and are represented in **Figure 3.1**.

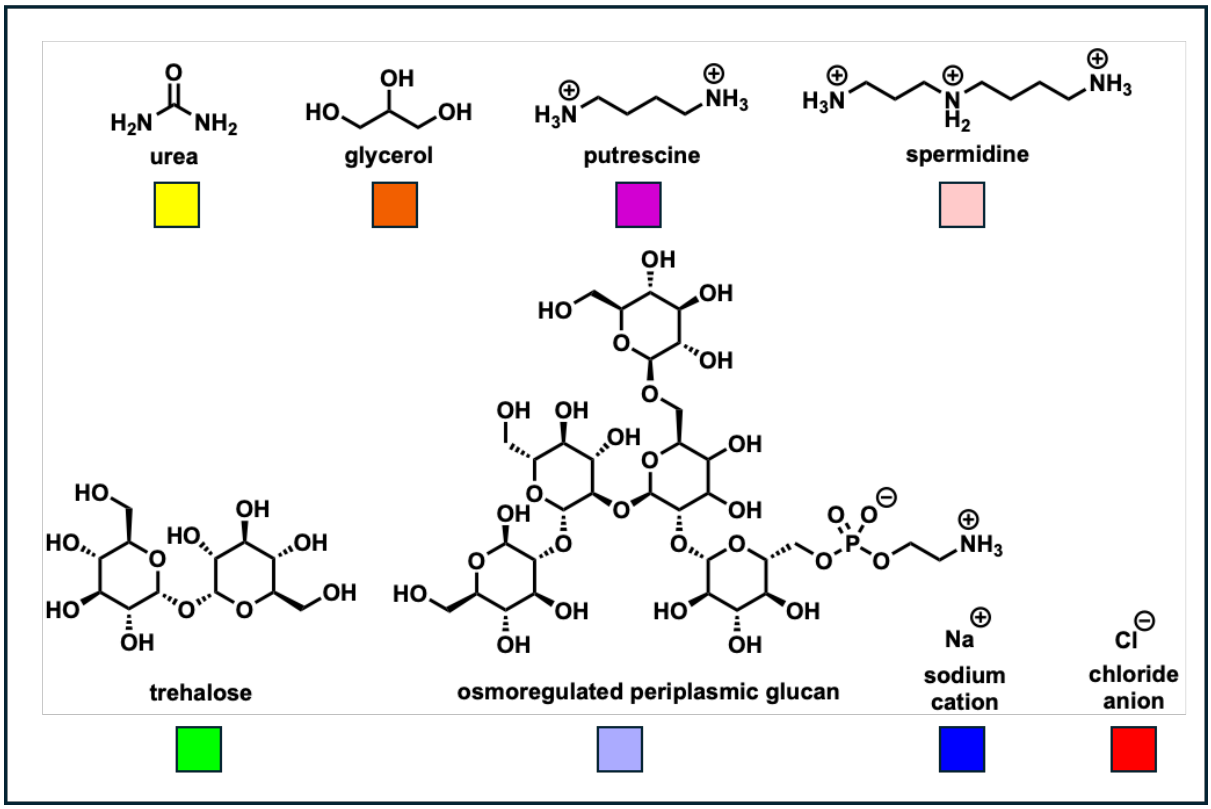

Figure 3.1. *Chemical structures of periplasmic solutes used in this chapter. The coloured squares beneath each structure indicate the colour scheme used for these species in subsequent molecular images.*

Osmoregulated periplasmic glucans (OPGs) are carbohydrate polymers produced directly in the periplasm, where they help modulate osmotic pressure and contribute to envelope mechanics.[6–8] Their concentrations have been estimated from compartmental water-volume studies under osmotic stress using radiolabelled tracers, which suggest millimolar levels in the periplasm.[5]

Trehalose is a disaccharide that accumulates under environmental stress, where it stabilises proteins against denaturation.[9,10] Its presence in the periplasm has been inferred indirectly from the induction of a periplasmic trehalase under high-osmolarity conditions, although absolute concentrations were not determined.[11]

Polyamines such as putrescine and spermidine are abundant cations that associate with anionic components of the cell envelope.[12,13] Their levels have been quantified only in whole-cell extracts, with millimolar concentrations reported for both species.[14,15]

Urea serves as a nitrogen source in urease-positive bacteria.[16–18] It is present at low millimolar concentrations, inferred from whole-cell urease activity assays in recombinant *E. coli*, though direct periplasmic measurements are currently unavailable.[19]

Glycerol functions as a carbon substrate and metabolic intermediate.[16,17] Periplasmic concentrations have been estimated indirectly from transport kinetics through aquaglyceroporins and metabolic flux analyses, yielding concentrations in the millimolar range.[20]

The crowded periplasm thus contains varied interaction partners for AMPs, which are unlikely to remain freely diffusing, as recent atomistic simulation studies showed that peptides readily engage in both transient and longer-lived contacts with solutes, proteins, and the cell wall.[3,4] Such interactions can modulate peptide activity; for example, magainin 2 and other AMPs display reduced potency under physiologically relevant salt conditions.[21] Yet most *in vitro* and *in silico* studies still consider AMPs in isolation, using simplified systems that exclude periplasmic solutes and metabolites, and thus overlook potential solution-phase effects that could shape peptide efficacy.[3,4,22,23]

To address this gap, I investigated three α-helical AMPs that display bactericidal activity against *E. coli* and differ in length, hydrophobicity, and charge density:

magainin 2, cupiennin 1a, and latarcin 1.[24–26] The structures of these AMPs are represented in **Figure 3.2**.

Magainin 2 (M2) was originally isolated from the skin of the African clawed frog (*Xenopus laevis*) and is a widely studied 23-residue peptide with a net charge of +4 *e* at physiological pH.[24,27–31] Magainin 2 is disordered in solution but adopts an amphipathic α-helical structure in membrane-mimicking environments, as shown by ^{1}H NMR spectroscopy in DPC micelles.[32] Early mechanistic models proposed a carpet mechanism, particularly at higher peptide concentrations, as well as pore-formation mechanisms.[33,34] Neutron scattering and solid-state NMR experiments support the current consensus that M2 disrupts membranes *via* a toroidal pore mechanism, in which both peptides and lipids line the channel.[35,36]

Cupiennin 1a (C1) is a 35-residue peptide isolated from the venom of the wandering spider (*Cupiennius salei*), with a high hydrophobic residue content and a net charge of +8 *e*.[25] It is unstructured in solution and adopts a helix-hinge-helix conformation in membrane-mimicking environments, as determined by CD spectroscopy and solution NMR.[25,37] C1 perturbs lipid bilayers, as shown by solid-state ^{31}P and ^{2}H NMR with multilamellar vesicles of zwitterionic DMPC and anionic DMPC/DMPG mixtures, and its helical form would be sufficient long to span lipid membranes.[38] Pore formation has thus been proposed as its mechanism of action, although alternative models, such as the carpet mechanism, cannot be excluded due to a lack of direct structural evidence.[38]

Latarcin 1 (L1) is a 26-residue peptide with a net charge of +10 *e* isolated from the venom of the ant spider *Lachesana tarabaevi*.[26] It adopts an amphipathic α-helical conformation in lipid environments, as shown by CD spectroscopy and ^{1}H NMR in SDS micelles and ^{31}P NMR on DOPE/DOPG liposomes.[39] L1 was found to induce a

voltage-dependent conductance in planar DOPE/DOPG bilayers, as measured by voltage-clamp recordings, where conductance occurred only when the applied potential mimicked the orientation of the bacterial inner-membrane potential.[39] The resulting electrical signals were characterised by noisy current fluctuations rather than the discrete traces typical of stable, well-defined pores, suggesting that L1 acts *via* transient, variable-sized membrane defects.[39] This interpretation is supported by complementary dye-leakage and ^{31}P NMR assays, which showed no wholesale bilayer disruption.[39]

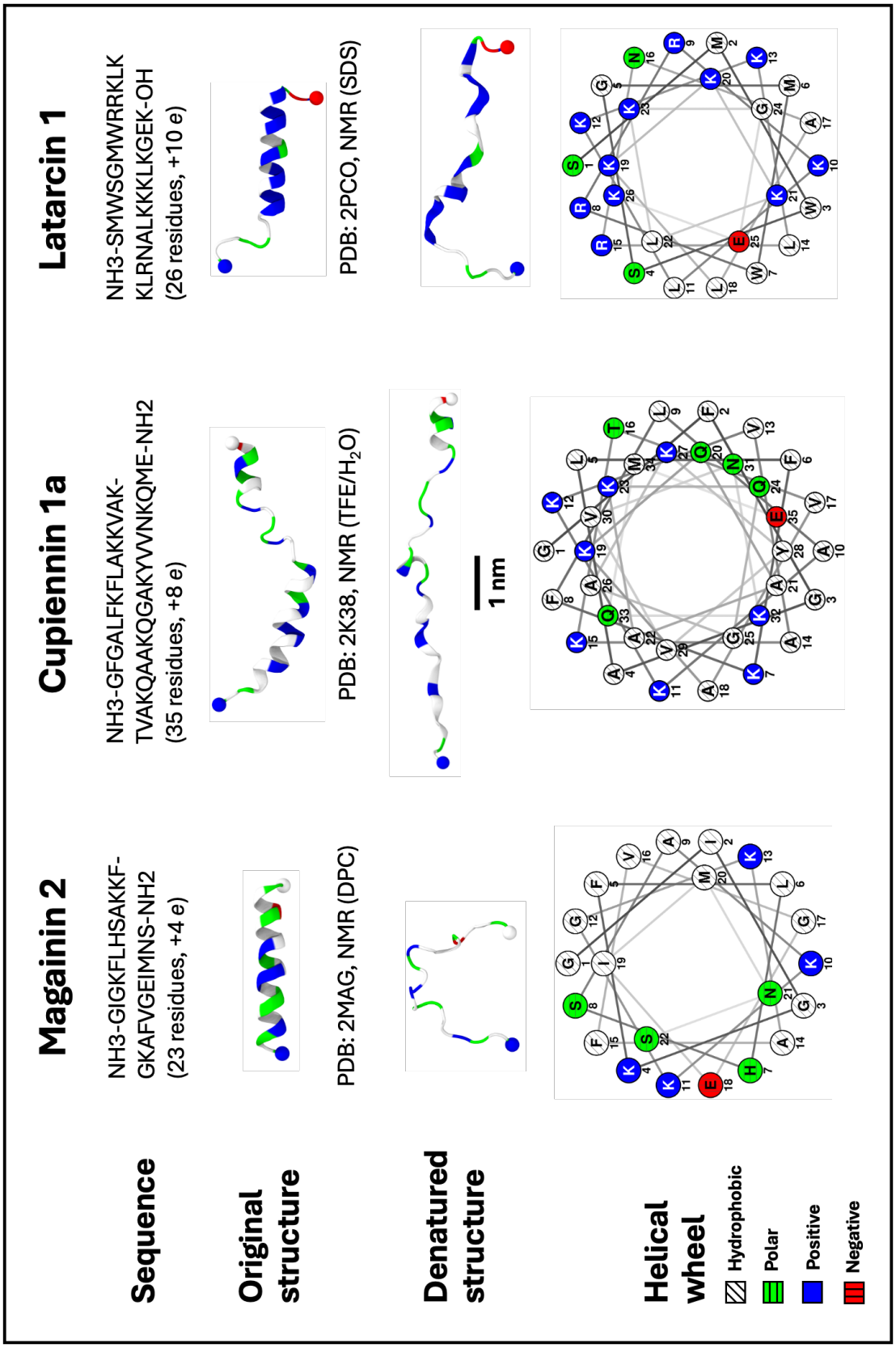

Figure 3.2. *Structural representations of the three antimicrobial peptides (magainin 2, cupiennin 1a, and latarcin 1) studied in this chapter. Original NMR structures of α-*

helical conformations in membrane-mimicking environments (top), denatured conformations (middle), and helical wheel projections (bottom).[32,38–40] *Residues are coloured by type: hydrophobic (white), polar (green), positively charged (blue), and negatively charged (red). Terminal modifications are shown as beads: blue for unmodified N-terminus, red for unmodified C-terminus, and white for amidated C-terminus.*

Since amphipathic α-helical AMPs are generally thought to undergo a coil-to-helix transition only upon membrane association, but most simulation studies begin from a helical structure, I have also modelled the AMPs in their unstructured form, since spontaneous folding events are beyond accessible timescales.[41–43]

3.2 Aims

This chapter aims to investigate whether native periplasmic osmolytes influence the solution behaviour of antimicrobial peptides, with particular attention to AMP aggregation, and whether different peptide conformations alter these interactions.

3.3 Methods

3.3.1 Molecular modelling for AA MD simulations

The initial α-helical structures of the three AMPs investigated in this study were obtained from experimental sources, as detailed in **Figure 3.2**.[32,39,44] Corresponding denatured structures were prepared through brief unrestrained high-temperature simulations (NPT, 10 ns at 403 K). The N-terminus of each peptide was left unmodified, while the C-terminus was amidated for magainin 2 and cupiennin 1a and left as a free acid for latarcin 1, in accordance with their experimentally reported modifications.[25,45,46] All protein side chains were modelled in their default protonation

states at physiological pH. Parameters for the osmolyte species were adopted from previous works.[3]

3.3.2 Simulation set-up

All molecular dynamics simulations were performed using GROMACS (version 2022.4) with the CHARMM36m all-atom force field.[47,48] The initial simulation boxes were cubic (12^3 nm³) with periodic boundary conditions applied in all directions. AMP and osmolyte concentrations were chosen to match concentrations reported in previous works.[3] The resulting molecular concentrations are summarised in **Table 3.1**.

Table 3.1. *Concentrations of AMPs and periplasmic solutes used in this chapter. By construction, molecule counts for each species are numerically equivalent to the listed millimolar values. These concentrations were derived from the solute-to-water ratios as used in previous simulation studies.[3]*

Species	**Concentration [mM]**
AMP	12
NaCl	Neutralising / 150 – system-dependent
Urea	30
Glycerol	34
Putrescine	30
Spermidine	3
Trehalose	10
OPG	20

Individual AMP molecules, and osmolytes in systems including them, were initially placed at random within the solvated water box, and sodium or chloride ions were added to neutralise the system charge, with an additional 150 mM NaCl included in selected systems, as illustrated in **Figure 3.3**. Each replicate system was independently constructed, with unique randomised initial placements of all solute species.

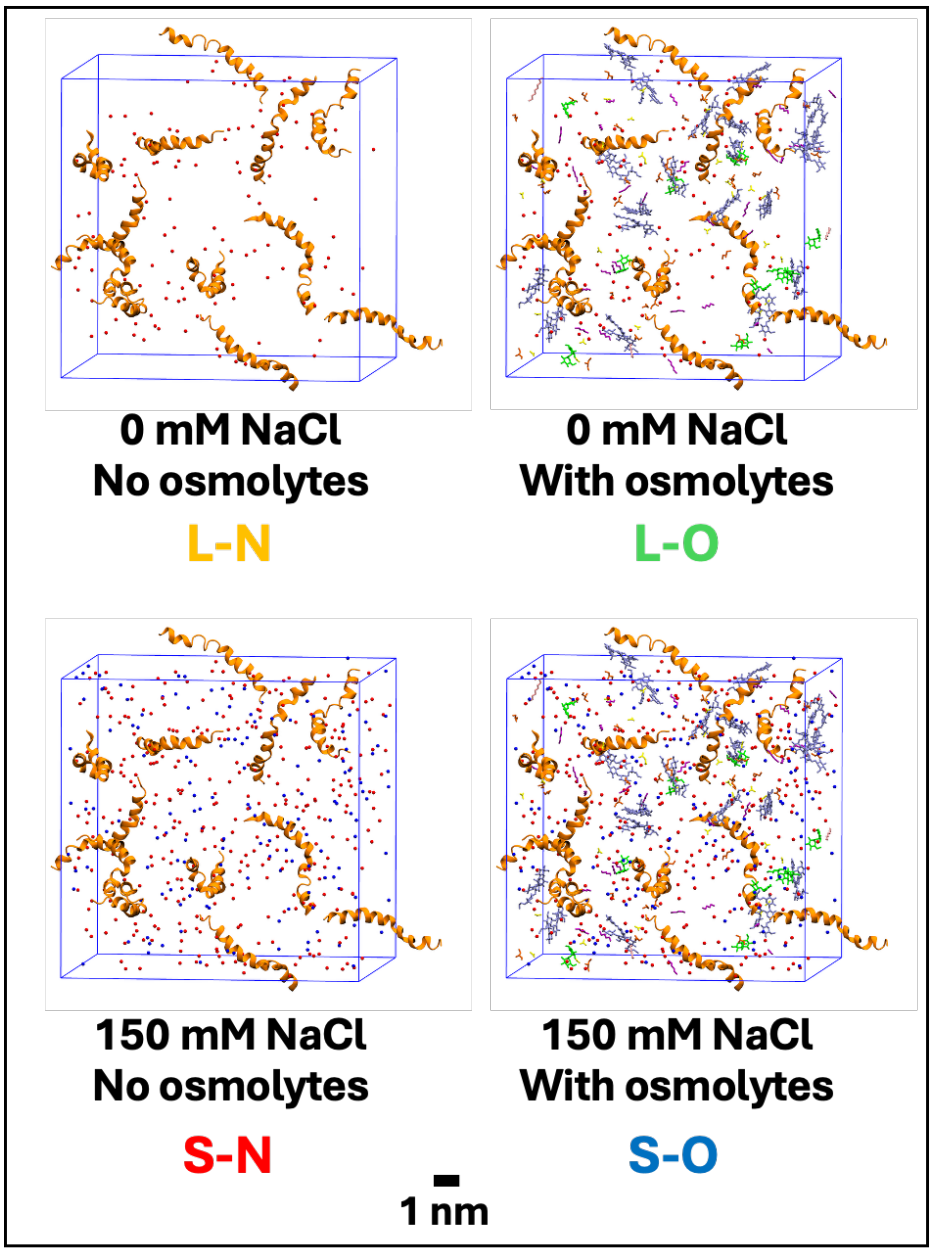

Figure 3.3. *Illustrative molecular images of the simulated system types under different salt and osmolyte conditions at the start of production runs. Systems were*

simulated under low salt (L; charge-neutralising ions only) or high salt (S; 150 mM NaCl) concentrations, and either without osmolytes (N) or with osmolytes (O). Peptides are shown as orange cartoon helices; other periplasmic solutes are shown in liquorice representations (colour scheme as in ***Figure 3.1****). Water not shown for clarity.*

The full set of performed simulations for this chapter is summarised in **Table 3.2** below.

Table 3.2. *Summary of simulation systems. Each system name is composed of its solute composition (L = low salt; S = high salt; N = no osmolytes; O = all osmolytes; OPG = only OPG) as shown in* ***Figure 3.3****, followed by an AMP identifier (M = magainin 2, C = cupiennin 1a, L = latarcin 1). The initial AMP conformation is appended as A (α-helical) or D (denatured). Replicates are then distinguished by appending an Arabic numeral (e.g. S-O-M-A-1: 150 mM NaCl, with osmolytes, magainin 2, α-helical conformation, replicate 1; each replicate represents an independently built system).*

AMP	System type	System name	Timescale
Magainin 2	L-N	L-N-M	500 ns (x3)
Magainin 2	L-O	L-O-M	500 ns (x3)
Magainin 2	S-N	S-N-M	500 ns (x3)
Magainin 2	S-O	S-O-M	500 ns (x3)
Magainin 2	L-OPG	L-OPG-M	500 ns (x3)
Magainin 2	S-OPG	S-OPG-M	500 ns (x3)
Cupiennin 1a	L-N	L-N-C	500 ns (x3)
Cupiennin 1a	L-O	L-O-C	500 ns (x3)
Cupiennin 1a	S-N	S-N-C	500 ns (x3)
Cupiennin 1a	S-O	S-O-C	500 ns (x3)
Cupiennin 1a	L-OPG	L-OPG-C	500 ns (x3)
Cupiennin 1a	S-OPG	S-OPG-C	500 ns (x3)
Latarcin 1	L-N	L-N-L	500 ns (x3)
Latarcin 1	L-O	L-O-L	500 ns (x3)
Latarcin 1	S-N	S-N-L	500 ns (x3)
Latarcin 1	S-O	S-O-L	500 ns (x3)
Latarcin 1	L-OPG	L-OPG-L	500 ns (x3)
Latarcin 1	S-OPG	S-OPG-L	500 ns (x3)

3.3.3 MD simulations

Each system was first energy minimised using the steepest descent algorithm for up to 50,000 steps (force tolerance < 1000 kJ mol^{-1} nm^{-1}). Minimisation was followed by a two-stage equilibration with position restraints on peptide heavy atoms: 1 ns in the NVT ensemble using the velocity-rescale thermostat under pressure monitoring, followed by 10 ns in the NPT ensemble using the velocity-rescale thermostat and Parrinello-Rahman barostat while monitoring system density. Systems were considered equilibrated once the monitored properties had converged with only minor fluctuations.

All equilibration and production runs employed the leap-frog integrator with a 2 fs timestep, with all bonds involving hydrogen atoms constrained using LINCS. Temperature was maintained at 310 K with the velocity-rescale thermostat (τ = 0.1 ps), using separate coupling groups for peptides and the remaining species. Pressure was controlled isotropically at 1.0 bar with the Parrinello~~Rahman~~-Raman barostat
(τ = 2.0 ps, compressibility 4.5 × 10^{-5} bar^{-1}). Electrostatics were treated with the Particle-Mesh Ewald method (cutoff 1.2 nm, dielectric constant ε_r = 2.5), and van der Waals interactions used a potential-shift Verlet scheme ~~with a~~ (1.~~1~~2 nm cutoff~~.~~ ~~Production~~). Unrestrained production simulations were run ~~without restraints~~ for 500 ns per replicate~~(~~, with three replicates per condition~~).~~.

3.4 Results and discussion

3.4.1 Solute and conformation effects on AMP aggregation

3.4.1.1 Qualitative aggregation evaluation

Visual inspection of the trajectories indicated marked variation in aggregate size and stability between peptides and across solute conditions, as summarised in **Figure 3.4**.

AMPs generally formed larger aggregates over time in systems containing 150 mM NaCl and/or osmolytes. Both transient and sporadic stable aggregation events with the periplasmic osmolytes were observed, as further characterised in subsequent subchapters.

Among the three peptides, latarcin 1 consistently formed smaller aggregates than magainin 2 or cupiennin 1a, consistent with its higher positive charge density and the resulting stronger electrostatic repulsion between individual peptides. In general, aggregate sizes were smallest for latarcin 1, followed by magainin 2, and largest for cupiennin 1a. The biggest difference in aggregate size was observed between latarcin 1 and magainin 2, while the increase from magainin 2 to cupiennin 1a was comparatively smaller.

For magainin 2 and cupiennin 1a, α-helical starting conformations generally produced larger aggregates than denatured states, while the opposite trend was observed for latarcin 1, as further discussed in subsequent subchapters.

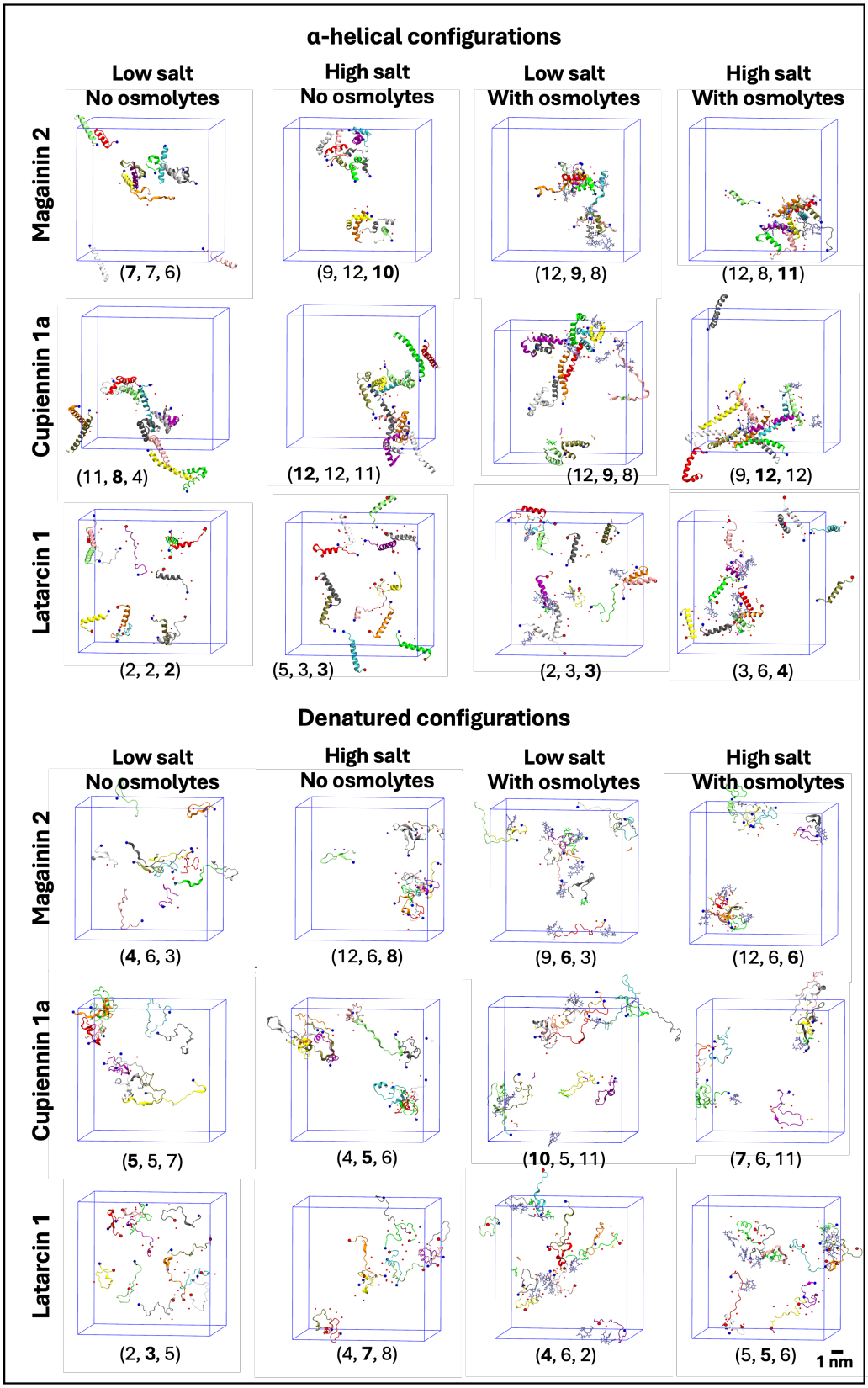

Figure 3.4. *Representative simulation snapshots taken at the end of a 500 ns production simulation for systems starting from α-helical AMP (top) and denatured*

(bottom) conformations. AMPs are shown in cartoon representation and coloured by chain. Solutes located within 4.5 Å of AMPs are shown using the same colour scheme as in ***Figure 3.1****. The numbers below each image indicate the size of the largest AMP aggregate observed at the end of the simulations (500 ns) for each replicate; the bolded value corresponds to the replicate number from which the snapshot was taken.*

As these qualitative observations suggested solute phase and AMP-conformation dependent effects, I next performed quantitative aggregation analyses to follow the time evolution of aggregation and enable systematic comparisons between conditions.

3.4.1.2 Quantitative aggregation evaluation

To quantitatively evaluate peptide aggregation as a function of time, aggregates were defined using a network-based approach. For each simulation frame, a graph was constructed in which every individual molecule (AMPs, solutes) constituted a node. An edge was formed between two molecule nodes if a contact between any of their atoms was detected (4.5 Å cutoff). An aggregate was then defined as a connected component within this network. I considered two definitions: aggregates formed solely through direct peptide-peptide contacts and those including indirect, solute-bridged interactions, as schematically illustrated in **Figure 3.5**. As the two approaches produced only minor differences, I present results using the latter, more inclusive definition to capture the full complexity of the system and avoid missing relevant interactions.

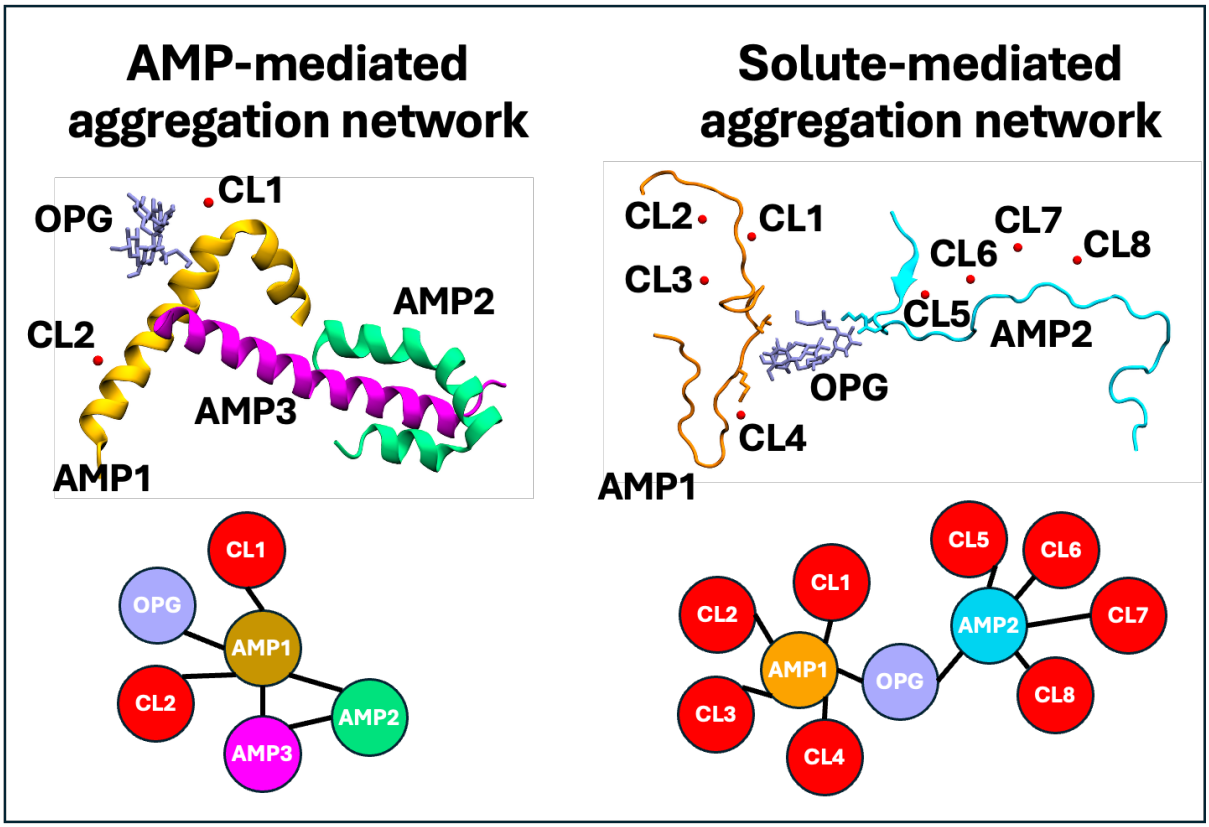

Figure 3.5. *Illustration of the interaction networks used to characterise AMP-solute aggregates. Each molecule (AMPs shown as helices and coloured by chain, with sidechains in contact with solutes shown as liquorice; OPG shown in purple liquorice representation; chloride ions shown as red beads) is represented as a node, with edges drawn when a contact (4.5 Å cutoff) is detected between any pair of atoms of two different molecules. Example molecular configurations (top) and their corresponding networks (bottom) are shown for a non-solute-mediated aggregate (left) and a solute-mediated aggregate (right).*

To summarise the AMP aggregation state of each frame into a single value, I used the weighted-average AMP aggregate size W_f:

$$W_f = \frac{\sum_i^j n_i^2}{\sum_i^j n_i} \tag{3.1}$$

where n_i is the number of AMPs in aggregate i, summed over all aggregates j observed at frame f. This metric is more sensitive to the formation of larger clusters than simpler metrics such as the median AMP count per aggregate, and describes the entire aggregate size distribution more comprehensively than focusing solely on the single largest aggregate.

To account for temporal correlation in my simulation data, I block-averaged the trajectories, where the final 100 ns of each simulation were split into 5 ns segments and used for all subsequent statistical analyses if not indicated otherwise. W_f values were then averaged within each block, giving a set of semi-independent aggregate distribution measurements per trajectory, as illustrated in **Figure 3.6**.

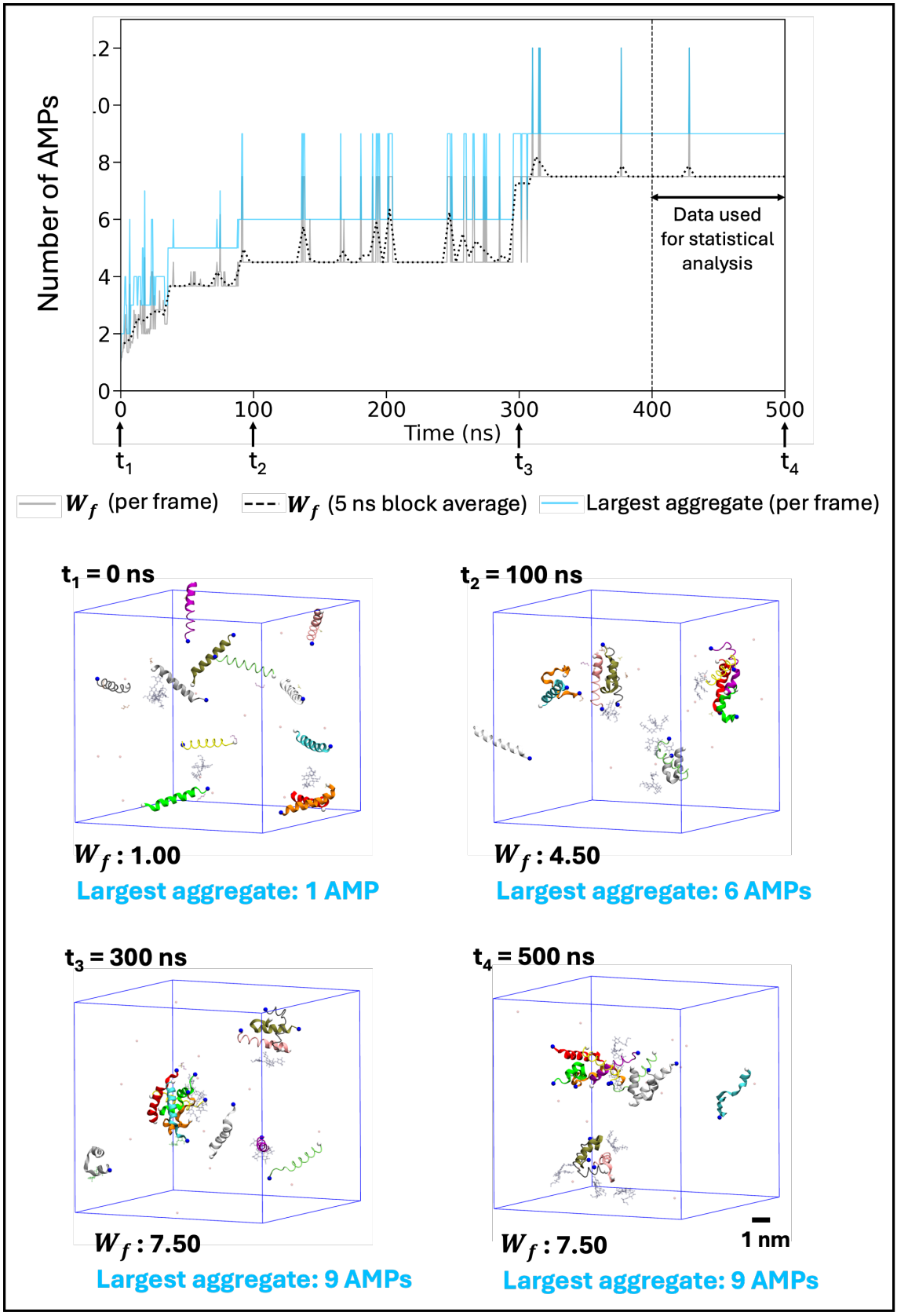

Figure 3.6. *Quantitative analysis of AMP aggregation over time for a representative simulation trajectory (system L-O-M-A-2). (Top) Time evolution of the weighted-*

average AMP aggregate size W_f, together with the number of AMPs in the largest aggregate. Data from the final 100 ns of the simulation were used for the statistical analysis presented in subsequent figures. (Bottom) Corresponding simulation snapshots, where AMPs are shown as cartoon helices coloured by chain, and osmolytes and salt ions are rendered in a transparent liquorice representation according to the colour scheme in ***Figure 3.1****. Water omitted for clarity.*

To statistically compare AMP aggregation across solute conditions, I performed a Kruskal-Wallis test on the block-averaged W_f values. This test is a non-parametric analogue of ANOVA, which checks whether the distribution of at least one group statistically differs from the others. The W_f distributions are shown in **Figure 3.7**. Where differences were found, I applied Dunn's post-hoc test in combination with the Holm-Bonferroni correction. This test identifies which specific pairs of conditions differ, and the correction adjusts significance thresholds to reduce false positives when multiple pairwise comparisons are made.

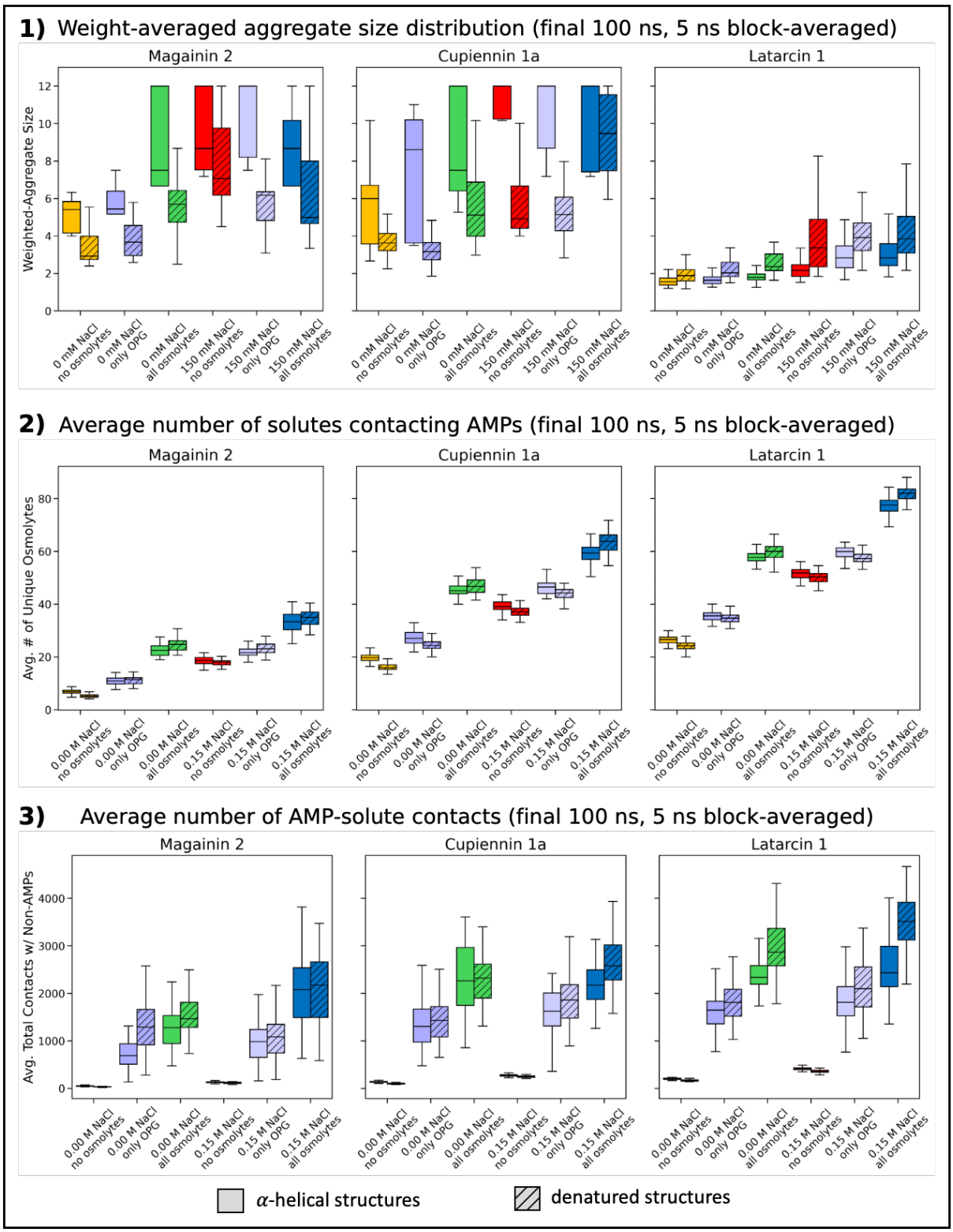

Figure 3.7. *Box plots showing the weighted-average AMP aggregate sizes* W_f *(1), the average number of unique solute molecules interacting with AMPs (2), and the average total number of AMP-solute contacts (3) across simulation conditions.*

Block-averaged values were computed for 5 ns blocks over the final 100 ns of each replicate and pooled per condition.

More complex solute environments correlated with increased AMP-osmolyte interactions and larger aggregate sizes, as shown in **Figure 3.7**. For all three peptides, Kruskal-Wallis tests on the W_f distributions yielded highly significant overall differences between conditions ($p \ll 0.001$), with post-hoc comparisons showing that both the addition of 150 mM NaCl and the inclusion of osmolytes promoted aggregation compared to low-salt conditions. The magnitude of this increase, however, varied across peptides.

For both magainin 2 and cupiennin 1a, salt and osmolytes each acted as significant and independent aggregation promoters. While their effects were of a comparable magnitude for magainin 2, salt was a significantly stronger aggregation enhancer trigger for cupiennin 1a. This observation could be rationalised by its higher net charge, where the resulting increase in inter-peptide repulsion would be more susceptible to salt-induced charge-screening effects.

In contrast, an additive response to the combined presence of salt and osmolytes was observed for latarcin 1a, suggesting that its high charge density necessitated both solute-mediated charge screening and macromolecular crowding to overcome the resulting electrostatic repulsion.

Across all conditions, latarcin 1 formed the smallest aggregates, followed by magainin 2, and cupiennin 1a forming the largest. This hierarchy was interpreted as reflecting differences in peptide charge density and total hydrophobic content: latarcin 1, carrying the highest net positive charge, experienced the strongest inter-

peptide electrostatic repulsion, while cupiennin 1a, the longest peptide with the largest number of hydrophobic residues, exhibited enhanced self-association driven by its comparatively larger hydrophobic surface.

Finally, Mann-Whitney tests confirmed that peptides starting in a denatured state aggregated significantly less than their α-helical counterparts across all conditions for magainin 2 and cupiennin 1a ($p \ll 0.001$), establishing initial structure as a significant and AMP-dependent factor in aggregation propensity.

Overall, these quantitative results corroborated my previous qualitative observations, with both solute phase and AMP-conformation influencing AMP aggregation behaviour.

3.4.2.1 AMP aggregation and solute-mediated stabilising effects

Across all conditions, AMP aggregation involved the formation of a hydrophobic core, with the hydrophobic faces of the peptides packed together and polar and charged residues oriented toward the solvent. This micelle-like organisation was a consistent structural feature and formed the basis of peptide association.

In addition to hydrophobic packing, aggregates were stabilised by solute-mediated linking interactions at their periphery, which reduced electrostatic repulsion and increased local crowding. These interactions ranged from specific shielding of cationic residues to less specific multivalent associations within or between peptides, as illustrated in **Figure 3.8**. Rather than representing separate processes, these interaction modes collectively stabilised the aggregates, as further characterised below.

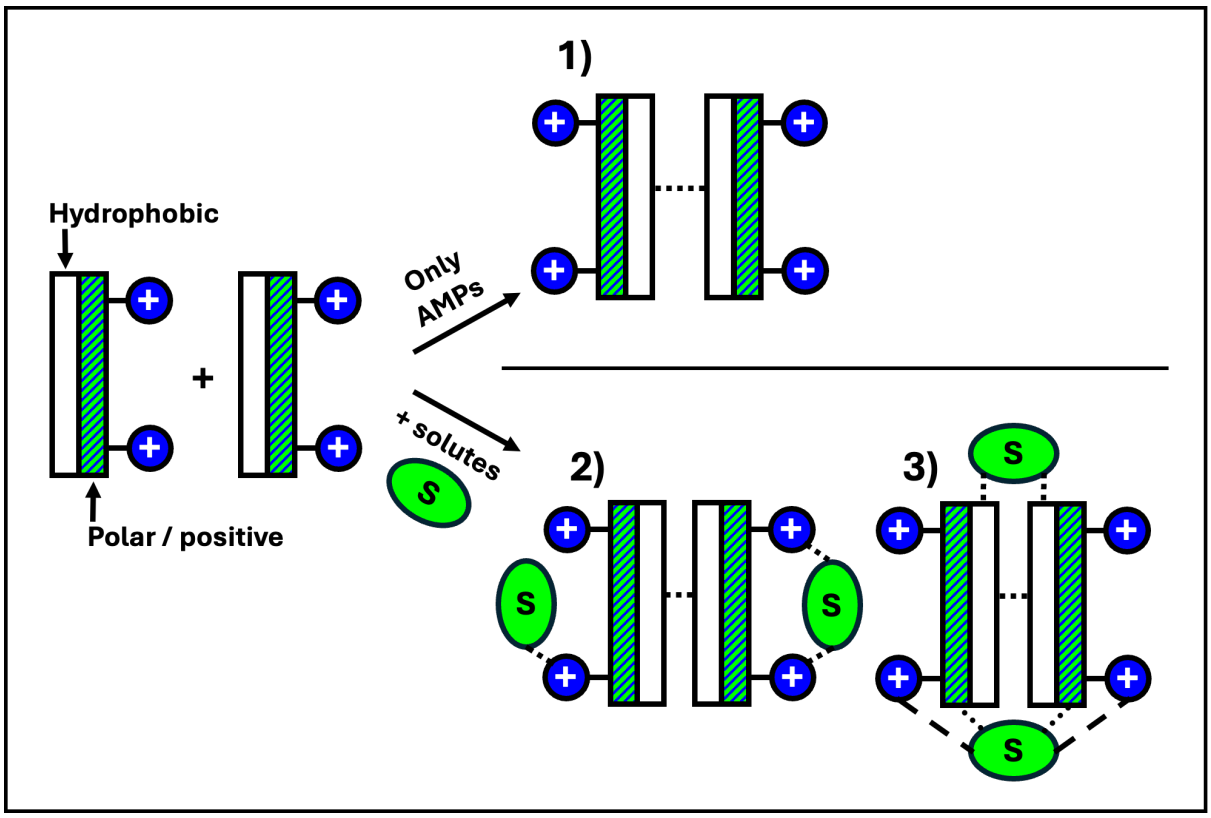

Figure 3.8. *Schematic representation of interaction modes between two amphipathic cationic AMPs (white: hydrophobic face, green/blue hatched: polar/positive face) in the absence (top) or presence (bottom) of polar (and potentially charged) solutes (S, green). Shown are 1) direct hydrophobic AMP-AMP association without additional stabilising effects; 2) single-AMP solute interactions, where one solute engages one or more residues on a single peptide; 3) inter-AMP bridging, where one solute simultaneously contacts residues on two peptides.*

In the following sections, I first examine hydrophobic packing itself, before turning to the contributions of the solute-mediated aggregate-stabilising effects.

3.4.2.1.1 Hydrophobic AMP-AMP association

As outlined above, hydrophobic packing formed the structural core of AMP aggregates across all systems. In this micelle-like organisation, hydrophobic residues clustered in the interior and polar and charged residues oriented toward the surrounding solvent, as shown in **Figure 3.9**.

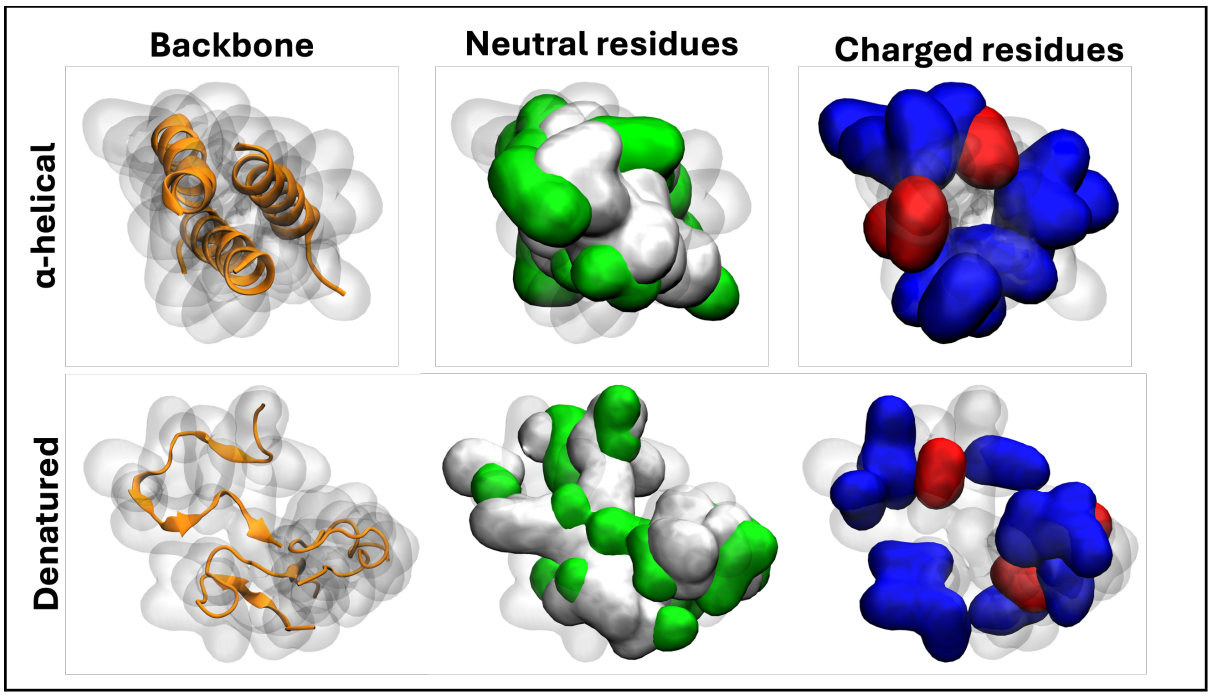

Figure 3.9. *Surface representations of representative AMP aggregates (M2 trimer) illustrating the hydrophobic core of AMP aggregates. Backbones (orange) are shown within the overall molecular surface in the left column, with surface representations highlighting charge-neutral residues (hydrophobic in white, polar uncharged in green), or charged residues (positive in blue, negative in red) in the middle and right columns.*

Across all peptides and solution conditions, most inter-peptide contacts consistently involved at least one hydrophobic residue, as shown in **Figure 3.10**. This suggested that hydrophobic interactions were important drivers for AMP-AMP aggregation.

For peptides starting from an α-helical conformation, the amphipathic organisation

facilitated packing of hydrophobic faces, leading to more ordered aggregates. The same aggregation mode was observed in simulations starting from denatured conformations.

For denatured magainin 2 and cupiennin 1, aggregates were smaller and less regular than their α-helical counterparts, as suggested in **Figure 3.4** and **Figure 3.9**. I rationalised this with their increased conformational flexibility, impeding the packing of hydrophobic residues and their now less efficiently segregated positive residues. This was confirmed by Mann-Whitney tests, which revealed a highly significant reduction in hydrophobic-hydrophobic contacts and a significant increase in positive-positive contacts, corroborating the diminished hydrophobic packing and greater electrostatic frustration ($p \ll 0.001$), as reflected in the relative proportions of contact types shown in **Figure 3.10**.

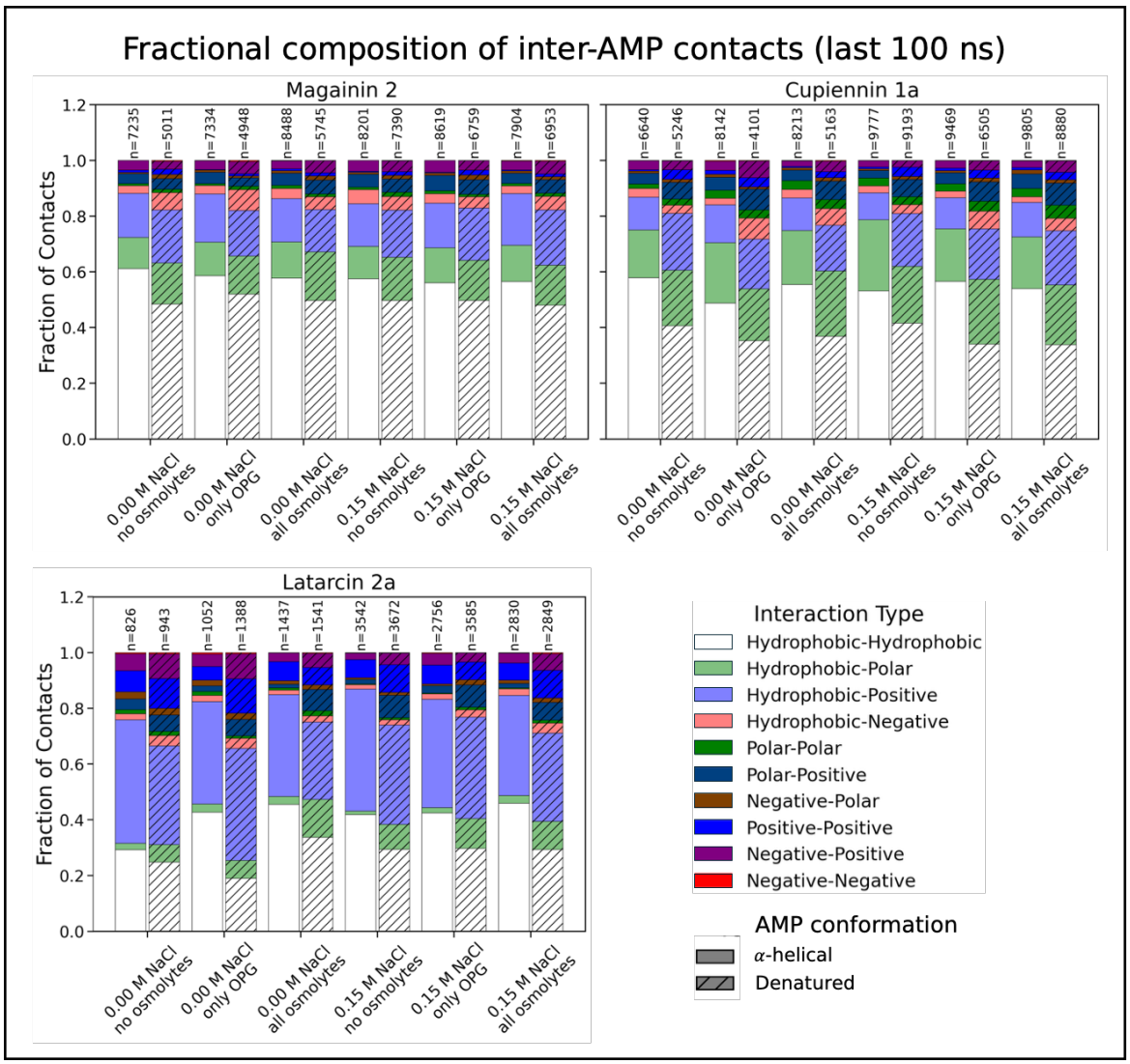

Figure 3.10. *Fractional composition of inter-peptide contacts from the last 100 ns of simulations. Data is averaged over three replicates and grouped by experimental condition. Within each group, α-helical AMP conformations are shown as solid bars and denatured AMP conformations as hatched bars. The pooled total number of contacts (n) is annotated above each bar.*

In contrast to magainin 2 and cupiennin 1a, the denatured form of latarcin 1 aggregated more readily than its α-helical form, accompanied by a significant increase in positive-negative residue contacts (Mann-Whitney test, $p \ll 0.001$). I hypothesised that the increased conformational flexibility of the denatured state enabled structural rearrangements that alleviated electrostatic repulsion between

cationic side chains and allowed the few anionic residues to form stabilising intra- and inter-peptide salt bridges, with the latter illustrated in **Figure 3.11**. While direct experimental quantification of AMP aggregate size distributions in periplasmic-mimetic environments currently remains absent from the literature, these findings could be experimentally tested using circular dichroism (CD) to correlate secondary structure transitions with changes in aggregate size, as measured by dynamic light scattering (DLS) or small-angle X-ray scattering (SAXS).

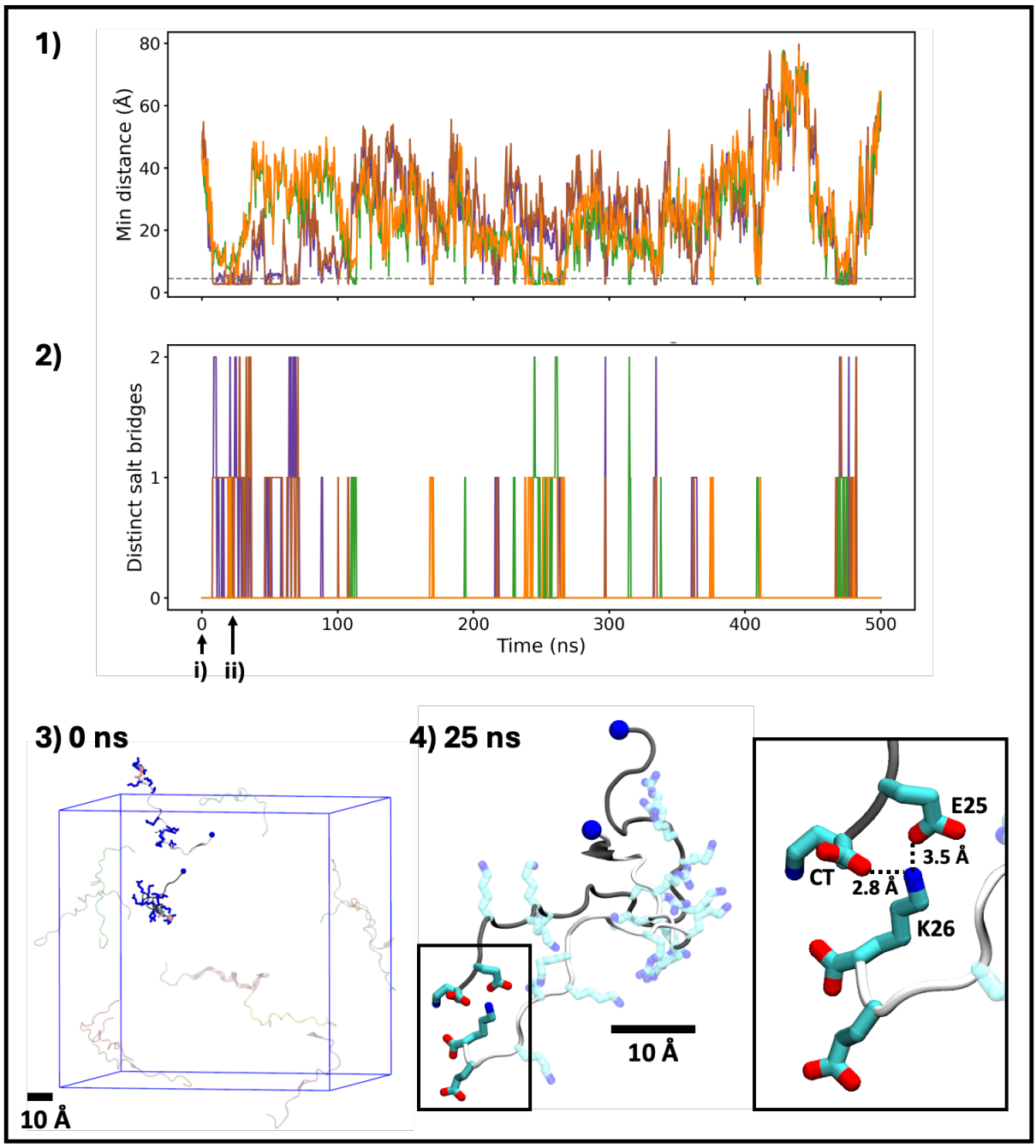

Figure 3.11. *Example time evolution and visualisation of inter-chain salt bridges in denatured latarcin 1 dimers. 1)-2) Time series of minimum distance (top) and number of distinct inter-chain salt bridges (bottom) between negative sites and positive residues on the opposite chain for two denatured latarcin 1. Purple and brown lines correspond to E25 and the C-terminus of chain A (grey) interacting with chain B (white); green and orange lines correspond to E25 and the C-terminus for the reversed interactions. The dashed line marks the 4.5 Å contact cutoff.*

3)-4) Chain positions at (i) 0 ns and (ii) 25 ns, AMPs coloured by chain, with charged residues represented as liquorice and coloured by element (carbon: cyan, nitrogen: red, oxygen: blue) and N-termini shown as blue beads on chains A and B. Hydrogens omitted for clarity, and residues not involved in the plots above are shown in transparent. C-terminal salt bridges between the two peptides are highlighted (right).

3.4.2.2 Osmolyte-mediated intra-AMP and inter-AMP shielding

3.4.2.2.1 Peripheral localisation of osmolyte-peptide interactions

Osmolyte-peptide interactions were predominantly observed at the aggregate periphery, where polar and charged residues were exposed to the solvent, as shown in **Figure 3.12**. This peripheral localisation was consistent across peptides, solutes, and conditions.

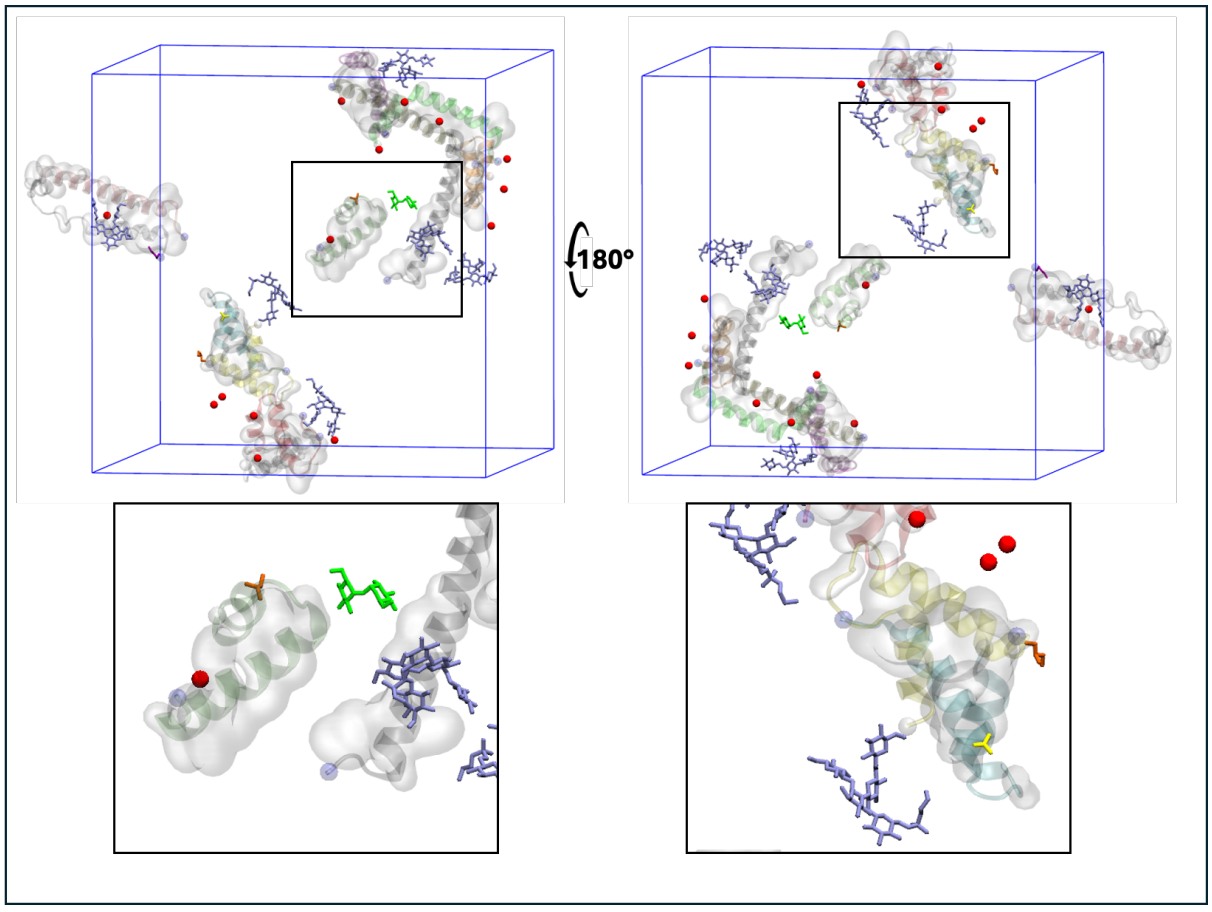

***Figure 3.12**. Representative molecular image illustrating osmolyte localisation at the aggregate-solvent interface. AMPs are shown as transparent surfaces and coloured by chain, with hydrophobic residues displayed in transparent surface representation. Osmolytes and salts within 4.5 Å of any AMP atom are shown in liquorice representation, respectively as beads, and coloured by species as in **Figure 3.1**.*

3.4.2.2.2 Interaction geometries

Interaction network analyses showed that the majority of solute interactions involved a single peptide, with fewer events bridging two peptides, as summarised in **Figure 3.13**.

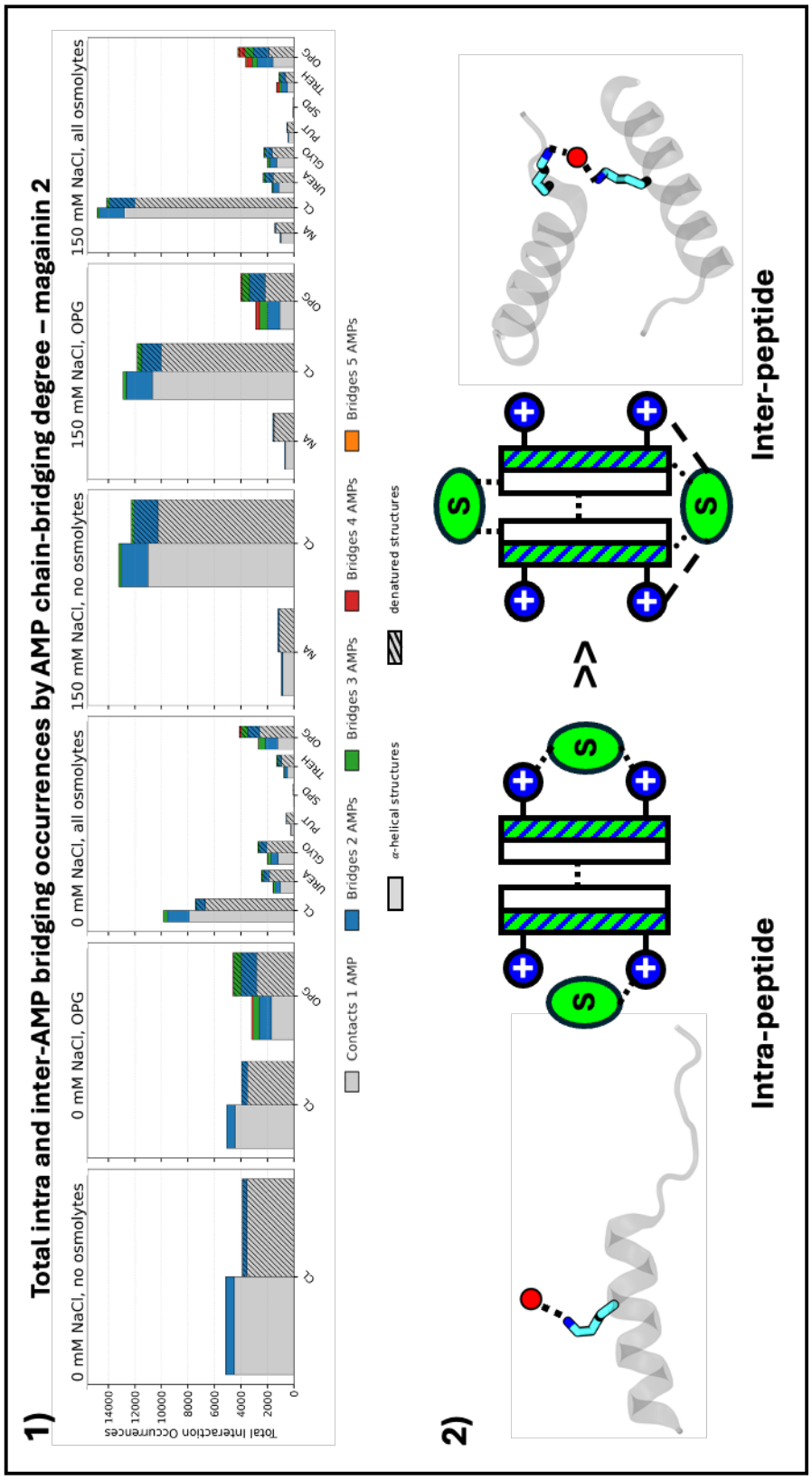

***Figure 3.13**. Comparison of single-AMP versus inter-AMP solute interactions.*

1) Classification of AMP-solute interactions by the number of peptide chains involved

(data aggregated over final 100 ns of condition replicates). Bars show total interaction occurrences for single-AMP interactions (solutes contacting residues on a single peptide) and inter-AMP interactions (solutes simultaneously contacting two peptides). 2) Graphical summary representing the numerical superiority of intra-AMP solute interactions over inter-AMP solute interactions, with corresponding molecular images (AMP backbone as cartoon helices, LYS: liquorice coloured by element: cyan: carbon, blue: nitrogen; Cl^- as red bead).

Furthermore, most of these single-peptide interactions involved only one or two AMP residues, as summarised in **Figure 3.14**.

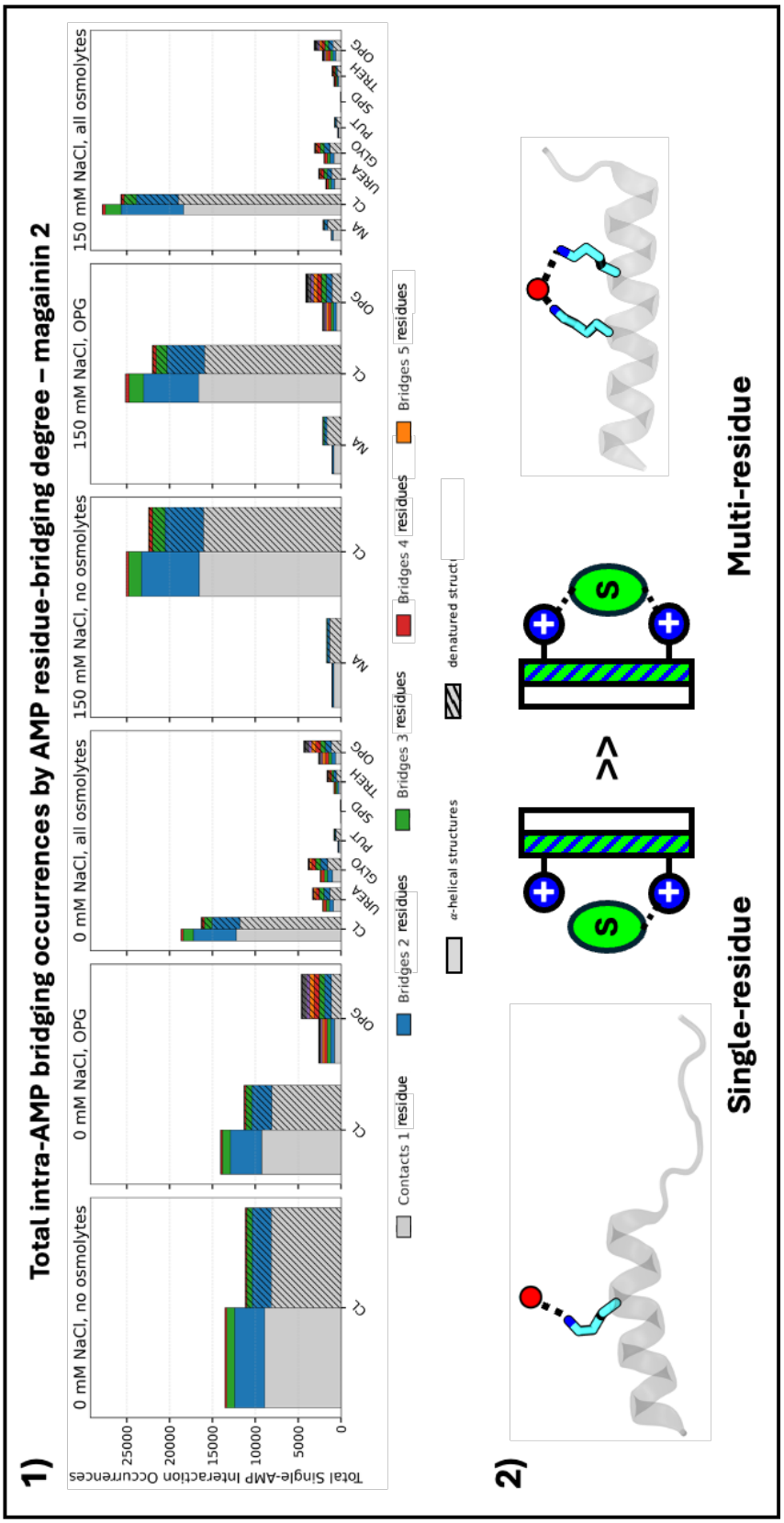

Figure 3.14. *Comparison of single-residue versus multi-residue solute interactions on individual AMPs. 1) Classification of single AMP-solute interactions by the*

number of residues involved (data aggregated over the final 100 ns of condition replicates). Bars show total occurrences of contacts involving one or more AMP residues on a single AMP simultaneously. 2) Graphical summary representing the numerical superiority of solute-single residue interactions over solute-multiple residue interactions, with corresponding molecular images (AMP backbone as cartoon helices, LYS: liquorice coloured by element: cyan: carbon; blue: nitrogen; Cl^- as red bead).

3.4.2.2.3 Interaction lifetimes

To assess the stability of these interactions, I compared the lifetimes of solute contacts involving one or two AMP residues on a single AMP chain with those involving residues on two peptides. All interaction classes showed similarly short lifetimes, with most survival curves decaying on the $O(10^0\text{-}10^1)$ nanosecond timescale, as summarised in **Figure 3.15**. This indicated that interactions between AMPs and solutes were generally transient, with some longer-lived interactions observed with OPG and trehalose.

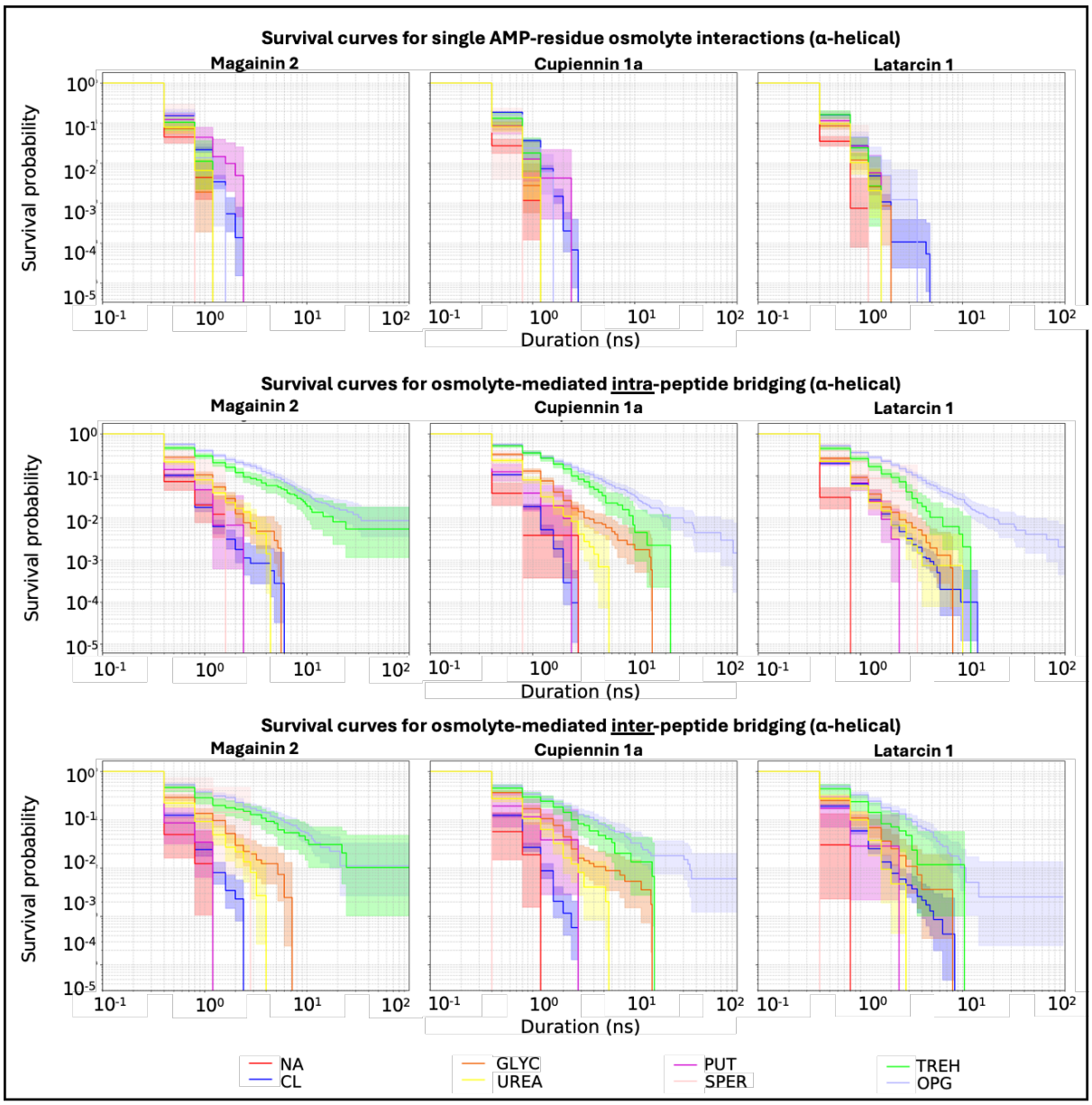

Figure 3.15. *Log-log Kaplan-Meier survival curves showing the stability of solute-AMP interactions in S-O-A systems (data pooled over the last 100 ns of the 3 replicates). The plots show the probability that a solute AMP-interaction will persist for at least a given duration, with solutes coloured individually and 95% confidence intervals shown as shaded regions. (Top) single peptide-single solute interaction, (middle) intra-peptide bridges (solutes connect residues on the same peptide), (bottom) inter-peptide bridges (solutes connect at least two different peptides).*

3.4.2.2.4 Chemical preferences

Most AMP-solute contacts were formed with OPG and Cl^-, followed by trehalose, glycerol, and urea, with the fewest contacts involving Na^+, putrescine, and spermidine, as shown in **Figure 3.13**, **Figure 3.14**, and **Figure 3.16**.

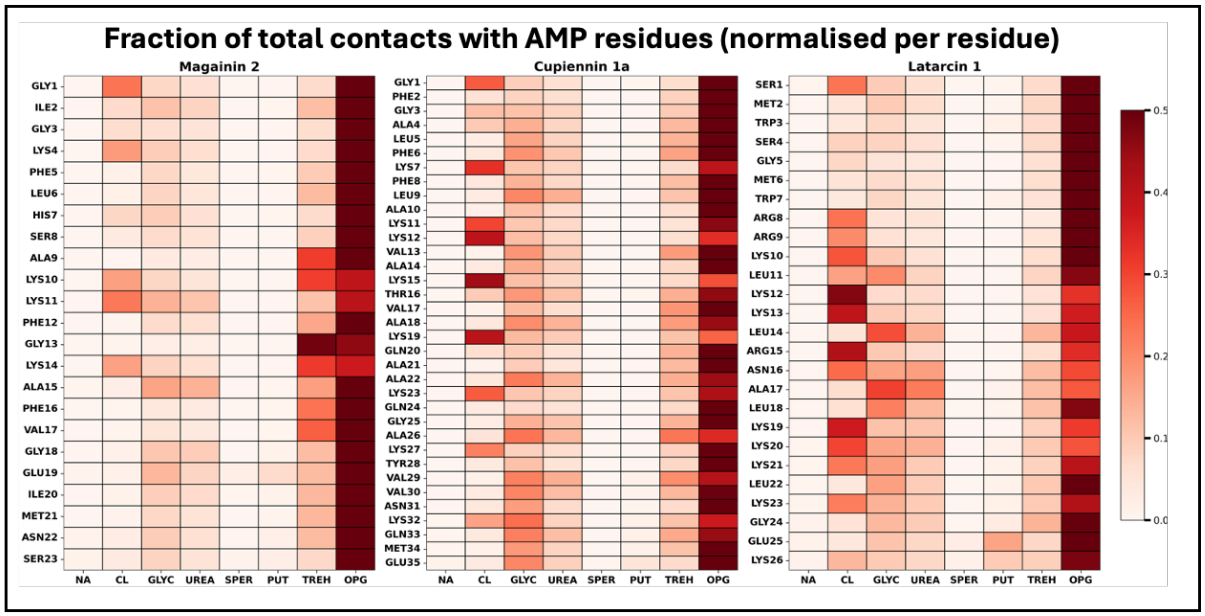

Figure 3.16. *Per-residue contact fraction, showing the distribution of total contacts for each AMP residue across all solute species (data aggregated over the last 100 ns of S-O-A system replicates), representing the contact preference of each residue.*

Charged solutes showed clear residue-specific preferences, interacting preferentially with oppositely charged AMP residues, as shown in **Figure 3.17**.

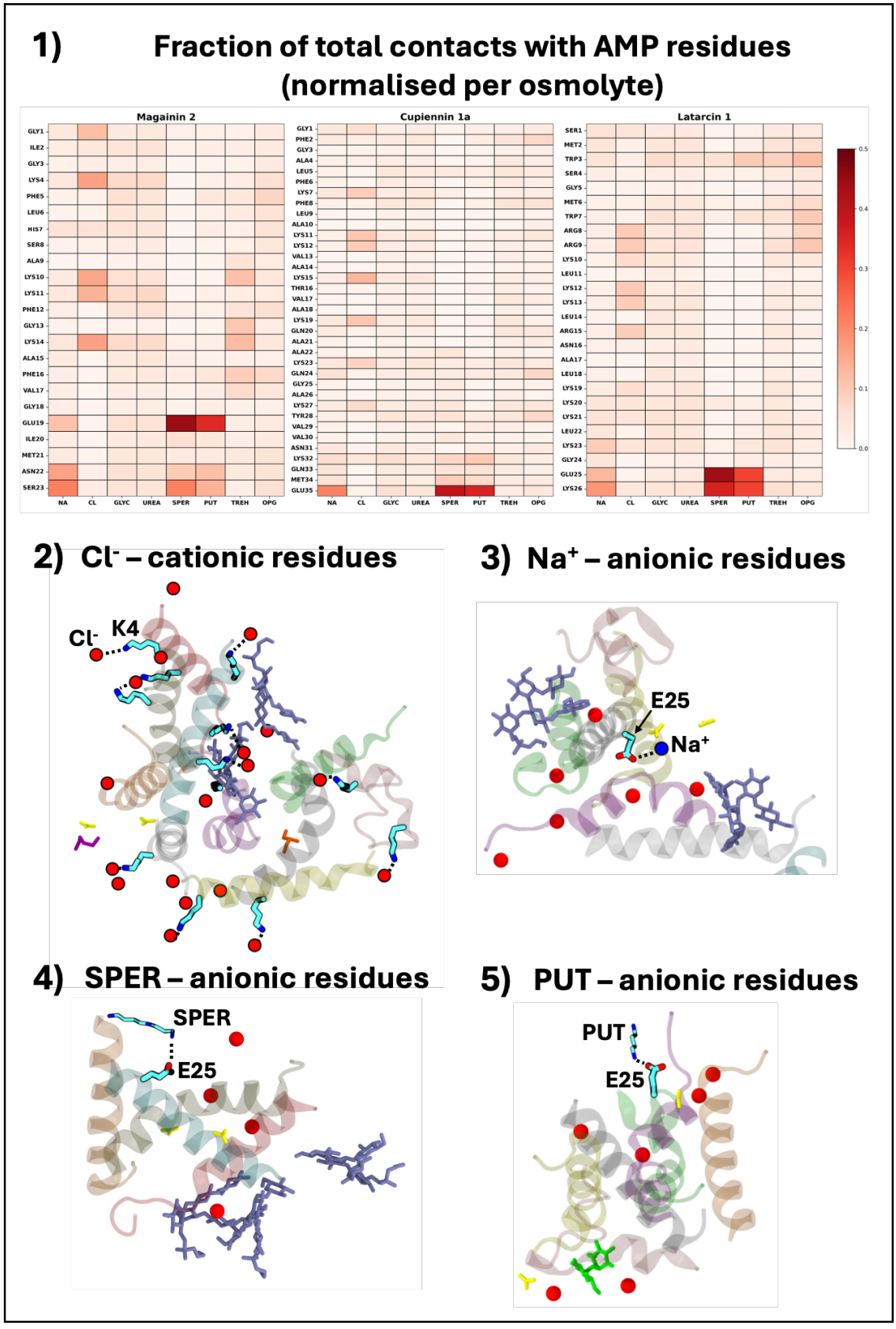

Figure 3.17. *Solute contact preferences and representative AMP-solute interactions.*

1) Per-solute contact fraction, showing the distribution of total contacts for each

*solute species across all AMP residues (same data analysed as in **Figure 3.16**), representing the contact preference of each solute. 2)-5) Representative molecular images (system S-O-M-A-3) highlighting interactions between charged solutes and AMP residues. AMP backbone as cartoon helices, charged residues and osmolytes shown as liquorice and coloured by element: cyan: carbon, blue: nitrogen, red: oxygen. Cl^- as red beads, Na^+ as blue beads. Neutral osmolytes are shown as liquorice and coloured according to the scheme in **Figure 3.1**. Only solutes within 4.5 Å of AMPs are shown.*

AMP interactions with neutral osmolytes were generally more promiscuous, as shown in **Figure 3.17.1** and **Figure 3.18**.

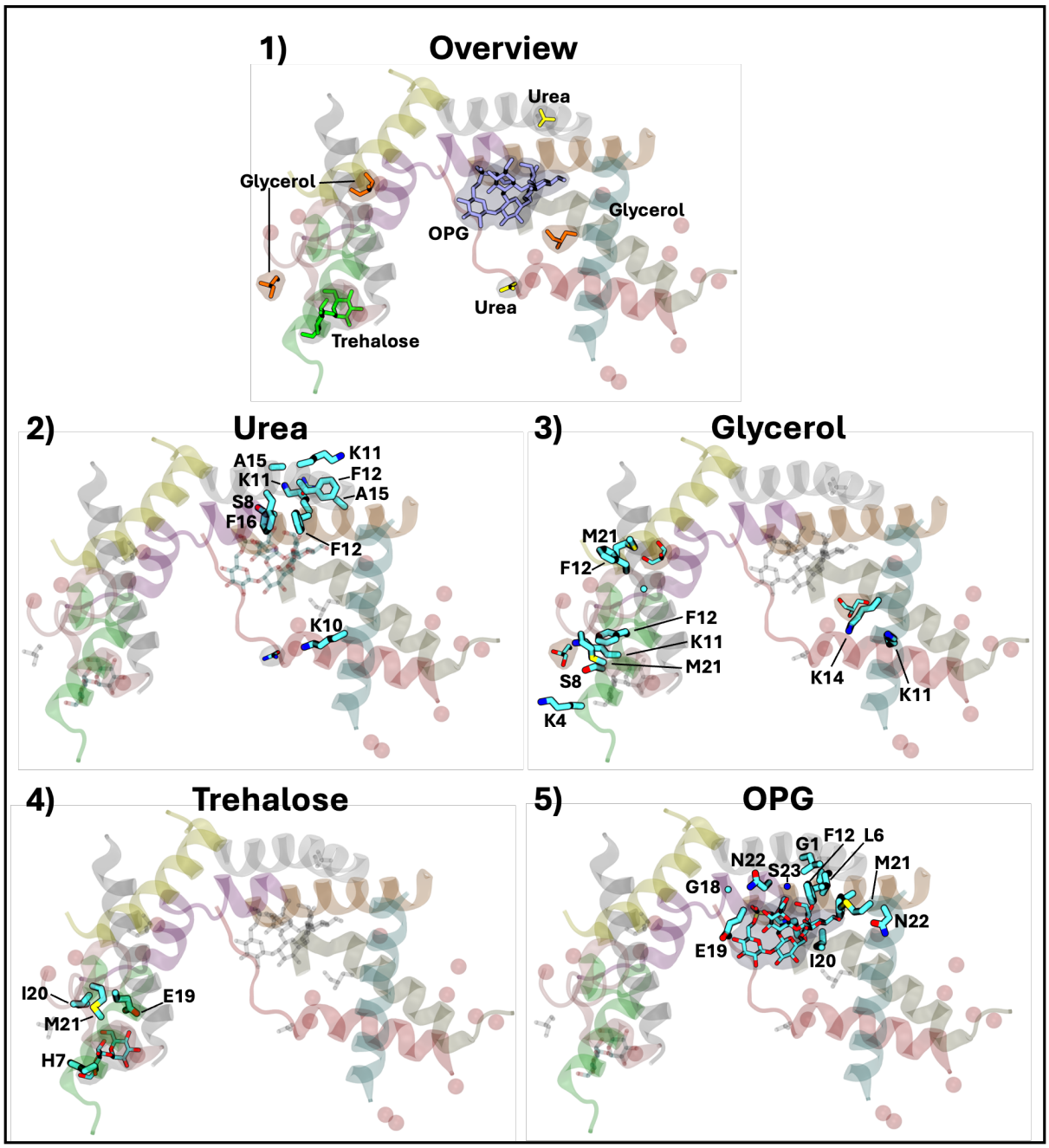

Figure 3.18. *Representative molecular images (system S-O-M-A-3) illustrating interactions between neutral solutes and AMP residues. AMP backbones as cartoon helices, residues and osmolytes shown as liquorice and coloured by element: cyan: carbon, blue: nitrogen, red: oxygen, yellow: sulphur, brown: phosphorus. Cl^- as red beads, Na^+ as blue beads. Osmolytes are shown as liquorice with a transparent*

*surface representation overlaid (coloured according to the scheme in **Figure 3.1**). Only solutes within 4.5 Å of AMPs are shown.*

To quantify the relative preference for interactions between specific AMP residues and functional groups on charge-neutral, promiscuously interacting osmolytes, I computed residue-osmolyte contact enrichment values $E_{s,r}$.[49] This quantity expresses how much more or less frequently a given residue interacts with a specific osmolyte functional group than would be expected if contacts were randomly distributed.

For each osmolyte group g and AMP residue r connected by $n_{g,r}$ contacts for a given frame, the observed and expected contact frequencies $f_{g,r}^{\mathrm{obs}}$ and f_r^{exp} were defined as

$$f_{g,r}^{\mathrm{obs}} = \frac{n_{g,r}}{\sum_{r'} n_{g,r'}} \tag{3.2}$$

and

$$f_r^{\mathrm{exp}} = \frac{\sum_{s'} n_{s',r}}{\sum_{s',r'} n_{s',r'}} \tag{3.3}$$

The corresponding contact propensity factor $E_{s,r}$ was then calculated as

$$E_{s,r} = log_2\left(\frac{f_{g,r}^{obs}}{f_r^{exp}}\right) \tag{3.4}$$

with positive values indicating residues that form contacts more frequently than expected by random, and negative values indicating avoidance.

Among the neutral osmolytes, OPG contacts were numerically dominated by unspecific interactions *via* their polar sugar rings, as shown in **Figure 3.19.1**. Specific interactions were observed between its phosphate groups and cationic AMP residues, as well as 2.8-fold enriched contacts between its amine groups and acidic residues, as shown in **Figure 3.19.2**. In contrast, $\mathrm{Enr}_{s,r}$ values close to zero were computed for the other charge-neutral osmolytes, indicating that their contacts with AMPs were largely opportunistic rather than chemically selective.

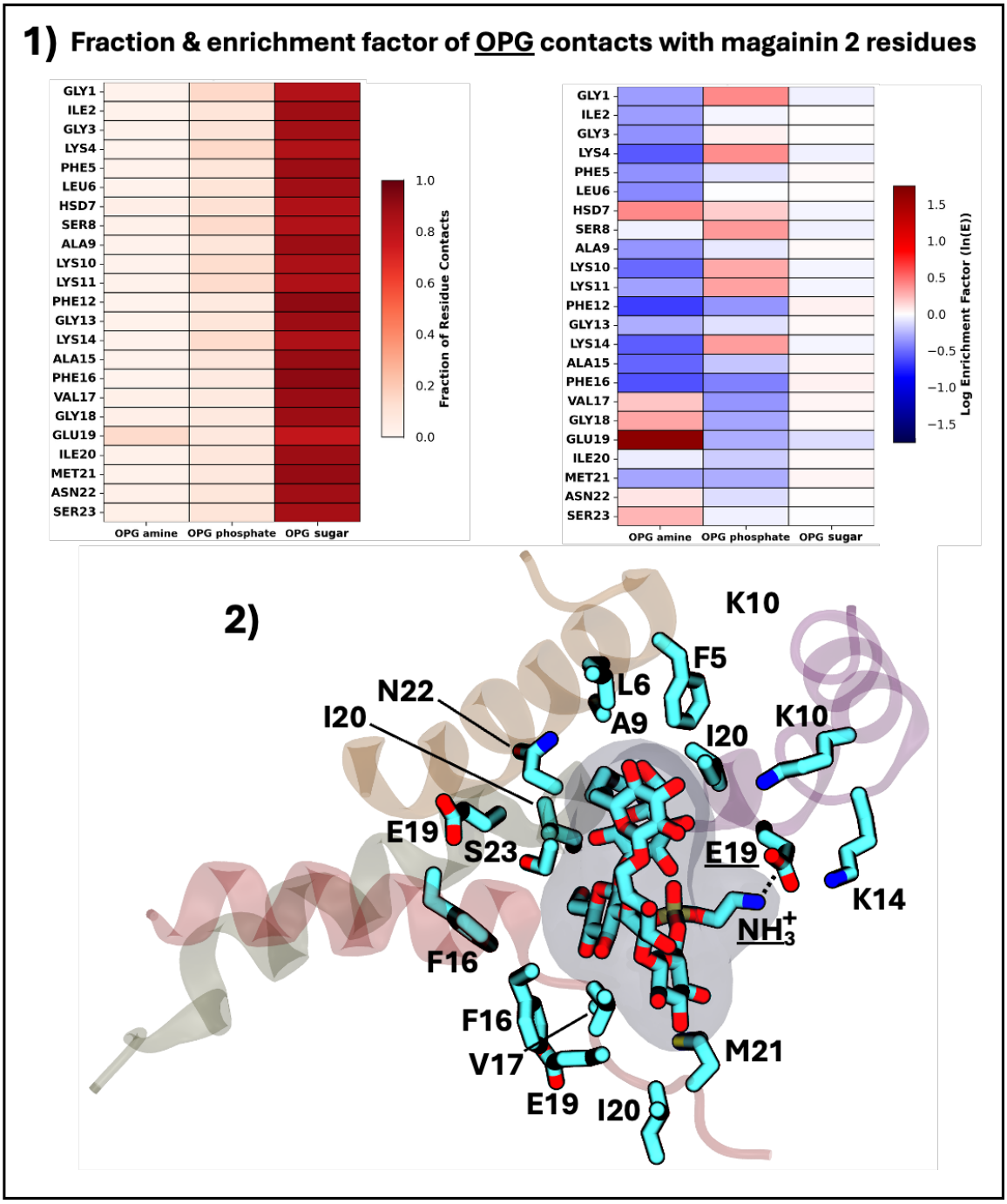

***Figure 3.19**. Residue-specific contact preferences and interactions between AMPs and OPG. 1) Per-residue contact fractions and enrichment factors with OPG chemical groups (data corresponds to S-O-M-A simulations). 2) Representative molecular image highlighting the polar interactions of OPG with multiple AMPs. AMP backbones as cartoon helices, interacting residues and OPG shown as liquorice and*

coloured by element: cyan: carbon, blue: nitrogen, red: oxygen, yellow: sulphur, brown: phosphorus. OPG has an overlaid transparent surface representation.

3.4.2.2.5 Cumulative effects of many short-lived interactions

Taken together, these analyses showed that solute-AMP interactions were characterised by numerous, short-lived peripheral contacts, with most involving one or two residues on a single AMP. Although individually transient, their combined effect was substantial and led to significant differences in AMP aggregation. For example, OPG contributed disproportionately to intra- and inter-AMP bridging, yet systems containing only OPG showed smaller aggregate size increases than those containing the full osmolyte mixture, indicating that aggregate stabilisation arose as an emergent property of the combined osmolyte species and interaction modes rather than being caused by individual species.

3.4.3 Summary and mechanistic interpretation

Across all analyses, peptide sequence, initial conformation, salt concentration, and osmolyte inclusion each had significant effects on AMP aggregation.

Cupiennin 1a consistently formed the largest aggregates, followed by magainin 2 and latarcin 1. This aggregation hierarchy reflected how differences in charge density and total hydrophobic surface governed the interplay between electrostatic repulsion and hydrophobic attraction. While α-helical conformations generally promoted aggregation by aligning their hydrophobic faces, the loss of this amphipathic order in denatured peptides reduced aggregation for magainin 2 and cupiennin 1a. In contrast, denatured latarcin 1 aggregated more readily than its helical form, as increased conformational flexibility alleviated electrostatic repulsion and enabled the formation of stabilising intra- and inter-peptide salt bridges. This exception highlights the diversity of association mechanisms even among structurally simple, linear, amphipathic peptides.

Hydrophobic packing consistently served as the structural basis for aggregate formation, while numerous short-lived, peripheral osmolyte contacts modulated repulsive electrostatic interactions and local crowding, thereby stabilising these assemblies. For magainin 2 and cupiennin 1a, either salt or osmolytes alone were sufficient to promote aggregation. For latarcin 1 however, both contributed independently and additively, as its high charge density required simultaneous screening and crowding to mitigate its stronger inter-peptide repulsion.

Most solute contacts involved single residues on individual peptides and were localised at the aggregate-solvent interface, where they typically persisted for only a few nanoseconds, although the sugars OPG and trehalose interactions exhibited slightly longer lifetimes.

Chemically, chloride and OPG dominated the interaction networks by occurrence and contact count respectively, but through distinct modes: chloride formed specific electrostatic interactions with cationic AMP residues, effectively screening electrostatic repulsion between peptides, whereas OPG engaged in less specific associations *via* its polar sugar rings, through steric and hydrogen-bonding interactions rather than direct electrostatic. Neutral osmolytes such as glycerol and trehalose interacted more transiently and without strong residue-type preferences, while polyamines interacted only minimally with the AMPs.

Importantly, osmolyte mixtures produced stronger aggregation effects than single species, as shown by the difference in AMP aggregation between systems containing only OPG and those containing the full osmolyte set. This demonstrated that the combined, cumulative action of multiple weakly interacting solutes stabilises peptide assemblies more effectively than individual osmolytes, an example of emergent cooperative behaviour arising from the complex chemical composition of periplasmic environments.

Together, these findings established a mechanistic model of osmolyte-modulated AMP aggregation, in which hydrophobic packing formed the structural aggregate core, electrostatic frustration was relieved through transient peripheral solute contacts, and multi-solute conditions produced cooperative aggregate stabilisation.

This work showed how the individual components of the periplasm could act together to shape AMP behaviour in an emergent manner, highlighting the need to account for this complexity when aiming to model peptide activity in biologically relevant conditions.

Future work could extend this framework to include additional periplasmic components that may influence AMP aggregation and translocation towards the inner membrane. Incorporating major chaperones such as Skp and SurA, or AMP-resistance proteins like YdeI, would enable investigating how osmolytes modulate AMP-periplasmic protein interactions and potentially influence AMP translocation across the periplasm, as observed for LolA and polymyxin B1.[3] Similarly, including the peptidoglycan cell wall would allow testing whether differences in AMP aggregation lead to altered translocation through the periplasm by modifying interactions with this structural barrier.

Such studies could bridge the present solution-phase mechanisms with the more complex envelope environments explored in subsequent chapters and provide a more complete description of how periplasmic species could influence AMP behaviour and activity.

To conclude, there is a need for greater standardisation across studies examining AMP behaviour. Reported results often cannot be directly compared due to variations in experimental and computational conditions, including peptide concentration, temperature, ionic strength, the usage of different force fields for simulations, as well as due to the common omission of membrane proteins and osmolytes.[3,4,50–54] Establishing consistent, physiologically motivated parameters across these factors would enable more meaningful comparisons between studies and a clearer understanding of how periplasmic chemistry governs AMP activity.

References

1. Li, J. *et al.* Membrane Active Antimicrobial Peptides: Translating Mechanistic Insights to Design. *Front. Neurosci.* **11**, (2017).
2. Mullineaux, C. W., Nenninger, A., Ray, N. & Robinson, C. Diffusion of Green Fluorescent Protein in Three Cell Environments in Escherichia Coli. *J. Bacteriol.* **188**, 3442–3448 (2006).
3. Pedebos, C., Smith, I. P. S., Boags, A. & Khalid, S. The hitchhiker's guide to the periplasm: Unexpected molecular interactions of polymyxin B1 in E. coli. *Structure* **29**, 444-456.e2 (2021).
4. Smith, I. P., Pedebos, C. & Khalid, S. Molecular crowding alters the interactions of polymyxin lipopeptides within the periplasm of E. coli: insights from molecular dynamics. *J. Phys. Chem. B* **128**, 2717–2733 (2024).
5. Scott Cayley, D., Guttman, H. J. & Thomas Record, M., Jr. Biophysical Characterization of Changes in Amounts and Activity of Escherichia coli Cell and Compartment Water and Turgor Pressure in Response to Osmotic Stress. *Biophys. J.* **78**, 1748–1764 (2000).
6. Bohin, J.-P. Osmoregulated periplasmic glucans in Proteobacteria. *FEMS Microbiol. Lett.* **186**, 11–19 (2000).
7. Bontemps-Gallo, S., Bohin, J.-P. & Lacroix, J.-M. Osmoregulated periplasmic glucans. *EcoSal Plus* **7**, 10.1128/ecosalplus. ESP-0001–2017 (2017).
8. Kennedy, E. P. Osmotic regulation and the biosynthesis of membrane-derived oligosaccharides in Escherichia coli. *Proc. Natl. Acad. Sci.* **79**, 1092–1095 (1982).
9. Vanaporn, M. & Titball, R. W. Trehalose and bacterial virulence. *Virulence* **11**, 1192–1202 (2020).

10. Jain, N. K. & Roy, I. Effect of trehalose on protein structure. *Protein Sci.* **18**, 24–36 (2009).
11. Boos, W., Ehmann, U., Bremer, E., Middendorf, A. & Postma, P. Trehalase of Escherichia coli. Mapping and cloning of its structural gene and identification of the enzyme as a periplasmic protein induced under high osmolarity growth conditions. *J. Biol. Chem.* **262**, 13212–13218 (1987).
12. Johnson, L., Mulcahy, H., Kanevets, U., Shi, Y. & Lewenza, S. Surface-localized spermidine protects the Pseudomonas aeruginosa outer membrane from antibiotic treatment and oxidative stress. *J. Bacteriol.* **194**, 813–826 (2012).
13. Gevrekci, A. Ö. The roles of polyamines in microorganisms. *World J. Microbiol. Biotechnol.* **33**, 204 (2017).
14. Cohen, S. S. A guide to the polyamines. 1998. *Oxf. Univ. Press Oxf. B Igarashi K Kashiwagi K Biochem Biophys Res* **271**, 559–564 (2000).
15. Shah, P. & Swiatlo, E. A multifaceted role for polyamines in bacterial pathogens. *Mol. Microbiol.* **68**, 4–16 (2008).
16. Mobley, H. L., Island, M. D. & Hausinger, R. P. Molecular biology of microbial ureases. *Microbiol. Rev.* **59**, 451–480 (1995).
17. Murarka, A., Dharmadi, Y., Yazdani, S. S. & Gonzalez, R. Fermentative utilization of glycerol by Escherichia coli and its implications for the production of fuels and chemicals. *Appl. Environ. Microbiol.* **74**, 1124–1135 (2008).
18. Beckers, G., Bendt, A. K., Krämer, R. & Burkovski, A. Molecular identification of the urea uptake system and transcriptional analysis of urea transporter-and urease-encoding genes in Corynebacterium glutamicum. *J. Bacteriol.* **186**, 7645–7652 (2004).

19. Krishnamurthy, P. *et al.* Helicobacter pylori containing only cytoplasmic urease is susceptible to acid. *Infect. Immun.* **66**, 5060–5066 (1998).
20. Wang, D., Weng, J. & Wang, W. Glycerol transport through the aquaglyceroporin GlpF: bridging dynamics and kinetics with atomic simulation. *Chem. Sci.* **10**, 6957–6965 (2019).
21. Lee, I. H., Cho, Y. & Lehrer, R. I. Effects of pH and salinity on the antimicrobial properties of clavanins. *Infect. Immun.* **65**, 2898–2903 (1997).
22. Kandasamy, S. K. & Larson, R. G. Effect of salt on the interactions of antimicrobial peptides with zwitterionic lipid bilayers. *Biochim. Biophys. Acta BBA-Biomembr.* **1758**, 1274–1284 (2006).
23. Mao, T. *et al.* Stabilizing effect of amino acids on protein and colloidal dispersions. *Nature* **645**, 915–921 (2025).
24. Zasloff, M. Magainins, a class of antimicrobial peptides from Xenopus skin: isolation, characterization of two active forms, and partial cDNA sequence of a precursor. *Proc. Natl. Acad. Sci. U. S. A.* **84**, 5449–5453 (1987).
25. Kuhn-Nentwig, L. *et al.* Cupiennin 1, a new family of highly basic antimicrobial peptides in the venom of the spider Cupiennius salei (Ctenidae). *J. Biol. Chem.* **277**, 11208–11216 (2002).
26. Kozlov, S. A. *et al.* Latarcins, antimicrobial and cytolytic peptides from the venom of the spider Lachesana tarabaevi (Zodariidae) that exemplify biomolecular diversity. *J. Biol. Chem.* **281**, 20983–20992 (2006).
27. Cruciani, R. A. *et al.* Magainin 2, a natural antibiotic from frog skin, forms ion channels in lipid bilayer membranes. *Eur. J. Pharmacol.* **226**, 287–296 (1992).

28. Hasan, M., Karal, M. A. S., Levadnyy, V. & Yamazaki, M. Mechanism of Initial Stage of Pore Formation Induced by Antimicrobial Peptide Magainin 2. *Langmuir ACS J. Surf. Colloids* **34**, 3349–3362 (2018).
29. Aisenbrey, C., Amaro, M., Pospíšil, P., Hof, M. & Bechinger, B. Highly synergistic antimicrobial activity of magainin 2 and PGLa peptides is rooted in the formation of supramolecular complexes with lipids. *Sci. Rep.* **10**, 11652 (2020).
30. Santo, K. P. & Berkowitz, M. L. Difference between magainin-2 and melittin assemblies in phosphatidylcholine bilayers: results from coarse-grained simulations. *J. Phys. Chem. B* **116**, 3021–3030 (2012).
31. Boughton, A. P., Andricioaei, I. & Chen, Z. Surface orientation of magainin 2: molecular dynamics simulation and sum frequency generation vibrational spectroscopic studies. *Langmuir ACS J. Surf. Colloids* **26**, 16031–16036 (2010).
32. Gesell, J., Zasloff, M. & Opella, S. J. Two-dimensional 1H NMR experiments show that the 23-residue magainin antibiotic peptide is an alpha-helix in dodecylphosphocholine micelles, sodium dodecylsulfate micelles, and trifluoroethanol/water solution. *J. Biomol. NMR* **9**, 127–135 (1997).
33. Gregory, S. M., Pokorny, A. & Almeida, P. F. F. Magainin 2 Revisited: A Test of the Quantitative Model for the All-or-None Permeabilization of Phospholipid Vesicles. *Biophys. J.* **96**, 116–131 (2009).
34. Imura, Y., Choda, N. & Matsuzaki, K. Magainin 2 in Action: Distinct Modes of Membrane Permeabilization in Living Bacterial and Mammalian Cells. *Biophys. J.* **95**, 5757–5765 (2008).
35. Ludtke, S. J. *et al.* Membrane pores induced by magainin. *Biochemistry* **35**, 13723–13728 (1996).

36. Bechinger, B., Zasloff, M. & Opella, S. J. Structure and orientation of the antibiotic peptide magainin in membranes by solid-state nuclear magnetic resonance spectroscopy. *Protein Sci.* **2**, 2077–2084 (1993).
37. Pukala, T. L. *et al.* Solution Structure and Interaction of Cupiennin 1a, a Spider Venom Peptide, with Phospholipid Bilayers. *Biochemistry* **46**, 3576–3585 (2007).
38. Pukala, T. L. *et al.* Solution structure and interaction of cupiennin 1a, a spider venom peptide, with phospholipid bilayers. *Biochemistry* **46**, 3576–3585 (2007).
39. Dubovskii, P. V. *et al.* Spatial structure and activity mechanism of a novel spider antimicrobial peptide. *Biochemistry* **45**, 10759–10767 (2006).
40. Ar, M., Ms, C. & W, F. NetWheels: A Web Application to Create High Quality Peptide Helical Wheel and Net Projections. *J. Bioinforma. Syst. Biol.* **7**, 98–100 (2024).
41. Wieprecht, T., Apostolov, O., Beyermann, M. & Seelig, J. Thermodynamics of the α-helix-coil transition of amphipathic peptides in a membrane environment: implications for the peptide-membrane binding equilibrium1. *J. Mol. Biol.* **294**, 785–794 (1999).
42. Pistolesi, S., Pogni, R. & Feix, J. B. Membrane Insertion and Bilayer Perturbation by Antimicrobial Peptide CM15. *Biophys. J.* **93**, 1651–1660 (2007).
43. Gottler, L. M. & Ramamoorthy, A. Structure, membrane orientation, mechanism, and function of pexiganan—a highly potent antimicrobial peptide designed from magainin. *Biochim. Biophys. Acta BBA-Biomembr.* **1788**, 1680–1686 (2009).
44. Pukala, T. L. *et al.* Solution Structure and Interaction of Cupiennin 1a, a Spider Venom Peptide, with Phospholipid Bilayers. *Biochemistry* **46**, 3576–3585 (2007).
45. Wadhwani, P. *et al.* Membrane interactions of latarcins: antimicrobial peptides from spider venom. *Int. J. Mol. Sci.* **22**, 10156 (2021).

46. Strandberg, E. *et al.* 2H-NMR and MD Simulations Reveal Membrane-Bound Conformation of Magainin 2 and Its Synergy with PGLa. *Biophys. J.* **111**, 2149–2161 (2016).
47. Huang, J. *et al.* CHARMM36m: an improved force field for folded and intrinsically disordered proteins. *Nat. Methods* **14**, 71–73 (2017).
48. Abraham, M. J. *et al.* GROMACS: High performance molecular simulations through multi-level parallelism from laptops to supercomputers. *SoftwareX* **1–2**, 19–25 (2015).
49. Glaser, F., Steinberg, D. M., Vakser, I. A. & Ben-Tal, N. Residue frequencies and pairing preferences at protein–protein interfaces. *Proteins Struct. Funct. Bioinforma.* **43**, 89–102 (2001).
50. Zhang, L., Rozek, A. & Hancock, R. E. W. Interaction of Cationic Antimicrobial Peptides with Model Membranes *. *J. Biol. Chem.* **276**, 35714–35722 (2001).
51. Wang, Y. *et al.* How reliable are molecular dynamics simulations of membrane active antimicrobial peptides? *Biochim. Biophys. Acta BBA - Biomembr.* **1838**, 2280–2288 (2014).
52. Gregory, S. M., Pokorny, A. & Almeida, P. F. F. Magainin 2 Revisited: A Test of the Quantitative Model for the All-or-None Permeabilization of Phospholipid Vesicles. *Biophys. J.* **96**, 116–131 (2009).
53. Mercer, D. K. *et al.* Antimicrobial Susceptibility Testing of Antimicrobial Peptides to Better Predict Efficacy. *Front. Cell. Infect. Microbiol.* **10**, (2020).
54. Juhl, D. W., Glattard, E., Lointier, M., Bampilis, P. & Bechinger, B. The Reversible Non-covalent Aggregation Into Fibers of PGLa and Magainin 2 Preserves Their Antimicrobial Activity and Synergism. *Front. Cell. Infect. Microbiol.* **10**, 526459 (2020).

Chapter 4

Computational Electrophysiology simulations of AMP-induced membrane pores: overview of pore formation mechanisms

4.1 Introduction

The antimicrobial peptide (AMP) magainin 2 (M2) exerts its antimicrobial activity by disrupting both the outer and inner membranes of bacterial cells.[1] In Gram-negative bacteria, it first penetrates or compromises the outer membrane, likely through displacement of stabilising divalent cations and direct interaction with lipopolysaccharides (LPS) - a process often referred to as “self-promoted uptake.”[1,2] Electron microscopy and fluorescence studies have shown that M2 inserts into LPS bilayers at physiologically relevant concentrations and can even localise within the cytoplasm of *E. coli*, suggesting it crosses both membranes.[3,4] Enhanced membrane disruption and bactericidal activity have also been observed for analogues with higher net positive charge, supporting the role of electrostatics in membrane penetration.[1] Once at the inner membrane, M2 causes rapid permeabilisation, leading to the immediate efflux of intracellular ions such as K^+, collapse of membrane potential, and leakage of small metabolites.[1,5]

These effects have been attributed to the formation of toroidal pores: transient, lipid-lined defects where the bilayer bends continuously through the pore, with both lipid headgroups and peptide helices contributing to the pore wall.[6] Fluorescence and neutron scattering experiments have reported toroidal pores of approximately

2.0-3.7 nm in diameter formed by M2 in phosphatidylglycerol-containing membranes, supporting a pore-forming mechanism with defined, finite size rather than detergent-like solubilisation.[7,8] This behaviour contrasts with detergent-like mechanisms, as it produces a discrete “all-or-none” permeabilisation response at the single-cell or vesicle level.[5] The formation of M2 pores has been described as a stochastic or chaotic process involving transient lipid-peptide structures rather than stable, well-defined peptide-lined channels, distinguishing it from barrel-stave-like mechanisms.[5] Recent computational studies have shown that M2 mutants can induce local membrane curvature and thinning consistent with toroidal pore formation.[9]

While AMP-induced pore formation at the inner membrane of Gram-negative bacteria has been widely studied in the literature, much less is known about the fate of antimicrobial peptides within the periplasm, a crowded intermediate compartment rich in salts, osmolytes, and proteins that could modulate peptide behaviour.[10] Although recent studies have begun addressing these questions, our understanding of AMP activity in realistic inner membrane models that include periplasmic components remains limited: Open questions persist regarding how such periplasmic species may influence the bactericidal activity of AMPs, including their effects on AMP-membrane aggregation, peptide-peptide interactions, and the mechanisms of pore formation, as schematically illustrated in **Figure 4.1**.[10]

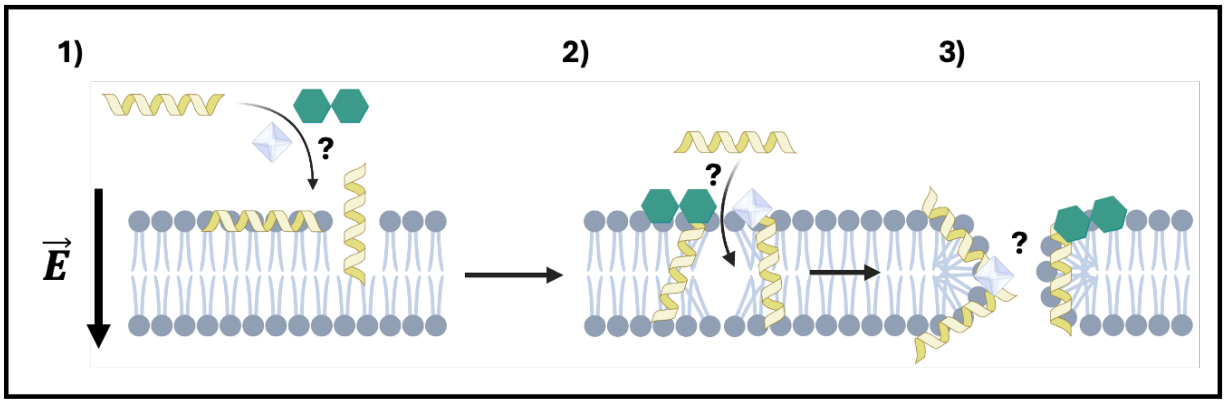

Figure 4.1. *Schematic representation of AMP (yellow α-helices) translocation across a lipid bilayer (grey) and pore formation under an applied electric field. Open questions remain about how periplasmic species, such as osmolytes (green hexagons) and salts (white cubes), influence 1) AMP-membrane and AMP-AMP interactions, 2) AMP insertion and membrane destabilisation, and 3) the formation of membrane pores, as indicated by question marks.*

The Computational Electrophysiology (CompEL) method was developed to enable molecular dynamics simulations under realistic transmembrane potentials by maintaining a constant charge imbalance across membranes. [11,12] In practice, CompEL is implemented using systems composed of two membrane bilayers that separate two aqueous compartments, as illustrated in **Figure 4.2**. Membrane pore proteins connect adjacent compartments, allowing ion and water exchange between them. A defined charge imbalance ΔQ is maintained by periodically replacing ions that have crossed compartments with water molecules from the side they originated from. This exchange sustains a constant electric field across the membranes.

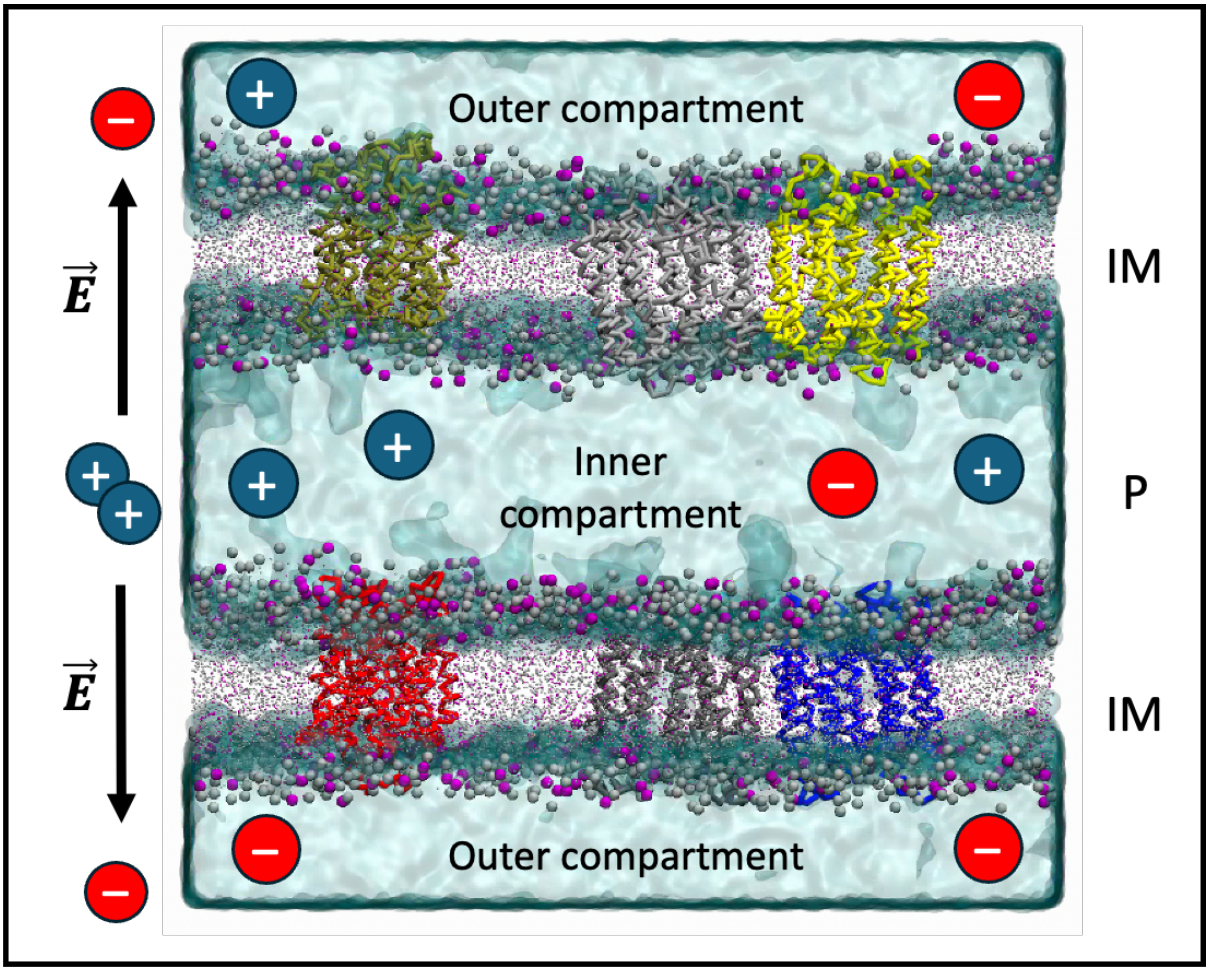

Figure 4.2. *Schematic representation of a double bilayer system used in this and subsequent chapters to induce an electric membrane potential using the Computational Electrophysiology (CompEL) protocol, representing the inner membrane (IM) and periplasm (P). Lipid headgroups are shown as grey (phosphatidylethanolamine, PE) and purple (phosphatidylglycerol, PG) beads, and tails as point representations. Aqueous compartments are shown as a transparent cyan surface. Membrane pore protein backbones are shown as stick representations.*

This method has been instrumental in studying the mechanisms of ion channel conductance and selectivity.[11,12] More recently, it has also been applied to investigate the membrane-penetrating behaviour of polymyxin AMPs in Gram-negative bacterial

inner membranes.[13] In particular, simulations using CompEL have revealed that polymyxin B1 can translocate through electroporation-induced pores at protein-phospholipid interfaces, suggesting that AMPs may be capable of exploiting local membrane defects such as membrane proteins to cross the inner membrane.[13]

In this work, the well-studied and relatively abundant (13.7-239.0 ppm) inner membrane protein lactose permease (LacY) was used as the membrane pore protein enabling water flow between the aqueous compartments in CompEL simulations.[14,15] Structurally, LacY consists of 12 transmembrane α-helices arranged in two symmetric bundles and transitions between outward and inward-facing conformations as part of its transport cycle.[16] The inward-facing conformation (as shown in **Figure 4.3**) was chosen for this work as it represents the most extensively studied and well-characterised form of LacY.[13,17–20]

LacY is a secondary active symporter from *E. coli* that harnesses the proton motive force (PMF) to transport lactose and other β-galactosides from the periplasm into the cytoplasm against their concentration gradient, as shown in **Figure 4.3**.[16,20,21] The transport cycle begins with LacY in an outward-facing conformation where E269 is rapidly protonated, ready to bind its substrate from the periplasm. Substrate binding triggers proton transfer from E269 to E325 and induces a conformational change to the inward-facing state. The substrate is then released into the cytoplasm, followed by E325 deprotonation. This proton release resets LacY to the outward-facing conformation, completing the cycle.

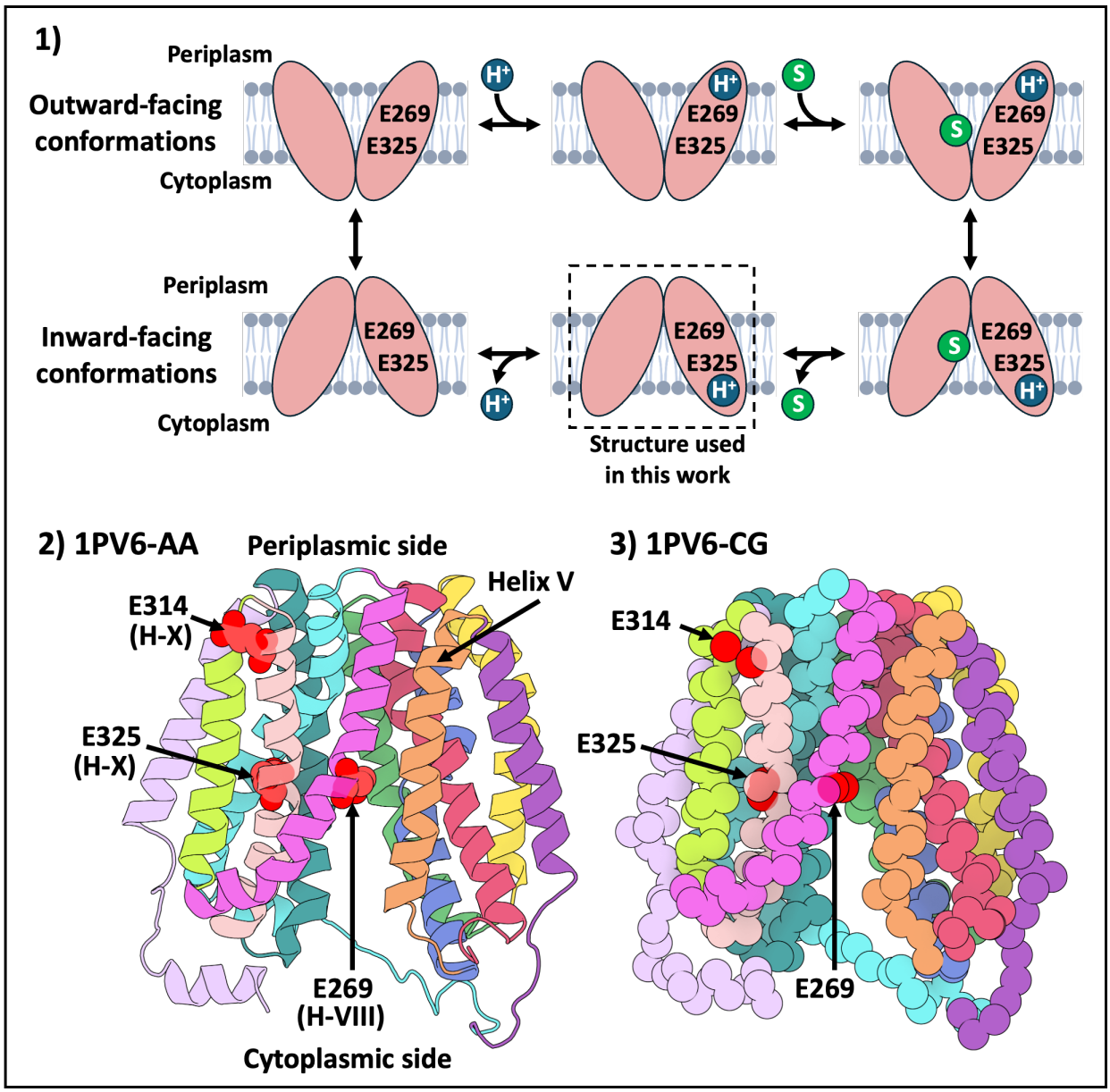

Figure 4.3. *Structure and transport mechanism of lactose permease (LacY) 1) Schematic representation of the LacY alternating-access transport cycle showing key protonation states of residues E269 and E325 during sugar (S) and proton (H^+) translocation into the cytoplasm.*[16,20,21] *2-3) Structural representations of the lactose permease LacY from E. coli (PDB: 1PV6, X-ray diffraction, 3.50 Å resolution) in the inward-facing conformation as used in this work, with the atomistic (AA) structure shown as cartoon in 2) and the backbone beads of the coarse-grained (CG, Martini 2.2p) structure shown in 3).*[19] *The colouring of individual helices is consistent across*

both representations, with key glutamate residues GLU269 on helix VIII (H-VIII), GLU314 and GLU325 on helix X (H-X) highlighted in red.

4.2 Aims

This chapter aims to introduce my investigations into the permeation of the antimicrobial peptide magainin 2 across the *E. coli* inner membrane under an induced electric field, and how system parameters such as the presence of periplasmic osmolytes could influence this process

4.3 Methods

4.3.1 Molecular modelling for CG MD simulations

The α-helical structure of magainin 2 (PDB: 2MAG, NMR spectroscopy) was converted to coarse-grained resolution using the *Martinize2* script.[22,23] The unmodified N-terminus (NT) was not modified and thus positively charged, while the C-terminus was either neutral (amidated form) or negatively charged (wild-type carboxylic acid form).[24] All protein side chains were modelled in their default protonation states at physiological pH, except for Glu325 in LacY, which was protonated in accordance with previous studies.[25,26] The ElNeDyn elastic network approach was used to maintain protein secondary and tertiary structures.[27] Constraints were applied between Glu269 and Trp151, and between Glu325 and Arg302, to preserve their orientation facing the substrate-binding pocket. These constraints were based on their average distances observed in a preliminary ensemble of energy-minimised structures.

Trehalose was modelled using the Martini 2 carbohydrate parameters.[28] Spermidine and putrescine were parametrised using *PyCGTOOL*.[29] Phosphate anions were modelled by analogy to the published parameters for the divalent calcium ion.[30]

4.3.2 Simulation set-up

All simulations were performed using the coarse-grained Martini 2.2p forcefield with polarisable water and proteins, implemented within the GROMACS simulation suite (version 2021.5). The initial simulation box measured 20 × 20 × 13 nm³ for the single bilayer system, while subsequent double bilayer systems had a box size of 20 × 20 × 26 nm³, with periodic boundary conditions applied in all dimensions.

The initial single POPE:POPG bilayer containing 3 LacY copies was derived from previous studies with its lipid composition adapted using an in-house Python script.[13] It was minimised and equilibrated following the CHARMM-GUI Martini Maker protocol before undergoing a 100 ns production run (20 fs timestep) in the isothermal-isobaric ensemble (NPT).[31] To generate the double bilayer systems, the final frame from the single bilayer simulations was mirrored along the z-axis, and the upper half was rotated 90° around the z-axis.

The number of M2 copies and osmolytes replicated concentrations from protocols described in **Chapter 3** and previous works, as summarised in **Table 4.1** and illustrated in **Figure 4.4** below.[10,13] Specifically, the number of solute molecules was determined using the same solute-to-water ratio method employed in **Chapter 3** to recreate literature concentrations within the coarse-grained system volume, taking into account the 4-to-1 mapping of water beads.[10,13] Included periplasmic solute species were Ca^{2+} (CA) and HPO_4^{2-} (PHOS) ions, as well as the following osmolytes:

the disaccharide trehalose (TREH), and the amines spermidine (SPER) and putrescine (PUT).

For systems containing AMPs, M2 copies were added to the central compartment of the pre-equilibrated membrane system and placed randomly in the XY-plane 0.75 nm away from the lipid headgroups in the z-direction, evenly distributing half the peptides near each inward-facing leaflet. Salts, as well as osmolytes in the corresponding systems, were added at identical concentrations to both internal and external compartments. The numbers of Na^+ (NA) and Cl^- (CL) ions were then adjusted in each compartment to achieve the desired final charge imbalance ΔQ between compartments. The charge imbalance was determined by a script summing the charges inside the compartment defined by the middles of the membranes, and the charges outside of this compartment respectively. In selected cases, simulations with an initial charge imbalance were continued with the electric field “switched off”, by using an in-house Python script to retain only the relevant half of the simulation box for further simulation. Regarding replicate generation, while distinct replicate numbers corresponded to independently built systems with unique random seeds, the specific initial coordinates of AMPs and osmolytes were preserved for the same replicate number across different system types (*e.g.*, replicate 1 of the “R” and “N” systems shared identical starting configurations for AMPs and osmolytes).

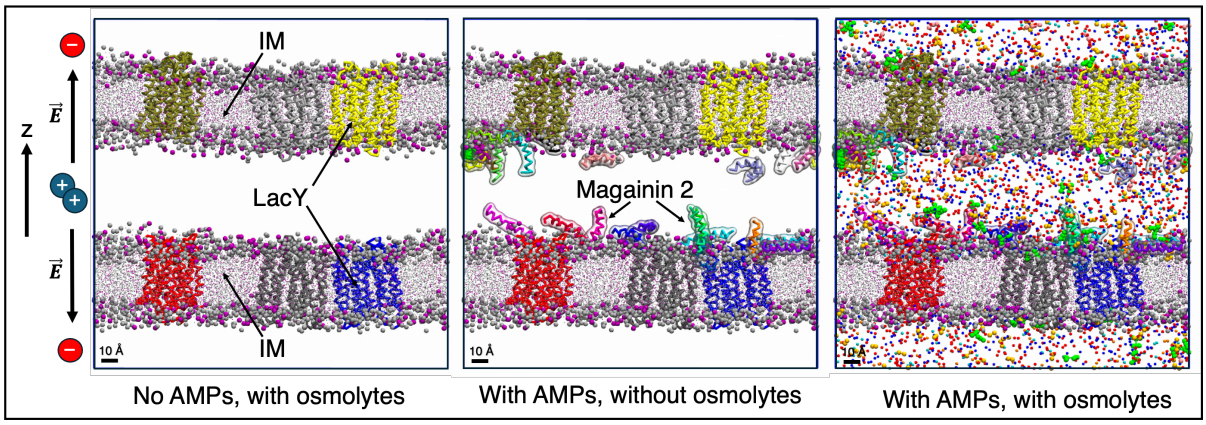

Figure 4.4. *Overview of simulated membrane systems with different periplasmic compositions, as detailed in* ***Table 4.1****. Double bilayer systems containing models of the E. coli inner membrane (lipid headgroups as grey and purple beads; tails as points) and embedded LacY proteins (backbone as stick representation). Left: system without AMPs, with periplasmic salts and osmolytes (omitted for clarity). Centre: system with M2 (coloured cartoon helices) and periplasmic salts, but without osmolytes (salts omitted for clarity). Right: system with M2, salts, and osmolytes (osmolytes and salts shown as coloured spheres).*

As indicated in **Table 4.1**, a subset of simulations was run without AMPs (“A” simulations) but with periplasmic salts and osmolytes. Other simulations included AMPs without or with periplasmic salts and osmolytes (“B” and “T” simulations), as well as with AMPs and with only a subset of the periplasmic salts and osmolytes (“D” and “E” simulations). Included periplasmic solute species were Ca^{2+} (CA) and HPO_4^{2-} (PHOS) ions, as well as the following osmolytes: the disaccharide trehalose (TREH), and the amines spermidine (SPER) and putrescine (PUT).

Table 4.1. *Top: overview of the osmolytes used in the performed simulations and their respective concentrations. Bottom: different solute phase compositions investigated in this work.*

Species	**Concentration [mM]**
1) Magainin 2	6
2) Na^+ (NA) & Cl^- (CL)	150
3) Ca^{2+} (CA)	70
4) Phosphate HPO_4^{2-} (PHOS)	50
5) Trehalose (TREH)	10
6) Putrescine (PUT)	30
7) Spermidine (SPER)	3
System type	**System composition**
A) No M2, with osmolytes	2 + 3 + 4 + 5 + 6 + 7
B) With M2, no osmolytes	1 + 2 + 3
C) With M2, with osmolytes	1 + 2 + 3 + 4 + 5 + 6 + 7
D) With M2, with osmolytes, minus (CA, PHOS)	1 + 2 + 5 + 6 + 7
E) With M2, with osmolytes, minus TREH	1 + 2 + 3 + 4 + 6 + 7

As summarised in **Table 4.2**, a range of simulations was performed to investigate the effects of different system modifications on the permeation of M2 across bacterial inner membranes.

The standard reference simulations “R” included M2 peptides with a neutral amidated C-terminus (total charge +4 *e*), LacY with E325 protonated and constrained as described above, and a membrane composed of POPE:POPG (8:2) with a charge imbalance of +138 *e* between compartments (inner AMP-containing compartment positively charged relative to outer compartment), inducing an electric field across the membrane.

The “N” simulations were identical to the “R” setup, except that the charge imbalance between compartments was set to zero, eliminating the electric field.

In the “T” simulations, the M2 peptides possessed a negatively charged carboxylated C-terminus, reducing their overall charge to +3 *e*.

The “M” simulations utilised an altered membrane composition of DPPE:DPPG (8:2).

Finally, in the “L” and “L^+” simulations, a protonation mutation was introduced at Glu314 in LacY; the “L^+” simulations additionally featured an increased charge imbalance (total imbalance: +144 *e*).

Combining the nomenclatures from **Table 4.1** and **Table 4.2**, simulation names consist of the simulation type, for example “R” for reference simulations, and the solute composition type, for example “A” for “no AMPs, all periplasmic species included”. Thus, the name for AMP-free reference simulations with all periplasmic species and an induced electric field is “R-A.”

Table 4.2. *Overview of simulated systems nomenclature and compositions. Conditions deviating from the reference simulations "R" are highlighted in bold. Simulation names are composed of the simulation type and the solute composition type as described in* ***Table 4.1****.*

Name	Magainin C-terminus	Key LacY Residue State	Membrane Composition	Δq (in - out)	Simulations (≥ 5 µs)	Comments
R^N	Amide (+4 *e*)	E325$^{constr,\ protonated}$ E314$^{constr,\ negative}$	POPE:POPG (8:2)	**+0 *e***	5x	"Reference" simulations without charge imbalance between compartments
R	**Amide (+4 *e*)**	**E325$^{constr,\ protonated}$** **E314$^{constr,\ negative}$**	**POPE:POPG (8:2)**	**+138 *e***	**25x**	**"Reference" simulations with charge imbalance between compartments**
C	**Carboxyl (+3 *e*)**	E325$^{constr,\ protonated}$ E314$^{constr,\ negative}$	POPE:POPG (8:2)	+138 *e*	10x	Wild type C-terminus
M	Amide (+4 *e*)	E325$^{constr,\ protonated}$ E314$^{constr,\ negative}$	**DPPE:DPPG** (8:2)	+138 *e*	10x	Saturated membrane lipids
L	Amide (+4 *e*)	E325$^{constr,\ protonated}$ **E314$^{constr,\ protonated}$**	POPE:POPG (8:2)	+138 *e*	10x	Mutated E314 on LacY neutralising its negative charge
L$^+$	Amide (+4 *e*)	E325$^{constr,\ protonated}$ **E314$^{constr,\ protonated}$**	POPE:POPG (8:2)	**+144 *e***	5x	Mutated E314 as in L + increased charge imbalance between compartments

4.3.3 MD simulations

After adding AMPs and other solute species, the pre-equilibrated double-membrane systems (100 ns NPT) were first energy-minimised using the steepest descent algorithm (≤ 50,000 steps). Equilibration was then performed in the NPT ensemble for 2 ns over six consecutive steps while monitoring volume convergence: Position restraints on peptides and lipid headgroups were gradually decreased from 1000 to 0 kJ mol^{-1} nm^{-2}, while the integration timestep was increased from 2 fs to 20 fs. Both equilibration and production runs used the velocity rescale thermostat (τ = 1 ps) at 310 K, with separate coupling groups for lipids, proteins, and solutes. Pressure was maintained semi-isotropically at 1 bar using the Berendsen barostat during equilibration (τ = 5 ps) and the Parrinello-Rahman barostat during production (τ = 12 ps), with a compressibility of 3 × 10^{-4} bar^{-1} for both. All simulations used the leap-frog integrator. Electrostatics were treated with the particle-mesh~~Particle-Mesh~~ Ewald method (cutoff 1.1 nm, dielectric constant ε_r = 2.5)~~,),~~ and van der Waals interactions used a potential-shift Verlet scheme with a 1.1 nm cutoff. Production simulations lasted 5 µs (extended to 6 or 10 µs in specific cases) and included the computational electrophysiology protocol: ion exchanges (Na^+, Cl^-, Ca^{2+}; additionally hydrogen phosphate anions HPO_4^{2-} in osmolyte-containing systems) were performed every 100 steps along the membrane normal (z-direction) to maintain the desired transmembrane potential.

4.4 Results and discussion

4.4.1 Membrane pore formation mechanisms

The formation of transient membrane-spanning pores was observed in a subset of the conducted simulations. Four primary mechanisms were identified, each involving distinct interactions between the membrane and M2 peptides, or the membrane protein LacY, or both. These different mechanisms are described in detail in subsequent subchapters and are summarised in order of decreasing observation frequency across the reference simulations “R” in **Figure 4.5**.

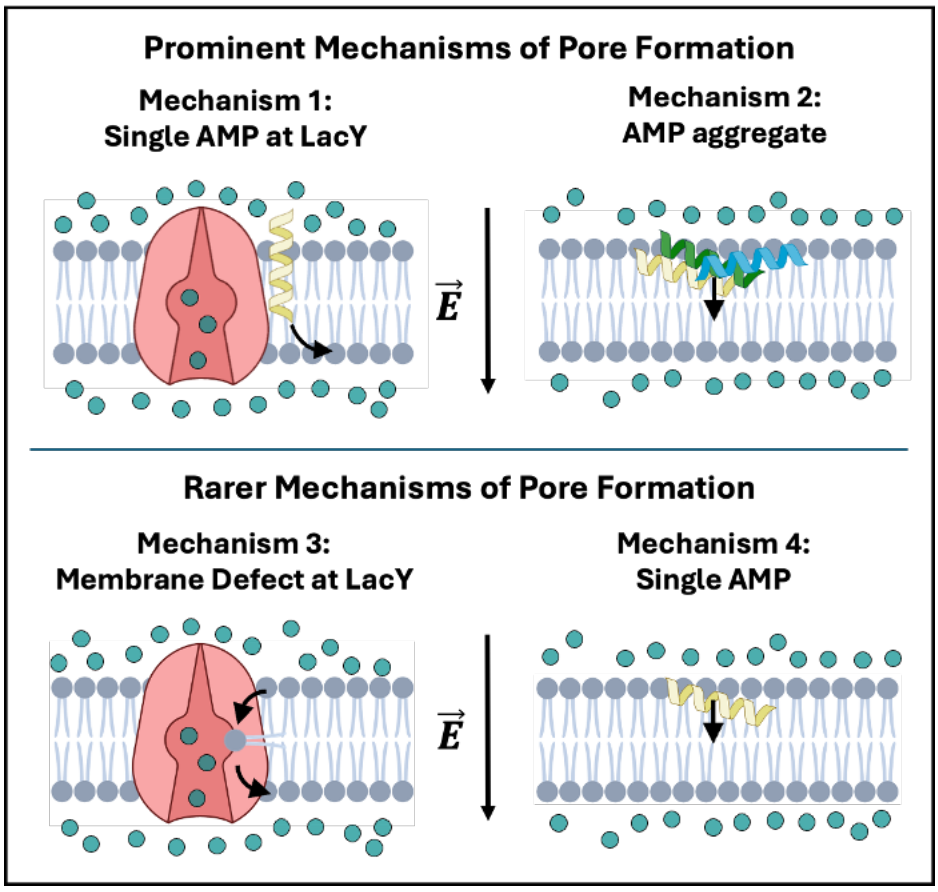

Figure 4.5. *Schematic overview of the four mechanisms of membrane pore formation by magainin 2 observed in my computational electrophysiology simulations in order of decreasing observation frequency from top left to bottom right. LacY is shown in pink, lipids in grey, and waters are represented as cyan circles.*

In mechanism 1, a single M2 peptide "snorkelled" along the surface of LacY, inserting into the membrane and contacting lipids in the opposing leaflet, ultimately triggering pore formation.

Mechanism 2 involved AMP aggregates at the membrane surface, which induced membrane local thinning and defect formation until membrane rupture occurred.

In mechanism 3, pore formation arose near LacY independently of AMPs, driven by lipid flip-flops at the side of LacY that destabilised the bilayer.

Mechanism 4 resembled mechanism 2, but involved only a single AMP that disrupted the bulk membrane without interaction with LacY.

Given the volume of data generated from my simulations of diverse systems with multiple components, mechanism-specific results are presented across **Chapter 5** and **Chapter 6** for clarity. **Chapter 5** focuses on mechanisms of pore formation independent of the membrane protein LacY, while **Chapter 6** addresses mechanisms involving LacY.

4.4.2 Effects of system variables on pore formation mechanism distribution

Pore formation behaviour varied markedly across condition types, as shown in **Table 4.3** below, and described in more detail in subsequent subchapters.

Table 4.3. *Summary of simulation types, corresponding pore formation events and pore formation mechanism frequencies.*

Name	AMP included	Osmolytes included	Simulations (≥ 5 µs)	Pore formed	AMP involved in pore formation	Mechanism 1: Single AMP, near LacY	Mechanism 2: AMP aggregate, bulk membrane	Mechanism 3: Pore at LacY, no AMP	Mechanism 4: Single AMP, bulk membrane	Reminder of Simulation Type
R-A	-	+	15	0% (0/15)	n/a	n/a	n/a	n/a	n/a	Reference simulations, with charge imbalance
R-B	+	-	25	64% (16/25)	100% (16/16)	69% (11/16)	25% (4/16)	0% (0/16)	6% (1/16)	
R-C	+	+	25	52% (14/25)	86% (12/14)	43% (6/14)	43% (6/14)	14% (2/14)	0% (0/14)	
R-D	+	+ (no Ca^{2+}, HPO_4^{2-})	15	60% (9/15)	89% (8/9)	33% (3/9)	56% (5/9)	11% (1/9)	0% (0/9)	
R-E	+	+ (no TREH)	15	46% (7/15)	86% (6/7)	43% (3/7)	43% (3/7)	14% (1/7)	0% (0/7)	
N-A	-	+	5	0% (0/5)	n/a	n/a	n/a	n/a	n/a	Reference simulations, without charge imbalance
N-B	+	-	5	0% (0/5)	n/a	n/a	n/a	n/a	n/a	
N-C	+	+	5	0% (0/5)	n/a	n/a	n/a	n/a	n/a	
T-B	+	-	10	30% (3/10)	100% (3/3)	33% (1/3)	33% (1/3)	0% (0/3)	33% (1/3)	Reduced magainin charge: +3 *e*
T-C	+	+	10	20% (2/10)	100% (2/2)	50% (1/2)	50% (1/2)	0% (0/2)	0% (0/2)	
M-A	-	+	5	0% (0/5)	n/a	n/a	n/a	n/a	n/a	Modified membrane composition: DPPE:DPPG
M-B	+	-	10	80% (8/10)	50% (4/8)	38% (3/8)	0% (0/8)	50% (4/8)	12% (1/8)	
M-C	+	+	10	70% (7/10)	71% (5/7)	42% (3/7)	29% % (2/7)	29% (2/7)	0% (0/7)	
L-B	+	-	10	10% (1/10)	100% (1/1)	100% (1/1)	0% (0/1)	0% (0/1)	0% (0/1)	E314 on LacY protonated
L-A	+	+	10	30% (3/10)	100% (3/3)	0% (0/3)	67% (2/3)	0% (0/3)	33% (1/3)	
L^+-*B*	+	-	5	100% (5/5)	60% (3/5)	0% (0/5)	0% (0/5)	40% (2/5)	60% (3/5)	Same as L simulations, increased ΔQ
L^+-*C*	+	+	5	20% (1/5)	100% (1/1)	0% (0/1)	100% (1/1)	0% (0/1)	0% (0/1)	

4.4.2.1 Effects of electric field and AMP inclusion

As visually summarised in **Figure 4.6**, no pore formation was observed in the “N” control simulations, which lacked an applied electric field, regardless of AMP presence. This indicated that AMPs alone were insufficient to induce membrane disruption under the conditions used, even though they bound to the membrane surface with a frequency comparable to simulations where an electric field was applied. Likewise, in the “R” and “M” simulations where an electric field was applied but AMPs were absent, membranes remained intact, suggesting that the induced electric field alone was also insufficient to induce membrane pore formation. Water flux through LacY pores was however observed in all simulations.

Pore formation was only observed when both AMPs and an electric field were present (“R-B/C” and “M-B/C”). Thus, both factors were required to trigger pore formation in my systems. This observation was deemed mechanistically reasonable, given that membrane potential alone is unlikely to induce substantial spontaneous membrane poration *in vivo* as it would compromise bacterial viability, and *in silico* experiments without an additional driving force do not capture such events within accessible timescales yet.

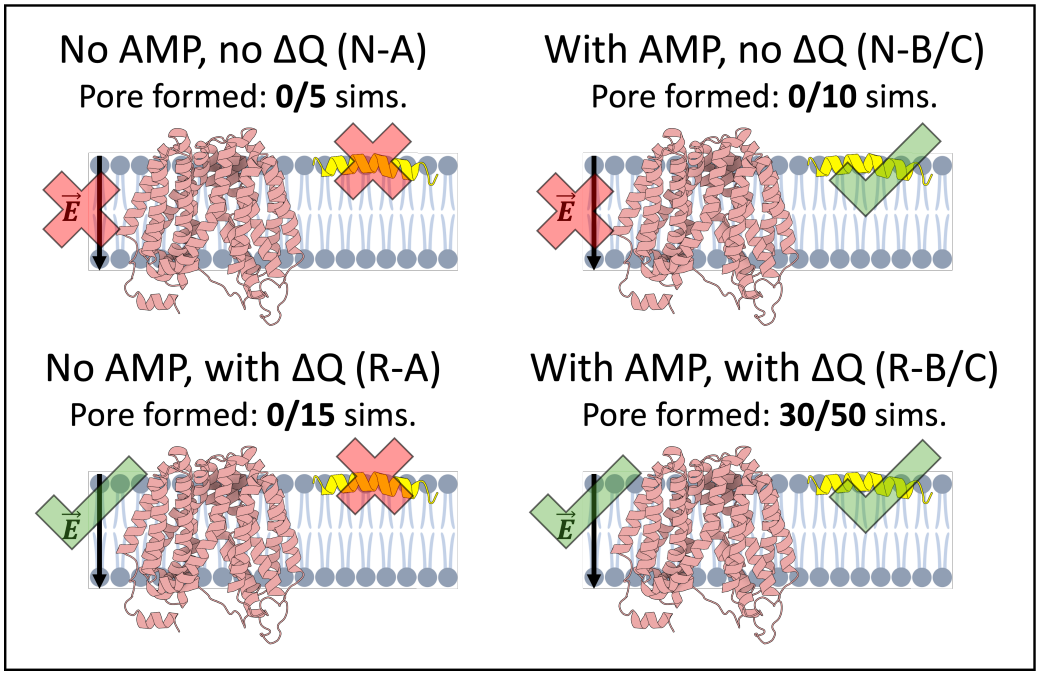

Figure 4.6. *Schematic representation of the effects of the inclusion of an induced electric field or AMPs on membrane pore formation, focusing on "R" simulations.*

4.4.2.2 Effects of osmolyte inclusion

In the "R-B" and "R-C" reference simulations, the occurrence of pore formation in AMP-containing systems was not statistically different between osmolyte-containing (52%) and osmolyte-free (64%) systems, as determined by Fisher's exact test. For these simulations, mechanism 1 (single AMP snorkelling along LacY leading to compounding membrane defects) was the predominant mode of pore formation, particularly in the absence of osmolytes, as represented in **Figure 4.7**. When osmolytes were present, the frequency of mechanism 1 decreased, while that of mechanism 2 (pores involving AMP aggregates) increased, resulting in both mechanisms occurring at similar rates. While the difference in mechanism preference between conditions did not reach statistical significance (Fisher's exact test > 0.05), the observed odds of mechanism 2 occurring relative to mechanism 1 were approximately 2.75 times higher in the presence of osmolytes, suggesting a

shift in the dominant pore formation pathway as a trend. Several factors likely contributed to this trend and will be discussed in more detail in subsequent subchapters.

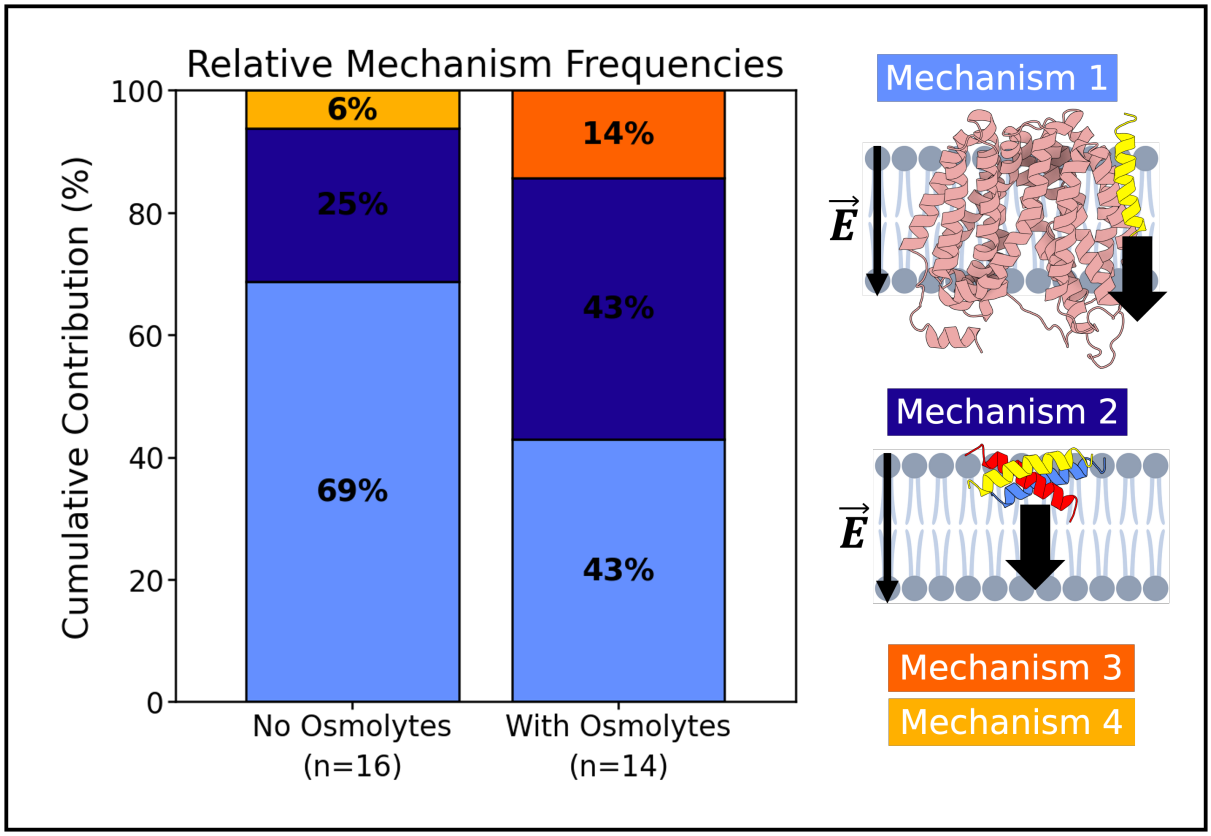

Figure 4.7. *Relative proportions of pore formation mechanisms observed in simulations without and with periplasmic osmolytes. Stacked bar plots show the distribution of four distinct mechanisms, with mechanism 1 (light blue), mechanism 2 (dark blue), mechanism 3 (orange), and mechanism 4 (yellow).*

To assess the role of individual solutes in this shift, additional simulations were performed excluding either Ca^{2+} and HPO_4^{2-} ("R-D") or TREH ("R-E") from the solute mixture. The pore formation frequencies in both "R-D" (60%) and "R-E" (47%) remained statistically indistinguishable from the osmolyte-free reference "R-B" as determined by Fisher's exact test. However, the mechanism preference in "R-D" differed from that of the osmolyte-free reference "R-B" with borderline statistical

significance ($p = 0.049$), with mechanism 2 dominating over mechanism 1. This suggested that the exclusion of Ca^{2+} and HPO_4^{2-}, or conversely the inclusion of TREH, enhanced the tendency for AMP aggregation-driven pore formation. In contrast, the mechanism distribution in “R-E” did not significantly deviate from the reference “R-B”, indicating that the removal of TREH, or conversely the inclusion of Ca^{2+} and HPO_4^{2-}, had less impact on the preferred pathway of pore formation.

In addition to the mechanisms described above, mechanisms 3 and 4 were also observed in the “R” condition, albeit infrequently. In all cases, AMPs were located near the pore formation site as single peptides or in proximity to an AMP aggregate, though their involvement was less evident than in mechanisms 1 or 2. While these peptides did not seem to directly drive pore formation, their spatial proximity suggested a possible facilitative role, for example by locally weakening the membrane.

4.4.2.3 Effects of AMP charge

As shown in **Figure 4.8**, pore formation occurred significantly less frequently (as tested by Fisher’s exact test) in the “T” simulations, which used the WT magainin variant with an un-amidated C-terminus and thus a reduced net charge (+3 *e* instead of +4 *e*), compared to the otherwise identical “R” simulations. This supported the notion that peptide charge was critical for effective electric field-enabled insertion in my systems, and aligned with experimental findings reporting that C-terminal amidation enhances antimicrobial potency, with the amidated form of magainin displaying a twofold lower MIC_{100} than its carboxylated counterpart (5.2 ± 1.0 μM and 12 ± 2 μM respectively).[32]

Interestingly, mechanisms 1 and 2 occurred with equal frequency in “T”, whereas mechanism 1 dominated in SR. This suggested that the additional positive charge on

the standard magainin used in “R” may have enhanced mechanism 1 by promoting monomeric peptide insertion, while simultaneously increasing electrostatic repulsion between peptides, thus reducing AMP aggregation and lowering the probability of mechanism 2. Notably, mechanism 4 (single AMP-mediated pore formation without LacY snorkelling) was observed once in “T-B”, accounting for 33% of the observed pores. This went against the intuition that the more highly charged AMP in “R” could have favoured this mechanism due to stronger electric drive across the membrane. However, the low number of pore formation events in “T” urged cautious interpretation of the above.

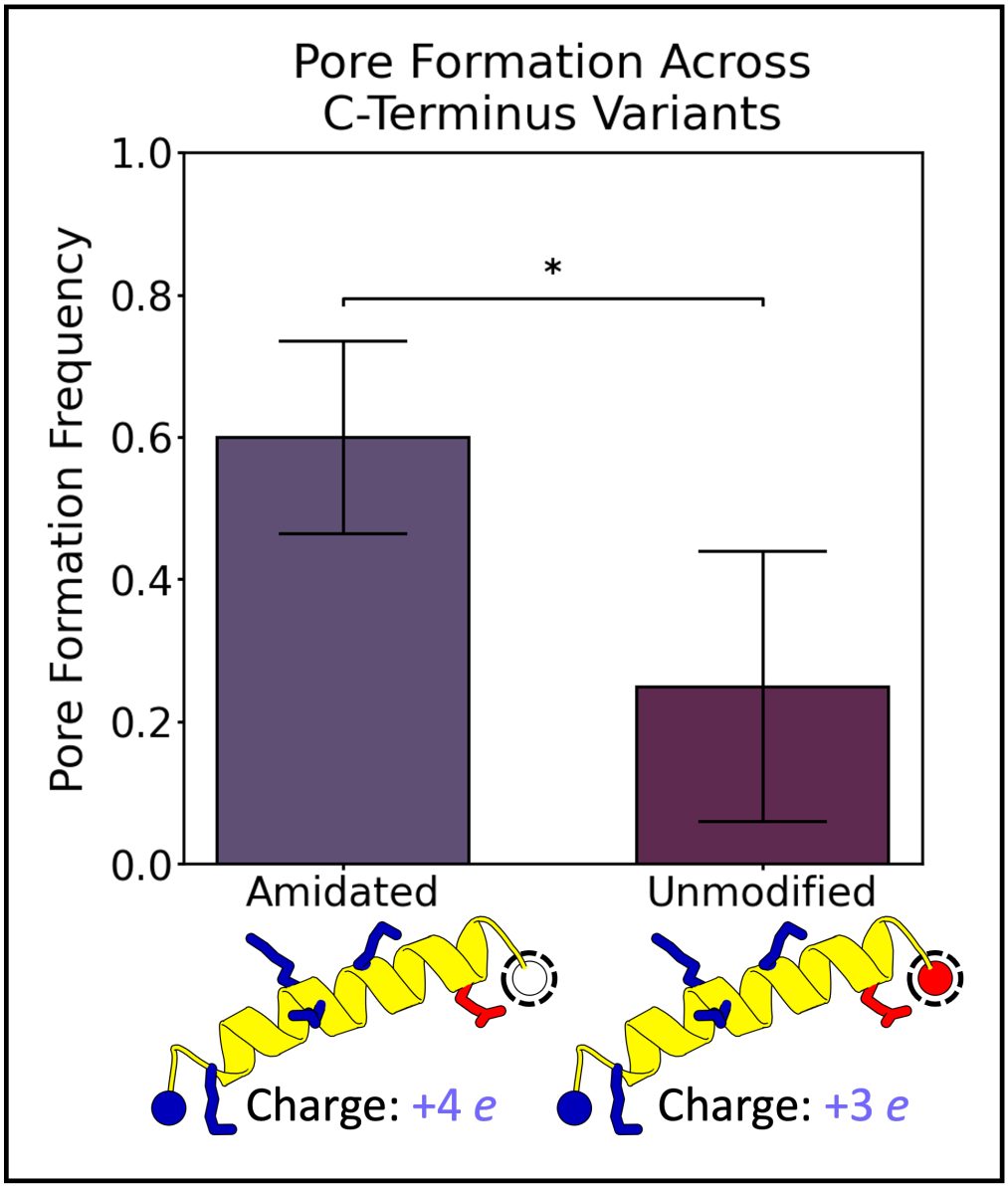

Figure 4.8. *Effect of peptide charge on pore formation frequency. Bar plot showing the average number of pores observed per simulation for standard magainin (net charge +4, averaged over "R-B/C" simulations) and a charge-reduced variant (net charge +3, averaged over "T-B/C" simulations). Error bars represent the 95% confidence interval; statistical significance ($p < 0.05$) was determined by Fisher's exact test. Schematic representations of the two peptide variants are shown below, with charged residues highlighted: blue = basic, red = acidic, and C-terminus as white (neutral) or red (acidic).*

4.4.2.4 Effects of membrane composition

Under the “M” condition, which used a fully saturated membrane composition (DPPE:DPPG, 80:20), no pores formed in the absence of AMPs. This reinforced the notion that AMPs were essential to pore formation in my systems. In simulations with AMPs but no osmolytes, mechanism 3 (LacY-centred pores without AMP involvement) was the most frequent, followed by mechanisms 1 and 4. In the presence of osmolytes, mechanism 1 was the predominant mode of pore formation, although mechanism 3 occurred with comparable frequency.

As shown in **Figure 4.9**, pores formed at a higher rate in saturated membranes than in the unsaturated POPE:POPG membranes used in the “R” condition, although this difference was not statistically significant (odds ratio = 2.00, Fisher’s exact test $p > 0.05$). This precluded definitive conclusions, particularly as the increased rigidity of saturated bilayers is typically associated with higher energy barriers for pore nucleation in the context of electroporation.[33]

Furthermore, the nature of AMP involvement in pore formation differed markedly between membrane types. AMPs were visibly involved in 28 out of 30 pore formation events in “R” simulations, compared to 9 out of 15 in “M” simulations, a difference that was statistically significant according to the Fisher-Irwin test ($p < 0.01$). Taken together with the complete absence of pores in AMP-free simulations, this suggested that AMPs may exert more subtle, less directly observable effects on membrane destabilisation in saturated systems. These may include perturbations that facilitate membrane defects without clear structural AMP involvement at the time of pore formation.

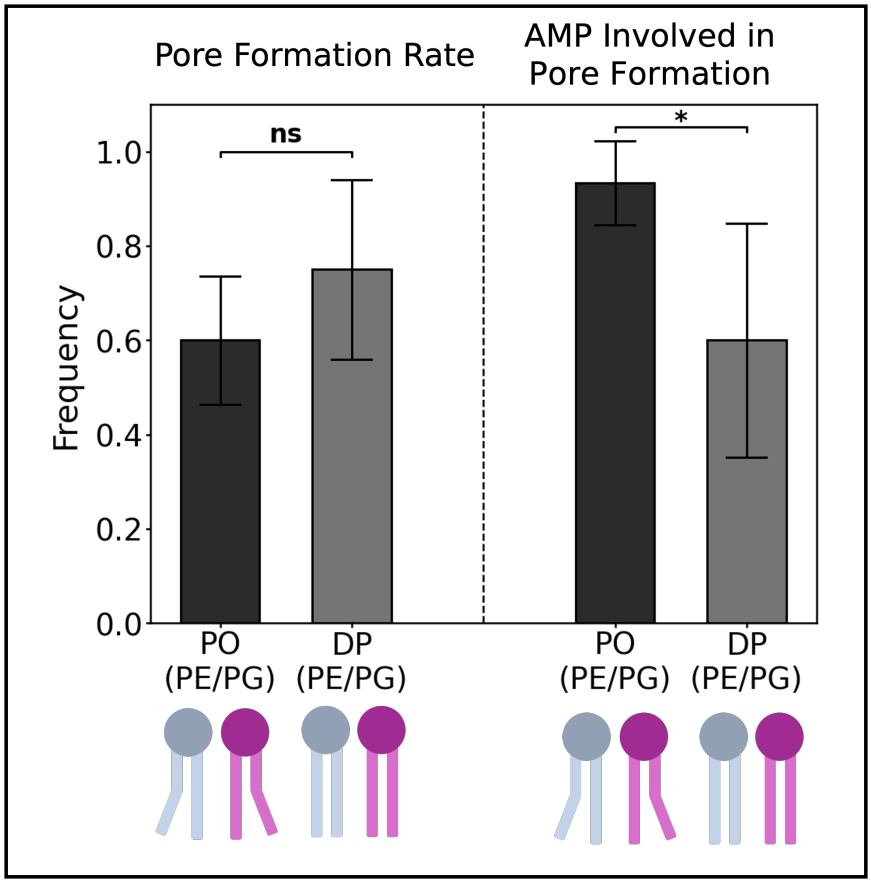

Figure 4.9. *Comparison of pore formation between unsaturated "R" and fully saturated "M" membrane simulations. Left: average pore formation frequency across AMP-containing simulations ("R-B/C" vs. "M-B/C"). Right: fraction of pores involving AMPs as active participants in the pore formation process. Error bars indicate the 95% confidence interval. Schematics below represent membrane lipid composition (POPE/DPPE: grey, POPG/DPPG: purple; 80:20 PE:PG for both).*

4.5 Conclusion

This chapter used computational electrophysiology simulations to investigate how different system factors influence pore formation by magainin 2 in bacterial inner membranes. Both the inclusion of AMPs and the application of an electric field were found to be necessary to induce membrane poration under my simulation conditions.

Four distinct mechanisms of pore formation were identified, with their relative probabilities of occurring depending on AMP charge, membrane composition, and the presence of osmolytes. Osmolytes tended to shift pore formation towards pathways involving AMP aggregation; saturated membranes showed a trend of higher pore formation rates, and less charged peptides led to significantly fewer pore formation events. These results provide a framework for the more detailed analyses of pore formation mechanisms and AMP behaviour in the following chapters.

References

1. Matsuzaki, K., Sugishita, K., Harada, M., Fujii, N. & Miyajima, K. Interactions of an antimicrobial peptide, magainin 2, with outer and inner membranes of Gram-negative bacteria. *Biochim. Biophys. Acta BBA - Biomembr.* **1327**, 119–130 (1997).
2. Hancock, R. E. Alterations in outer membrane permeability. *Annu. Rev. Microbiol.* **38**, 237–264 (1984).
3. Ding, L. *et al.* Interaction of Antimicrobial Peptides with Lipopolysaccharides. *Biochemistry* **42**, 12251–12259 (2003).
4. Haukland, H. h., Ulvatne, H., Sandvik, K. & Vorland, L. h. The antimicrobial peptides lactoferricin B and magainin 2 cross over the bacterial cytoplasmic membrane and reside in the cytoplasm. *FEBS Lett.* **508**, 389–393 (2001).
5. Gregory, S. M., Pokorny, A. & Almeida, P. F. F. Magainin 2 Revisited: A Test of the Quantitative Model for the All-or-None Permeabilization of Phospholipid Vesicles. *Biophys. J.* **96**, 116–131 (2009).
6. Imura, Y., Choda, N. & Matsuzaki, K. Magainin 2 in Action: Distinct Modes of Membrane Permeabilization in Living Bacterial and Mammalian Cells. *Biophys. J.* **95**, 5757–5765 (2008).
7. Ludtke, S. J. *et al.* Membrane pores induced by magainin. *Biochemistry* **35**, 13723–13728 (1996).
8. Tachi, T., Epand, R. F., Epand, R. M. & Matsuzaki, K. Position-Dependent Hydrophobicity of the Antimicrobial Magainin Peptide Affects the Mode of Peptide−Lipid Interactions and Selective Toxicity. *Biochemistry* **41**, 10723–10731 (2002).

9. Leontiadou, H., Mark, A. E. & Marrink, S. J. Antimicrobial Peptides in Action. *J. Am. Chem. Soc.* **128**, 12156–12161 (2006).
10. Pedebos, C., Smith, I. P. S., Boags, A. & Khalid, S. The hitchhiker's guide to the periplasm: Unexpected molecular interactions of polymyxin B1 in E. coli. *Structure* **29**, 444-456.e2 (2021).
11. Computational Electrophysiology: The Molecular Dynamics of Ion Channel Permeation and Selectivity in Atomistic Detail: Biophysical Journal. https://www.cell.com/biophysj/fulltext/S0006-3495(11)00706-5.
12. Kutzner, C. *et al.* Insights into the function of ion channels by computational electrophysiology simulations. *Biochim. Biophys. Acta BBA - Biomembr.* **1858**, 1741–1752 (2016).
13. Weerakoon, D., Marzinek, J. K., Pedebos, C., Bond, P. J. & Khalid, S. Polymyxin B1 in the *Escherichia coli* inner membrane: A complex story of protein and lipopolysaccharide-mediated insertion. *J. Biol. Chem.* **300**, 107754 (2024).
14. Wang, M. *et al.* PaxDb, a Database of Protein Abundance Averages Across All Three Domains of Life*. *Mol. Cell. Proteomics* **11**, 492–500 (2012).
15. Huang, Q., Szklarczyk, D., Wang, M., Simonovic, M. & von Mering, C. PaxDb 5.0: Curated Protein Quantification Data Suggests Adaptive Proteome Changes in Yeasts. *Mol. Cell. Proteomics* **22**, 100640 (2023).
16. Madej, M. G. Function, Structure, and Evolution of the Major Facilitator Superfamily: The LacY Manifesto. *Adv. Biol.* **2014**, 523591 (2014).
17. Holyoake, J. & Sansom, M. S. P. Conformational Change in an MFS Protein: MD Simulations of LacY. *Structure* **15**, 873–884 (2007).

18. Stelzl, L. S., Fowler, P. W., Sansom, M. S. P. & Beckstein, O. Flexible Gates Generate Occluded Intermediates in the Transport Cycle of LacY. *J. Mol. Biol.* **426**, 735–751 (2014).
19. Abramson, J. *et al.* Structure and Mechanism of the Lactose Permease of Escherichia coli. *Science* **301**, 610–615 (2003).
20. Kaback, H. R. Structure and mechanism of the lactose permease. *C. R. Biol.* **328**, 557–567 (2005).
21. Mirza, O., Guan, L., Verner, G., Iwata, S. & Kaback, H. R. Structural evidence for induced fit and a mechanism for sugar/H+ symport in LacY. *EMBO J.* **25**, 1177–1183 (2006).
22. Gesell, J., Zasloff, M. & Opella, S. J. Two-dimensional 1H NMR experiments show that the 23-residue magainin antibiotic peptide is an α-helix in dodecylphosphocholine micelles, sodium dodecylsulfate micelles, and trifluoroethanol/water solution. *J. Biomol. NMR* **9**, 127–135 (1997).
23. Kroon, P. C. *et al.* Martinize2 and Vermouth: Unified Framework for Topology Generation. *eLife* **12**, (2023).
24. Gesell, J., Zasloff, M. & Opella, S. J. Two-dimensional 1H NMR experiments show that the 23-residue magainin antibiotic peptide is an alpha-helix in dodecylphosphocholine micelles, sodium dodecylsulfate micelles, and trifluoroethanol/water solution. *J. Biomol. NMR* **9**, 127–135 (1997).
25. Chaptal, V. *et al.* Crystal structure of lactose permease in complex with an affinity inactivator yields unique insight into sugar recognition. *Proc. Natl. Acad. Sci.* **108**, 9361–9366 (2011).
26. Grytsyk, N., Sugihara, J., Kaback, H. R. & Hellwig, P. pKa of Glu325 in LacY. *Proc. Natl. Acad. Sci.* **114**, 1530–1535 (2017).

27. Periole, X., Cavalli, M., Marrink, S.-J. & Ceruso, M. A. Combining an elastic network with a coarse-grained molecular force field: structure, dynamics, and intermolecular recognition. *J. Chem. Theory Comput.* **5**, 2531–2543 (2009).
28. De Jong, D. H. *et al.* Improved parameters for the martini coarse-grained protein force field. *J. Chem. Theory Comput.* **9**, 687–697 (2013).
29. PyCGTOOL: Automated Generation of Coarse-Grained Molecular Dynamics Models from Atomistic Trajectories | Journal of Chemical Information and Modeling. https://pubs.acs.org/doi/full/10.1021/acs.jcim.7b00096#.
30. Periole, X. & Marrink, S.-J. The Martini coarse-grained force field. *Biomol. Simul. Methods Protoc.* 533–565 (2012).
31. Qi, Y. *et al.* CHARMM-GUI martini maker for coarse-grained simulations with the martini force field. *J. Chem. Theory Comput.* **11**, 4486–4494 (2015).
32. Aisenbrey, C., Amaro, M., Pospíšil, P., Hof, M. & Bechinger, B. Highly synergistic antimicrobial activity of magainin 2 and PGLa peptides is rooted in the formation of supramolecular complexes with lipids. *Sci. Rep.* **10**, 11652 (2020).
33. Polak, A. *et al.* On the Electroporation Thresholds of Lipid Bilayers: Molecular Dynamics Simulation Investigations. *J. Membr. Biol.* **246**, 843–850 (2013).

Chapter 5

Computational Electrophysiology simulations: osmolyte effects on AMP interactions in membrane protein-independent pore formation

5.1 Introduction

Most antimicrobial peptides (AMPs) exert their bactericidal activity primarily through interactions with bacterial membranes, compromising their integrity and leading to cell death.[1] Classical AMP mechanisms of action include barrel-stave, toroidal pore, and carpet models, as schematically represented in **Figure 5.1**.[1] In the barrel-stave model, AMPs insert perpendicularly into the membrane, forming well-defined pores resembling barrels lined with peptides.[1] In contrast, the toroidal pore mechanism involves peptides intercalating into lipid headgroups, causing lipids to bend continuously from the outer to the inner leaflet, creating pores lined by AMPs and lipids.[1] The carpet mechanism is characterised by peptides accumulating on the membrane surface, destabilising the membrane and inducing disintegration without discrete pore formation.

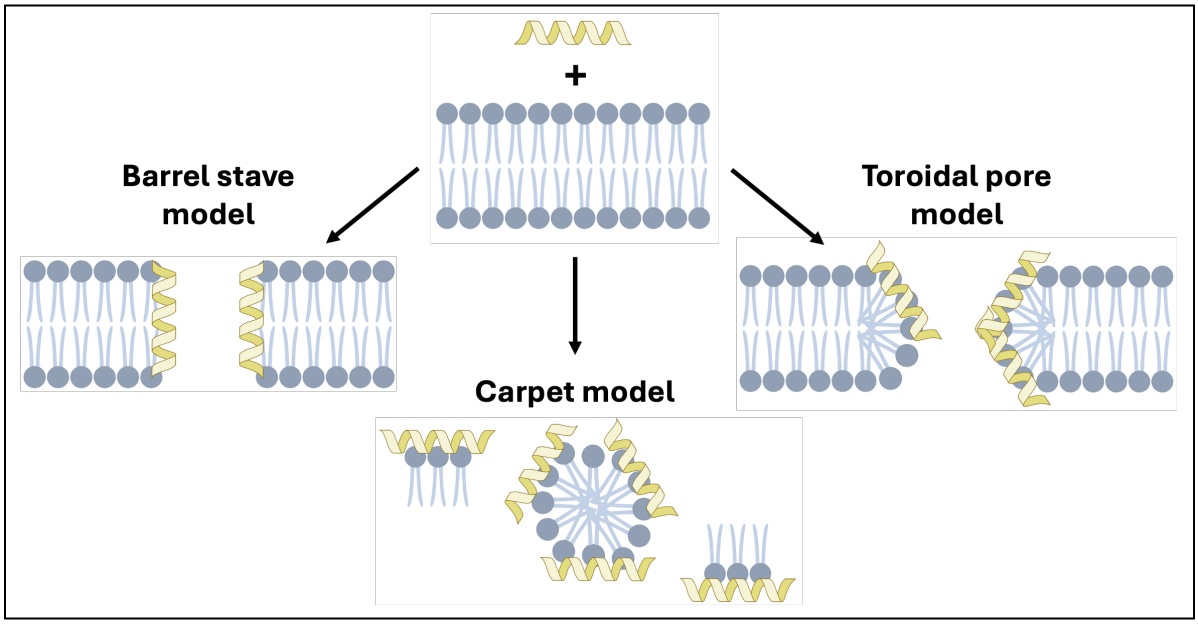

Figure 5.1. *Schematic overview of classical antimicrobial peptide mechanisms of membrane disruption. Top centre: Initial interaction of AMPs (yellow helices) with the membrane surface (grey). Left: barrel-stave model; right: toroidal pore model; bottom: carpet model.*

Complementing these AMP-driven membrane-disrupting mechanisms, classical electroporation theory describes how externally applied electric fields can induce transient membrane permeabilisation.[2,3] The process begins with the formation of a local defect in the membrane, where a small number of lipid headgroups protrude toward the bilayer centre.[3] This defect promotes the entry of polarisable water molecules into the hydrophobic core, stabilised by interactions with the displaced headgroups, with a single-file water channel, or “water file”, subsequently spanning the membrane.[3] This is followed by further lipid reorganisation, with headgroups migrating inward to stabilise the water-filled defect, ultimately forming a hydrophilic pore.[3] These “electropores” are typically short-lived and reversible, with their stability influenced by membrane composition, electric field strength, and local curvature.[4,5]

Electroporation is widely utilised in biotechnology, particularly for the delivery of DNA and other cargo into cells during genetic transformation.[6]

5.2 Aims

This chapter aims to investigate how periplasmic osmolytes influence the permeation of the antimicrobial peptide magainin 2 across the *E. coli* inner membrane under an induced electric field, with a focus on the two membrane protein-independent pore formation mechanisms, described in **Chapter 4**, mechanisms 2 and 4, as schematically represented in **Figure 5.2**. This electric field mimics the natural, inside-negative membrane potential of the Gram-negative inner membrane, which is induced by the proton motive force comprising both an electrical potential difference ($\Delta\psi$) and a transmembrane pH gradient (ΔpH).[7–9]

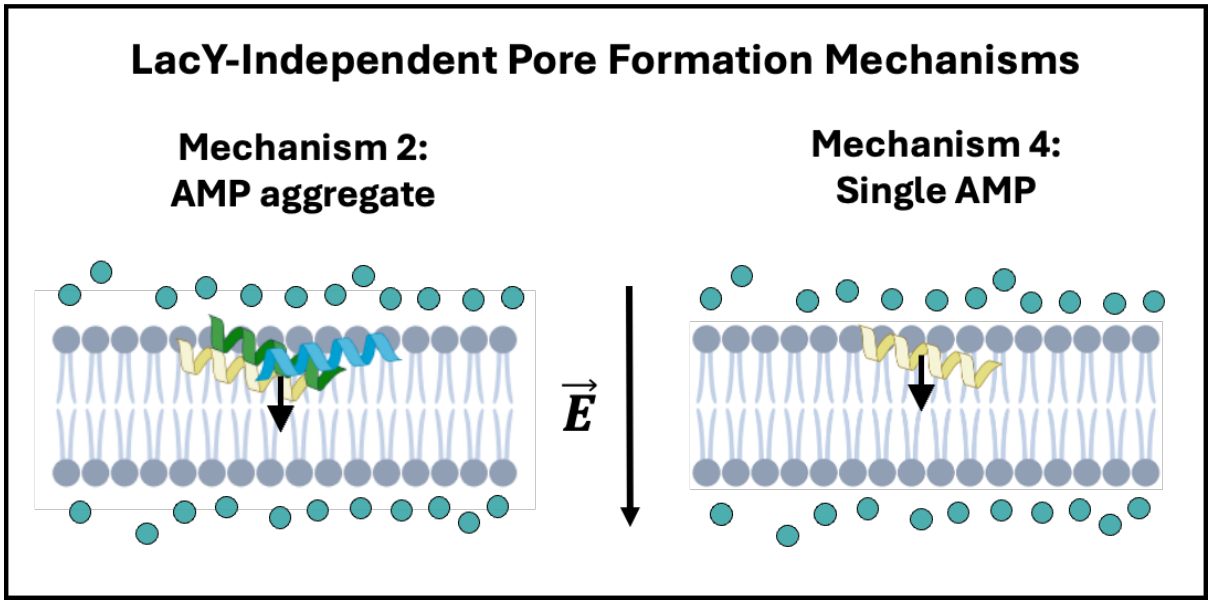

Figure 5.2. *Schematic representation of the two LacY-independent pore formation mechanisms of magainin 2 observed in my computational electrophysiology (CompEL) simulations in order of decreasing observation frequency: mechanisms 2 and 4.*

5.3 Methods

The simulation methods used in this chapter were identical to those described in **Chapter 4**. The system preparation, simulation protocols, and analysis methods followed the same procedures in full.

5.4 Results and discussion

5.4.1 Mechanism characterisation

The following subsections will initially focus on qualitative characterisation of the two membrane protein-independent pore formation mechanisms observed in my simulations.

5.4.1.1 Mechanism 2: AMP aggregate breaking through the bulk membrane

In mechanism 2, pores formed through the cooperative action of AMP aggregates that penetrated and destabilised the bilayer. This induced local membrane thinning, enabling water to enter the hydrophobic core deeply and ultimately leading to the formation of transient, water-filled pores, as shown in **Figure 5.3**.

This pore formation sequence began with AMP aggregates partially inserted into the periplasmic leaflet, with no water present in the deep bilayer interior. Water molecules would then infiltrate the membrane bilayer, while neighbouring lipids started to reorient horizontally to accommodate the expanding water column and expose their headgroups towards the intruding water. As this progressed, several lipids would adopt fully horizontal orientations, further stabilising the developing channel. The AMP aggregates subsequently spanned both leaflets, and a continuous water column formed across the bilayer. This finding is consistent with

continuous water column formed across the bilayer. This finding is consistent with the toroidal pore model, in which peptides and tilted lipid headgroups line the hydrophilic pore interior. Once initiated, this process led to irreversible pore formation, consistent with the all-or-none permeabilisation behaviour described for magainin 2.[10]

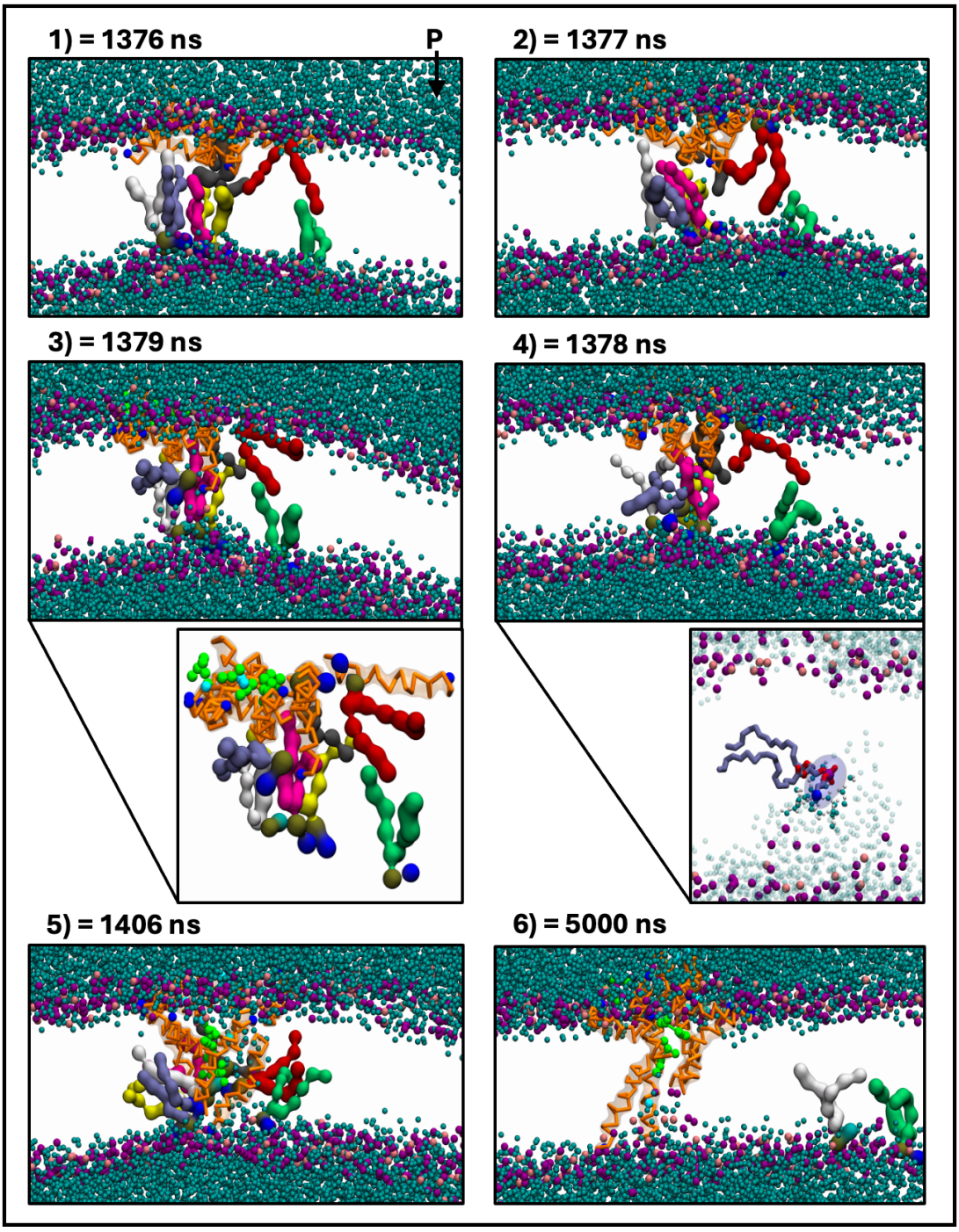

Figure 5.3. *Molecular images ("R-C" simulation) which show examples of the membrane pore formation via mechanism 2, an AMP aggregate-induced pore formation. Water is shown as cyan beads, and is highlighted by circles in 2). Peptides are depicted as orange backbones with overlaid surface, and N-termini as blue beads. Lipid headgroups are shown as grey (POPE) and purple (POPG) beads. Selected lipids directly involved in pore formation are highlighted with coloured*

surfaces and headgroups: phosphate groups in blue, PE in brown, and PG in light blue. The inset in 3) highlights the AMP aggregate together with selected lipids and solutes (trehalose in green, phosphate ions in cyan). The inset in 4) shows an atomistic backmapping of a lipid in a horizontal orientation, with nearby waters (≤ 6 Å) shown in solid cyan.

Overall, this sequence of events aligned with classical electroporation theory.[2,3] In the classical model, pore formation begins with the intrusion of water molecules into the hydrophobic core, forming “water fingers” that are subsequently stabilised by the reorientation of lipid headgroups, leading to the formation of a conductive, hydrophilic pore.[2,3]

The observed final states with membrane-inserted AMPs were long-lived: at the end of the simulation, the water columns had dissipated, but the peptide aggregates maintained a transmembrane arrangement that remained stable and persisted after removal of the electric field. This suggested the ability of such peptide aggregates to form metastable transmembrane states.

Stabilising interactions between peptide sidechains and periplasmic species could be observed in these states, including contacts between asparagine residues and trehalose, and between lysines and phosphate ions, as shown in **Figure 5.4**.

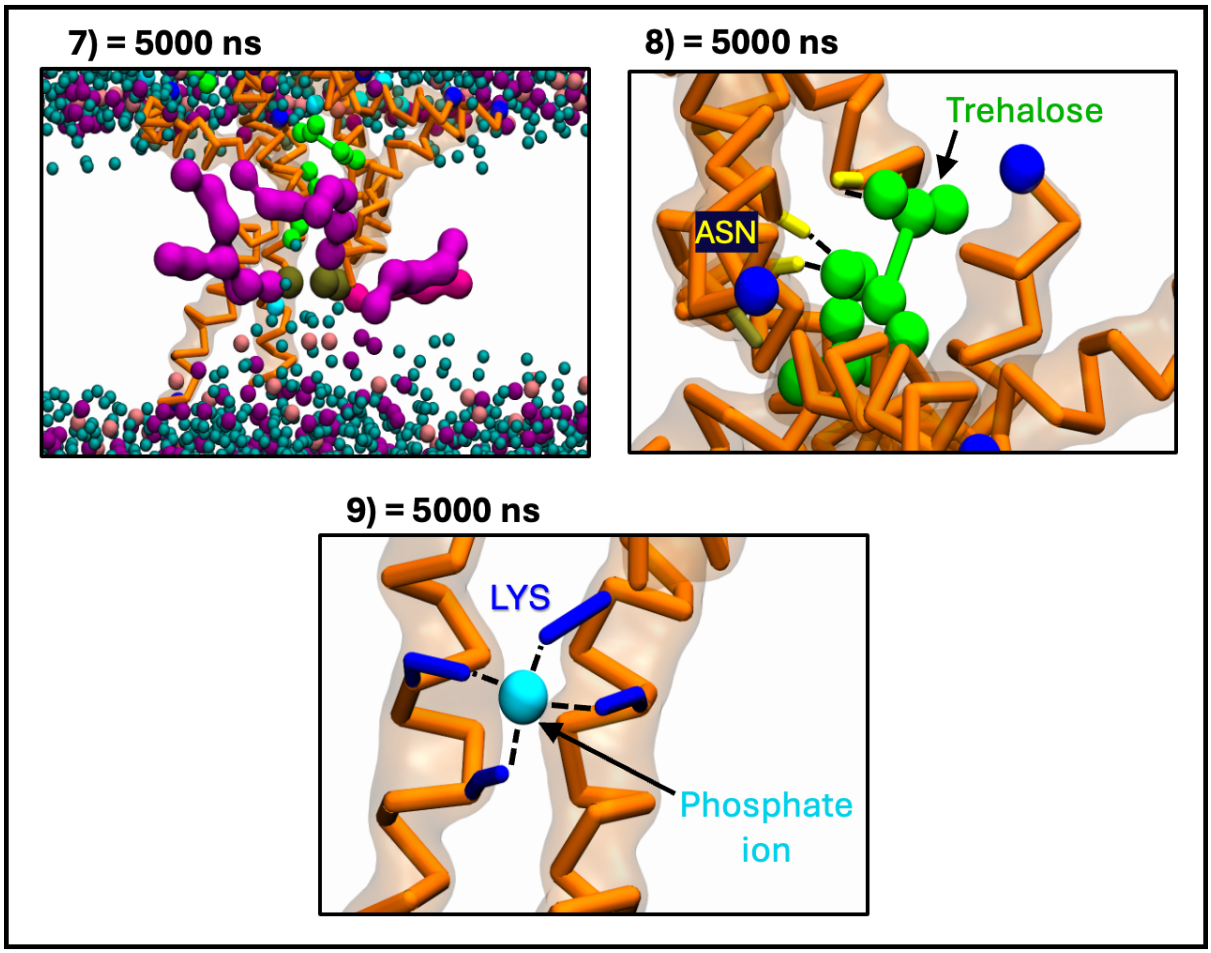

Figure 5.4. *Continuation of* ***Figure 5.3****, showing the final simulation state at 5 μs with the AMP aggregate spanning the bilayer and the stabilised pore structures. 7) highlights lipids in horizontal orientations. 8) and 9) show stabilising interactions between AMP sidechains (backbone in orange with transparent surface overlay, C-termini as blue beads) and periplasmic solutes. Asparagine residues are shown in yellow, trehalose in green, lysine residues in dark blue, and phosphate ions in cyan.*

Furthermore, directional lipid redistribution was observed during pore formation: negatively charged POPG lipids exhibited a net movement toward the positively charged inner compartment, while POPE lipids underwent compensatory flipping in the opposite direction, as shown in **Figure 5.5**. This asymmetry indicates charge balancing through the redistribution of lipids between leaflets, a phenomenon

explored further in a subsequent subchapter. Previous studies have shown that AMPs, and magainin 2 in particular, can enhance the rate of lipid flip-flop *in vitro*.[11]

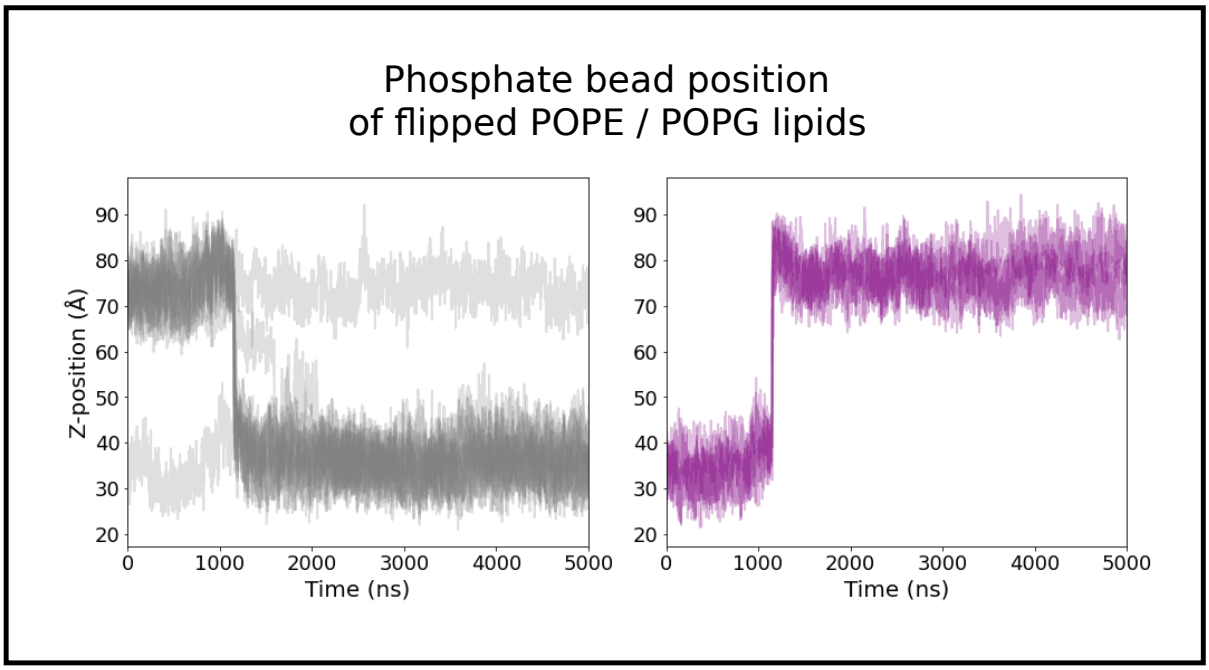

Figure 5.5. *Lipid redistribution during pore formation via mechanism 2, showing the same simulation as in* ***Figure 5.3*** *and* ***Figure 5.4****. The plot shows the Z-positions of phosphate beads from lipids that underwent leaflet exchange, as identified using the MDA LeafletFinder algorithm, with POPE in grey (left) and POPG in purple (right).*[12] *The periplasmic-facing leaflet corresponds to the higher positive Z values.*

Pores formed by mechanism 2 arose from AMP aggregates in both areas close to and distant from LacY, confirming that the aggregates themselves were sufficient to destabilise the membrane. To quantify the effect of AMP aggregates on membrane structure, local membrane thickness was computed by interpolating a thin-plate spline surface through the phosphate headgroups of each leaflet. The resulting thickness maps showed membrane deformations caused by AMP aggregates in both "R-B" and "R-C" conditions, as shown in **Figure 5.6**. This thinning effect reached deformations of up to 8 Å below the membrane average of 40 Å and was observed in

multiple simulations as early as 10-50 ns before pore formation.

This membrane thinning aligned with previous experimental findings showing that magainin actively reduces membrane thickness, supporting the notion that AMP aggregates destabilise the bilayer and create conditions conducive to pore formation.[13,14]

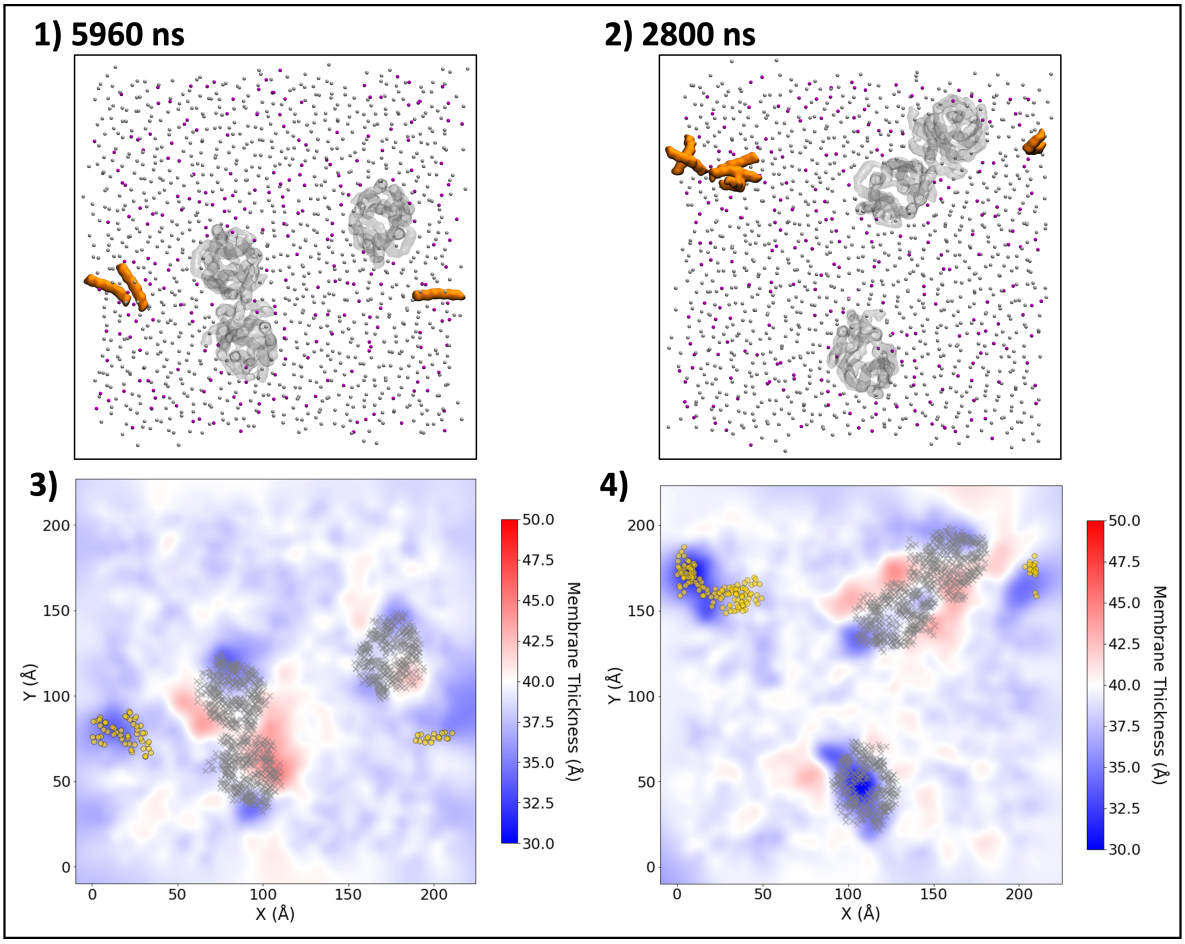

Figure 5.6. *Representative examples of AMP aggregate positioning prior to mechanism 2 pore formation. 1-2) Molecular images (left: "R-B", right: "R-C") showing examples of AMP aggregate positions 10 ns before a pore formed below them via mechanism 2. AMP aggregates are represented as orange surfaces, LacY shown as grey transparent surfaces. 3-4) Heatmaps corresponding to 1-2), showing local membrane thickness averaged over the 10 ns before pore formation. AMP*

backbone beads as orange circles, LacY backbone beads as grey crosses. Blue areas show membrane thinning, red areas show membrane thickening.

5.4.1.2 Mechanism 4: single AMP breaking through the bulk membrane

Pores formed *via* mechanism 4 resulted from the membrane rupturing beneath a single membrane-inserted AMP, independently of aggregation with other peptides, and occurred in regions far from LacY membrane proteins. As in mechanism 2, the process involved AMP-facilitated water infiltration into the bilayer core and progressive lipid headgroup reorientation, as shown in **Figure 5.7**.

Mechanism 4 occurred the least frequently compared to other mechanisms, suggesting that it may arise from low-probability, stochastic events such as specific insertion geometries, transient favourable peptide-lipid interactions, or local amplification of the electric field.

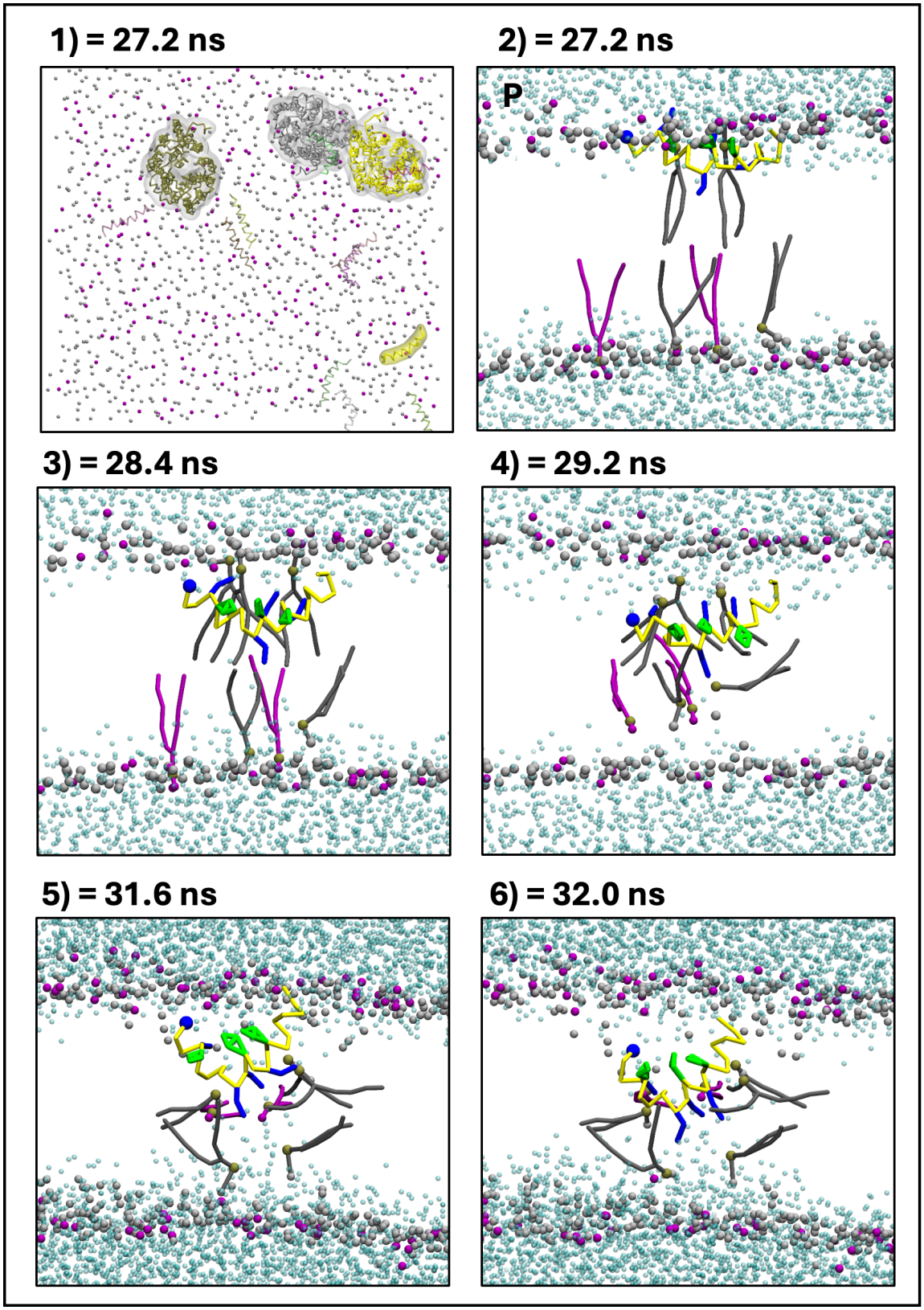

Figure 5.7. *Molecular images ("R-B" simulation) which show examples of membrane pore formation via mechanism 4: a single AMP-induced bulk membrane rupture. 1) shows a top-down view with AMPs shown as opaque backbones and LacY proteins*

as transparent backbones, both coloured by chain. The AMP implicated in the membrane rupture as well as LacY proteins are highlighted with a transparent surface representation to highlight their distance. Lipid headgroups are shown as grey (POPE) and purple (POPG) beads. 2)-6) show side views of the pore formation process. Water molecules are shown as cyan beads. Selected lipid tails are shown as sticks and coloured according to lipid type (POPE in grey, POPG in purple). Selected AMP side chains are shown in stick representation (lysine: blue, phenylalanine: green).

5.4.2 Osmolyte effects on AMP-membrane interactions

After observing the membrane-thinning effect of M2 on the bulk membrane, I investigated how osmolytes could influence the localisation of AMPs in the periplasmic compartment with respect to the bulk membrane and membrane proteins.

All solute species appeared to penetrate the membrane headgroup region to some extent, with AMPs, calcium, and trehalose showing particularly deep penetration, as shown in **Figure 5.8**. This was consistent with their chemical properties (amphipathic, doubly positively charged, and polar nature, respectively) and the overall negative charge of the membrane. AMP penetration into the membrane itself appeared broadly similar between the two osmotic conditions. However, in the “R-C” simulations, AMPs appeared to be more spatially displaced from the membrane surface and localised further into the periplasmic space compared to the osmolyte-free simulations “R-B”.

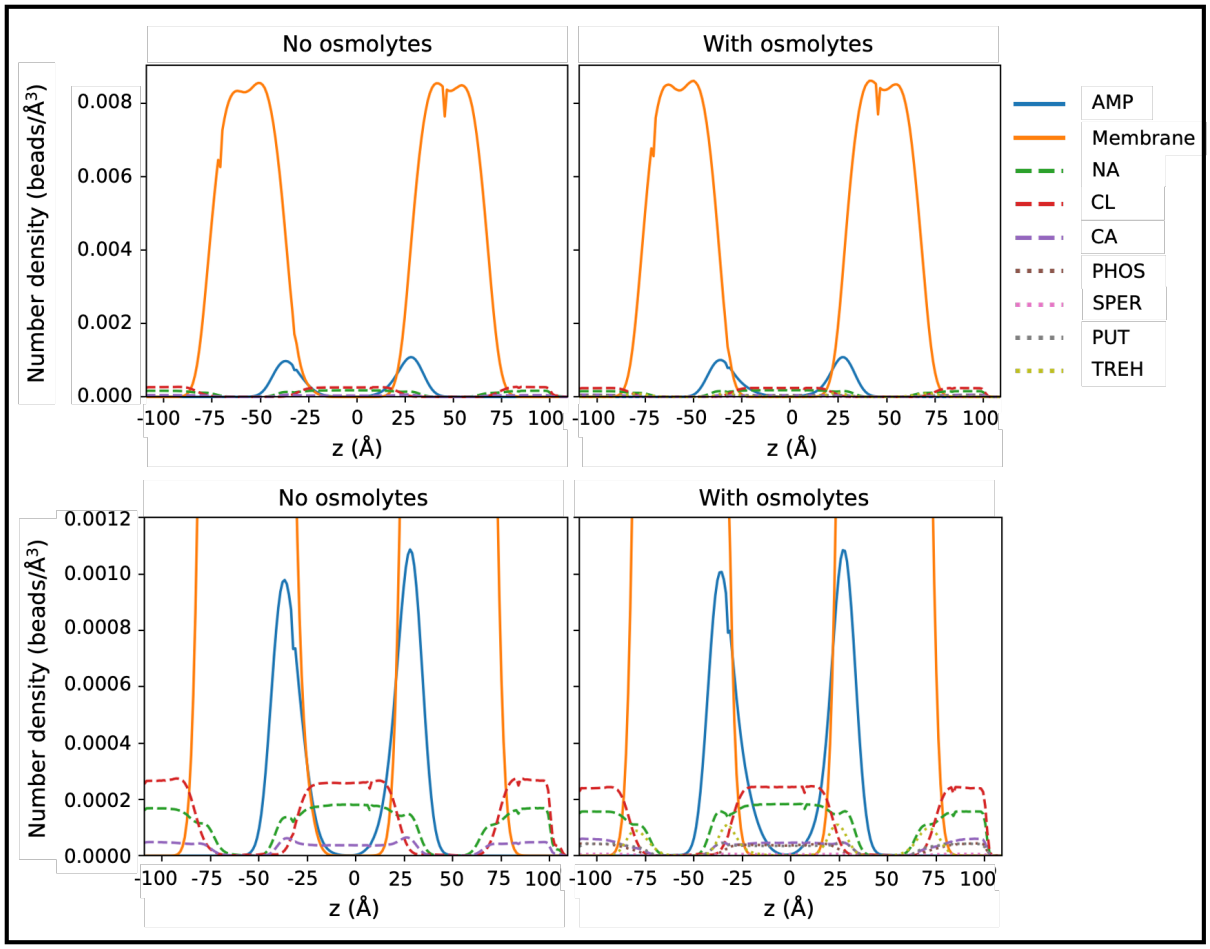

Figure 5.8. *Number density profiles averaged over all "R-B" and "R-C" simulations. Top row: full system profiles; bottom row: zoomed-in representation of the top row.*

To quantify AMP interactions with LacY and the membrane, I computed the proportion of AMPs in contact with each throughout the simulations, as shown in **Figure 5.9**. Notably, the "neither" category, as defined here, included both truly unbound AMPs in solution as well as those at the top of AMP-LacY or AMP-AMP aggregates that therefore did not make direct contact with LacY or the membrane. Visual inspection confirmed that the latter was the predominant case, with most AMPs reaching LacY or the membrane indirectly *via* other AMPs.

Welch's t-tests indicated that the mean values for all contact categories differed significantly between conditions ($p < 0.001$). The "membrane only" population was the only one more prevalent in the “R-B” simulations, while all others ("neither", "LacY only", and "LacY and membrane") were more prominent under osmolyte-containing conditions. Corresponding Cohen's d values ranged from 0.27 to 0.58, indicating small-to-moderate effects, and highlighting a meaningful influence of osmolytes on AMP-LacY and AMP-membrane interactions. These findings reinforced my earlier observations on the role of osmolytes in modulating AMP-AMP interactions and aggregation dynamics.

The temporal evolution of contact distributions further supported the effect of osmolytes on AMP-membrane interactions: “R-C” simulations showed consistently higher average values for the "neither", "LacY only", and "LacY and membrane" categories, while the number of direct AMP-membrane interactions diminished, as shown in **Figure 5.9**. This supported the visual observation of progressive AMP aggregation around LacY, now additionally stabilised under osmotic conditions, as further discussed in **Chapter 6**.

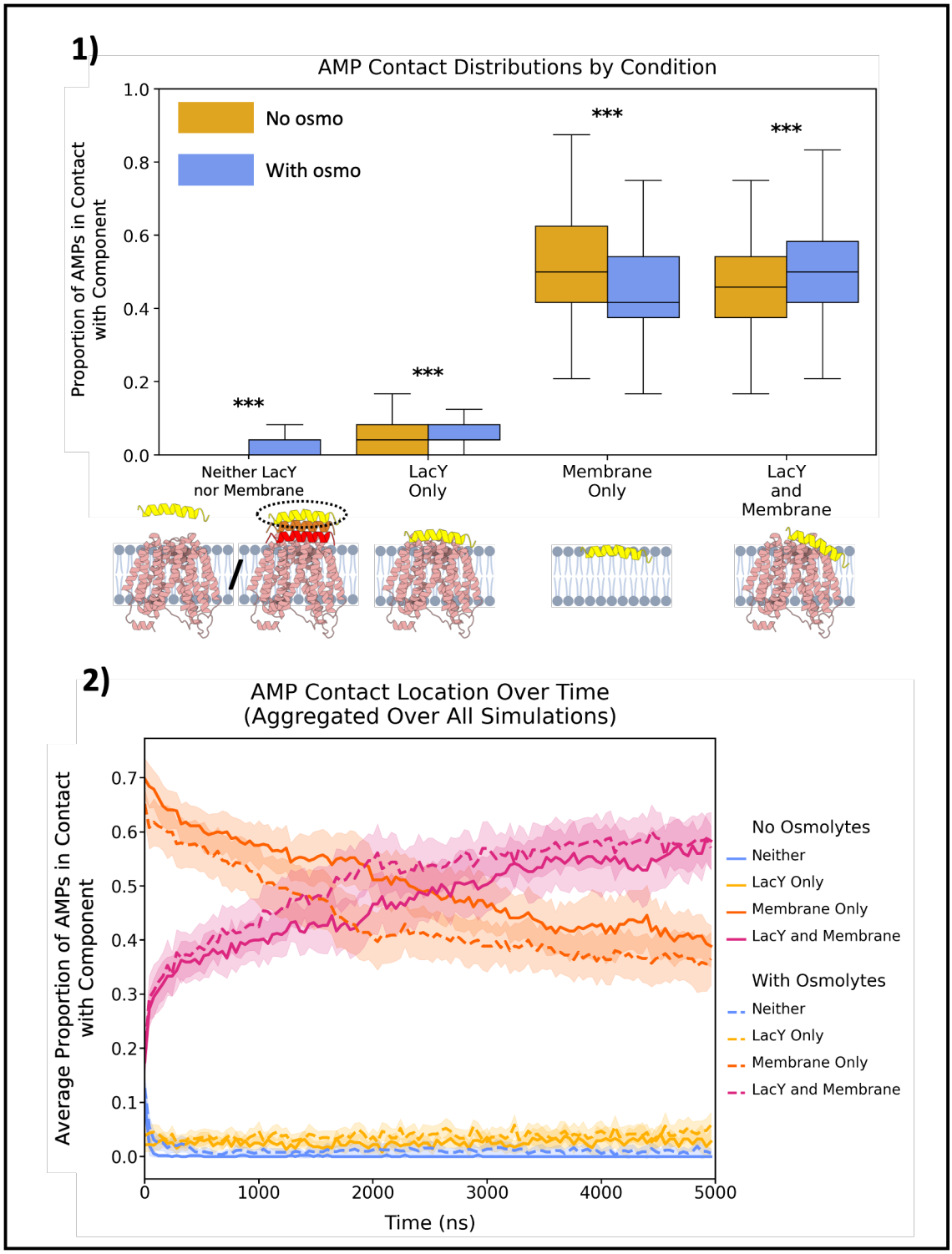

Figure 5.9. *AMP contact preferences with membrane and LacY in osmolyte-free versus osmolyte-containing conditions. 1) Per-frame proportion of AMPs contacting the membrane, LacY, both, or neither, averaged over all "R-B" and "R-C" simulations (6 Å cutoff). 2) Temporal evolution of the average AMP contact distribution,*

aggregated over all simulations. Lines represent the mean proportion of AMPs in each contact category per frame, with shaded areas indicating 95% confidence intervals.

A likely explanation for the diminished "membrane only" contacts was that charged osmolytes, such as spermidine and putrescine, competed with AMPs for access to anionic lipid headgroups, consistent with the electrical double layer theory, thereby weakening AMP-membrane association and favouring aggregation with LacY or other AMPs instead.[15,16] To better understand this osmolyte-correlated reduction in AMP-membrane association, I quantified contacts between AMPs and lipids, as shown in **Figure 5.10**.

In simulations containing osmolytes, AMP chains formed significantly fewer contacts with lipid headgroups ($p < 0.001$), as well as fewer overall lipid contacts ($p < 0.05$), while interactions with lipid tails were not significantly affected. Cohen's d values indicated a large effect for headgroup contacts ($d = 1.5$) and moderate effects for overall and tail contacts ($d = 0.6$ and $d = 0.4$, respectively), supporting the notion that osmolytes primarily interfered with AMP interactions at the membrane surface. This was consistent with the idea that charged osmolytes, such as spermidine and putrescine, could compete with AMPs for access to negatively charged lipid headgroups, effectively impeding AMP interactions with the membrane surface. This notion helped explain the reduced number of "membrane only" contact classifications and the increased aggregation around LacY observed under osmotic conditions, as AMP-membrane interactions became less favourable and were increasingly substituted by AMP-AMP or AMP-LacY contacts.

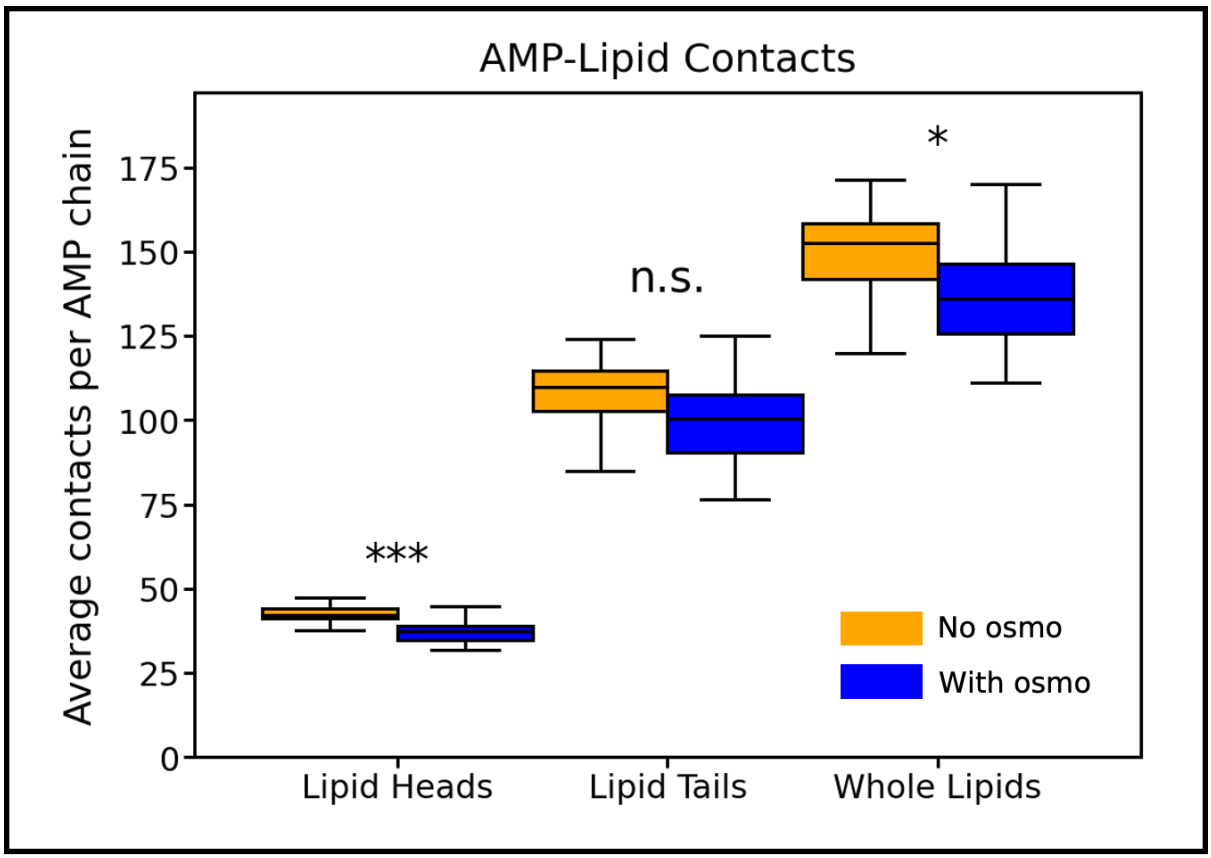

Figure 5.10. *Average number of contacts per AMP chain with lipid headgroups, lipid tails, and whole lipids, computed across all "R-B" and "R-C" simulations (6 Å cutoff). Boxplots show distributions over all AMP chains, coloured by condition (orange: no osmolytes, blue: with osmolytes). Asterisks denote statistical significance of pairwise comparisons using Welch's t-test: *** ≡ $p < 0.001$, * ≡ $p < 0.05$, n.s. = not significant.*

Together, these findings started suggesting that osmolytes could diminish direct AMP-membrane association by competing for lipid headgroups, thus favouring AMP clustering around LacY or with other AMPs and ultimately shifting the balance of interactions towards cooperative, protein-associated modes of membrane disruption.

5.4.3 Osmolyte effects on AMP-AMP interactions

After observing the effects of periplasmic osmolytes on AMP-membrane interactions, I next investigated how these species could modulate AMP-AMP interactions, such as AMP aggregation behaviour, as their presence seemed relevant for the increased probability of pore formation according to mechanism 2 relative to mechanism 1.

5.4.3.1 Case studies of osmolyte effects on AMP-AMP interactions

Aggregate-driven pore formation was observed in both osmolyte-free and osmolyte-containing systems, but the nature and stability of peptide-solute and solute-mediated peptide-peptide interactions showed marked differences between the two conditions, as illustrated in **Figure 5.11** and **Figure 5.12**.

In the absence of osmolytes, AMP clusters that initiated pores were only loosely associated and showed more dynamic behaviour, as shown in **Figure 5.12**. Salt ions such as Cl^- and Ca^{2+} bound transiently to peptide sidechains, rarely bridged more than one peptide, and did not remain to interact beyond the moment of pore formation. Aggregates remained less stable, splitting and reforming, with no evidence that the salts in the osmolyte-free systems contributed to long-term stabilisation.

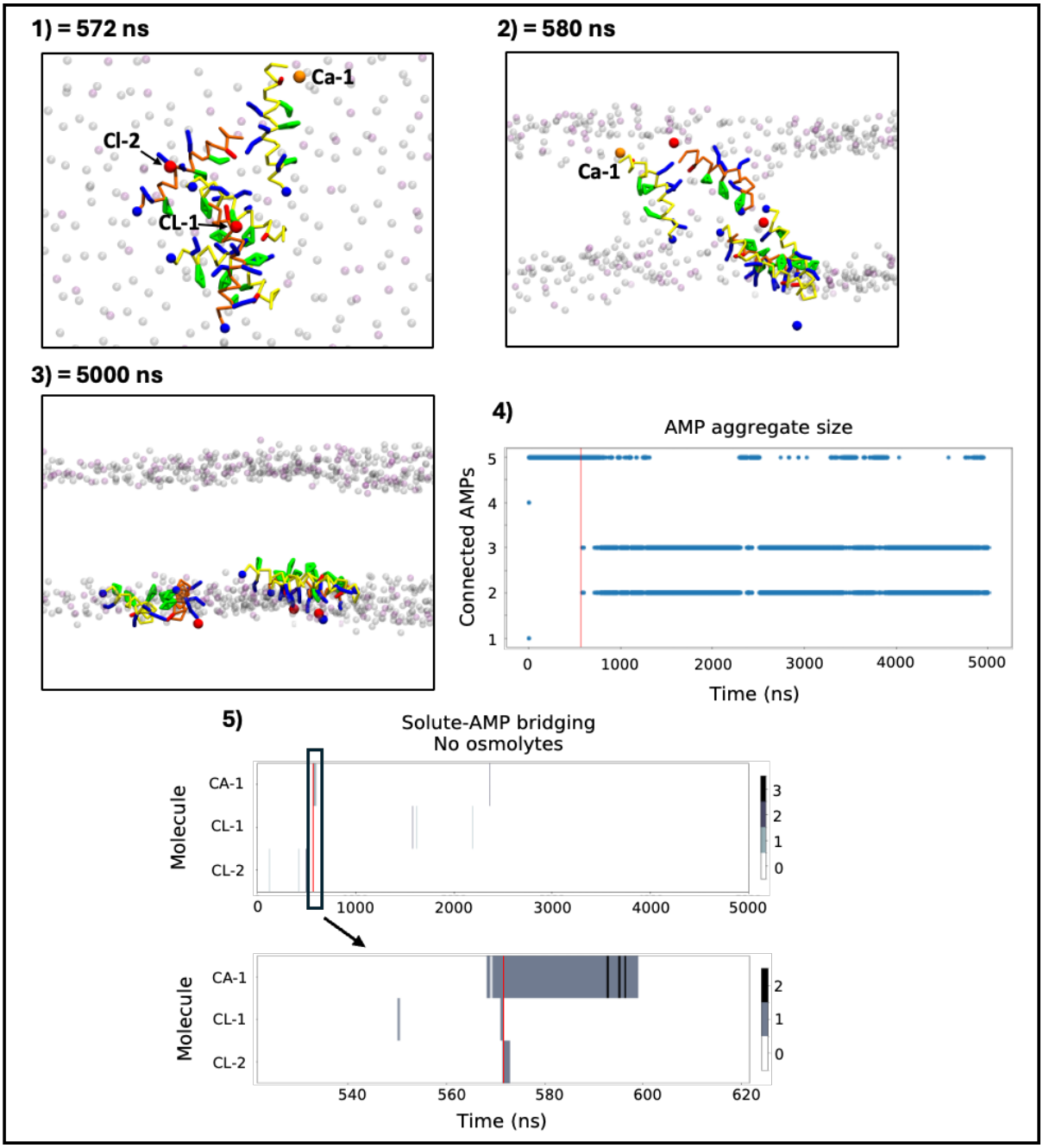

Figure 5.11. *Pore formation by an AMP aggregate in the absence of osmolytes, showing minimal solute-mediated bridging interactions. 1-4) Molecular snapshots (side and top views) of a peptide aggregate-induced pore formation. Lipid headgroups are shown as grey (POPE) and purple (POPG) spheres, tails are omitted for clarity. AMP backbones in orange or yellow, LYS chains in blue, GLU chains in red, PHE chains in green, C-termini as blue beads. Salts in contact (≤ 6 Å) with the relevant AMPs shown as coloured spheres (blue: Na, red: Cl, orange: Ca),*

and those in contact with the AMP aggregate at the pore formation beginning in 2) also annotated in the other snapshots in 1) and 3). 4) Time trace of cluster multiplicity (number of peptides per aggregate) over the full trajectory; vertical red line marks the pore-formation beginning. 5) Solute-AMP bridging plots, tracking the solute molecules from the pore formation frame in 1) and the number of AMPs in the aggregate they are in contact with. Top: Solute-AMP bridging plot across the entire simulation, with a close-up below of ± 50 ns before and after pore formation.

In contrast, aggregates were supported by persistent solute interactions in osmolyte-containing systems and thus were more stable, as shown in **Figure 5.12**. Trehalose molecules frequently bridged multiple AMPs simultaneously, forming long-lived interactions, while phosphate ions contributed by shielding charges and occasionally bridging neighbouring peptides. These persistent interactions maintained aggregate integrity during and after pore formation, often leaving AMP aggregates embedded in the bilayer over extended timescales.

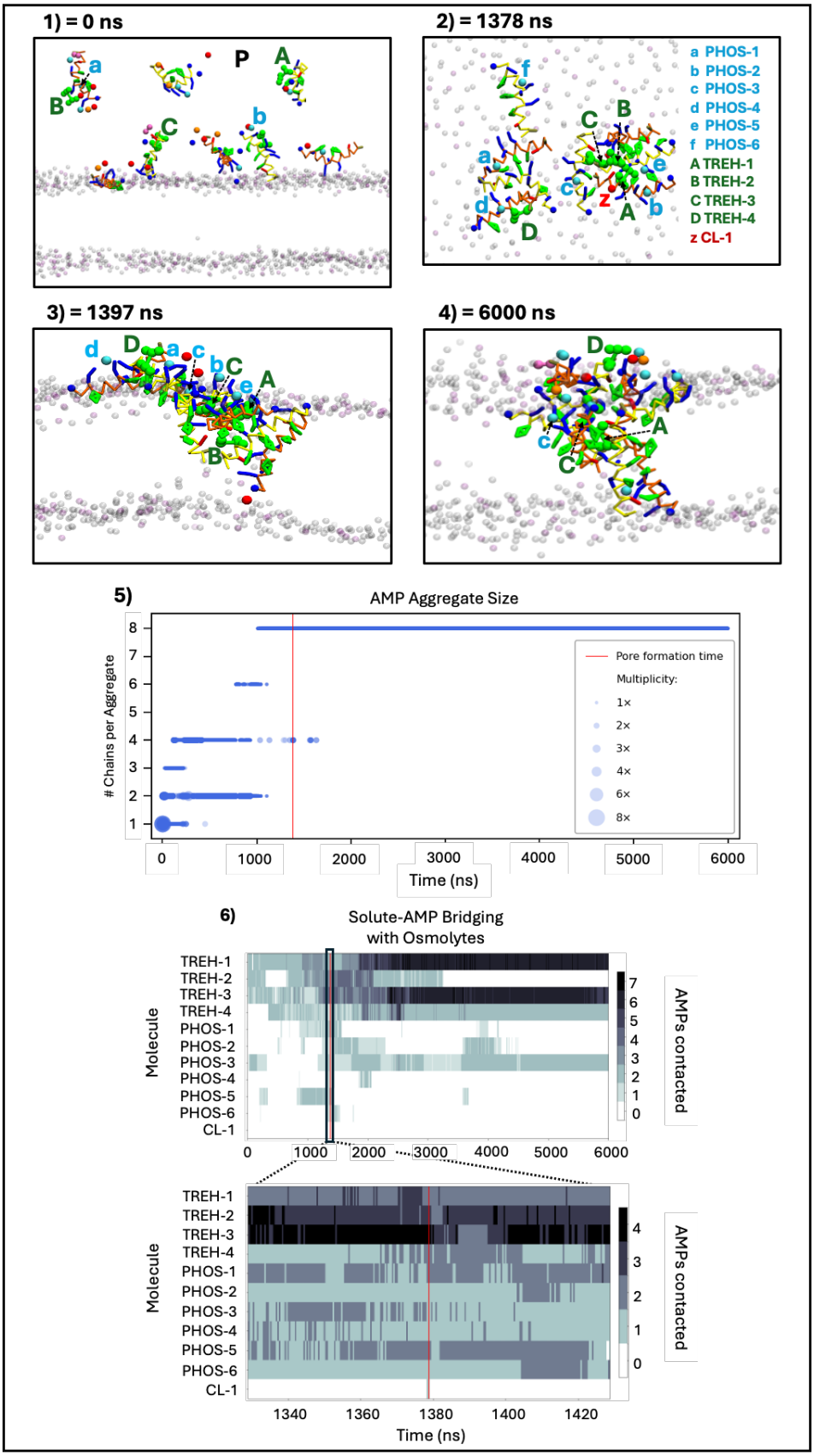

Figure 5.12. *Pore formation by an AMP aggregate in the presence of osmolytes, showing extensive solute-mediated bridging interactions. 1-4) Molecular snapshots*

(side and top views) of a peptide aggregate-induced pore formation. Lipid headgroups are shown as grey (POPE) and purple (POPG) spheres, tails are omitted for clarity. AMP backbones in orange or yellow, LYS chains in blue, GLU chains in red, PHE chains in green, C-termini as blue beads. Solute molecules in contact (≤ 6 Å) with the relevant AMPs are shown as coloured spheres (red: Cl, cyan: phosphate, green: trehalose), and those in contact with the AMP aggregate at the pore formation beginning in 2) are also annotated in the other snapshots. 5) Time trace of cluster multiplicity (number of peptides per aggregate) over the full trajectory; vertical red line marks the pore-formation beginning. 6) Solute-AMP bridging plots, tracking the solute molecules from the pore formation frame in 2) and the number of AMPs in the aggregate these solute molecules are in contact with. Top: Solute-AMP bridging plot across the entire simulation, with a close-up below of ± 50 ns before and after pore formation.

Taken together, these observations identified trehalose as the key stabiliser of AMP aggregates in osmolyte-containing conditions, with phosphate playing a secondary supportive role, as further quantified in the following subchapter.

5.4.3.2 Osmolyte-stabilised AMP-AMP bridges

I investigated AMP-solute contact patterns across all "R-B" and "R-C" simulations to further characterise the role of periplasmic solute species in AMP aggregation. Examining individual AMP aggregates revealed which residues participated in solute interactions and provided an initial qualitative understanding of how solutes engaged with peptides, as shown in **Figure 5.13**. These aggregates showed that phosphate ions preferentially coordinated individual positively charged side chains, while

trehalose engaged more broadly across multiple polar and charged residues, suggesting different modes of aggregate stabilisation.

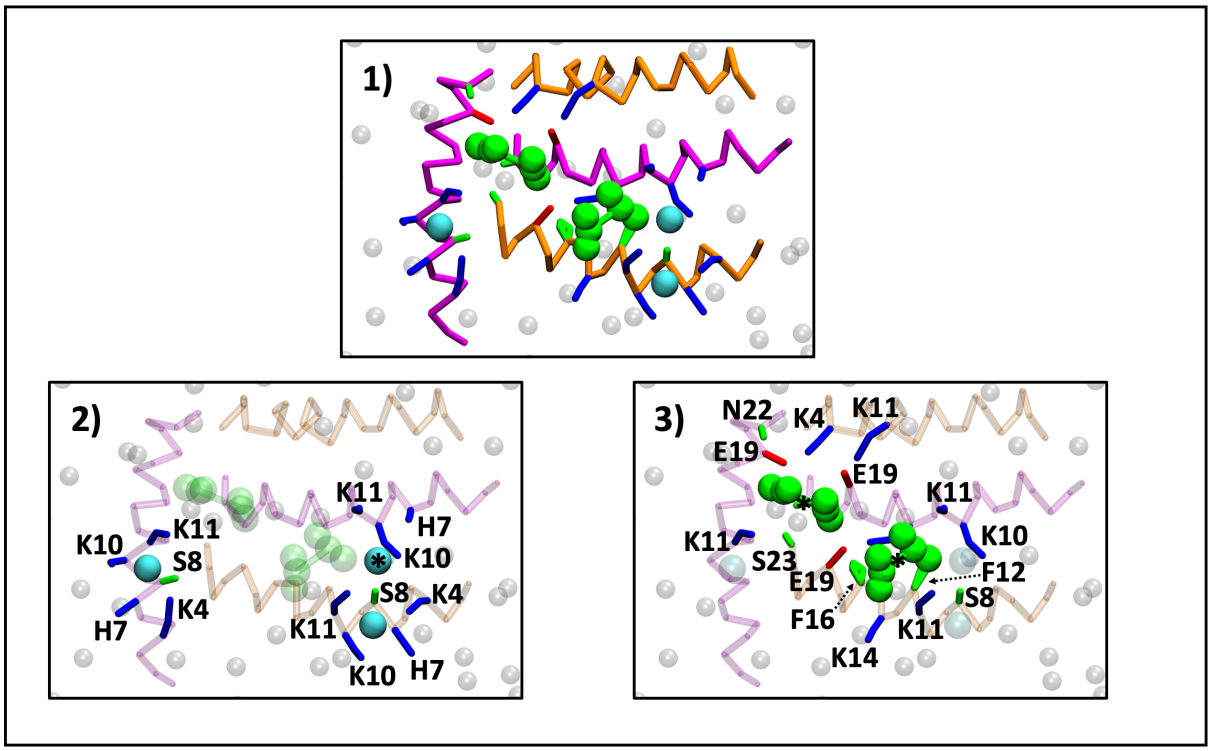

Figure 5.13. *Example molecular images showing an M2 tetramer interacting with the key bridging solute species (trehalose and phosphate) in an "R-C" simulation. 1) All AMP backbones are coloured individually by chain. AMP side chains in contact (cutoff 6 Å) with trehalose (green beads) or phosphate ions (cyan beads) are colour-coded by residue type, with non-polar residues (white), basic residues (blue), acidic residues (red), and polar residues (green). 2) Phosphate-specific interactions are highlighted, with phosphate ion contacting multiple peptides marked by an asterisk (*). 3) Trehalose-specific interactions are shown analogously to 2).*

I then quantified the mean number of solute contacts at the AMP residue level to verify the previous qualitative observations, revealing systematic preferences in residue-solute interactions, as shown in **Figure 5.14**.

In the absence of osmolytes, Cl^- ions preferentially contacted the positively charged

AMP lysine side chains and their immediate neighbours on the same, solution-oriented AMP face, while Na^+ and Cl^- preferentially contacted the negatively charged GLU19 and the uncharged polar C-terminus.

In systems including osmolytes, a different distribution of solute contacts was observed. Phosphate and trehalose accounted for the majority of all solute-AMP contacts, with the doubly negatively charged phosphate HPO_4^{2-} largely replacing Cl^- as the main coordinating anion. The reduced prevalence of Cl^- interactions in the presence of phosphate suggested competitive displacement by the multivalent anion. Trehalose contacts were more broadly distributed across polar and charged residues, both interacting with solute-facing and more membrane-oriented residues, corroborating the previous visual observation of its more promiscuous interaction mode with AMPs.

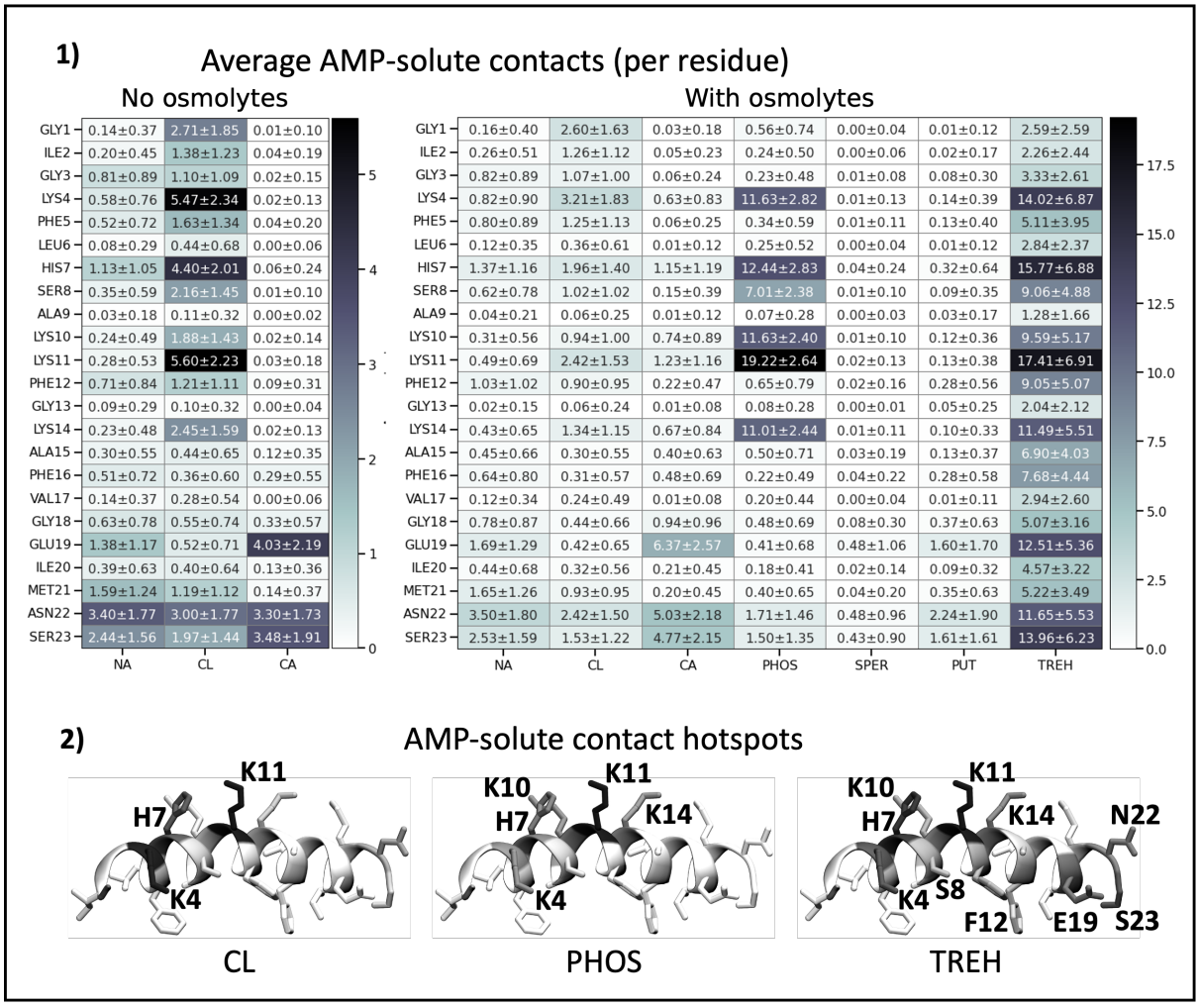

Figure 5.14. *Residue-resolved contacts between AMP side chains and periplasmic solutes, showing that interactions are concentrated at positively charged and polar residues. 1) Average number of contacts (± standard deviation) between AMP side chains and solute molecule types across all "R-B" and "R-C" simulations. 2) Projection of the results from 1) onto the 3D structure of magainin 2, with residue colouring reflecting contact propensity with chloride ions, phosphate ions, and trehalose.*

Since residue-level contacts do not necessarily translate into aggregate stabilisation, I next analysed solute-mediated bridging events across all reference simulations "R-B" and "R-C, as shown in **Figure 5.15**. In the absence of osmolytes, the predominant bridging species was Cl^-, followed by Na^+ and Ca^{2+}. This trend could be rationalised

from a combination of electrostatics, with cationic AMPs favouring interactions with anionic Cl^-, and relative abundance, with Cl^- and Na^+ present at higher initial concentrations than Ca^{2+}.

In contrast, simulations containing osmolytes showed a marked shift: trehalose was now the primary bridging species, followed by phosphate ions, largely surpassing Cl^- as the most frequent coordinator of multi-AMP aggregates. This pattern mirrored the previously observed solute-AMP contact preferences.

The distribution of the number of AMPs contacted per solute molecule further supported these observations. In osmolyte-free simulations, the majority of solute molecules interacted with only a single AMP chain, indicating that bridging interactions were relatively rare. By contrast, in simulations containing osmolytes, two species, trehalose and phosphate anions, showed a majority of interactions involving simultaneous contact with two or more AMP chains, reinforcing their previously suggested role in stabilising AMP aggregates.

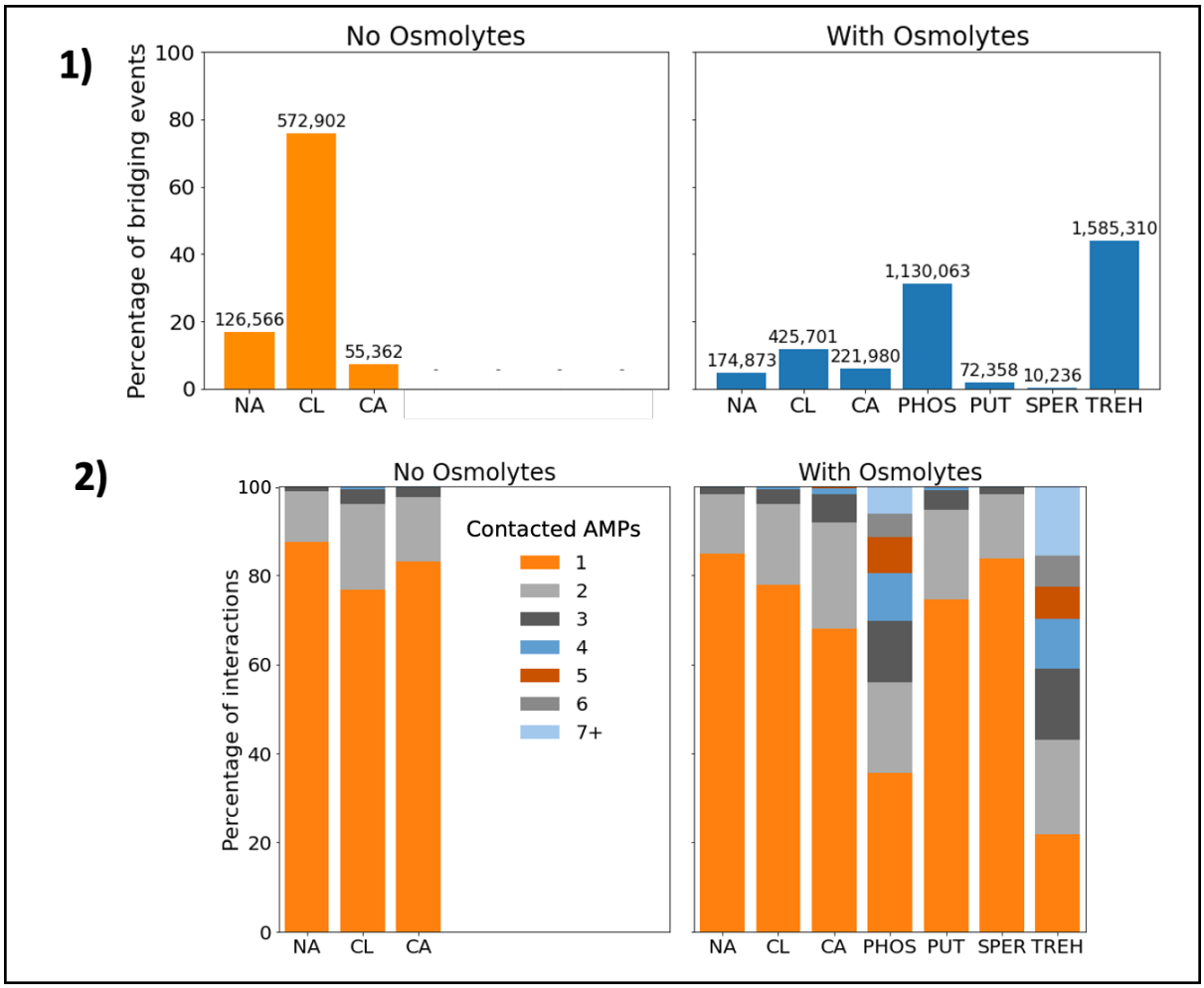

***Figure 5.15**. Comparison of AMP-bridging propensities across different solute species, showing solute-mediated bridging interactions across all aggregated "R-B" and "R-C" simulations. 1) Bar plots of the relative contribution of each solute species to the total number of bridging events, defined as simultaneous contact (cutoff 6 Å) with two or more AMP chains, with the total number of bridging observations per species indicated above each bar. 2) Stacked bar plots of the distribution of the number of distinct AMP chains individual solute molecules contacted during bridging events.*

Finally, to assess whether these bridging interactions were transient or stabilising, I evaluated their lifetimes using survival analysis, as shown in **Figure 5.16**. This survival analysis showed that the interaction lifetimes of sodium and chloride ions

with AMPs were comparable between simulations “R-B” and “R-C”. Furthermore, Cl^-, phosphate anions, and trehalose formed longer-lived bridges compared to the other investigated solutes. Among these, trehalose-mediated AMP-bridging interactions exhibited the slowest decay, confirming the previous qualitative visual observation regarding the extended lifetime of trehalose-AMP bridges.

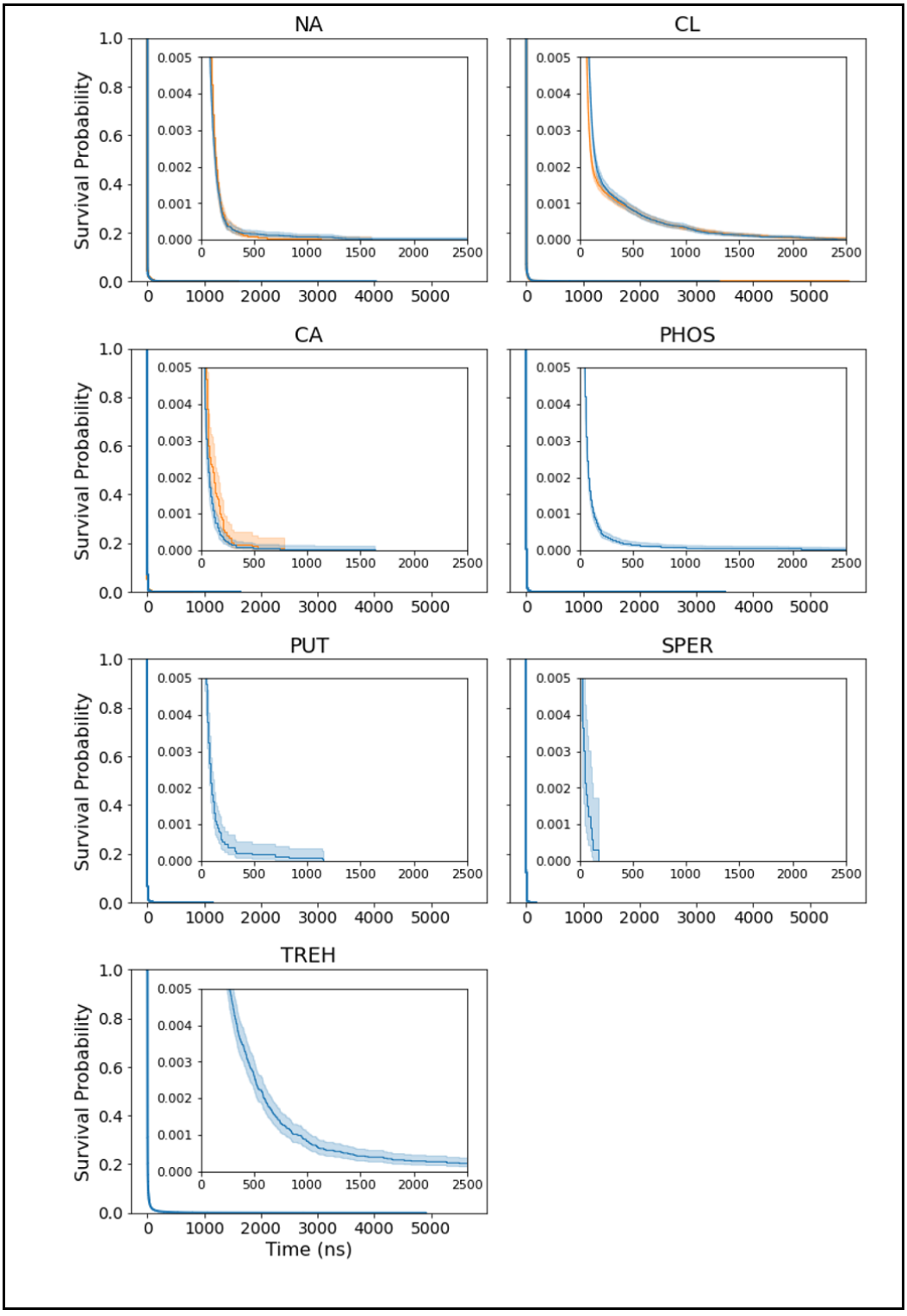

Figure 5.16. *Survival functions for bridging interactions between solutes and two or more AMP chains, with shaded 95% confidence interval and "no osmolytes" in orange, "with osmolytes" in blue, and insets zooming in on function elbow.*

Taken together, these results highlight trehalose as a key contributor to AMP aggregation under crowded periplasmic conditions, with small anionic salts such as phosphate and chloride ions providing a supportive role.

5.4.3.3 Quantitative AMP-AMP aggregate characterisation

To understand whether osmolytes influence not just the occurrence but also the organisation and persistence of AMP aggregates, I quantitatively characterised aggregate size distributions, lifetimes, and peptide orientations across simulations with and without osmolytes, as well as in systems selectively lacking doubly charged ions (phosphate anions, calcium) or trehalose, which had previously been found to co-aggregate with AMPs.

No statistical difference between any of the AMP aggregate size distributions at the moment of pore formation was determined by a Kruskal-Wallis H-test ($p > 0.05$), as shown in **Figure 5.17**. Both the average and median AMP aggregate size at the start of pore formation events *via* mechanism 2 were 4 across all conditions. This consistency suggested that the formation of such pores may require AMP aggregates to reach a minimal size threshold. Notably, the only observed cases of membrane pore formation by AMP dimers occurred near LacY, likely aided by local LacY-induced membrane defects, whereas pores forming further from LacY *via* the same mechanism consistently involved larger AMP aggregates. While not defining a strict lower bound, the observation that most pores formed *via* mechanism 2 involved aggregates of more than three AMPs supported the idea that larger assemblies increased the likelihood of pore formation *via* AMP-cooperative mechanisms. These observations were consistent with prior experimental and computational studies of

magainin 2, which suggested that toroidal pore formation typically involves 4-6 peptides involved in all-or-none membrane permeabilisation.[10,11,17]

Solid-supported flip-flop and leakage assays by Fujii *et al.* suggested that approximately five magainin helices are required to span the membrane and enable lipid translocation through peptide-lined pores.[11] Furthermore, coarse-grained simulations demonstrated that magainin-mediated pores mediated by a magainin 2 analogue in DPPC emerge through the cooperative insertion of peptide clusters within this size range.[17] Together, these findings support the notion that AMP dimers are generally insufficient for pore formation, and that larger assemblies are required to initiate and stabilise membrane-spanning pores.

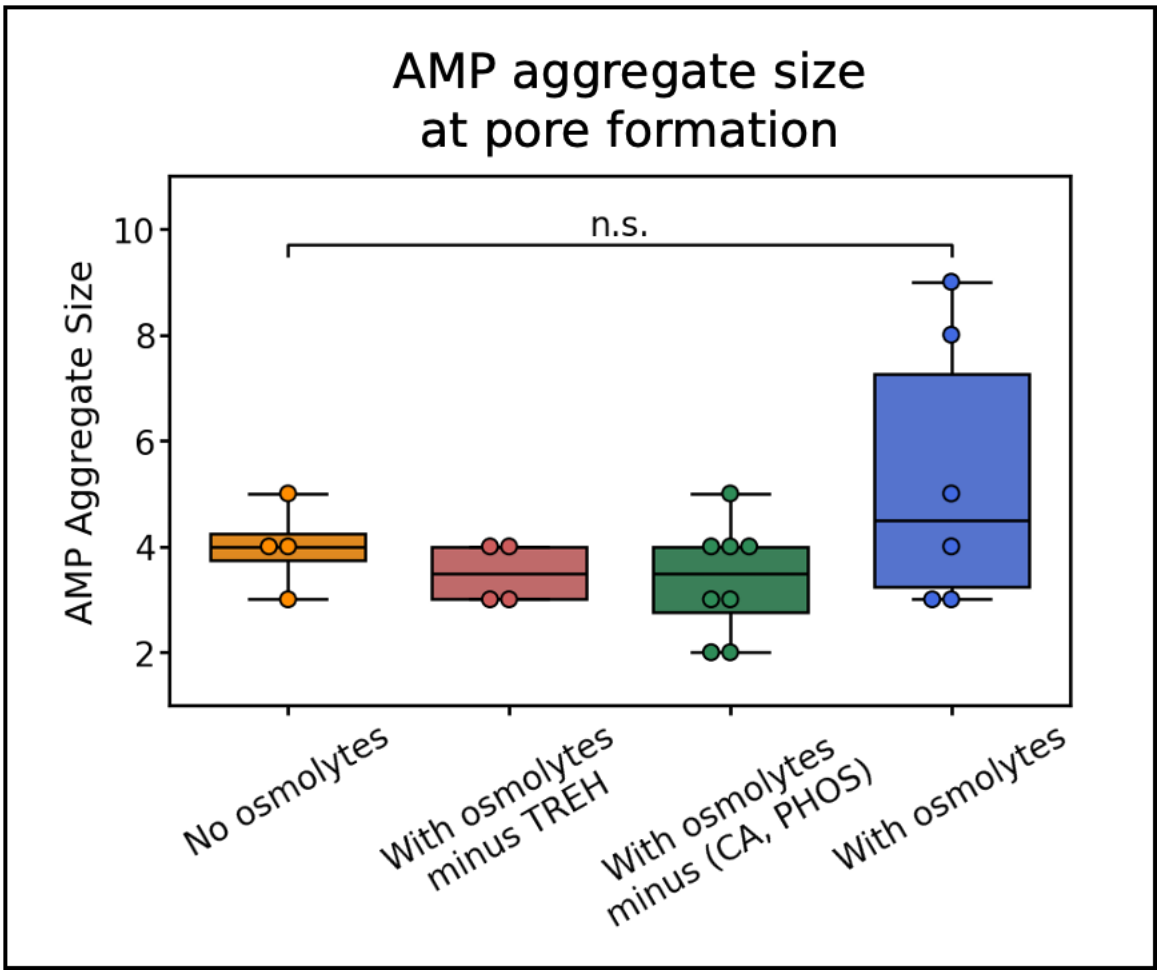

***Figure 5.17**. AMP aggregation behaviour in simulations without ("R-B", orange) and with ("R-C", blue) osmolytes, and with osmolytes but without trehalose ("R-D", red) or without phosphate ions ("R-E", green). 1) Box plot of the distributions of AMP aggregate sizes involved in pore formation via mechanism 2 as taken at the start of pore formation events, with the result of a Kruskal-Wallis H-test noted above.*

When I broadened the analysis to all frames rather than just pore formation events, clear solute-dependent differences emerged, as shown in **Figure 5.18**. In simulations without osmolytes, AMPs were more frequently found in smaller aggregates - primarily as monomers, dimers, or trimers - compared to systems containing osmolytes, where larger aggregates were both more frequent and more stable. Interestingly, the dimer emerged as the preferred aggregation state across all

conditions, consistent with the experimental and computational literature.[18–20] This dimer preference was notably diminished in the presence of osmolytes, where higher-order aggregates became more prominent.

Logistic regression confirmed this shift quantitatively: compared to the no-osmolyte condition, the likelihood of observing aggregates of size ≥4 increased significantly ($p < 0.0001$) by a factor of ~2.8 in the full-osmolyte system, ~3.8 in the trehalose-free osmolyte condition, and ~2.0 in the calcium and phosphate ion-free osmolyte condition.

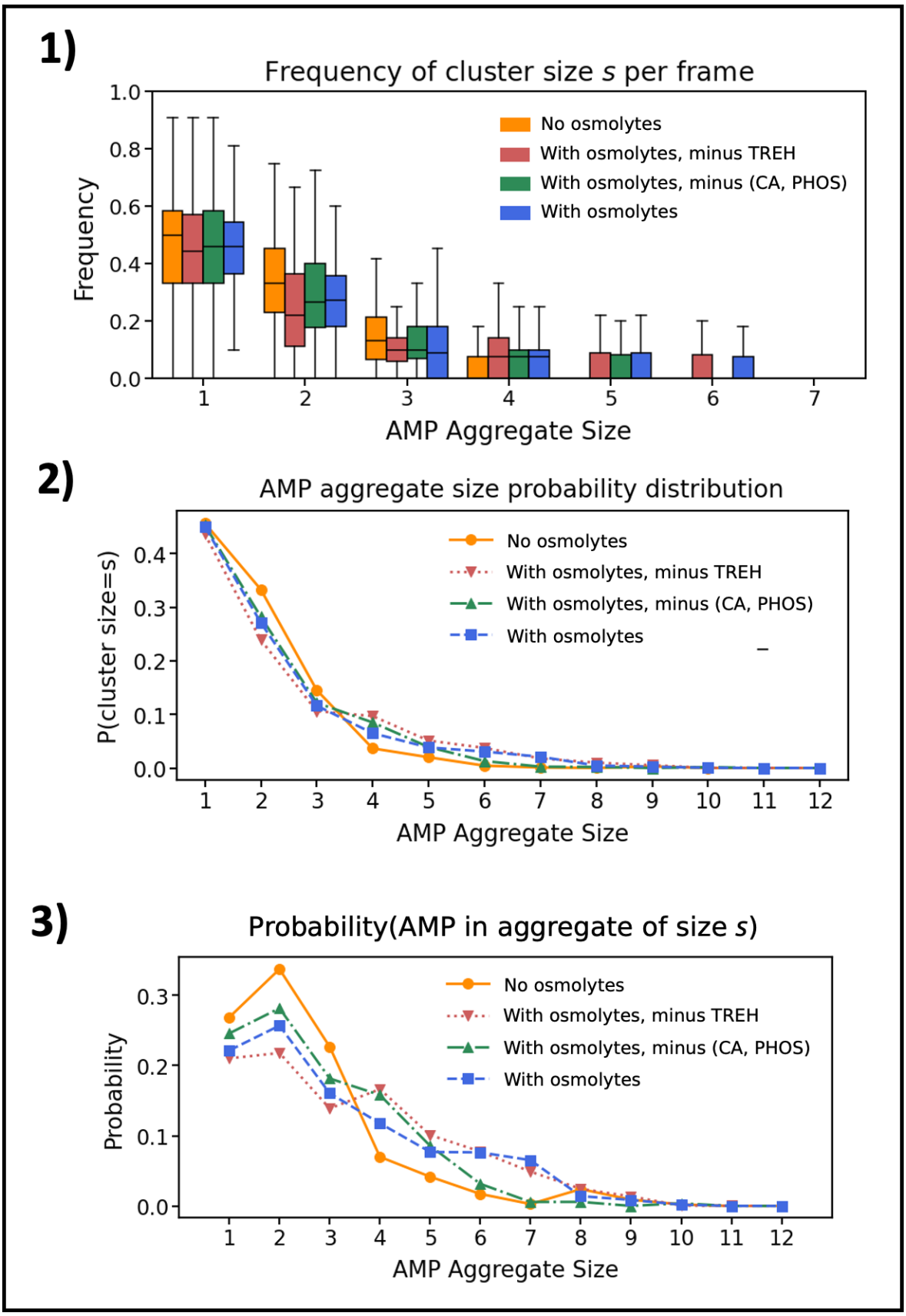

Figure 5.18. *AMP aggregation behaviour in simulations without ("R-B", orange) and with ("R-C", blue) osmolytes, and with osmolytes but without trehalose ("R-D", red) or*

without phosphate ions ("R-E", green). 1) Per-frame frequency distribution of AMP aggregate sizes, shown as a boxplot across all frames. 2) Normalised probability distribution of aggregate sizes observed across all frames. 3) Aggregate size-weighted size distribution, corresponding to the probability that an AMP is part of an AMP-aggregate of a given size.

I next examined aggregate lifetimes to assess whether osmolytes also stabilised these assemblies over time. Aggregates were tracked across simulation frames, and their lifetimes were calculated based on the number of consecutive frames in which the same aggregate could be identified without AMP joining/leaving the aggregate. The results of this analysis, shown in **Figure 5.19**, confirmed that larger aggregates were not only more frequent in osmolyte-containing simulations but also tended to persist longer than those observed in osmolyte-free systems. This enhanced stability may be explained by the previously described long-lived bridging interactions between AMPs and trehalose and phosphate anions, which were absent in the control systems lacking osmolytes. These findings suggested that osmolytes not only promoted AMP aggregation but also stabilised these assemblies over time, thus potentially influencing their ability to disrupt bacterial membranes *via* cooperative self-aggregation mechanisms.

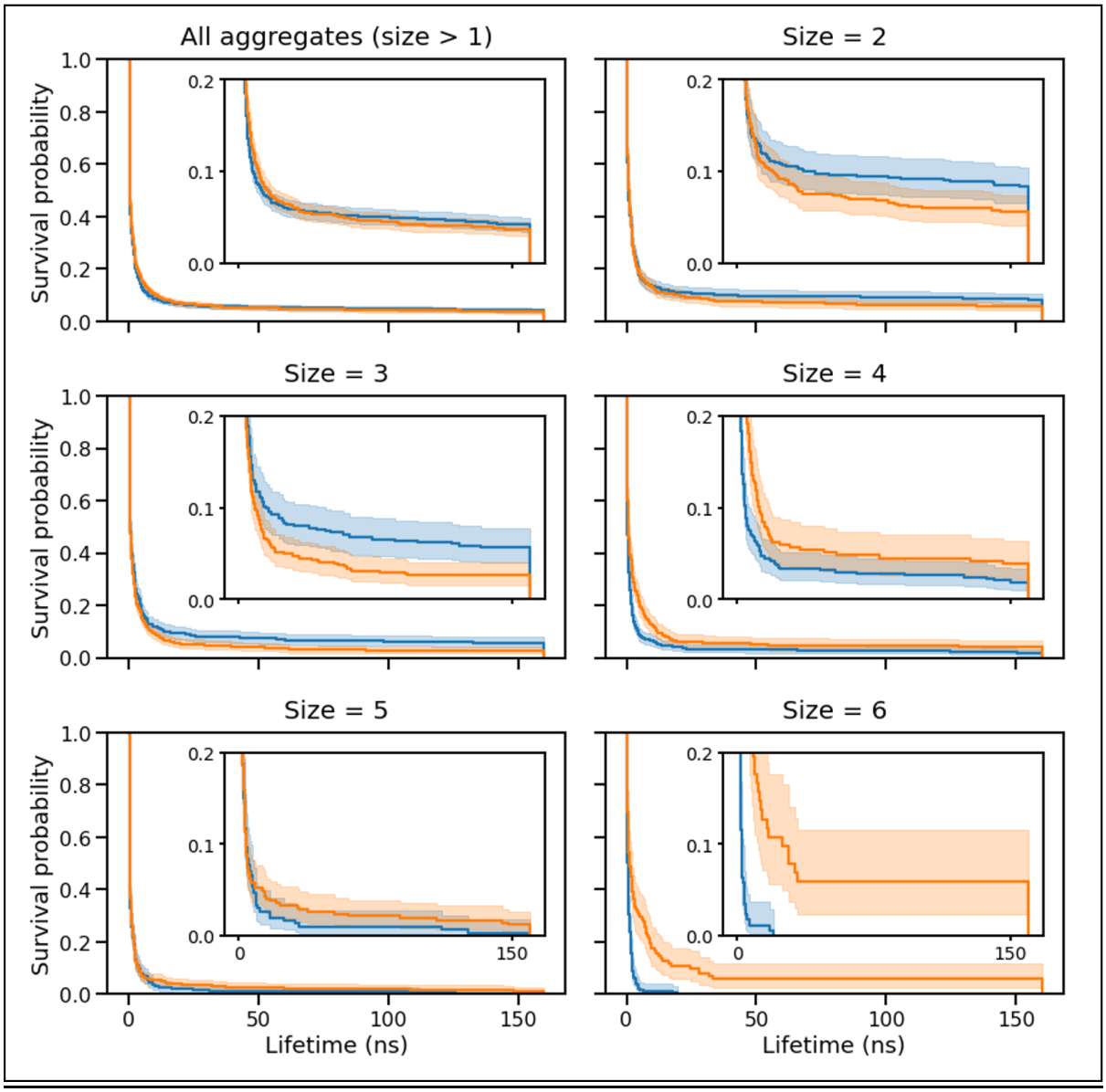

Figure 5.19. *Survival functions of AMP aggregates as a function of their lifetime, stratified by aggregate size and osmolyte condition. Shaded regions represent 95% confidence intervals. Insets within each panel highlight the corresponding elbow region.*

Finally, I analysed the relative orientations of AMP pairs within aggregates to determine whether osmolytes altered the AMP clustering geometries, as shown in **Figure 5.20**. Antiparallel orientations (defined here as angles ≥150°) were shown to

be stabilised by the formation of two salt bridges between K4 and E19, in contrast to just a singular salt bridge between these residues being possible in parallel arrangements. While both osmotic conditions exhibited enrichment of antiparallel dimers, this preference was significantly stronger in the absence of osmolytes (Fisher's exact test, $p < 0.001$; log odds ratio = 1.779). When directly comparing extreme orientations, strongly antiparallel dimers (≥ 150°) were markedly more frequent than strongly parallel ones (≤ 30°) under osmolyte-free conditions, with an antiparallel-to-parallel ratio of 4.24 versus 1.89 for osmolyte-containing simulations (odds ratio = 2.25, Fisher's exact test $p < 0.0001$, Cramér's V = 0.176). This shift likely reflected the reduced disruption of AMP-AMP salt bridge interactions in the absence of osmolytes, as previously demonstrated to occur through competitive AMP charge shielding by charged solute species such as sodium, chloride, spermidine, or putrescine.

Importantly, osmolytes introduced not only competitive but also favourable interactions, particularly *via* trehalose and phosphate anions, as described above. This reduced the relative energetic favourability of antiparallel orientations and simultaneously allowed for more varied and stable spatial configurations in larger AMP aggregates, as illustrated by the broader distribution in the bottom panel of **Figure 5.20**. As aggregate size increased, the corresponding increased geometric flexibility and aggregation *via* neutral trehalose or negative phosphate ions would begin to outweigh the energetic penalty from disrupted salt bridges, thereby favouring the formation of larger, less ordered, and longer-lived AMP clusters under osmolyte-containing conditions.

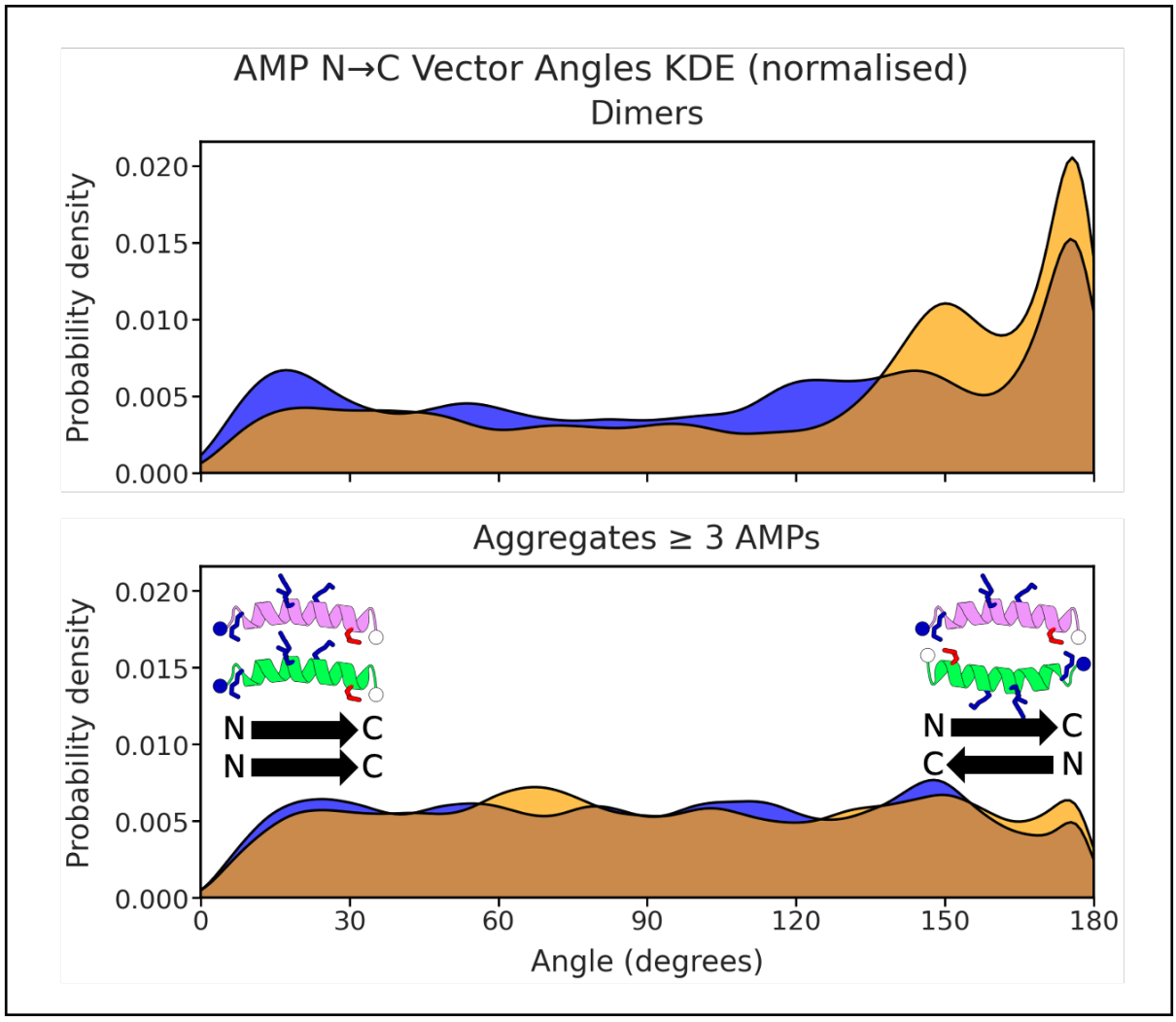

Figure 5.20. *Kernel density estimates (KDE) showing the distribution of angles between the N-to-C terminal vectors of AMP pairs in dimers (top panel) and larger aggregates (bottom panel) for "R-B" and "R-C" simulations. Data are stratified by simulation condition: no osmolytes (orange), with osmolytes (blue). Angles near 0° or 180° indicate parallel or antiparallel orientation respectively.*

Together, these findings of differential AMP-aggregate size preference began to explain the observed shift in dominant pore formation mechanisms as a function of periplasmic compositions: whereas osmolyte-free systems tended to favour mechanism 1, which involved individual AMP insertion near LacY, the presence of osmolytes promoted a higher relative frequency of mechanism 2, in which stable AMP aggregates collectively initiated membrane rupture. This mechanistic shift, emerging as a direct consequence of environmental complexity, highlighted the relevance of osmolyte-mediated modulation of AMP behaviour.

5.5 Conclusion

This chapter investigated the molecular mechanisms of LacY-independent pore formation by magainin 2 and explored how periplasmic osmolytes modulated these processes. Two distinct, stochastic pathways were characterised: a cooperative mechanism driven by AMP aggregates that caused local membrane thinning, and a substantially rarer mechanism initiated by a single AMP rupturing the bulk membrane.

My findings revealed that periplasmic osmolytes could significantly alter AMP behaviour by reducing direct interactions with the membrane surface, while simultaneously promoting the formation of larger and more stable AMP aggregates. Specifically, trehalose and phosphate ions were identified as key AMP-aggregation enhancers, forming long-lived bridging interactions stabilising multi-peptide aggregates. This contrasted with osmolyte-free conditions, where AMP aggregation was less pronounced and was characterised by more transient salt-mediated bridging.

These results provided an initial molecular rationale for the shift towards aggregate-driven pore formation in the presence of osmolytes, as observed in **Chapter 4** and schematically represented in **Figure 5.21**. By promoting aggregation, osmolytes increased the probability of pore formation *via* cooperative, multi-peptide mechanisms. Furthermore, the inclusion of osmolytes reduced the likelihood of pathways dependent on single peptides, such as mechanisms 1 or 4, by diminishing the population of available monomers.

In this way, I showed that the crowded periplasmic environment could play a critical role in shaping the antimicrobial activity of magainin 2 by directly modulating its aggregation state.

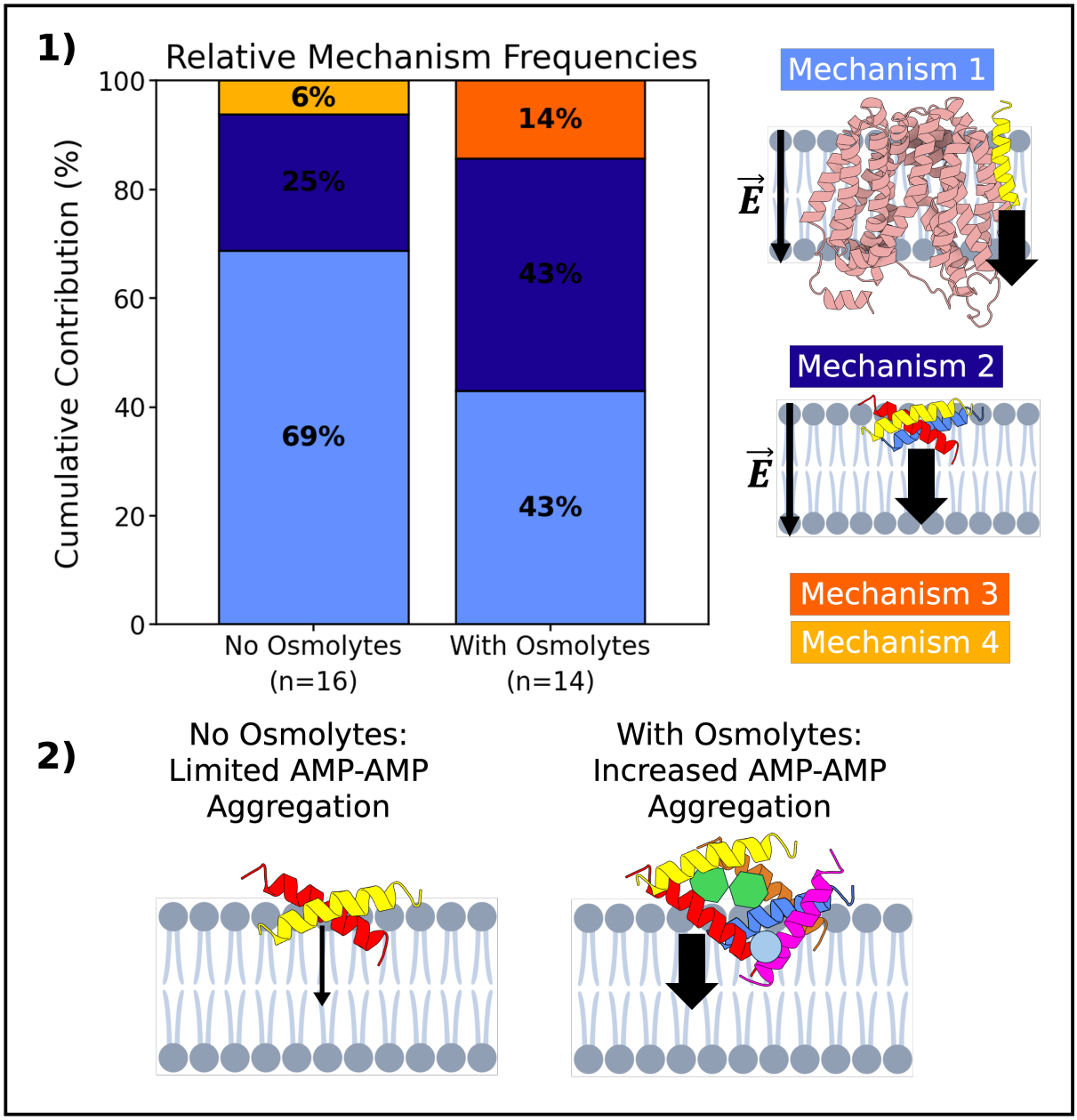

Figure 5.21. *Mechanisms of pore formation in AMP-containing reference systems with and without osmolytes. 1) Stacked bar chart illustrating the relative frequency of the four observed pore formation mechanisms in "R-B" (no osmolytes) and "R-C" (with osmolytes) simulations, with accompanying schematics of the two predominant mechanisms. 2) Schematic representations of the first hypothesised osmolyte-related effect driving the shift in mechanism prevalence: osmolyte-induced increased AMP-AMP aggregation led to an increased likelihood of pores forming via the AMP-*

aggregate-defined mechanism 2, while reducing the pool of AMP monomers available for single-AMP-defined mechanisms 1 and 4.

References

1. Oliveira Júnior, N. G., Souza, C. M., Buccini, D. F., Cardoso, M. H. & Franco, O. L. Antimicrobial peptides: structure, functions and translational applications. *Nat. Rev. Microbiol.* 1–14 (2025) doi:10.1038/s41579-025-01200-y.

2. Tieleman, D. P. The molecular basis of electroporation. *BMC Biochem.* **5**, 1–12 (2004).

3. Piggot, T. J., Holdbrook, D. A. & Khalid, S. Electroporation of the E. coli and S. aureus membranes: molecular dynamics simulations of complex bacterial membranes. *J. Phys. Chem. B* **115**, 13381–13388 (2011).

4. Teissie, J., Golzio, M. & Rols, M. P. Mechanisms of cell membrane electropermeabilization: A minireview of our present (lack of ?) knowledge. *Biochim. Biophys. Acta BBA - Gen. Subj.* **1724**, 270–280 (2005).

5. Kramar, P. & Miklavčič, D. Effect of the cholesterol on electroporation of planar lipid bilayer. *Bioelectrochemistry* **144**, 108004 (2022).

6. Chassy, B. M., Mercenier, A. & Flickinger, J. Transformation of bacteria by electroporation. *Trends Biotechnol.* **6**, 303–309 (1988).

7. Booth, I. R. Regulation of cytoplasmic pH in bacteria. *Microbiol. Rev.* **49**, 359–378 (1985).

8. Zilberstein, D., Agmon, V., Schuldiner, S. & Padan, E. Escherichia coli intracellular pH, membrane potential, and cell growth. *J. Bacteriol.* **158**, 246–252 (1984).

9. Kashket E R. Effects of aerobiosis and nitrogen source on the proton motive force in growing Escherichia coli and Klebsiella pneumoniae cells. *J. Bacteriol.* **146**, 377–384 (1981).

10. Gregory, S. M., Pokorny, A. & Almeida, P. F. F. Magainin 2 Revisited: A Test of the Quantitative Model for the All-or-None Permeabilization of Phospholipid Vesicles. *Biophys. J.* **96**, 116–131 (2009).
11. Matsuzaki, K., Murase, O., Fujii, N. & Miyajima, K. An Antimicrobial Peptide, Magainin 2, Induced Rapid Flip-Flop of Phospholipids Coupled with Pore Formation and Peptide Translocation. *Biochemistry* **35**, 11361–11368 (1996).
12. Michaud-Agrawal, N., Denning, E. J., Woolf, T. B. & Beckstein, O. MDAnalysis: a toolkit for the analysis of molecular dynamics simulations. *J. Comput. Chem.* **32**, 2319–2327 (2011).
13. Ludtke, S., He, K. & Huang, H. Membrane thinning caused by magainin 2. *Biochemistry* **34**, 16764–16769 (1995).
14. Grage, S. L., Afonin, S., Kara, S., Buth, G. & Ulrich, A. S. Membrane Thinning and Thickening Induced by Membrane-Active Amphipathic Peptides. *Front. Cell Dev. Biol.* **4**, 65 (2016).
15. Grahame, D. C. The electrical double layer and the theory of electrocapillarity. *Chem. Rev.* **41**, 441–501 (1947).
16. Marcus, R. A. On the theory of electron-transfer reactions. VI. Unified treatment for homogeneous and electrode reactions. *J. Chem. Phys.* **43**, 679–701 (1965).
17. Leontiadou, H., Mark, A. E. & Marrink, S. J. Antimicrobial Peptides in Action. *J. Am. Chem. Soc.* **128**, 12156–12161 (2006).
18. Hara, T. *et al.* Effects of peptide dimerization on pore formation: Antiparallel disulfide-dimerized magainin 2 analogue. *Biopolymers* **58**, 437–446 (2001).
19. Wakamatsu, K., Takeda, A., Tachi, T. & Matsuzaki, K. Dimer structure of magainin 2 bound to phospholipid vesicles. *Biopolymers* **64**, 314–327 (2002).

20. Boughton, A. P., Andricioaei, I. & Chen, Z. Surface orientation of magainin 2: molecular dynamics simulation and sum frequency generation vibrational spectroscopic studies. *Langmuir ACS J. Surf. Colloids* **26**, 16031–16036 (2010).

Chapter 6

Computational Electrophysiology simulations: osmolyte effects on AMP interactions in membrane protein-dependent pore formation

6.1 Introduction

Lactose permease (LacY) is primarily recognised as a bacterial proton-driven sugar symporter operating *via* an alternating-access mechanism.[1–3] However, recent studies have uncovered a secondary, "moonlighting" function: LacY can also act as a lipid scramblase, facilitating the bidirectional movement of phospholipids across the membrane bilayer.[4] This lipid scrambling activity operates independently of its sugar transport function and remains an area of ongoing investigation.[4]

The precise molecular mechanisms governing protein-mediated lipid transport are not fully understood. A common characteristic of lipid scramblases appears to be the presence of a hydrophilic groove extending into the hydrophobic core of the lipid bilayer, as well as an induced localised thinning of the membrane.[4] Intriguingly, several members of the membrane protein insertase family, which exhibit these features, have recently been demonstrated to possess lipid scrambling activity.[5–7] Experimental research has also shown that some AMPs, such as magainin 2, induce similar bilayer perturbations, promoting thinning, lipid disorder, lipid flip-flops, and pore formation in model membranes.[8,9] Given these parallels between membrane protein-mediated and peptide-induced bilayer perturbation, it seems worth investigating whether AMPs could exploit LacY-mediated defects at the protein-lipid

interface as alternative entry pathways into the membrane, as schematically represented in **Figure 6.1**.

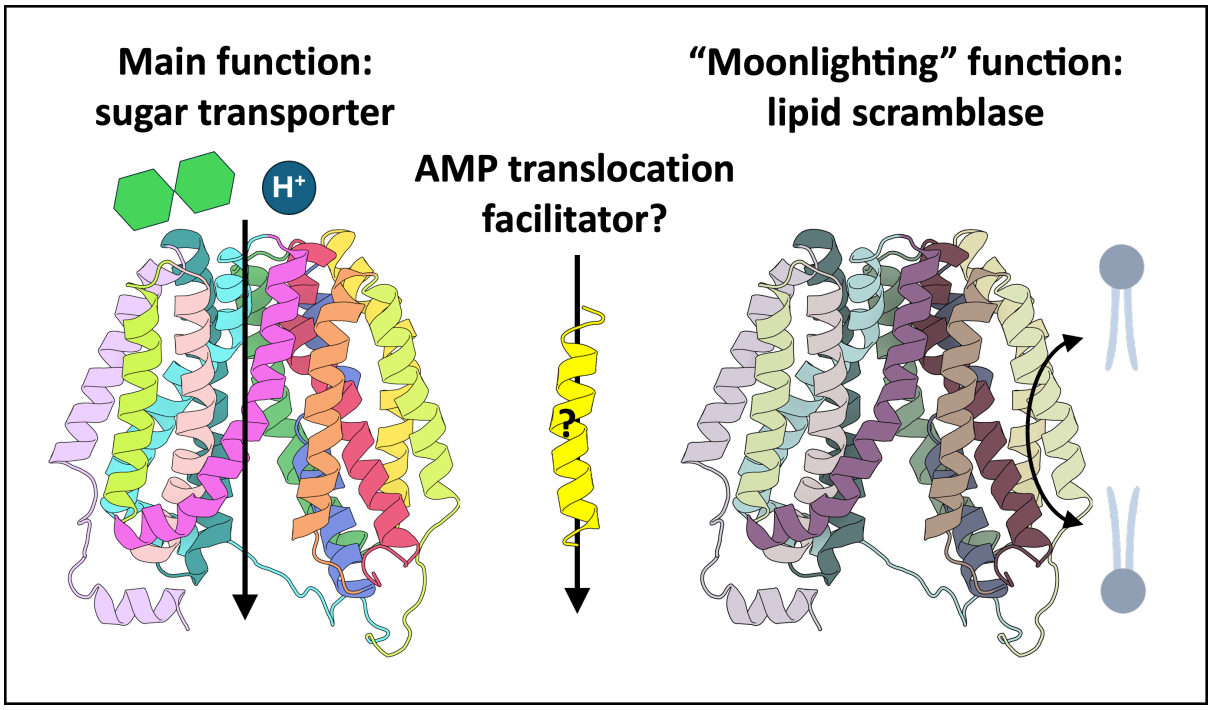

Figure 6.1. *Schematic illustration of known and hypothesised LacY functions (cartoons coloured by individual helices). Left: main function as sugar/proton symporter (green hexagons, blue sphere respectively), right: "moonlighting" function as lipid (grey) scramblase, with a central question regarding a possible role in facilitating AMP (yellow cartoon helix) translocation.*

6.2 Aims

This chapter aims to investigate how periplasmic osmolytes influence the permeation of the antimicrobial peptide magainin 2 across the *E. coli* inner membrane under an induced electric field, with a focus on the two membrane protein-dependent pore formation mechanisms described in **Chapter 4**, mechanisms 1 and 3, as described in **Figure 6.2**. This electric field mimics the natural, inside-negative membrane potential of the Gram-negative inner membrane, which is induced by the proton

motive force comprising both an electrical potential difference (Δψ) and a transmembrane pH gradient (ΔpH).[10–12]

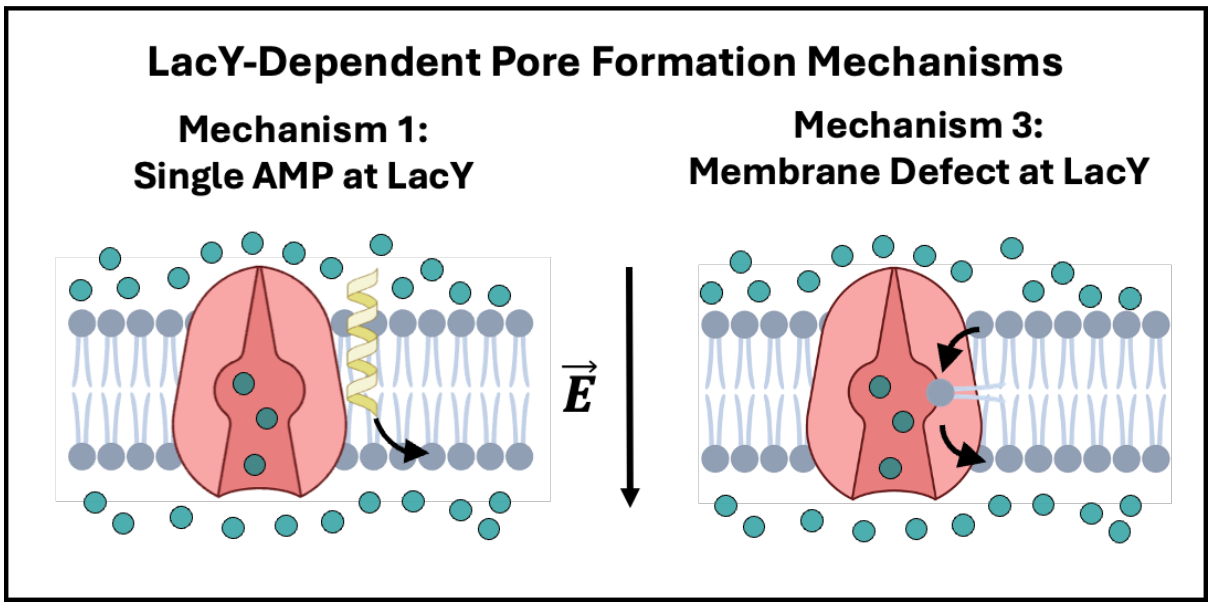

Figure 6.2. *Schematic representation of the two LacY-dependent pore formation mechanisms of magainin 2 observed in my computational electrophysiology (CompEL) simulations in order of decreasing observation frequency: mechanisms 1 and 3.*

6.3 Methods

The simulation methods used in this chapter were identical to those described in **Chapter 4**. The system preparation, simulation protocols, and analysis methods followed the same procedures in full.

6.4 Results and discussion

6.4.1 Mechanism characterisation

The following subsections will focus on the characterisation of the two membrane protein-dependent pore formation mechanisms observed in my simulations.

6.4.1.1 Mechanism 1: single AMP "snorkelling" along LacY

Pores formed *via* mechanism 1 occurred when a single M2 peptide crossed the membrane by "snorkelling" along the surface of LacY. This process was consistently facilitated by transient electrostatic interactions between positively charged M2 residues and a negatively charged glutamic acid (E314) located on the "shallow" periplasmic side of LacY, which is further characterised below. In most cases (80 or 91% of mechanism 1 events in the presence or absence of osmolytes, respectively), the N-terminus (NT) or lysine residues (K4, K10, K11, K14) made direct contact with E314 prior to insertion, a pre-translocation contact pattern not observed for other acidic LacY residues. This suggested a facilitating role of E314 in stabilising AMPs at the protein surface and guiding their progression into the bilayer, as shown in **Figure 6.3**.

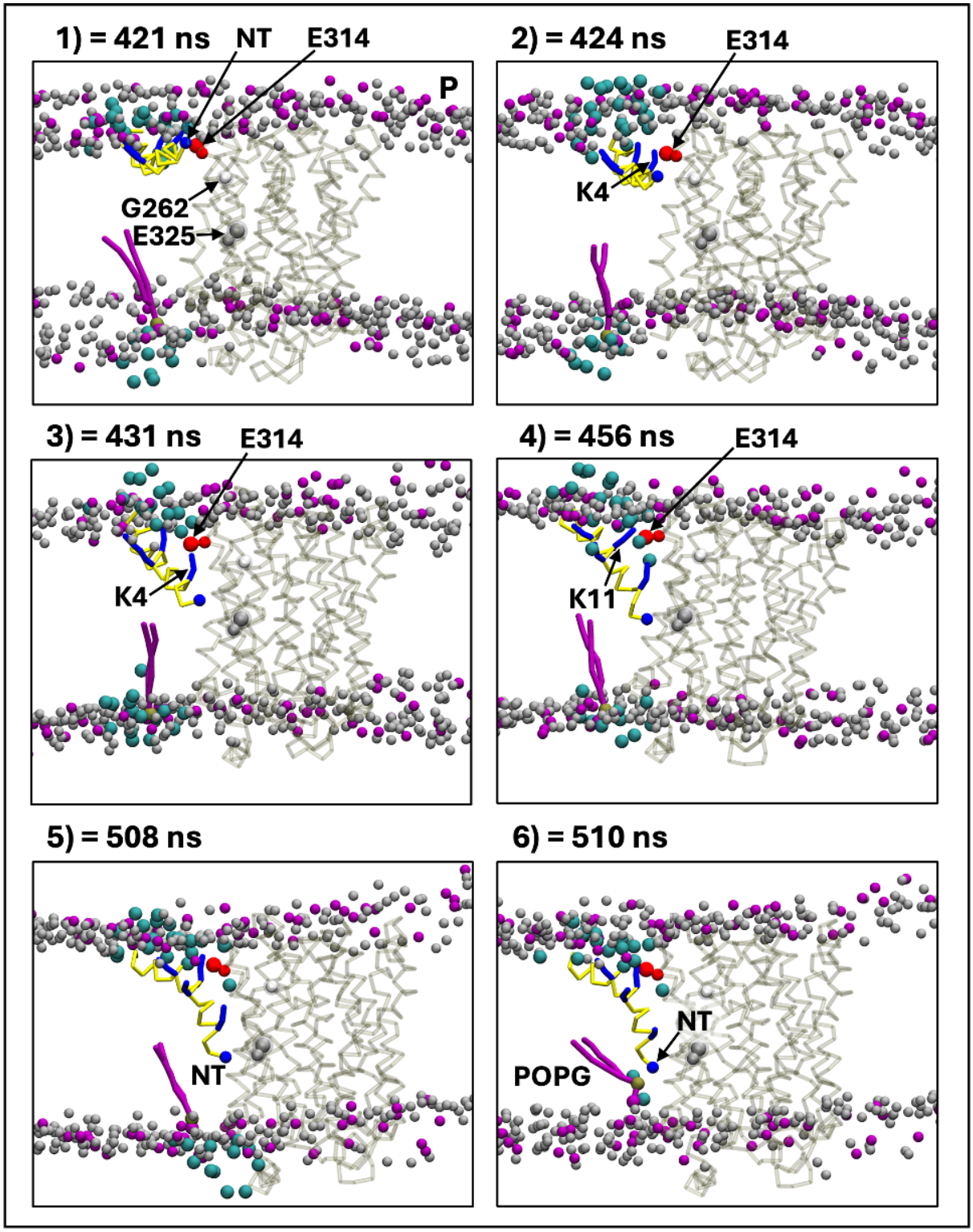

Figure 6.3. *Molecular images ("R-B" simulation) showing an example of pore formation initiation via mechanism 1. A single AMP "snorkelled" along LacY to reach the distal leaflet. "P" indicates the periplasmic compartment in this and all subsequent subfigures. Lipid headgroups are shown as grey (POPE) and purple*

(POPG) beads. M2 backbone in yellow stick representation, with its N-terminus (NT) as blue bead and its lysine residues as blue sticks. LacY as a transparent backbone, with residues G262 and E325 highlighted in white/grey for orientation. E314 in red is successively forming transient contacts (cutoff ≤ 6 Å) with positively charged groups of M2. Relevant POPG in the opposing leaflet is shown in purple stick representation. Water particles within 6 Å of the peptide or the highlighted POPG are shown as cyan beads.

After the initial interaction with E314, AMPs advanced NT-first into the membrane along the direction of the applied electric field. These sequential contacts with E314 stabilised the peptide orientation and enabled their N-terminus to reach the distal leaflet, where they interacted with lipid headgroups. Such peptide-lipid interactions helped draw lipid headgroups upward toward the bilayer midplane, while polarisable water molecules infiltrated the hydrophobic core, as shown in **Figure 6.4**. This combination of lipid distortion and water penetration was reminiscent of classical electroporation, where water fingers invade the bilayer core from both sides prior to pore formation.[13,14]

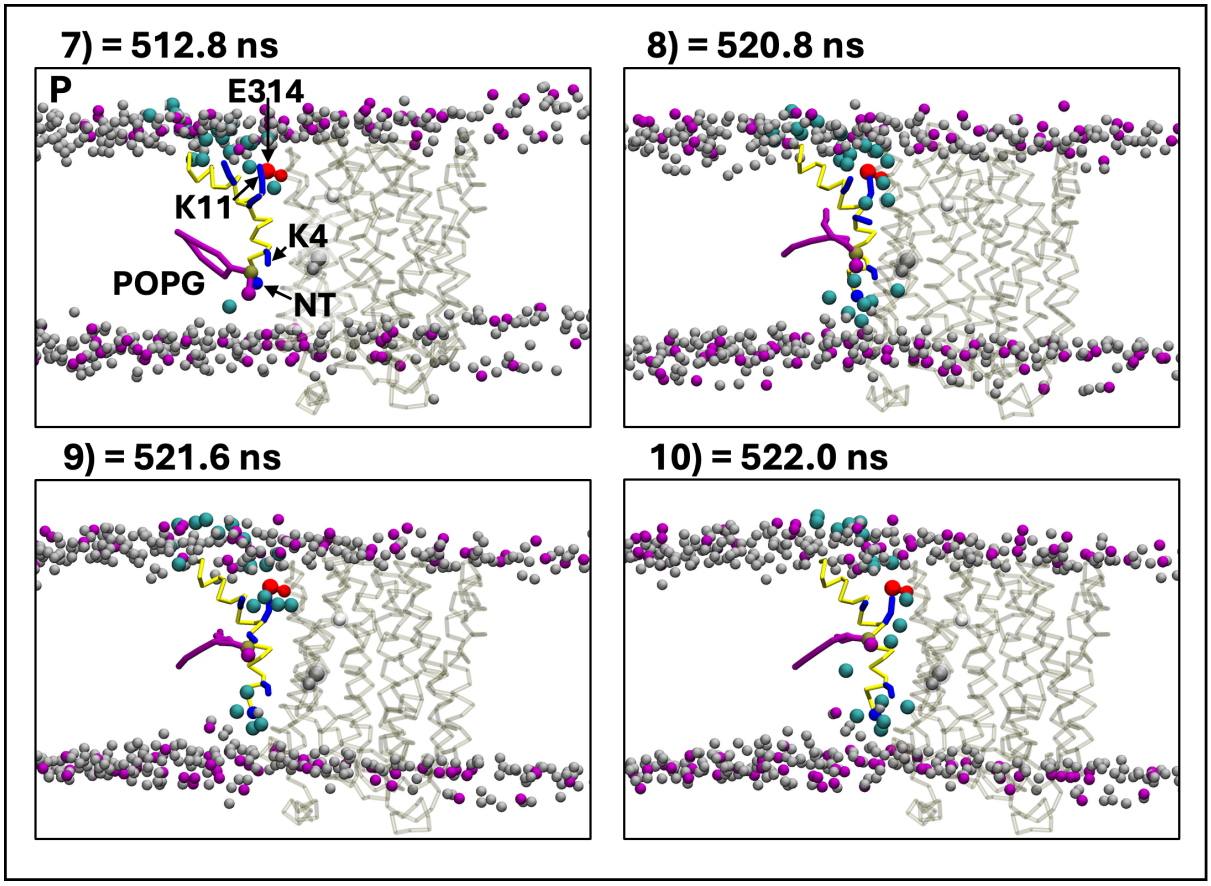

Figure 6.4. *Continuation of* ***Figure 6.3****, with the same representations used. Molecular images ("R-B" simulation) show an example of pore formation via mechanism 1, where the membrane-inserted AMP shuttled a lipid from the distal leaflet across the membrane, leading to increased water infiltration into the hydrophobic core. Waters within 6 Å of the peptide or the highlighted POPG are shown as cyan beads.*

Not all "snorkelling" events led directly to pore formation. In five simulations, peptides stabilised in a transmembrane configuration near LacY without inducing a continuous pore, consistent with prior atomistic simulations that showed spontaneous AMP translocation in bulk lipid membranes without pore formation.[15] Furthermore, across simulations in which a pore formed according to mechanism 1, while a single AMP translocation per trajectory was typical, two independent snorkelling events along separate LacY proteins were also observed in two separate simulations. These

findings suggested that AMP translocation via mechanism 1 could occur even under a weaker induced electric field than the one applied in this work.

The lipid perturbations initiated by this process resulted in local membrane thinning close to LacY, as lipid headgroups were pulled inward. This thinning facilitated further water entry and lipid translocation, allowing the nascent defect to expand rapidly into a water-filled pore within a few nanoseconds, as shown in **Figure 6.5**.

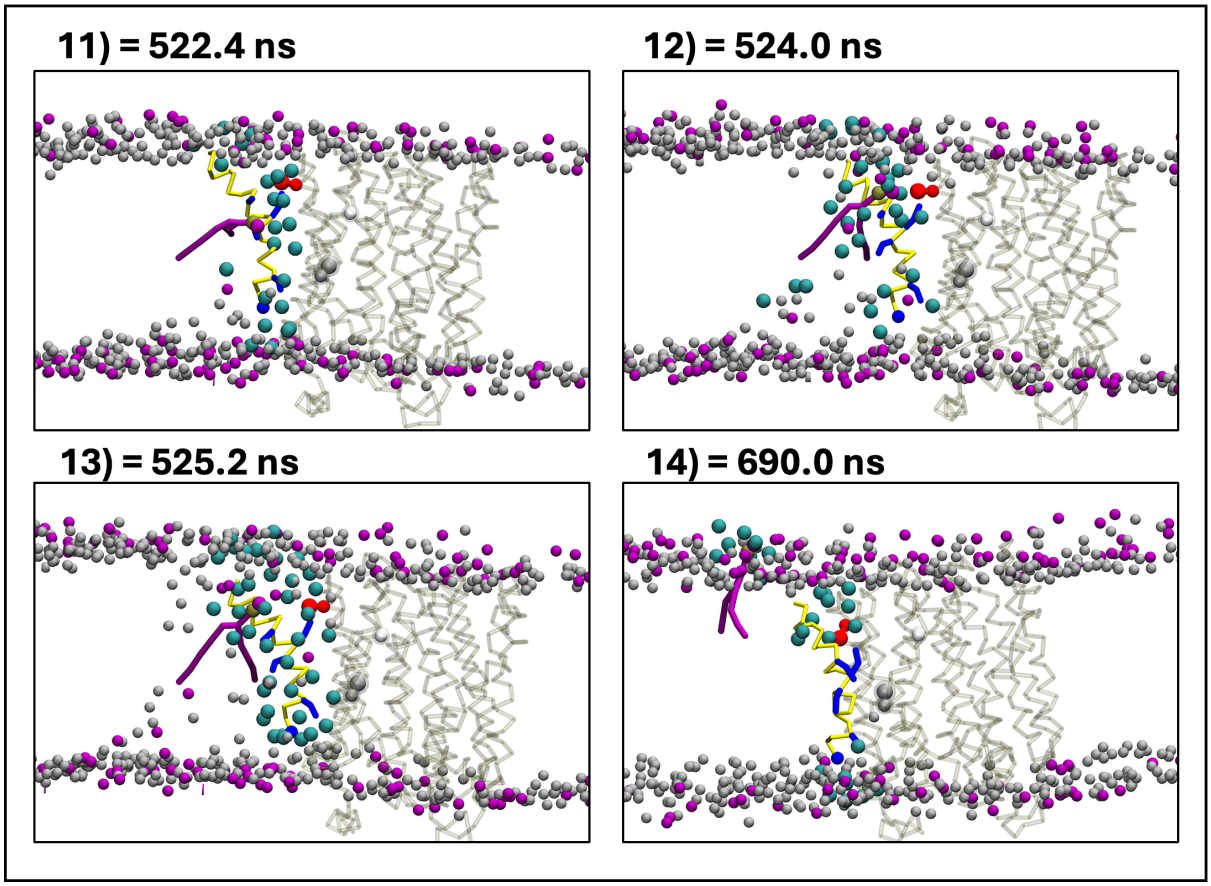

Figure 6.5. *Continuation of* ***Figure 6.4****, with the same representations used. Molecular images ("R-B" simulation) show an example of pore formation via mechanism 1, where the membrane-inserted AMP shuttles a lipid from the distal leaflet across the membrane, leading to increased water infiltration into the hydrophobic core and formation of a transient water pore.*

Lipid flip-flop directionality was observed in pores formed *via* mechanism 1: negatively charged POPG lipids preferentially moved from the outer leaflet toward the positively charged inner compartment, while POPE lipids showed no clear bias, as shown in **Figure 6.6**. This increased AMP-induced lipid exchange between leaflets was consistent with findings from **Chapter 5** and aligned with experimental reports that magainin 2 enhances lipid flip-flop *in vitro*.[16]

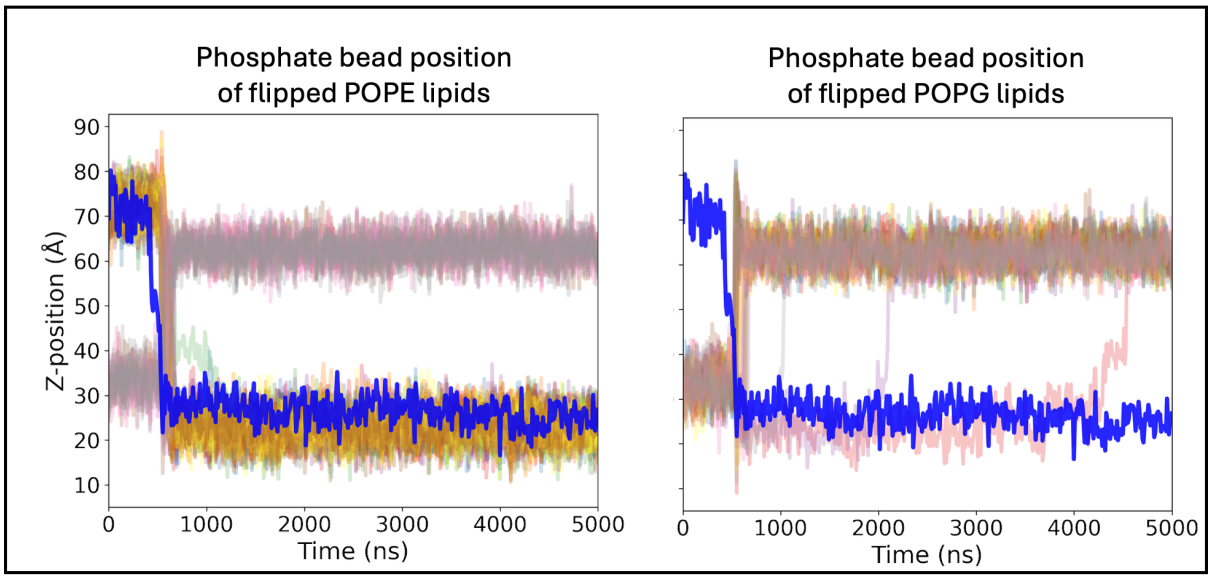

Figure 6.6. *Temporal correlation between AMP transmembrane insertion and lipid flip-flop events. Z-position of phosphate beads of lipids which have changed leaflet (as determined by the MDA LeafletFinder algorithm) are coloured individually, and the Z-position of the AMP N-terminus overlaid in blue.*[17,18]

To conclude this section, mechanism 1 showed how individual AMPs could exploit membrane proteins to translocate across biological membranes, ultimately leading to pore formation.

6.4.1.1.1 Non-pore mechanism of membrane depolarisation by transmembrane AMPs

In addition to causing full water-filled pores, the stable transmembrane state, which was only achieved by M2 peptides near LacY *via* mechanism 1, was also observed to cause membrane depolarisation through two subtler and rarer non-pore-forming pathways: AMP-facilitated lipid flip-flops and ion translocation, as described below.

6.4.1.1.1.1 AMP-induced lipid flip-flops

Membrane-inserted AMPs (*via* LacY-assistance) were repeatedly observed facilitating lipid flip-flop even in the absence of pore formation. In these cases, lipids traversed from the outer to the inner leaflet by sequentially interacting the N-terminus and lysine side chains of the inserted peptide, forming a “shuttling ladder” across the bilayer, as shown in **Figure 6.7**. This observation suggested that peptide insertion alone could locally perturb the membrane to promote lipid flip-flop at membrane-protein interfaces. Such events could thus contribute to membrane depolarisation *via* redistribution of charged lipids, without requiring the formation of water-filled pores.

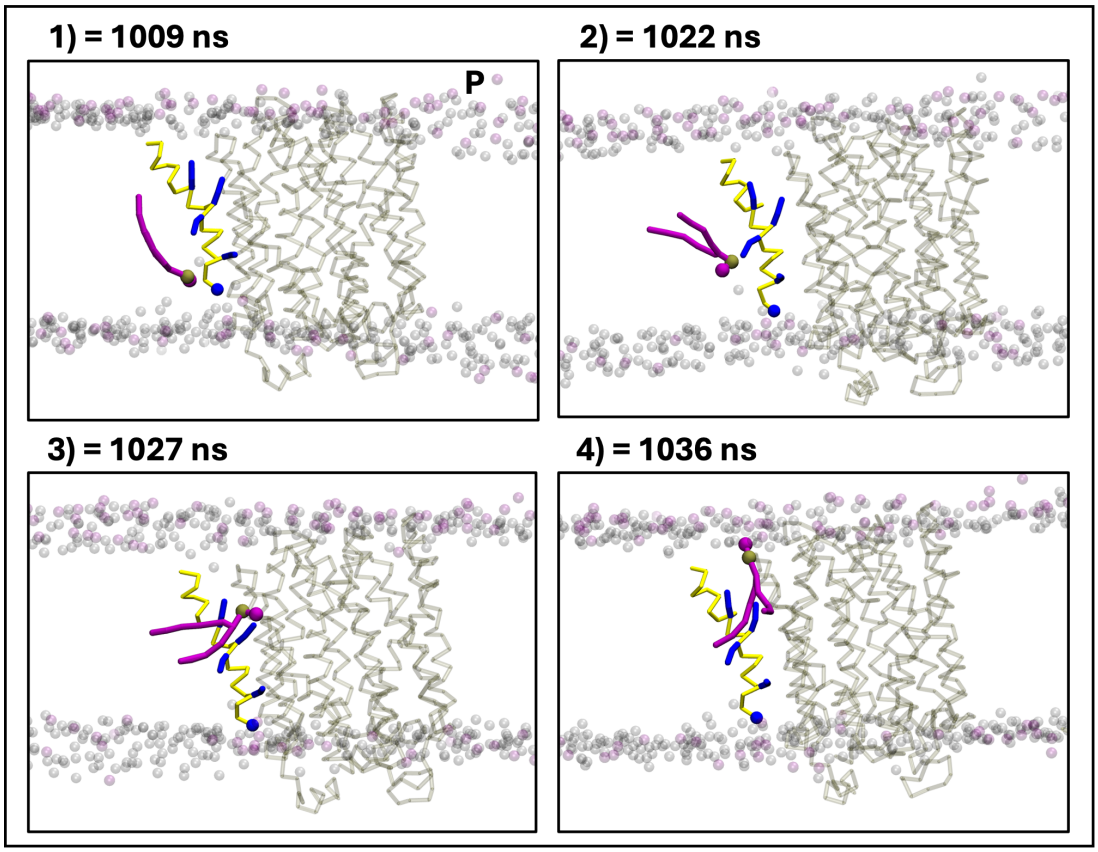

***Figure 6.7**. Example of AMP-facilitated lipid flip-flop without pore formation. Molecular images show a spontaneous POPG flip-flop event occurring alongside a fully inserted M2 peptide at the shallow side of LacY. Lipid headgroups are shown as transparent grey (POPE) and purple (POPG) beads. LacY is shown as a beige backbone. The M2 peptide is represented as a yellow backbone with lysine side chains and its N-terminus in blue. The flipping POPG is highlighted with a purple tail and its headgroup as beads (phosphate headgroup: brown, glycerol bead: purple).*

6.4.1.1.1.2 AMP-induced ion “shuttling”

In addition to lipid flip-flop, membrane-inserted AMPs occasionally enabled individual ions to translocate across the bilayer without the formation of continuous water-filled pores. In these events, chloride ions were the most frequently observed “shuttled” species, moving from one solute compartment to the other while remaining closely associated with the inserted peptide. The ions followed a path along the N-terminus and lysine side chains, suggesting that the charged residues provided a transient, stabilising “shuttling” track across the membrane, as shown in **Figure 6.8**. This behaviour was conceptually analogous to the lipid shuttling ladder described above.

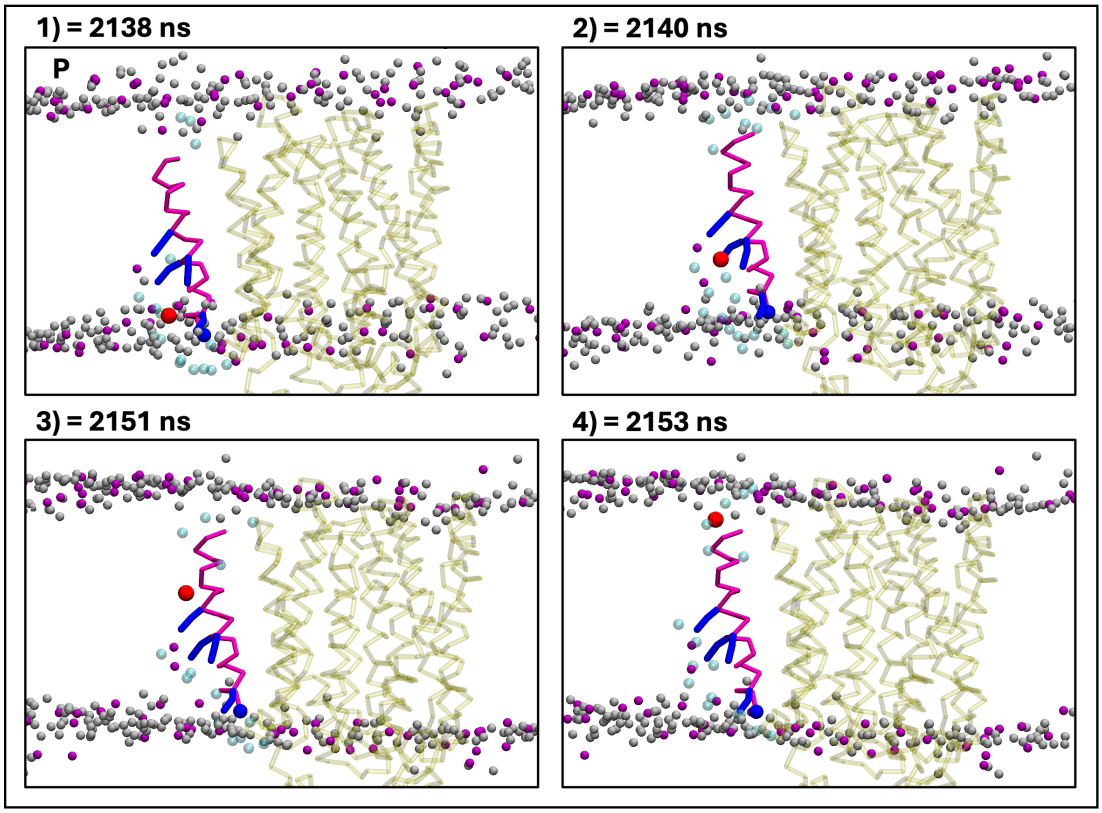

Figure 6.8. *Molecular images which show examples of a spontaneous chloride translocation event along a fully snorkelled M2 peptide at the shallow side of LacY. Lipid headgroups are shown as grey (POPE) and purple (POPG) beads. LacY is represented as a beige backbone. The M2 peptide is shown as a magenta backbone with lysine side chains and N-terminus in blue. The chloride ion is shown as a red bead, and nearby (≤ 6 Å) water molecules as transparent cyan beads.*

Across all reference simulations, ion translocation events occurred at similar frequencies with and without osmolytes, and their directionality was consistent with the applied electric field, as summarised in **Table 6.1**. No solute species other than small ions were observed crossing the bilayer, and ions were only seen traversing regions of the membrane with the involvement of inserted peptides.

Table 6.1. *Summary of ion-shuttling events mediated by stably membrane-inserted transmembrane AMPs across all "R" simulations with an induced electric field. Out = outer compartment, in = inner compartment.*

Name	Simulations with stable transmembrane AMP	Simulations with ion ferrying	Total Cl^- out → in	Total Na^+ in → out	Total Ca^{2+} in → out
R-B	11	6	9	2	2
R-C	6	2	1	3	0

Although ion shuttling was relatively infrequent, my findings indicated that membrane-inserted AMP could facilitate ion translocation without forming classical transmembrane pores. This phenomenon aligned closely with Wimley's interfacial activity model, which proposes that membrane-bound antimicrobial peptides can sufficiently disrupt membrane integrity to enable ion permeation without explicit pore formation.[19] This non-pore-mediated mode of ion permeation may represent an additional mechanism through which AMPs induce membrane depolarisation, complementing classical pore-mediated mechanisms.[19]

6.4.1.1.2 Membrane thickness around LacY in mechanism 1

In both "R-B" and "R-C" simulations, "snorkelled" AMPs responsible for pore formation *via* mechanism 1 were consistently positioned on the LacY-E314 side, near helices V, VIII, and X. Here, the positively charged AMP residues interacted with E314, and local membrane thickness maps showed relative thinning on this side of the protein, as shown in **Figure 6.9**. Thinning was detectable at least 10 ns before visible pore opening, suggesting that AMP-LacY interactions at this site promoted early destabilisation of the bilayer.

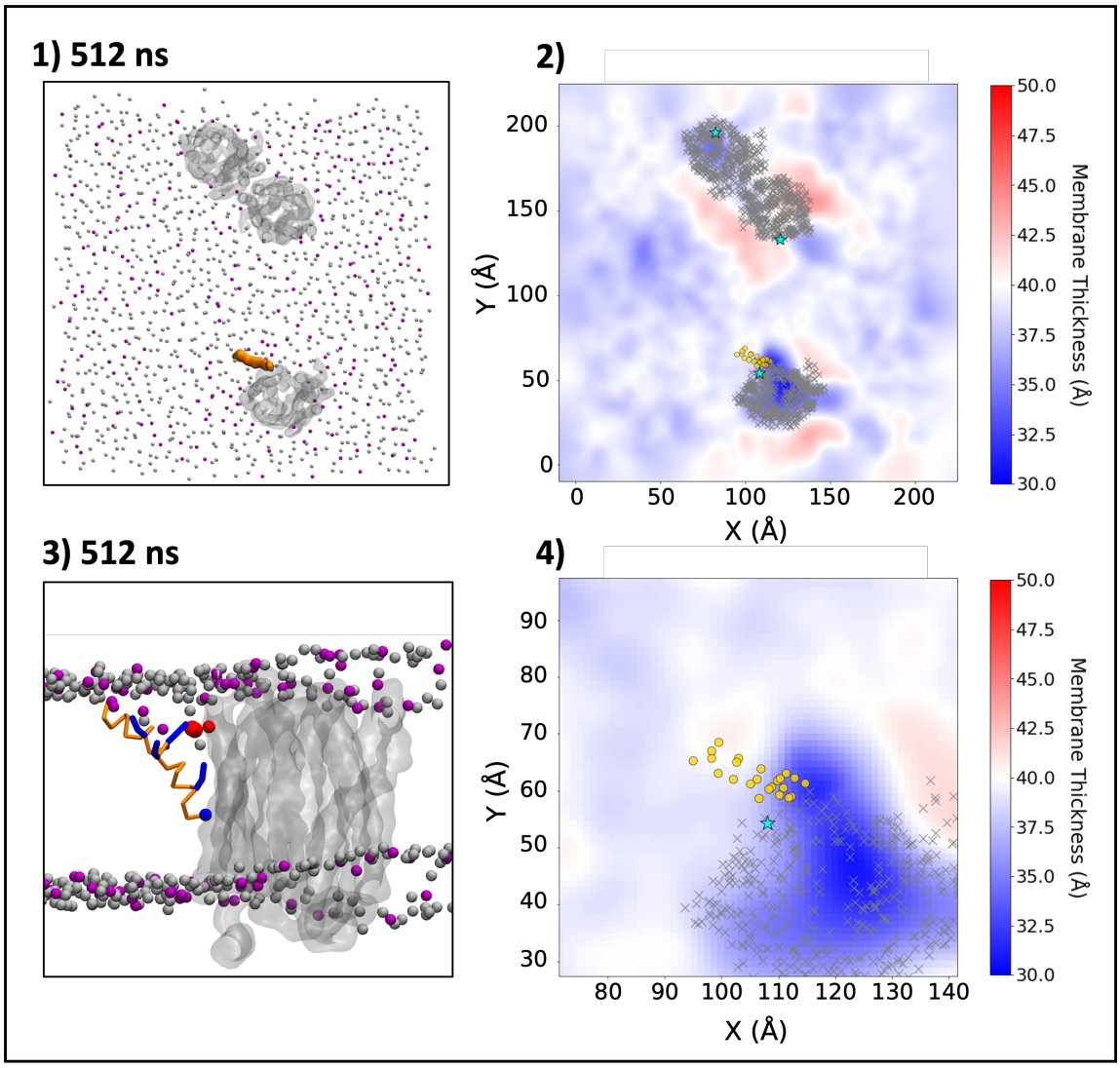

Figure 6.9. *Molecular images and membrane thickness heatmaps ("R-B" simulation), showing the "snorkelled" AMP at LacY 10 ns prior to pore formation via mechanism 1. 1) Relative position of the "snorkelled" M2 (orange surface) and LacY proteins (grey transparent surfaces). 2) Local membrane thickness averaged over the 10 ns before pore formation. AMP backbone beads as orange circles, LacY backbone beads as grey crosses and E314 as cyan stars; membrane thinning in blue, thickening in red. 3) Zoomed-in molecular image of the AMP (orange surface) and LacY (grey transparent surface) of interest. AMP lysines as blue sticks, NT as*

blue bead, LacY E314 as red beads. 4) Zoomed-in membrane thickness map around AMP and LacY of interest, with the same colouring scheme as in 2).

To determine whether such thinning required AMP involvement or could potentially be an intrinsic LacY property, I also analysed local bilayer deformation around LacY in AMP-free "R-A" simulations. Using a radial thickness analysis relative to the protein centre, LacY alone was found to perturb its immediate lipid environment, as shown in **Figure 6.10**. The shallow side around E314 exhibited membrane thinning, while thickening occurred around other regions, indicating that LacY could anisotropically influence bilayer thickness. The thinning effect in AMP-free systems was modest (~2 Å), but became more pronounced when AMPs were present, suggesting that peptide binding reinforced and amplified this LacY intrinsic membrane perturbation.

Interestingly, my findings contrasted with the data available in the MemProtMD database for LacY (PDB: 1PV6), which predicted a membrane-thickening effect on the E314 side, the direct opposite of the thinning observed here.[20] I hypothesised that this discrepancy could stem from methodological differences: the single coarse-grained MemProtMD simulation was conducted in a pure DPPC bilayer, whereas my work used a mixed POPE:POPG membrane, whose distinct physical properties may have produced different protein-lipid packing. Furthermore, my simulations included an induced electrical field, which could also have influenced membrane properties in ways not accounted for in the database simulation.

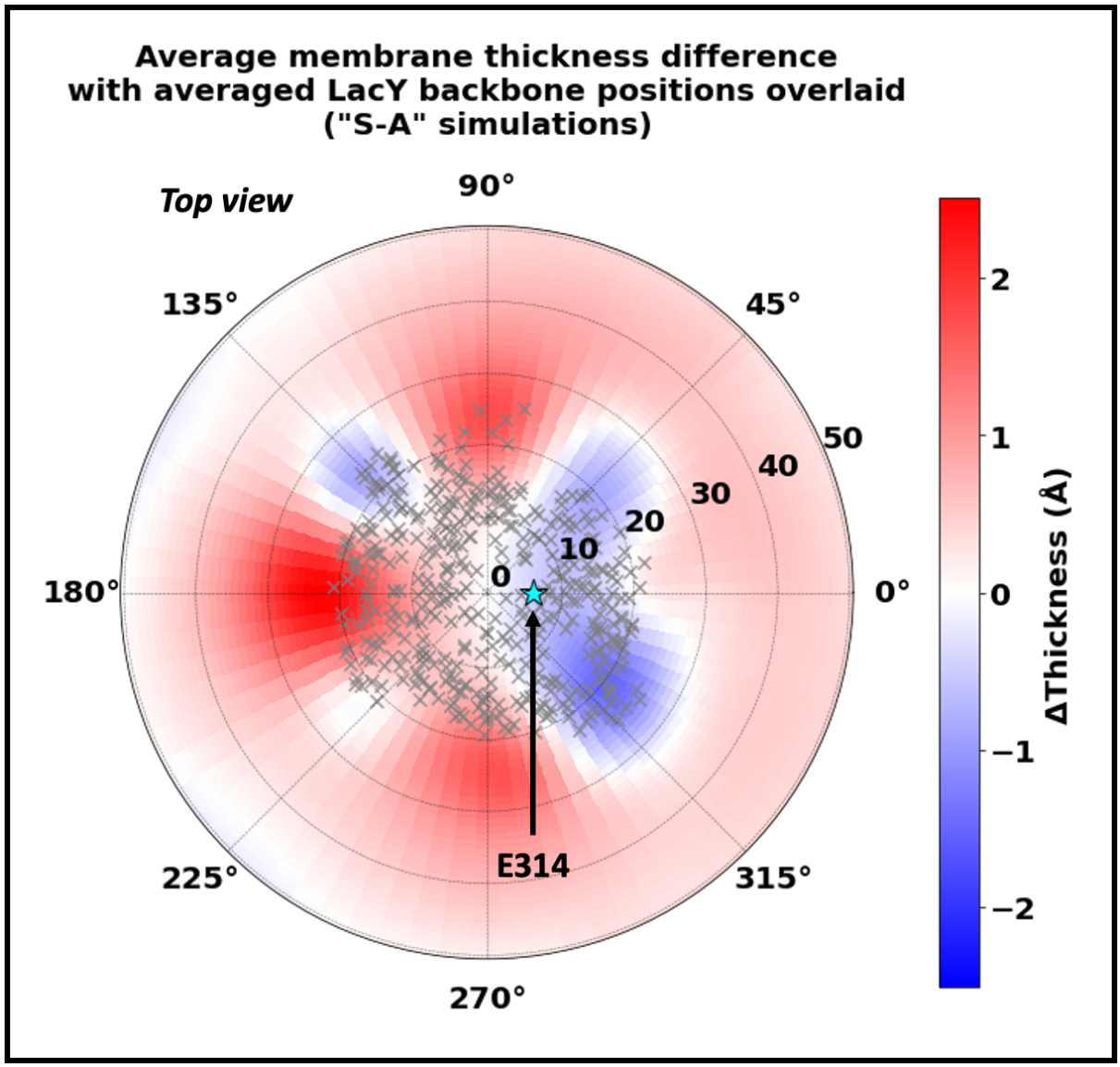

Figure 6.10. *Average membrane thickness difference around LacY in "R-A" simulations, top view onto periplasm-facing side. The polar plot displays the average difference in membrane thickness (in Ångströms) relative to the point at the centre of LacY, calculated in "R-A" (AMP-free) simulations. Averaged backbone positions of LacY are overlaid as grey crosses, with E314 shown as a cyan star. Blue regions denote membrane thinning, red regions indicate membrane thickening. The concentric circles represent the radial distance from the LacY centre in Angstroms, and angular positions are indicated by degrees.*

To conclude, the coincidence of intrinsic thinning around E314 with the presence of a negatively charged residue created a particularly susceptible site for AMP binding and insertion in my systems.

6.4.1.2 Mechanism 3: Lipid defect near LacY without evident AMP involvement

A second, less frequent pore formation mechanism was identified in which local lipid rearrangements at LacY triggered membrane destabilisation without direct AMP involvement. On the shallow side of LacY near helices V/VIII/X, individual lipids were observed to reorient their headgroups into the hydrophilic LacY cavity. This lipid reorientation created a small defect that allowed water molecules to penetrate the bilayer core, after which surrounding lipids progressively tilted their headgroups inward to stabilise the defect. The resulting hydrophilic lining enabled the defect to expand into a continuous water-filled pore, as illustrated in **Figure 6.11**.

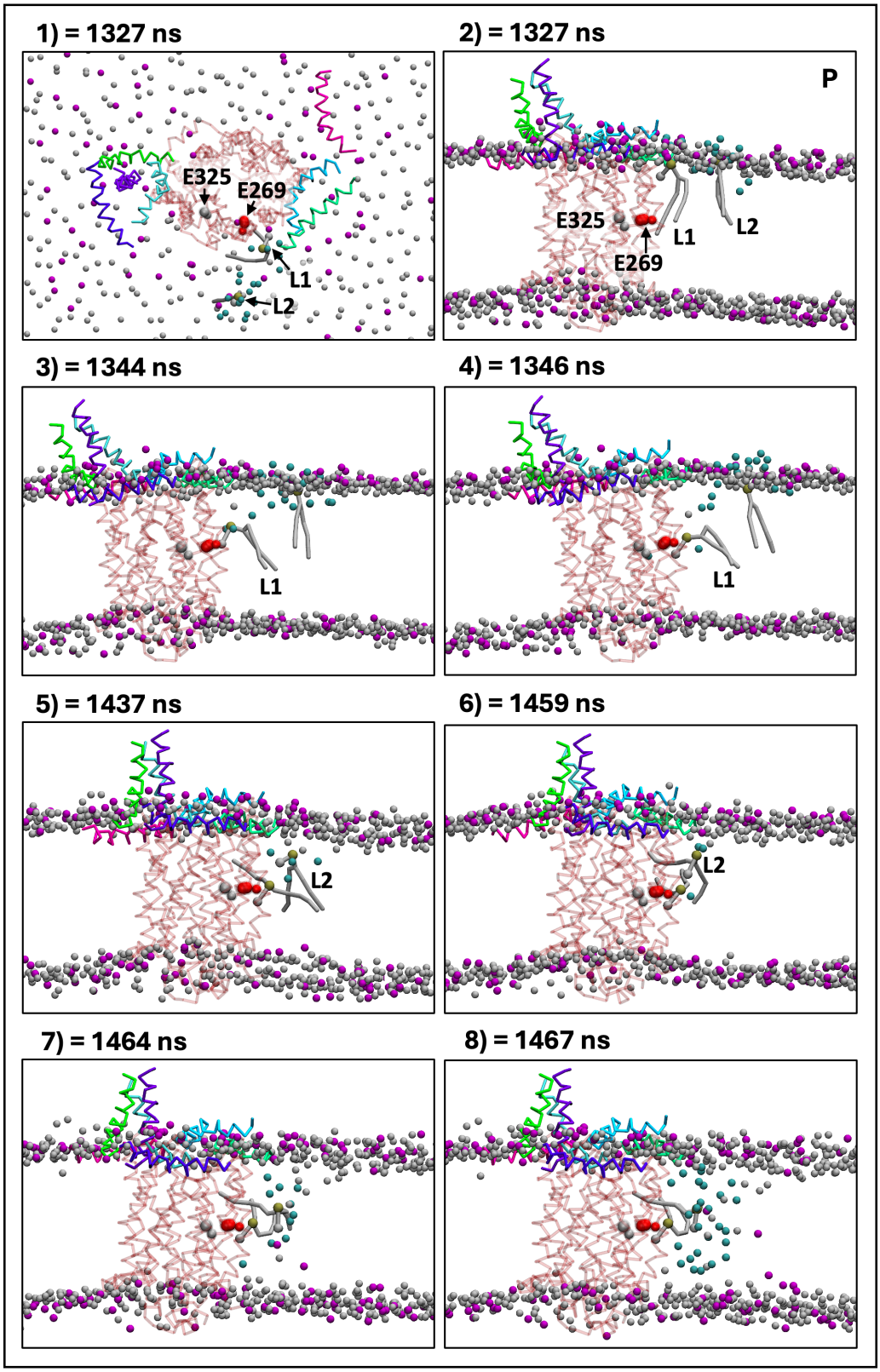

Figure 6.11. *Molecular images ("R-B" simulation) which show examples of the beginning of pore formation via mechanism 3, where a lipid accessed the hydrophilic cavity of LacY and adopted a horizontal orientation, initiating membrane defect and*

subsequent pore formation. AMP backbones are coloured by chain, LacY backbone backbone is shown in red. Lipid headgroups are shown as grey (POPE) and purple (POPG) beads. Selected lipids involved in the early defect (L1, L2) are shown with surface representation. Water beads within 6 Å of selected lipids are shown as cyan beads. LacY residues E269 and E325 are shown for orientation. 1) and 2) show the same simulation frame from top and side views, respectively. 3)-8) show the progression of membrane deformation and pore development over time in a side view.

This mechanism was distinct from AMP-driven modes (mechanisms 1, 2, and 4) in that pore initiation occurred independently of direct peptide involvement and was instead initiated by individual LacY-aided lipid flip-flops. Such individual flip-flop events were infrequent, in contrast to the substantially more numerous lipid flip-flops that accompanied established pores. Although infrequent, this behaviour was consistent with reports that LacY exhibits a “moonlighting” lipid scramblase activity, potentially linked to its transport-cycle conformation.[4]

These findings raise the possibility that the intrinsic scramblase activity of LacY could occasionally initiate defects under an applied field, with AMPs playing a more dominant role in pore expansion. Future computational work could investigate whether mutations such as G46W or G262W, which are known to abolish LacY-induced lipid flip-flops, lock the protein in intermediate conformational states, and are hypothesised to block the periplasmic protein-phospholipid interface, alter lipid scrambling primarily by constraining LacY conformation or through steric hindrance.[4]

6.4.2 Effects of LacY E314 protonation state

In the “L” condition, the E314 residue of LacY was protonated and thus neutral,

effectively mimicking a charge-neutralising mutation such as E314V, also under a +138 *e* charge imbalance as the “R” simulations. Pores formed significantly less frequently ($p < 0.01$, Fisher’s exact test) in the “L” condition than in the reference “R” systems, as shown in **Figure 6.12**. Furthermore, formation *via* mechanism 1 was observed only once across all “L” simulations, at a significantly lower frequency than in the “R” condition ($p < 0.05$, Fisher’s exact test), reinforcing the notion that a negatively charged E314 was an important promoter for this pathway. The sole instance of mechanism 1 in the “L” condition occurred in an osmolyte-free system and involved AMP insertion at the typical "shallow" LacY face, suggesting that this site retained some favourability for AMP “snorkelling” despite the lack of charged E314. This was hypothesised to be linked to the locally reduced membrane thickness, as described above.

By contrast, mechanism 2 was not observed once in the absence of osmolytes, highlighting the importance of osmolyte-mediated AMP-AMP aggregation for this pathway. When osmolytes were present, three pore formation events were detected: two followed mechanism 2, and one followed mechanism 4. Notably, both mechanisms 2 and 4 do not involve AMP-LacY interaction, consistent with the observation that the majority of pores in “L” simulations formed independently of LacY involvement due to the neutralised E314 charge.

Taken together, these results suggested that mechanism 1 was strongly dependent on a charge-based interaction between AMPs and E314 as a “guiding” residue to initiate productive insertion.

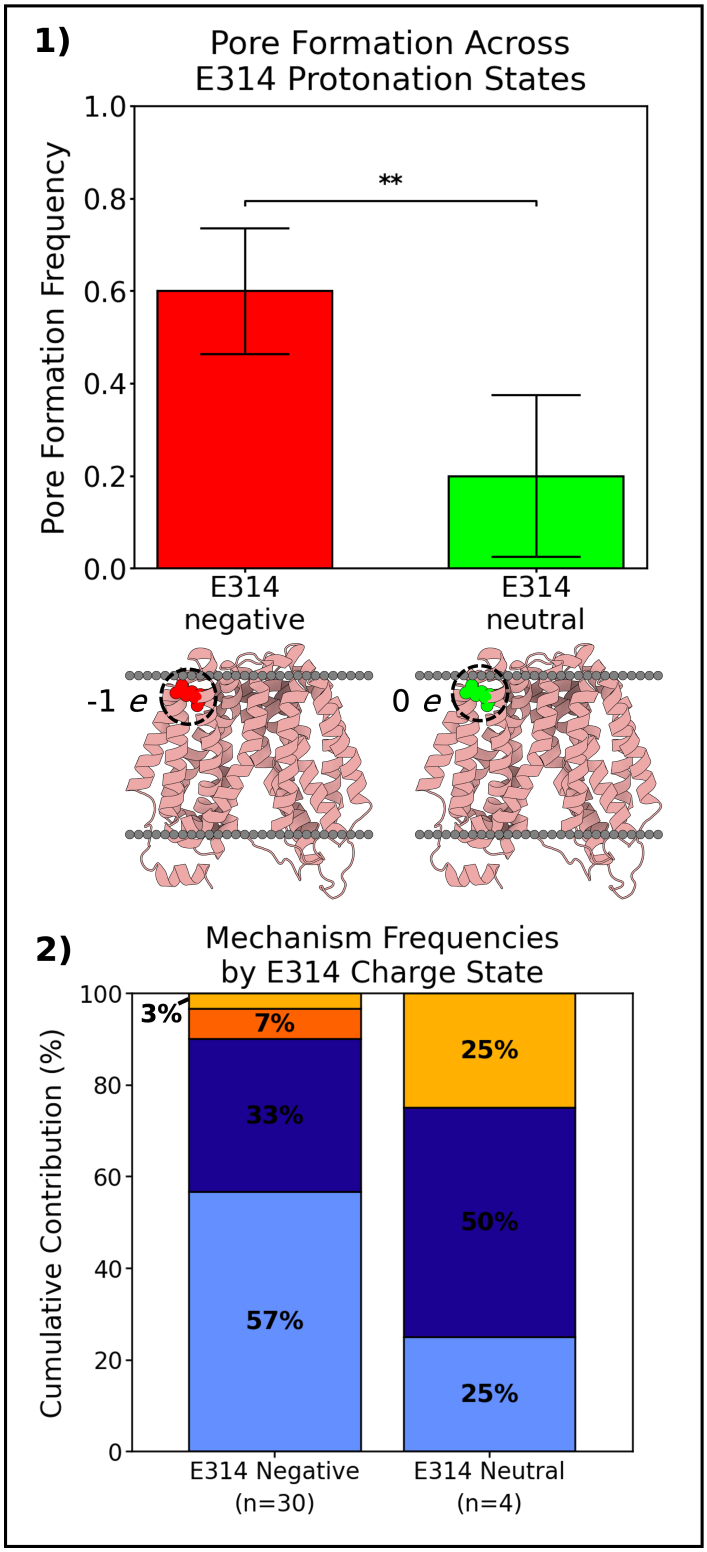

Figure 6.12. *Effect of E314 charge on pore formation frequency and mechanism distribution. 1) Frequency of pore formation in reference simulations containing LacY with a charged (red) or neutralised (green) E314 residue. Bars represent the mean across replicates with 95% confidence intervals, with structural schematics*

illustrating E314 location on LacY below. 2) Stacked bar charts showing the distribution of observed pore formation mechanisms as a function of E314 charge.

The "L^+" condition, which maintained E314 protonation but increased the transmembrane charge imbalance to 144 *e*, resulted in a higher overall rate of pore formation. However, all observed pores were formed *via* mechanisms 3 and 4. As with "M" simulations, this raised concerns about the physiological relevance of these events, as indiscriminate pore formation at membrane proteins was unlikely to be compatible with cell viability. The pronounced membrane deformations observed in this condition suggested that the increased electric field may have been excessively strong for these systems, potentially inducing artefactual pore formations. Crucially, mechanism 1 remained absent in both "L" and "L^+", reinforcing the conclusion that the E314 residue was essential for AMP-assisted "snorkelling" along LacY and membrane insertion in my simulations, and thereby for mechanism 1-driven pore formation.

6.4.3 Osmolyte effects on AMP-LacY aggregation

The following subchapters investigate the effects of osmolytes on AMP-LacY aggregation.

6.4.3.1 LacY surface characterisation

To better understand how LacY acted as an AMP aggregation site, I examined structural and electrostatic features of the membrane pore protein, as shown in **Figure 6.13**. This analysis revealed that the periplasm-facing LacY residues, particularly around the central pore typically involved in sugar transport, present a chemically favourable environment for cationic AMPs. These regions exhibit a high density of polar and charged residues, creating a pronounced negative surface charge that can attract and accommodate the peptides. I also noted that these same features would favour the accumulation of polar osmolytes such as trehalose, a notion consistent with the biological function of LacY as a sugar transporter.

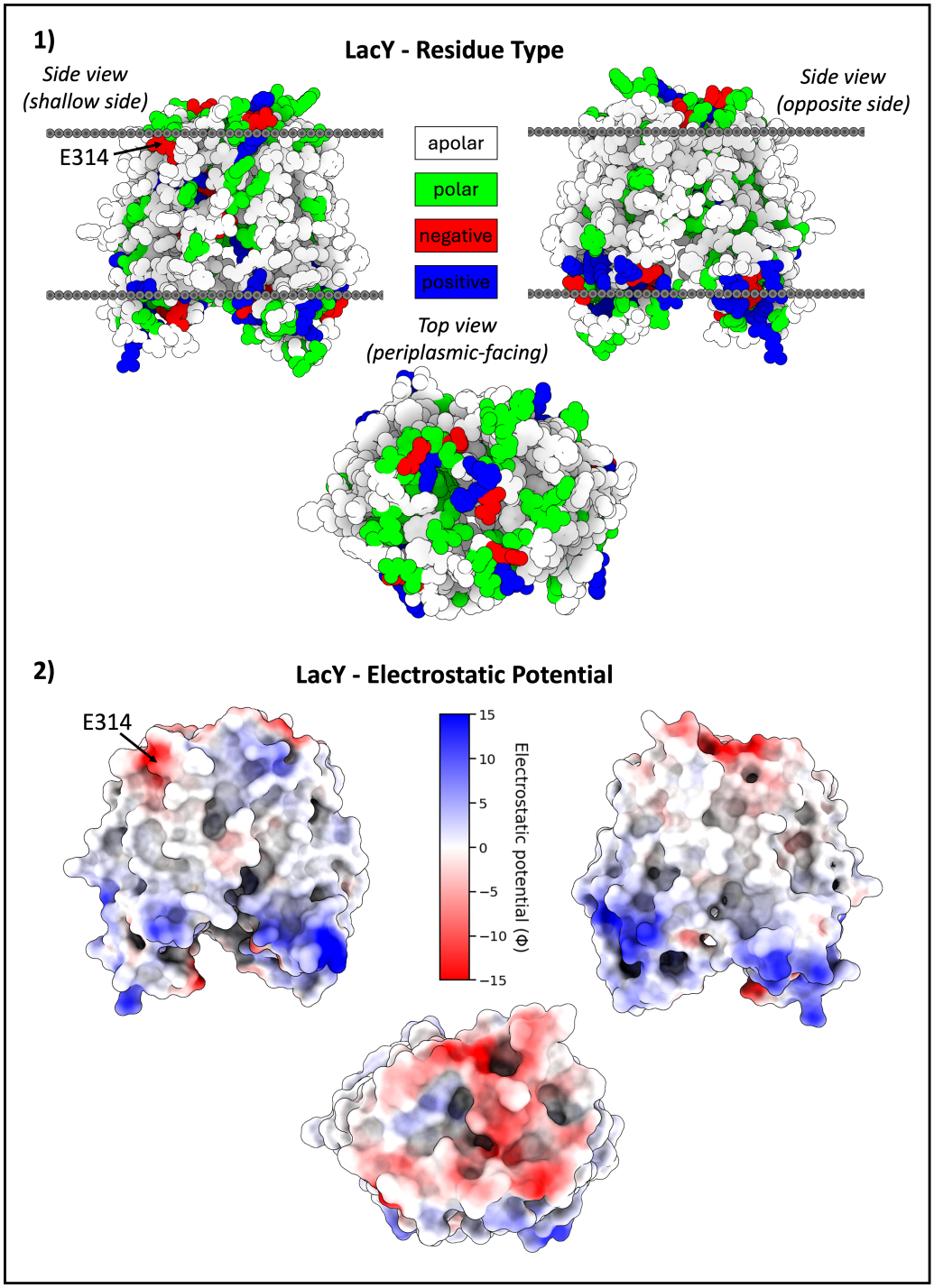

Figure 6.13. *Charge distribution and electrostatic surface potential of LacY. 1) Surface representation of LacY embedded in the membrane and coloured by residue type (apolar: white, polar: green, negatively charged: red, positively charged: blue). Side and top-down views are shown. 2) Electrostatic surface potential (ϕ) of LacY mapped onto the solvent-accessible surface, as calculated using ChimeraX*

and the Adaptive Poisson-Boltzmann Solver (APBS).[21,22] The potential is displayed on a scale of ±15 kT/e, with k being the Boltzmann constant, T the absolute temperature, and e the elementary charge; 1 kT/e ≈ 26.7 mV at 310 K. Red indicates negative potential and blue indicates positive potential. Views correspond to the same orientations as in 1.

6.4.3.2 AMP-LacY surface contacts

I then investigated the influence of osmolytes on AMP localisation relative to LacY in more detail by mapping per-residue contact patterns, as shown in **Figure 6.14**. As expected, the most frequently contacted residues were those exposed on the periplasmic side of LacY, particularly those surrounding the central pore opening. Visual comparison between conditions revealed a subtle but notable shift in contact localisation when osmolytes were present: residues located below the phospholipid headgroup layer, such as E314, previously identified as critical for mechanism 1 (single-AMP snorkelling), were contacted less frequently, while residues clustered near the periplasmic pore entrance (notably D36, H39, and S249) showed increased contact.

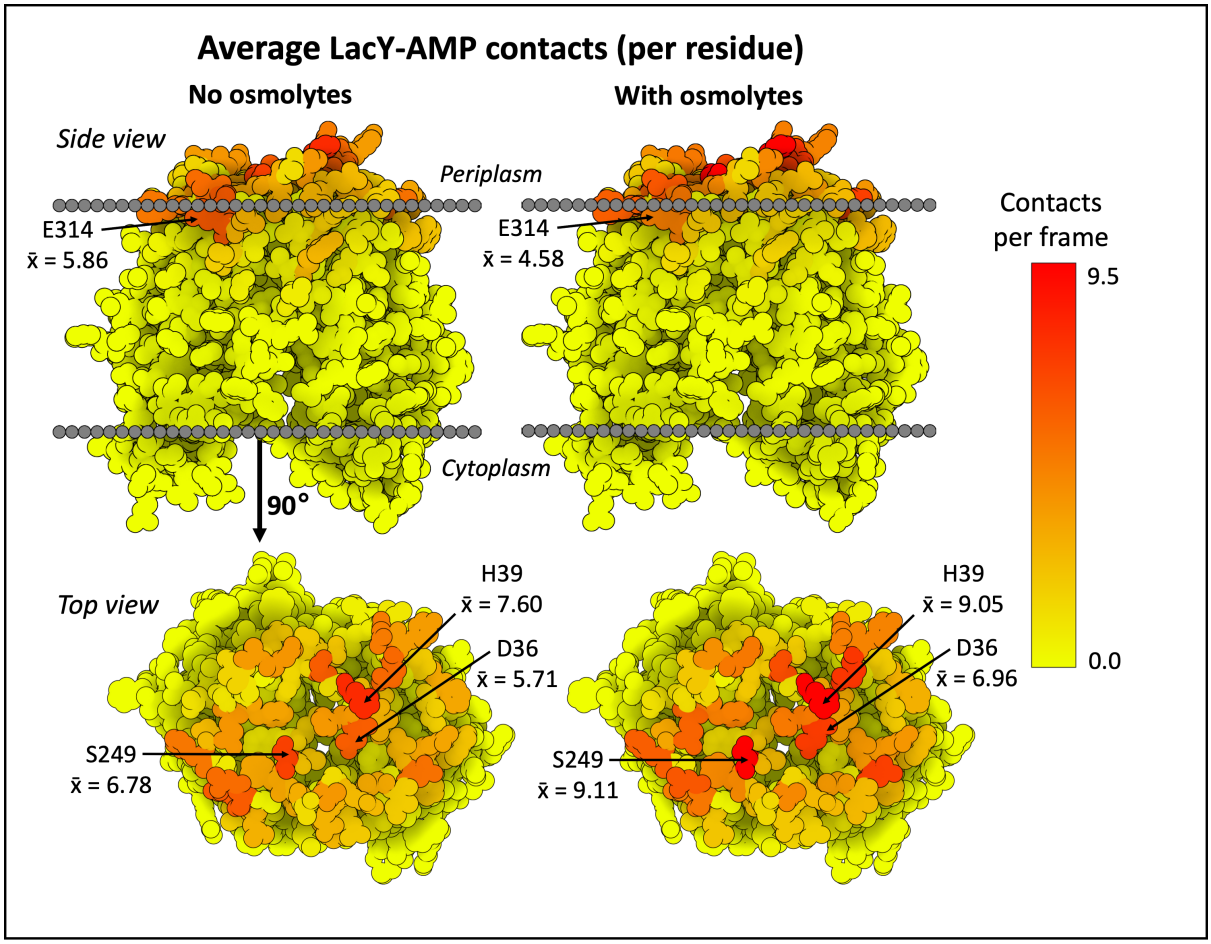

Figure 6.14. *Average number of contacts between LacY and AMPs per LacY residue per frame (over all "R-B" and "R-C" simulations prior to pore formation), with side and top views of LacY. Residue E314 is annotated with its corresponding average contact value.*

To characterise how osmolytes altered AMP interactions with LacY, I first mapped the average per-residue contact frequency across the protein surface, as shown in **Figure 6.15.1**. Contacts were concentrated on the periplasmic side, consistent with the localisation of AMPs in my simulations. In osmolyte-free systems, residues below the headgroup layer, including E314 on the shallow side, were among the most contacted. In contrast, osmolyte-containing systems showed a redistribution of

contacts towards residues at the pore entrance, such as D36, H39, and S249, suggesting that osmolytes promoted AMP interactions closer to the pore channel.

I quantified this redistribution by comparing per-residue contact frequencies across conditions, as shown in **Figure 6.15**. The mapping of these residues confirmed the spatial shift: decreased AMP engagement at E314 and surrounding sub-headgroup residues, and increased contacts at the pore entrance. Notably, the residues most affected were polar or charged side chains, pointing to a role for electrostatic and hydrogen-bonding interactions in driving the redistribution.

Because large datasets can inflate statistical significance, I complemented Mann-Whitney U tests with effect size analysis, with all periplasmic-facing residues showing highly significant differences ($p < 0.0001$) after correction. Cohen's d values demonstrated that the osmolyte-induced changes were not only statistically significant but also substantial in magnitude, as shown in **Figure 6.15**. This further supported the interpretation of a meaningful osmolyte-induced spatial reorganisation of AMP-LacY interactions.

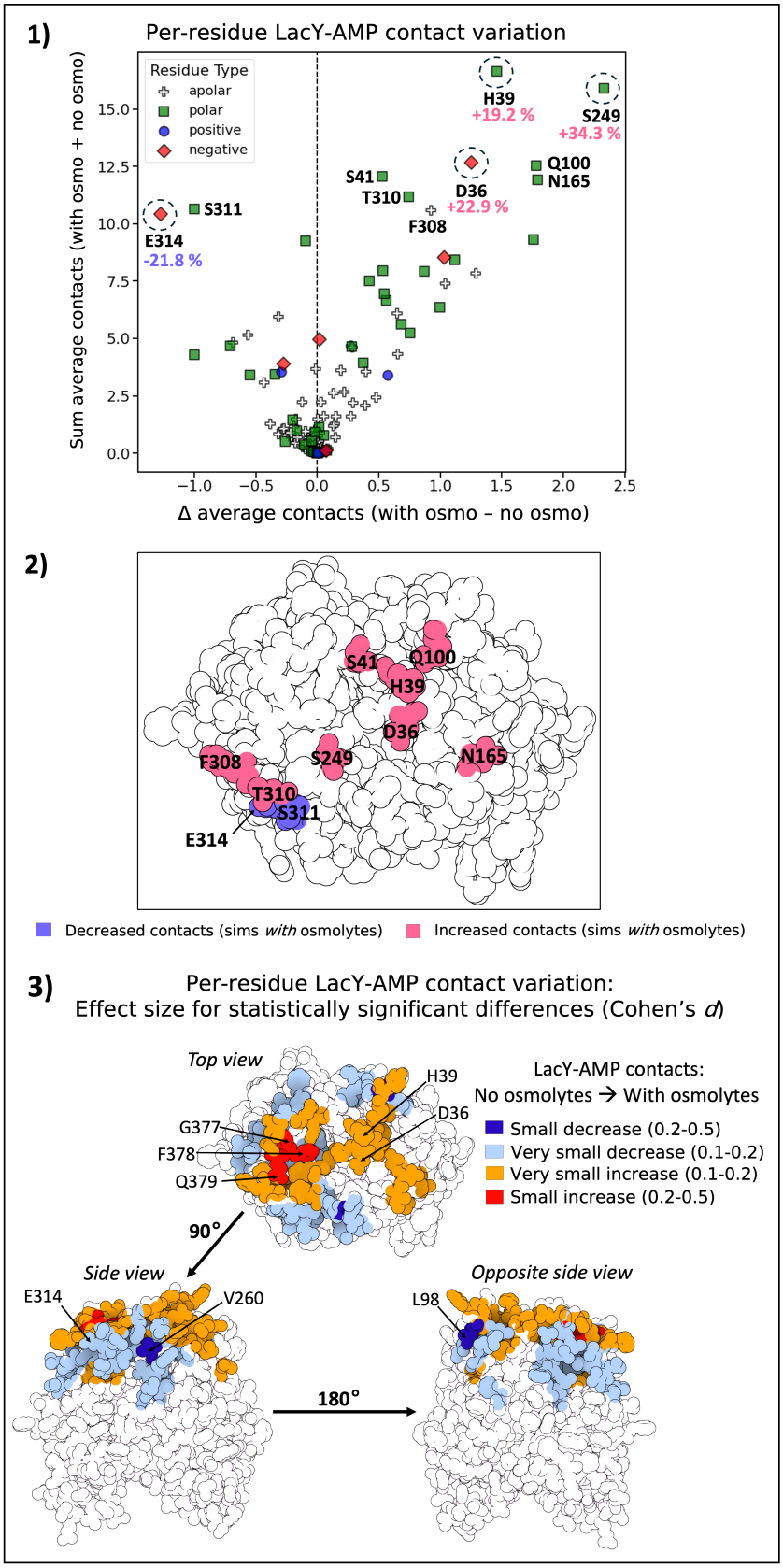

Figure 6.15. *Impact of osmolytes on LacY-AMP contact patterns, showing residue-specific changes in interaction frequency. 1) Per-residue variation in LacY-AMP*

contact number, with scatter plot showing the difference in average contacts ("with osmolytes" minus "without osmolytes") on the x-axis, and the summed average number of contacts across both conditions on the y-axis. Selected LacY residues are annotated with their percentual difference between conditions. 2) Structural molecular representation of LacY highlighting residues with summed average contacts exceeding 10; residues contacted more in the presence of osmolytes are in pink, those contacted less in blue. 3) Per-residue contact variation between osmolyte conditions expressed as effect sizes (Cohen's d), coloured by magnitude and direction of effect: dark blue (small decrease), light blue (very small decrease), orange (very small increase), and red (small increase).

To further investigate the spatial redistribution in AMP-LacY contacts observed in the presence of osmolytes, I analysed average per-residue contact correlations between LacY and different periplasmic solutes respectively AMPs across all "R-C" simulations as shown in **Figure 6.16**. Focusing again on the periplasmic-facing half of LacY, I computed the average number of contacts each residue made with AMP chains and with individual solute species. This allowed us to identify potential overlaps in solute and AMP binding patterns, thereby pinpointing candidate species that could either compete with AMPs for LacY interactions or mediate bridging interactions. Indeed, a strong correlation between solute-LacY and AMP-LacY contacts with high contact numbers for both species would suggest shared binding regions, which may indicate either competitive exclusion or bridging potential. Notably, both calcium ions and trehalose emerged as potential competitors or bridging agents, consistently interacting with the same LacY residues that were most contacted by AMPs-particularly D36, H39, S249, and E314.

Given the prominent role of trehalose in AMP-AMP aggregation as observed previously, I selected it for further analysis as a potential mediator of AMP-LacY interactions. While calcium also showed similar correlation patterns with AMP-LacY contacts, I did not readily observe LacY-CA-AMP bridging configurations in my visual inspections. In contrast, trehalose frequently appeared in such triads, leading us to explore its role further.

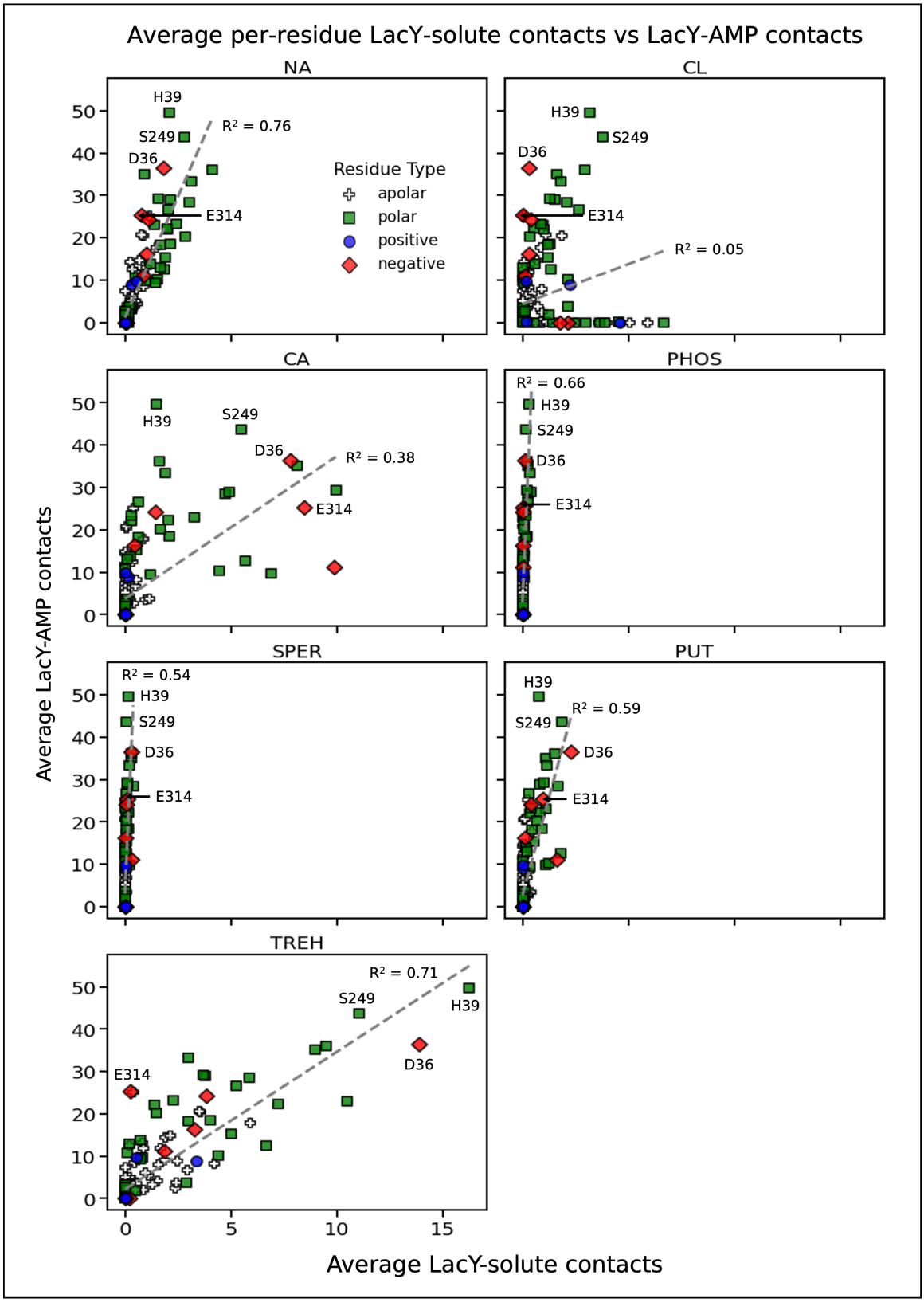

Figure 6.16. *Correlations between average solute-LacY contacts and AMP-LacY contacts, per LacY residue, computed over all frames for simulations containing osmolytes. Each point corresponds to a single LacY residue, colour-coded by*

residue type: apolar (white cross), polar (green square), positive (blue circle), and negative (red diamond). Annotated residues with high contact values with AMPs. The dashed line indicates the best-fit linear regression.

6.4.3.3 LacY-TREH-AMP bridging triads

To test whether trehalose could stabilise AMP-LacY interactions by acting as a bridging agent, I systematically searched for triads in which LacY, an AMP, and a trehalose molecule were simultaneously in contact. Such events were frequently detected across the “R-C” simulations, encompassing both transient and long-lived interactions. The representative trajectory shown in **Figure 6.17** illustrates a particularly stable case: trehalose molecules first accumulated near the periplasmic pore entrance of LacY, followed by the co-localisation of AMPs and trehalose around residue D36. This arrangement persisted for several microseconds, remaining intact until the end of the 5 μs trajectory.

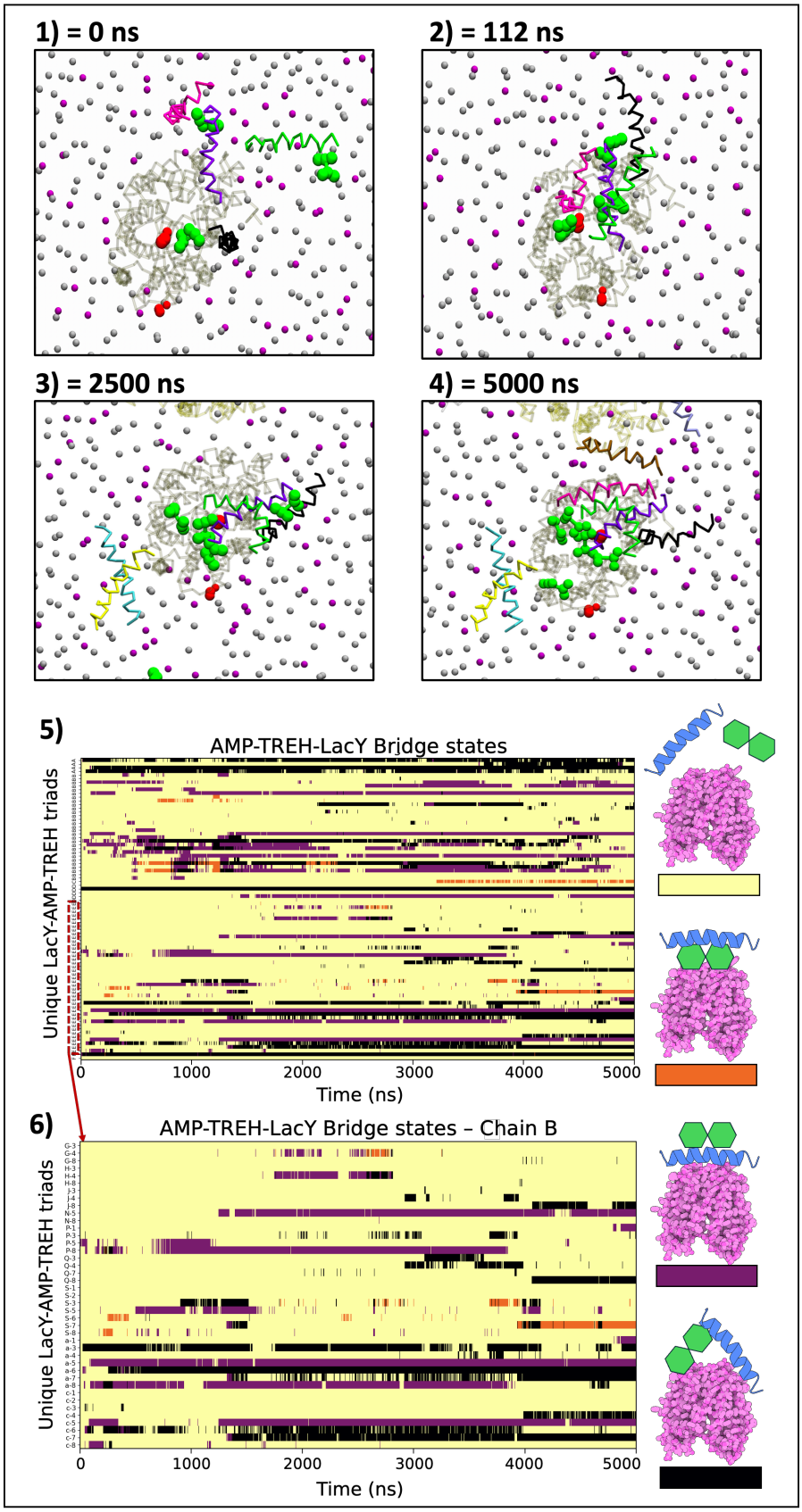

Figure 6.17. *Example of trehalose-mediated bridging between AMPs and LacY, showing how trehalose facilitates AMP-LacY contacts.1)-4) Representative*

molecular snapshots from simulation showing colocalised M2 and trehalose interactions with LacY. LacY is shown as a transparent backbone with E314 as red beads, AMP backbones are coloured and rendered opaquely, and trehalose beads are shown in green. 5)-6) Time-resolved LacY-trehalose-AMPs bridging interactions (cutoff 6 Å) from the simulation shown in 1-4), with 5) representing all LacY-AMP-trehalose triads (for all LacY) detected during the simulation and 6) focusing on the individual LacY shown in 1-4). Each row represents the state of one individual "LacY chain-AMP chain-trehalose molecule" triad. Different states and their colour-coding schematically represented on the right: no active triad = yellow, trehalose-mediated triad = orange, AMP-mediated triad = purple, all three molecules in simultaneous contact = black.

I next examined the spatial distribution of these interactions across all "R-C" simulations. Average LacY-AMP contact frequencies were elevated in the presence of osmolytes, as shown in **Figure 6.18.1**, and agreed with the enhanced aggregation behaviour described earlier. LacY-trehalose contacts were localised primarily at the periplasmic pore entrance, but the central region was partially depleted of trehalose when AMPs were present, suggesting competition for shared binding hotspots, as shown in **Figure 6.18.2**. Finally, bridging events involving all three partners (LacY, AMP, and trehalose) were also concentrated around the central periplasmic pore entrance, as shown in **Figure 6.18.3**, in agreement with my previous observations.

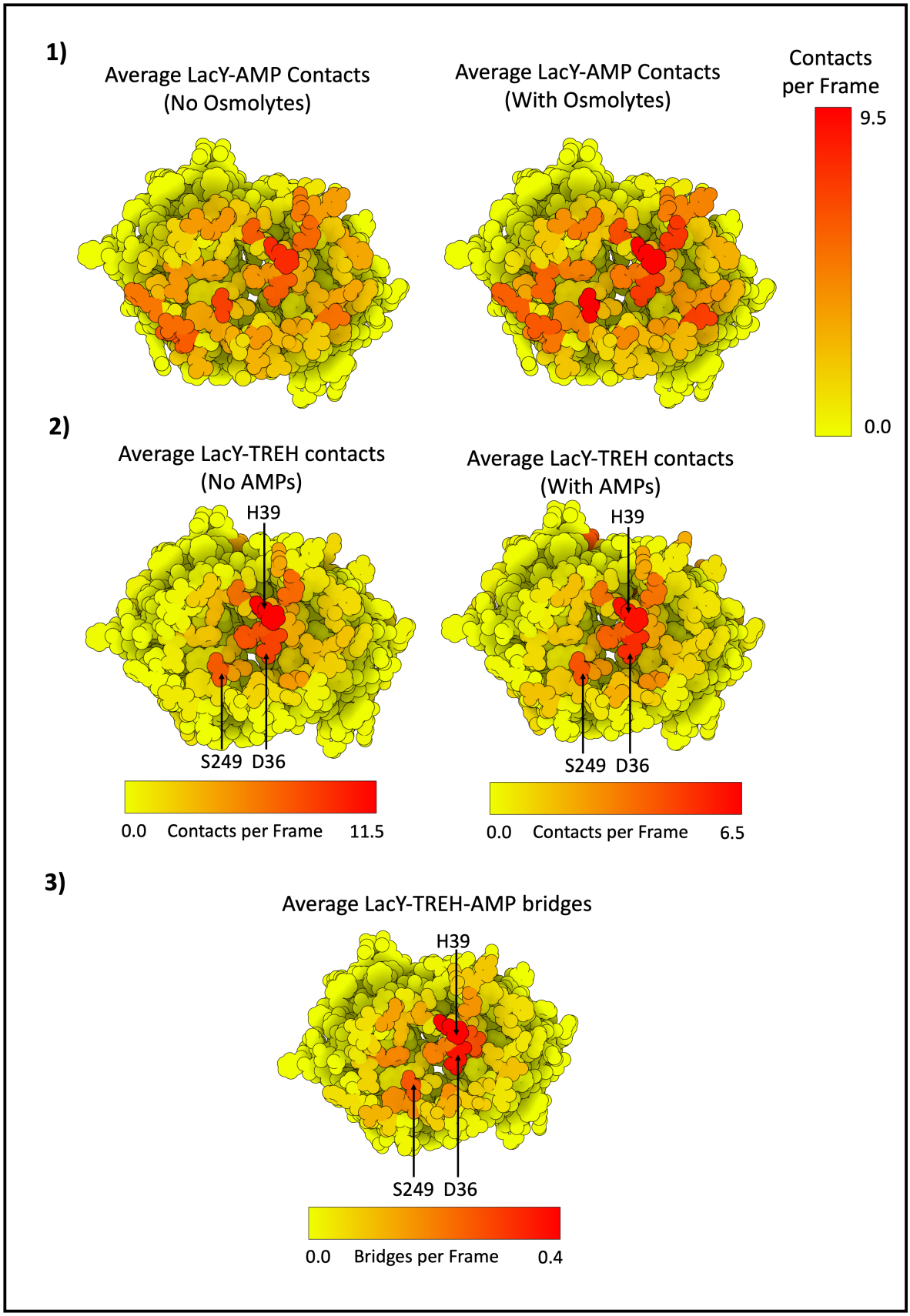

Figure 6.18. *Comparison of LacY contact patterns with AMPs and trehalose.*

1) Average LacY-AMP contacts in the absence (left) and presence (right) of

osmolytes, showing per-residue contact frequencies over all "R-B" and "R-C" simulations. 2) Average LacY-trehalose contacts in the absence (left) and presence (right) of AMPs, computed over all relevant osmolyte-containing simulations. 3) Average occurrence of LacY-trehalose-AMP bridging interactions, defined as frames where trehalose molecules simultaneously contacted both LacY and at least one AMP chain. Colour gradients indicate contact frequency or bridge occurrence, with darker colours denoting higher values.

Taken together, these results suggested that AMPs inherently favoured interaction with LacY near the central pore, and in the presence of trehalose, these interactions were further stabilised and concentrated *via* trehalose-mediated bridging. I interpreted these triads as an important factor contributing to the shift in AMP localisation on LacY observed under osmolyte-containing conditions.

6.4.3.4 LacY-solute contacts

To determine if the observed shift in AMP activity was driven by competitive osmolyte binding at key sites, I analysed solute interactions at specific LacY residues previously identified as functionally relevant, showing occupancy probabilities and number of contacts with solute species, as summarised in **Figure 6.19**. I focused on two distinct regions: the pore entrance residues (D36, H39, S249), which my prior analysis highlighted for their polarity and increased AMP interaction propensity in osmolyte-containing conditions, and the critical residue E314, which I had determined to be highly relevant for pore formation mechanism 1.

These analyses revealed distinct and opposing trends for these two sites. In the presence of osmolytes, the pore entrance residues experienced a significant increase in AMP occupancy. This enhanced interaction, alongside a strong

recruitment of trehalose, resulted in a more crowded local environment and a corresponding decrease in hydration, as can be seen from the decrease in probability of contact and average number of contacts with water molecules (PW). In contrast, E314 showed a marked decrease in AMP contacts as well as a notable increase in its interactions with water and Ca^{2+}, indicating that it had become relatively more accessible to the solvent due to the locally diminished AMP presence.

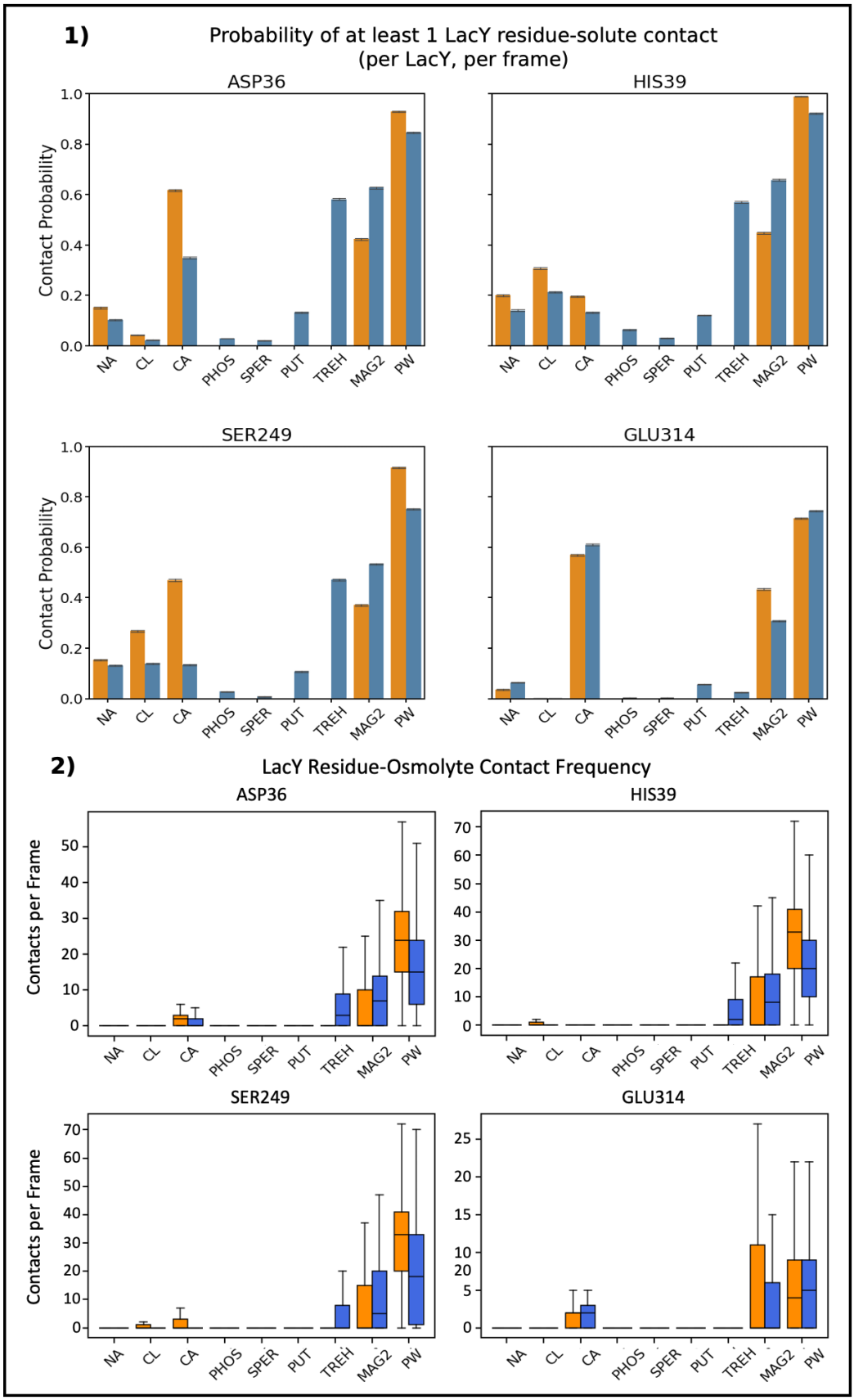

Figure 6.19. *Solute occupancy and contact frequency at key LacY residues involved in AMP binding. 1) Per-residue average solute occupation of selected LacY residues*

with 95% confidence interval. Bar plots show the average per-frame occupancy of individual LacY residues (D36, H39, S249, and S311) by different solute molecules, aggregated over all chains for all "R-B" and "R-C" simulation frames. Occupancy is defined as the fraction of frames in which at least one molecule of a given solute type is within 6 Å of the residue; simulations without osmolytes in orange, with osmolytes in blue. 2) Per-frame number of contacts (6 Å cutoff) per LacY chain for selected residues in "R-B" and "R-C" simulations as boxplots. Outliers not shown for visual clarity.

Taken together, these results allowed us to exclude the hypothesis that osmolytes simply obstruct access to E314. Instead, my data supported a redirection mechanism: while AMPs intrinsically favoured interaction with LacY near the periplasmic pore entrance, the presence of trehalose stabilised and concentrated these interactions, effectively sequestering the peptides at this site. This redistribution drew AMPs away from E314 on the "shallow side" of LacY and shifted the balance of pore formation away from LacY-dependent mechanism 1 towards LacY-independent pathways.

6.5 Conclusion: a multi-faceted model of osmolyte-modulated AMP activity

In this chapter, I investigated how common periplasmic salts and osmolytes affected the interplay between antimicrobial peptides and the bacterial inner membrane. By simulating magainin 2 in systems with an induced electric field in the absence and presence of osmolytes, I developed a model explaining how solutes like trehalose could alter the mechanistic pathways of AMP-induced membrane disruption. The resulting shift in pore formation mechanisms, summarised in **Figure 6.20**, appeared to be driven by two main effects.

Firstly, I observed that periplasmic salts and osmolytes substantially promoted AMP self-aggregation, as described in **Chapter 5**. This change in AMP-AMP intermolecular contacts reduced the pool of monomers available for the E314 "snorkelling" mechanism while increasing the likelihood of pore formation by larger peptide aggregates through the bulk membrane.

Furthermore, as characterised in this chapter, my results indicated a novel AMP redirection and sequestration process centred on LacY, where trehalose accumulated at the pore entrance of LacY, creating a binding hotspot that sequestered AMPs. This preferential binding at the protein pore entrance physically separated the peptides from key residue E314 on its "shallow side," impeding the previously dominant “snorkelling” mechanism.

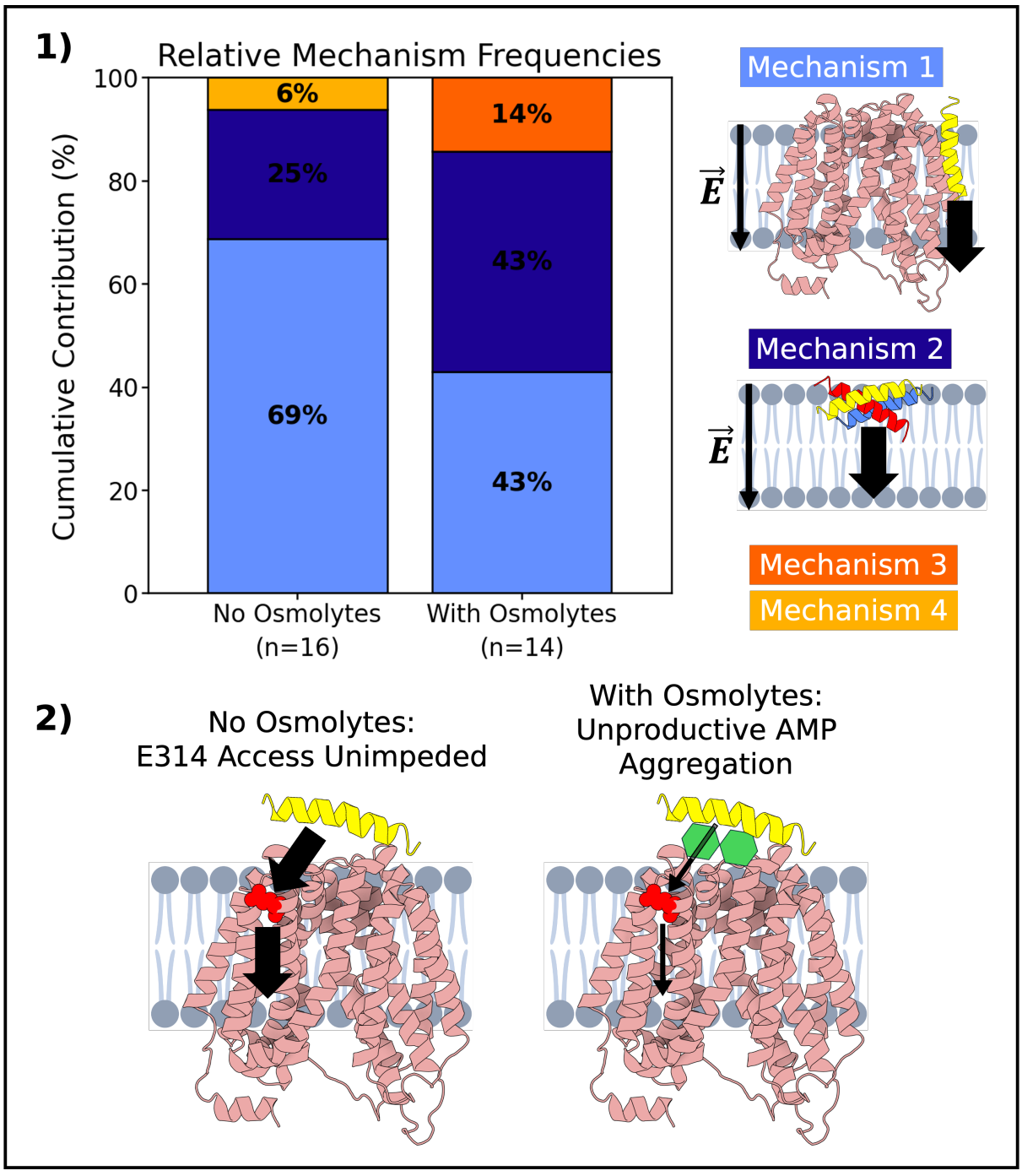

Figure 6.20. *Mechanisms of pore formation in AMP-containing reference systems with and without osmolytes. 1) Stacked bar chart illustrating the relative frequency of the four observed pore formation mechanisms in "R-B" (no osmolytes) and "R-C" (with osmolytes) simulations, with accompanying schematics of the two predominant mechanisms. 2) Schematic representations of the second hypothesised osmolyte-related effect driving the shift in mechanism prevalence: altered AMP-LacY*

aggregation patterns where AMPs become unproductively sequestered at LacY, spatially removed from E314.

The findings of this work have important implications for our understanding of antimicrobial resistance, suggesting that the efficacy of AMPs could be critically modulated by components of a more realistic cellular environment, which are often overlooked in traditional, simplified models. My findings underscore the importance of treating the bacterial cell envelope not as a simple passive background, but as a dynamic and complex system that intimately interacts with therapeutics. A deeper understanding of these intricate, environment-dependent interactions is therefore essential for developing next-generation antimicrobial strategies that can overcome such sophisticated defences.

References

1. Stelzl, L. S., Fowler, P. W., Sansom, M. S. P. & Beckstein, O. Flexible Gates Generate Occluded Intermediates in the Transport Cycle of LacY. *J. Mol. Biol.* **426**, 735–751 (2014).
2. Holyoake, J. & Sansom, M. S. P. Conformational Change in an MFS Protein: MD Simulations of LacY. *Structure* **15**, 873–884 (2007).
3. Mirza, O., Guan, L., Verner, G., Iwata, S. & Kaback, H. R. Structural evidence for induced fit and a mechanism for sugar/H+ symport in LacY. *EMBO J.* **25**, 1177–1183 (2006).
4. Wang, L. & Bütikofer, P. Lactose Permease Scrambles Phospholipids. *Biology* **12**, 1367 (2023).
5. Jahn, H. *et al.* Phospholipids are imported into mitochondria by VDAC, a dimeric beta barrel scramblase. 2022.10.17.512472 Preprint at https://doi.org/10.1101/2022.10.17.512472 (2023).
6. Li, D., Rocha-Roa, C., Schilling, M. A., Reinisch, K. M. & Vanni, S. Lipid scrambling is a general feature of protein insertases. 2023.09.01.555937 Preprint at https://doi.org/10.1101/2023.09.01.555937 (2023).
7. Bartoš, L., Menon, A. K. & Vácha, R. Insertases Scramble Lipids: Molecular Simulations of MTCH2. 2023.08.14.553169 Preprint at https://doi.org/10.1101/2023.08.14.553169 (2023).
8. Ludtke, S., He, K. & Huang, H. Membrane thinning caused by magainin 2. *Biochemistry* **34**, 16764–16769 (1995).
9. Grage, S. L., Afonin, S., Kara, S., Buth, G. & Ulrich, A. S. Membrane Thinning and Thickening Induced by Membrane-Active Amphipathic Peptides. *Front. Cell Dev. Biol.* **4**, 65 (2016).

10. Booth, I. R. Regulation of cytoplasmic pH in bacteria. *Microbiol. Rev.* **49**, 359–378 (1985).
11. Zilberstein, D., Agmon, V., Schuldiner, S. & Padan, E. Escherichia coli intracellular pH, membrane potential, and cell growth. *J. Bacteriol.* **158**, 246–252 (1984).
12. Kashket E R. Effects of aerobiosis and nitrogen source on the proton motive force in growing Escherichia coli and Klebsiella pneumoniae cells. *J. Bacteriol.* **146**, 377–384 (1981).
13. Tieleman, D. P. The molecular basis of electroporation. *BMC Biochem.* **5**, 1–12 (2004).
14. Piggot, T. J., Holdbrook, D. A. & Khalid, S. Electroporation of the E. coli and S. aureus membranes: molecular dynamics simulations of complex bacterial membranes. *J. Phys. Chem. B* **115**, 13381–13388 (2011).
15. Ulmschneider, J. P. Charged Antimicrobial Peptides Can Translocate across Membranes without Forming Channel-like Pores. *Biophys. J.* **113**, 73–81 (2017).
16. Matsuzaki, K., Murase, O., Fujii, N. & Miyajima, K. An Antimicrobial Peptide, Magainin 2, Induced Rapid Flip-Flop of Phospholipids Coupled with Pore Formation and Peptide Translocation. *Biochemistry* **35**, 11361–11368 (1996).
17. Michaud-Agrawal, N., Denning, E. J., Woolf, T. B. & Beckstein, O. MDAnalysis: a toolkit for the analysis of molecular dynamics simulations. *J. Comput. Chem.* **32**, 2319–2327 (2011).
18. Gowers, R. J. *et al.* MDAnalysis: A Python Package for the Rapid Analysis of Molecular Dynamics Simulations. *Proc. 15th Python Sci. Conf.* 98–105 (2016) doi:10.25080/Majora-629e541a-00e.

19. Wimley, W. C. Describing the Mechanism of Antimicrobial Peptide Action with the Interfacial Activity Model. *ACS Chem. Biol.* **5**, 905–917 (2010).
20. Newport, T. D., Sansom, M. S. P. & Stansfeld, P. J. The MemProtMD database: a resource for membrane-embedded protein structures and their lipid interactions. *Nucleic Acids Res.* **47**, D390–D397 (2019).
21. Goddard, T. D. *et al.* UCSF ChimeraX: Meeting modern challenges in visualization and analysis. *Protein Sci. Publ. Protein Soc.* **27**, 14–25 (2018).
22. Jurrus, E. *et al.* Improvements to the APBS biomolecular solvation software suite. *Protein Sci.* **27**, 112–128 (2018).

Chapter 7: Conclusions and future work

7.1 Conclusions

In this thesis, I investigated the interactions between antimicrobial peptides and the crowded molecular environment of the *E. coli* periplasm and its inner membrane. I used atomistic and coarse-grained molecular dynamics simulations to examine the influence of periplasmic osmolytes on peptide aggregation in solution, as well as in the context of membrane systems under an imposed transmembrane potential.

In **Chapter 3**, which investigated peptide behaviour in solution prior to membrane association, I found that peptide sequence, initial conformation, ionic strength, and osmolyte inclusion each influenced aggregation. I considered three representative linear α-helical amphipathic cationic peptides, magainin 2, cupiennin 1a, and latarcin 1, which I selected to represent AMPs with different charge densities.

Across all conditions, the three peptides aggregated into micelle-like structures with hydrophobic cores and outward-facing polar and charged residues. Aggregation strength varied with sequence, reflecting differences in charge density between the peptides. Even within this small set of amphipathic cationic peptides, I observed different responses to AMP conformation: α-helical structures favoured aggregation for magainin 2 and cupiennin 1a, whereas the denatured form of latarcin 1 aggregated more readily than its helical counterpart.

Increasing salt concentration promoted aggregation by shielding cationic AMP sidechains from each other and thus reduced electrostatic repulsion between them. Osmolytes further modulated aggregation through numerous short-lived peripheral contacts, which affected charge screening and local crowding, effectively stabilising

AMP aggregates. Charged species showed clear residue-specific preferences, while neutral osmolytes engaged more broadly through polar interactions. The combined action of multiple solutes acting through different modes increased the overall aggregation behaviour.

Together, these findings provided a first mechanistic insight into how interactions with periplasmic osmolytes could influence AMP behaviour during their transit across the periplasm.

Subsequent double-membrane simulations in **Chapters 4, 5, and 6** extended these findings to more complex models, simulating AMPs in the environment of the polarised *E. coli* inner membrane. These systems were used with the Computational Electrophysiology protocol, which mimicked the native transmembrane potential and enabled observations of peptide-driven pore formation both with and without the involvement of the membrane protein LacY.

Pores were observed only when both AMPs and an applied field were present, with neither factor alone being sufficient to induce pores under my simulation conditions. Four distinct pathways were observed, among which two were more common: mechanism 1, defined by single-AMP “snorkelling” along LacY *via* E314, and mechanism 2, characterised by bulk membrane rupture induced by AMP aggregates. Two substantially rarer mechanisms were further observed: mechanism 3, a LacY-centred lipid defect without direct AMP involvement, and mechanism 4, in which a single AMP led to bulk-membrane rupture.

The relative prevalence of these pathways depended on the solute composition: overall pore frequencies were comparable between systems with and without

osmolytes, but the inclusion of osmolytes increased the proportion of pores formed *via* mechanism 2 and reduced those formed *via* mechanism 1.

In aggregate-driven pores, AMP clusters locally thinned the bilayer and facilitated water entry, following a mechanistic sequence consistent with the classical electroporation model. The inclusion of osmolytes promoted increased peptide aggregation, mainly through transient trehalose- and phosphate-mediated AMP-AMP contacts on the membrane surface.

In membrane protein-dependent pores, AMPs typically first formed transient electrostatic interactions between their positively charged residues and E314 on LacY, located just beneath the lipid headgroups on the periplasmic membrane side. From this position, they advanced along the protein surface and inserted into the membrane, a process I referred to as “snorkelling”. Neutralising the charge of E314 through *in silico* mutation markedly reduced the frequency of this pore formation mechanism.

In the presence of osmolytes, AMPs were preferentially sequestered near the periplasmic pore opening of LacY, where they formed complexes with LacY and trehalose instead of “snorkelling” through the membrane along the E314 side, leading to relatively fewer pores formed *via* mechanism 1.

Taken together, these results provided molecular insights into how the chemical and structural complexity of the periplasmic space could influence AMP behaviour in distinct ways. Comparisons with simulation and experimental AMP studies reinforced the notion that the solute composition can significantly affect peptide behaviour.[1–6]

7.2 Limitations and future work

The lack of precise experimental data on the molecular composition and concentrations of solutes within the periplasm currently limits the accuracy of models of the *E. coli* envelope. This uncertainty may also mean that important biological context is missing, potentially explaining why the mechanisms of action of AMPs remain incompletely understood to date and making these peptides difficult to translate into effective therapeutics.

Future work should therefore focus on developing more biologically informed models that better approximate the environment AMPs encounter when traversing bacterial cell envelopes. For example, including the peptidoglycan cell wall into double-membrane systems with AMPs in different aggregate states would extend upon previous simulation works, whose focus was primarily on differential AMP-cell wall interactions rather than on the influence of aggregate size on AMP translocation across the cell wall.[2] Additionally, the inclusion of major periplasmic chaperones such as Skp or SurA, or specific AMP-resistance proteins like YdeI, could reveal unexpected modes of interaction with AMPs, potentially modifying their translocation behaviour, as previously shown for polymyxin B1 and the lipoprotein carrier LolA.[1,7] Furthermore, testing additional membrane proteins within the CompEL framework would clarify whether the mechanisms identified in this work are specific to LacY or extend to other scramblases and potentially to membrane proteins in general. Within the same framework, it would also be valuable to include AMP mixtures such as magainin 2 and PGLa, which are known to act synergistically, and to test the magnitude of cooperative effects under an applied transmembrane potential.

To further assess the robustness of the molecular mechanisms observed in this work, it would be informative to repeat key simulations using alternative force fields, since biases in peptide aggregation and protein-protein interactions are known to vary across parameter sets.[8–12] Such differences can influence oligomerisation behaviour and interaction strengths, which would likely have downstream effects in all the systems examined in my work, where protein-protein aggregation played a central role.[8–12]

Beyond these system-specific extensions, broader methodological issues affect the reproducibility and comparability of AMP studies. Variability in *in vitro* experimental parameters such as membrane lipid composition, peptide-to-lipid ratio, temperature, pH, and medium conditions has been reported to lead to conflicting observations.[13–15] For example, kinetic dye-release studies showed that seemingly contradictory conclusions in the literature regarding the mechanism of action of magainin 2 could be explained by differences in the lipid systems used by the respective research groups.[13] More generally, antimicrobial susceptibility testing studies have shown that variations in pH, ionic strength, and medium all substantially affect measured AMP activity, with a lack of experimental condition standardisation hampering meaningful comparisons of AMP efficacy.[14]

Equivalent challenges exist in *in silico* studies, where differences in force fields, system composition, and simulation protocols can yield opposing outcomes. For example, using different versions from the same coarse-grained force field family, Martini 2 and Martini 3, has been shown to produce qualitatively opposite behaviours for peptide insertion into zwitterionic model membranes.[16] Such methodological variability, with the choice of force field in particular, has also been noted in studies

of peptide aggregation and protein-protein interactions, and may influence key mechanistic observables such as oligomerisation propensity or membrane insertion pathways.[11,16,17]

Standardising physiologically motivated conditions in *in vitro* experiments and adopting harmonised simulation protocols would allow for more meaningful comparisons between studies and a clearer understanding of the mechanistic determinants of AMP activity. Community-wide benchmarks and the use of shared protocols, particularly for simulation force fields and membrane models, will be essential to achieve this.

References

1. Pedebos, C., Smith, I. P. S., Boags, A. & Khalid, S. The hitchhiker's guide to the periplasm: Unexpected molecular interactions of polymyxin B1 in E. coli. *Structure* **29**, 444-456.e2 (2021).
2. Smith, I. P., Pedebos, C. & Khalid, S. Molecular crowding alters the interactions of polymyxin lipopeptides within the periplasm of E. coli: insights from molecular dynamics. *The Journal of Physical Chemistry B* **128**, 2717–2733 (2024).
3. Kandasamy, S. K. & Larson, R. G. Effect of salt on the interactions of antimicrobial peptides with zwitterionic lipid bilayers. *Biochimica et Biophysica Acta (BBA)-Biomembranes* **1758**, 1274–1284 (2006).
4. Hilpert, K. *et al.* Short Cationic Antimicrobial Peptides Interact with ATP. *Antimicrobial Agents and Chemotherapy* **54**, 4480–4483 (2010).
5. Yu, H.-Y. *et al.* Easy strategy to increase salt resistance of antimicrobial peptides. *Antimicrobial agents and chemotherapy* **55**, 4918–4921 (2011).
6. Chu, H.-L. *et al.* Boosting salt resistance of short antimicrobial peptides. *Antimicrobial agents and chemotherapy* **57**, 4050–4052 (2013).
7. Pilonieta, M. C., Erickson, K. D., Ernst, R. K. & Detweiler, C. S. A protein important for antimicrobial peptide resistance, YdeI/OmdA, is in the periplasm and interacts with OmpD/NmpC. *Journal of bacteriology* **191**, 7243–7252 (2009).
8. Robustelli, P., Piana, S. & Shaw, D. E. Developing a molecular dynamics force field for both folded and disordered protein states. *Proceedings of the National Academy of Sciences* **115**, E4758–E4766 (2018).
9. Piana, S., Robustelli, P., Tan, D., Chen, S. & Shaw, D. E. Development of a force field for the simulation of single-chain proteins and protein–protein complexes. *Journal of chemical theory and computation* **16**, 2494–2507 (2020).

10. Best, R. B., Zheng, W. & Mittal, J. Balanced Protein–Water Interactions Improve Properties of Disordered Proteins and Non-Specific Protein Association. *J. Chem. Theory Comput.* **10**, 5113–5124 (2014).

11. Javanainen, M., Martinez-Seara, H. & Vattulainen, I. Excessive aggregation of membrane proteins in the Martini model. *PLOS ONE* **12**, e0187936 (2017).

12. Lamprakis, C. *et al.* Evaluating the efficiency of the Martini force field to study protein dimerization in aqueous and membrane environments. *Journal of Chemical Theory and Computation* **17**, 3088–3102 (2021).

13. Gregory, S. M., Pokorny, A. & Almeida, P. F. F. Magainin 2 Revisited: A Test of the Quantitative Model for the All-or-None Permeabilization of Phospholipid Vesicles. *Biophysical Journal* **96**, 116–131 (2009).

14. Mercer, D. K. *et al.* Antimicrobial Susceptibility Testing of Antimicrobial Peptides to Better Predict Efficacy. *Front. Cell. Infect. Microbiol.* **10**, (2020).

15. Aisenbrey, C., Amaro, M., Pospíšil, P., Hof, M. & Bechinger, B. Highly synergistic antimicrobial activity of magainin 2 and PGLa peptides is rooted in the formation of supramolecular complexes with lipids. *Sci Rep* **10**, 11652 (2020).

16. Spinti, J. K., Neiva Nunes, F. & Melo, M. N. Room for improvement in the initial martini 3 parameterization of peptide interactions. *Chemical Physics Letters* **819**, 140436 (2023).

17. Stark, A. C., Andrews, C. T. & Elcock, A. H. Toward Optimized Potential Functions for Protein–Protein Interactions in Aqueous Solutions: Osmotic Second Virial Coefficient Calculations Using the MARTINI Coarse-Grained Force Field. *J. Chem. Theory Comput.* **9**, 4176–4185 (2013).